The Influence of Salivary Statherin, Histatin-1 and Their 21 N-terminal Peptides Individually and When in Combination on the Demineralisation of Hydroxyapatite and Enamel. The Effect of Peptides Adsorption, Aggregation, Surface Charge and Secondary Structure

Huda Barak A Almandil BDS (KSU), MClinDent Paediatric Dentistry(QMUL)

Supervised by Prof. Paul Anderson, Dr Maisoon Al-Jawad

Thesis submitted in fulfilment of the requirements for the degree of Doctor of Philosophy in the University of London

2018

Dental Physical Sciences Unit, Institute of Dentistry,

Barts and the London School of Medicine and Dentistry,

Queen Mary University of London

I Huda Barak Almandil, confirm that the research included within this thesis is my own work or that where it has been carried out in collaboration with, or supported by others, that this is duly acknowledged below, and my contribution indicated. Previously published material is also acknowledged below.

I attest that I have exercised reasonable care to ensure that the work is original and does not to the best of my knowledge break any UK law, infringe any third party's copyright or other Intellectual Property Right, or contain any confidential material.

I accept that the College has the right to use plagiarism detection software to check the electronic version of the thesis.

I confirm that this thesis has not been previously submitted for the award of a degree by this or any other university.

Signature: Huda Almandil

Date:14/2/2018

Table of Contents

Figure Index viii
Table Index xvi
List of Abbreviations xvii
Acknowledgements xviii
Abstract xix
Chapter 1. General Introduction 1
1.1 Aims and Objectives 2
Chapter 2. Enamel and Enamel Demineralisation 5
2.1 Dental Hard Tissues 5
2.2 Enamel 5
2.3 Enamel Mineral Composition 9
2.4 Enamel Caries 10
2.4.1 Histological Changes in Caries Enamel 11
2.4.2 Dissolution Models 13
2.5 Erosion 17
2.6 Hydroxyapatite as a Model System for Dental Enamel 20
Chapter 3. Saliva and Dental Health 22
3.1 Saliva 22
3.2 Salivary Secretion 23
3.3 General Function of Saliva 26
3.3.1 Food Taste, Clearance and Digestion 26
3.3.2 Lubrication 27
3.3.3 Buffering 27
3.3.4 Antimicrobial Effects 28
3.3.5 Preservation of Tooth Integrity 29
3.4 Acquired Enamel Pellicle 30
Chapter 4. Salivary Statherin and Histatin 33
4.1 Salivary Human Statherin (STN) 33
4.2 Salivary Human Histatins 38
Chapter 5. Salivary Proteins/Peptides and The Mineralised Tissue Affinity 42
5.1 Hydroxyapatite and Enamel as an Adsorbent Surface 42

5.2 Role of Amino Acids and Their Functional Groups in Peptide/Protein and HA Adsorption43

5.3 Sequences and Conformation of Peptide/Protein Accountable for the Adsorption onto HA 46

5.4 Thermodynamics of Peptide/Protein Adsorption to HA..... 48

5.5 Effect of Different Biological Molecules on Protein/Peptide Adsorption 49

5.6 Affinity of Salivary Proteins/Peptides for HA/Enamel 50

5.7 Salivary Proteins/Peptides and Enamel Homeostasis..... 51

5.7.1 Buffering Capacity..... 51

5.7.2 Inhibition of Calcium Phosphate Salts Precipitation..... 52

5.7.3 Inhibition of Mineral Demineralisation 52

TECHNIQUES USED IN THIS STUDY 54

Chapter 6. Scanning Microradiography (SMR) 55

6.1 Scanning Microradiography (SMR) 55

6.1.1 Foundation of Electromagnetic Radiation 55

6.1.2 X-ray Production 56

6.1.3 X-ray Tube 57

6.1.4 Micro-focus Tubes 58

6.1.5 Electron Impact X-ray Source 58

6.2 X-ray Interaction with Matter 59

6.2.1 Photoelectric Absorption 60

6.2.2 Compton Scattering 60

6.2.3 Rayleigh Scattering 61

6.2.4 Pair Scattering 61

6.2.5 X-ray Attenuation: Beer's law 61

6.3 X-ray Detection 63

6.3.1 Semiconductor Detectors 63

6.4 Multi-channel Analyser (MCA) 64

6.5 SMR Apparatus 65

6.5.1 X-ray Generator 65

6.5.2 X-ray Detector 66

6.5.3 SMR Stage 66

6.5.4 SMR Cell 66

6.6 Data Analysis at a Scanning Position 67
6.7 Calculation of The Mineral Mass loss 68
6.7.1 Percent Reduction in the Rate of Mineral Loss (PRRML) 69
6.8 Responsiveness of SMR 71
6.9 Advantages of SMR 71
Chapter 7. Nano-Spectrophotometry 73
7.1 Introduction 73
7.2 Beer-Lambert Law 74
7.3 Protein Absorption 75
7.4 Advantages of Nano-Spectrophotometry 76
Chapter 8. Dynamic Light Scattering (DLS) 77
8.1 Particle Size Measurement 77
8.2 Zeta Potential 79
8.3 Advantages of DLS 79
Chapter 9. Circular Dichroism (CD) 81
9.1 Background 81
9.2 Theory 81
9.3 CD Data Analysis 82
9.4 Deconvolution of the CD Spectra 83
9.5 CD of Proteins 83
9.6 Application of CD in biology 85
Chapter 10. Secondary Structure Prediction of Individual Peptides 86
10.1 Protein Secondary Structure Prediction Using Robetta software 86
10.2 Protein Secondary Structure Prediction Using PSIPRED (Bioinformatics Group) 88
EXPERIMENTAL STUDIES 90
Chapter 11. Spectrophotometric Characterisation of the Adsorption of Statherin, Histatin-1 and Their 21 N-terminal Peptides Individually and When in Combination onto HA Beads, HA Discs and Enamel 91
11.1 Introduction 91
11.2 Materials 92
11.2.1 Chemical Solutions and Peptide Samples 92
11.2.2 Particle Size Analysis of HA Beads 95

11.2.3 Spectrophotometric Calibration of STN, HTN, F-STN21, and C-HTN21 Absorbance 96

11.3 Spectrophotometric Methods 97

11.3.1 Adsorption of STN, HTN, F-STN21, and C-HTN21 Individually onto HA Beads 97

11.3.2 Adsorption of Peptides When in Combination onto HA Beads 99

11.3.3 Desorption of STN, HTN, F-STN21, and C-HTN21 Individually or When in Combination from HA Beads 100

11.3.4 Adsorption of STN, HTN, F-STN21, and, C-HTN21 Individually onto HA Discs, and Enamel 101

11.4 Results 102

11.4.1 Adsorption of STN, HTN, F-STN21, and C-HTN21 Individually onto HA Beads 102

11.4.2 Adsorption of STN, HTN, F-STN21, and C-HTN21 When in Combination onto HA Beads 105

11.4.3 Desorption of STN, HTN, F-STN21, and, C-HTN21 Individually and When in Combination from HA Beads 110

11.4.4 Adsorption of STN, HTN, F-STN21, and, C-HTN21 Individually onto HA Discs, and Enamel 111

11.5 Discussion 113

11.5.1 Adsorption of STN, HTN, STN21, and HTN21 Individually onto HA Beads 113

11.5.2 Adsorption of STN, HTN, F-STN21, and C-HTN21 When in Combination onto HA Beads 117

11.5.3 Desorption of Peptides individually and When in Combination from HA Beads 120

11.5.4 Adsorption of STN, HTN, F-STN21, and, C-HTN21 Individually onto HA Discs, and Enamel 121

11.6 Conclusions 124

Chapter 12. Aggregation, Surface Charge and Secondary Structure of Statherin, Histatin-1 and Their 21 N-terminal Peptides Individually and When in Combination in Solution 126

12.1 Introduction 126

12.2 Materials and Method 127

12.2.1 Aggregation and Surface Charges of STN, HTN, STN21, and HTN21 Individually and When in Combination 127

12.2.2 CD Investigation of the Secondary Structures of STN, HTN, STN21, and HTN21 Individually, and When in Combination....128
12.2.3 Secondary Structure Predictions of STN and HTN Individually ...129
12.3 Results....130
12.3.1 Particle Size, Surface Charge and Secondary Structure of STN, HTN, STN21, and HTN21 Individually....130
12.3.2 Particle Size, Surface Charge and Secondary Structure of STN, HTN, STN21, and HTN21 when in Combination 138
12.4 Discussion....141
12.4.1 Aggregation, and Surface Charge of STN, HTN, STN21, and HTN21 Individually 141
12.4.2 Secondary Structure Conformation of STN, HTN, STN21, and HTN21 Individually 143
12.4.3 Aggregation, Surface Charge and Structural Conformation of STN, HTN, STN21, and HTN21 when in Combination....148
12.5 Conclusions 151
Chapter 13. The Effect of Statherin, Histatin-1 and Their 21 N-terminal Peptides Individually and When in Combination on HA and Enamel Demineralisation Rates 153
13.1 Introduction 153
13.2 Materials and Method 154
13.2.1 Hydroxyapatite Discs and Enamel Block Preparation....154
13.2.2 Chemical Solutions and Peptide Samples....155
13.2.3 SMR Experimental Method....156
13.3 SMR Results....161
13.3.1 Effect of STN, HTN, STN21 and HTN21 Individually on HA and Enamel Demineralisation Rates....161
13.3.2 Effect of STN, HTN, STN21, HTN21 When in Combination on HA and Enamel Demineralisation Rates....164
13.4 Discussion....169
13.4.1 The Effect of STN and STN21 Individually on Reducing HA and Enamel Demineralisation Rates....169
13.4.2 The Effect of HTN and HTN21 Individually on HA and Enamel Demineralisation Rates....170
13.4.3 Comparing the Effect of STN, and STN21 with HTN, and HTN21 on HA and Enamel Demineralisation Rates 171

13.4.4 The Effect of Peptides When in Combination on HA and Enamel Demineralisation Rates 172
13.4.5 Differences in Demineralisation Rates Between Hydroxyapatite and Enamel 175
13.5 Conclusions 176
Chapter 14. Overall Discussion 178
14.1 Overall Discussion of the Studies of STN, HTN, STN21, and HTN21 Individually 179
14.2 Overall Discussion of the Studies of STN, HTN, STN21, and HTN21 When in Combination 183
Chapter 15. Using Non-Human STN21 Sequences to Investigate the N-terminal Sequence Features Needed for the Adsorption onto HA and Demineralisation Reduction 186
15.1 Rationale Behind Using Non-human Statherin Sequences 186
15.2 Materials and Methods 188
15.3 Results 191
15.3.1 Adsorption of the 21 N-terminal Non-Human Peptides onto HA Beads 191
15.3.2 Effect of the 21 N-terminal Non-Human Peptides on HA Discs Demineralisation Rate 192
15.3.3 Secondary Structure Prediction of the Non-human STN Peptides 192
15.4 Discussion 201
15.5 Conclusions 205
Chapter 16. Conclusions, Clinical Implications and Future Work 206
16.1 Conclusions 206
16.2 Clinical Implications 207
16.3 Future Work 209
References 213
Appendix 1 239
Appendix 2 240
Appendix 3 241
Appendix 4 249

Figure Index

Figure 2.1 Enamel extracellular matrix proteins and proteinases, gene localisation and suggested role (Moradian-Oldak, 2012). 8

Figure 2.2 Enamel and (part of dentine) caries zones and as classified by Silverstone (Sapp et al., 2004). When the caries process spread along the EDJ, rapid involvement of the dentinal tubules occurs and act as tract leading to the pulp. 11

Figure 2.3 Dissolution model according to diffusion theory. Enamel minerals are dissolved according to their building units and their subsequent and transported to the bulk solution through the diffusion layer. 14

Figure 2.4 Mono- and polynuclear dissolution models. A: Mononuclear model; B: Polynuclear model; C: Polynuclear model with multiple steps (Ehrlich et al., 2009). 15

Figure 2.5 Unit cell of HA crystallite 20

Figure 4.1 Jpred4 secondary structure prediction of STN, showing secondary helical confirmation confined mostly to the N-terminus (in red). 36

Figure 4.2 STN functional characteristics according to the amino acid sequence. (Helmerhorst et al., 2010) 37

Figure 4.3 Jpred4 secondary structure prediction of HTN, showing secondary helical confirmation confined mostly to the N-terminus (in red). 41

Figure 5.1 Typical chemical structure of an amino acid, R is the function group specific for each amino acid as shown in Figure 5.2. 43

Figure 5.2 The twenty-one amino acids that appear in the genetic code; categorized according to their hydrophobicity, charge, and functional groups (Fleming and Ulijn, 2014). 44

Figure 5.3 Structural change of phosphorylated serine. In peptides such as STN and HTN, a post-translational modification occurs in which the N-terminal serines are phosphorylated by a protein kinase by the addition of a covalently bound phosphate group (Moreno et al., 1991). 45

Figure 6.1 Schematic of SMR X-Y scanning stage with SMR cells, an X-ray beam is targeted on the specimen and the attenuated X-ray photon is detected by a photon counting detector. 55

Figure 6.2 Electromagnetic radiation is a wave in space or through matter with the electric and magnetic field components perpendicular to each other and perpendicular to the direction of energy propagation (Seibert, 2004). 56

Figure 6.3 Schematic diagram showing basic components of an X-ray tube (A) and X-ray tube used in SMR machine with silver (Ag) target (B). 57

Figure 6.4 X-ray spectrum produced by a tube with tungsten target showing continuous and characteristic radiation. 58

Figure 6.5 X-ray attenuation mechanisms 60

Figure 6.6 Schematic diagram of SMR cell containing HA disc. Water or acidic solutions are circulated through the cell by introducing the solutions through the bottom input (solution in) and then removed by the upper output (solution out). A third output is used to de-pressure the cell (Lingawi, 2012). 67

Figure 6.7 SMR raw data showing a linear change in mineral mass loss per unit area plotted against time (≈48 h) during exposure to an acidic environment (pH 4.0) at a single scan position on a HA sample. RML_{HA} was determined by linear regression fitting of the slope and the number of data points, (y = a + bx), 2.27Ex 10^{-4} g cm^{-2} h^{-1}, SE = 5.3420x 10^{-6} g cm^{-2} h^{-1}). 69

Figure 6.8 The gradient of the measured slops before (circles) and after exposure to HTN (triangles) measured at a single scan position on a HA sample. Exposure to 200 µmol/l of HTN reduced the mineral loss rate by 36.4%. The SE of the rates before and after the exposure to the peptide were 2.45x10^{-6} g cm^{-2} s^{-1} and 2.59x10^{-6} g cm^{-2} s^{-1} respectively. 70

Figure 6.9 Mineral mass changes in a scan position in a HA sample during exposure to in vitro acidic solution. After the first 29 hrs of demineralisation, the enamel block was exposed to PBS (negative control) for 24 hr. Demineralisation was noted to halt immediately and the mineral density measurement changed accordingly. The demineralisation continued when the acidic solution was reintroduced to the cell and mineral loss was measured again. The gap noted in the data after the introduction of the acidic solution represents the X-ray halting time needed for the removal of PBS and sample wash with distal water (±15 min). 71

Figure 7.1(A) Spectra scan of aromatic amino acids. (B) The three aromatic amino acids that give absorbance between 275 and 280 nm: tryptophan (W), tyrosine (Y) and phenylalanine (F) (Held, 2003). 76

Figure 9.1 Secondary structure conformations, shown in a characteristic CD spectrum, α-helix (referred to in red), β-strand (blue), and random coil (green) (Correa and Ramos, 2009). 84

Figure 10.1 An example of online Robetta software structure prediction submission web page, showing the method for secondary structure prediction (Ginzu), target name, and analysis using the primary sequence (AA). 87

Figure 10.2 Typical 3D structure predictions using Robetta software. Where the N-terminals are shown in blue, while the C-terminals are shown in orange. Each model A), (B), (C), (D), and (E) is possible to occur. The presence of a repeated conformation in each model such as the helical conformation in the N-terminal indicates that it is more probable to occur in the secondary conformation of a peptide. 87

Figure 10.3 An example of UCL Bioinformatics Group server structure prediction submission web page, showing the method for secondary structure prediction (PSIPRED), and analysis using the primary sequence (Input Sequence). 88

Figure 10.4 Typical structural prediction diagram using PSIPRED. Where Conf. represent the confidence value at each position in the alignment, given as a series of blue bar graphs. Pred. is the predicted secondary structure, and AA is the target sequence. 89

Figure 11.1 Instrumental absorbance plot of F-STN21 and C-HTN21 combined. (A) Absorbance peak of C-HTN21 at 327 nm. (B) Absorbance peak of F-STN21 at 498 nm. STN21 was synthesised with fluorescein at the C-terminus and HTN21 with Coumarin for two reasons. These tags increased the absorbance and allowed the peptides to be measured separately while in combination. 94

Figure 11.2 Scanning electron microscopy of the Bio-Rad ceramic HA beads (CHT Type I), demonstrating the HA particle size variation and surface discrepancy. 95

Figure 11.3 Peptides calibration plots. (A) STN standard solution concentration and its dilutions plotted versus absorbance at 278 nm. (B) HTN standard solution concentration and its dilutions plotted versus absorbance at 278 nm. (C) F-STN21 standard solution concentration and its dilutions plotted versus absorbance at 498 nm. (D) C-HTN21 standard solution concentration and its dilutions plotted versus the absorbance of coumarin at 352 nm. All peptides showed a linear relation between the absorbance and the changes in concentration. 97

Figure 11.4 Examples of a saturation plot calculated from the spectrometric absorbance. The plots show the MAPA (at 200 nmol/ml) after exposure to 1.0 mg of HA beads for 120 min. The MAPA was obtained at saturation. $T_{0.5}$ was determent from the curve when half-saturation was achieved. 98

Figure 11.5 Saturation plots of STN(A) and F-STN21(B) showing the MAPA vs. time when exposed to 1.0 mg of HA. Changes in the MAPA was measured until a plateau was achieved. 102

Figure 11.6 (A) Mean amounts of STN and F-STN21 adsorbed (MAPA) at two different concentrations to 1 mg of HA beads (B) The mean time during which half of the peptide adsorbed onto HA beads. The error bars represent the standard errors of the means (n=4, $p< 0.05$*, $p< 0.01$**) 103

Figure 11.7 Saturation plots of HTN(A) and C-HTN21(B) showing the MAPA vs. time when exposed to 1.0 mg of HA. Changes in the MAPA was measured until a plateau was achieved 104

Figure 11.8 (A) Mean amounts of HTN and C-HTN21 adsorbed (MAPA) at two different concentrations to 1 mg of HA bead. (B) The time during which half of the peptide adsorbed onto HA beads. The error bars represent the standard error of the means (n=4, $p< 0.05$*, $p< 0.01$**, $p < 0.001$ ***) 104

Figure 11.9 Saturation plot of STN measured at 278 nm and, C-HTN21 measured at 327 nm, when in combination at 100 nmol/ml of each, after the exposure to 1.0 mg of HA. 106

Figure 11.10 Saturation plot of F-STN21 measured at 498 nm and, HTN measured at 278 nm, when in combination at 100 nmol/ml of each, after the exposure to 1.0 mg of HA. 106

Figure 11.11 Saturation plot of F-STN21 measured at 498 nm and, C-HTN21 measured at 327 nm, when in combination at 100 nmol/ml of each, after the exposure to 1.0 mg of HA.....107

Figure 11.12 Saturation plot for STN and HTN when added sequentially to 1 mg of HA. (A) The MAPA of STN after the exposure of 1.0 mg of HA to 100 nmol/ml of HTN. (B) The MAPA of HTN after the exposure of 1.0 mg HA to 100 nmol/ml of STN. 107

Figure 11.13 MAPA individually and when in combination onto 1.0 mg of HA beads and the time during which half of the peptide adsorbed onto HA beads. (A) MAPA for STN at 100 nmol/ml, and, at 200 nmol/ml (blue stripes), and when combined with HTN or C-HTN21(B) MAPA for F-STN21 at 100 nmol/ml, and, at 200 nmol/ml (blue stripes), and when combined with HTN or HTN21(C) $T_{0.5}$, for STN individually and when in combination (D)$T_{0.5,}$ for F-STN21 individually and when combined. The error bars represent the standard error of the means (n=4, $p < 0.05$ *, $p< 0.01$ **, $p < 0.001$ ***). 108

Figure 11.14 MAPA individually and when in combination onto 1.0 mg of HA beads and the time during which half of the peptide adsorbed onto HA beads. (A) MAPA for HTN individually at 100 nmol/ml, and, at 200 nmol/ml (blue stripes), and individually when combined with STN or F-STN21(B) MAPA for C-HTN21 individually at 100 nmol/ml, and, at 200 nmol/ml (blue stripes), and individually when combined with STN or F-STN21(C) $T_{0.5}$, for HTN individually and when in combination (D)$T_{0.5,}$ for C-HTN21 individually and when combined. The error bars represent the standard error of the means (n=4, $p < 0.05$ *, $p< 0.01$ **, $p < 0.001$ ***).....109

Figure 11.15 Typical desorption plots of peptides. (A) Desorption plot of STN after the exposure to 1ml of acetic acid pH 4.0. (B) Desorption plot of STN after the exposure to 1 ml of 2M of NaCl. STN did not show any desorption from HA bead when exposed to either of the desorption solutions.....111

Figure 11.16 Mean percent of peptides adsorbed onto HA discs and enamel samples used in SMR demineralisation study at 100 and 200 nmol/ml. (A) MPPA of STN and F-STN21, (B) MPPA of HTN and C-HTN21. The error bars represent the standard error of the means (n=3, $p < 0.001$ ***). 111

Figure 11.17 Amino acid sequence starting from the N-terminus. (A) STN, (B)HTN. 115

Figure 11.18 Schematic illustrations of proteins adsorption and orientation changes. (A) At low concentration, surface density is dependent on peptide-surface interaction. (B) At higher concentration the peptide surface density is partially dependent on peptide-peptide interactions that affect surface interactions. 116

Figure 11.19 Schematic illustration of co-operative peptide-peptide adsorption, in this co-operative adsorption the incoming peptide (orange) diffuse to the adsorbent surface at the same time it is repelled horizontally (guided) by another adjacent peptide (blue). 118

Figure 11.20 Schematic HA model showing the four crystal faces that proteins adsorb on (Masica et al., 2010). 123

Figure 12.1 Mean zeta-potential measurements of STN, HTN, STN21 and HTN21 individually at 100 and 200 µmol/l, and the standard error of the mean (n=3, p< 0.001***). 131

Figure 12.2 Mean residue ellipticity vs wavelength of individual peptides at 100 µmol/l and at 200 µmol/l, measurements were taken at 37 °C and pH 7. Fitting of the spectra was done using SigmaPlot 10.0 (Systat Software, CA, USA). 132

Figure 12.3 Fraction of folding of the structural components present in (A) STN, and (B) STN21, both at 100 and 200 µmol/l. (C) HTN, and (D)HTN21 both at 100 and 200 µmol/l, using CONTINLL SP43 fit. Error bars represent the RMSD. The RMSD calculated by the CD apps software at 100 µmol/l, STN-0.022, STN21-0.05, HTN-0.094, HTN21-0.022. At 200 µmol/l STN-0.0.21, STN21-0.023, HTN-0.088, HTN21-0.023. 133

Figure 12.4 (A), (B), (C), (D), and (E) 3D structural predictions of human STN using Robetta software. 135

Figure 12.5 Secondary structure prediction of STN by PSIPRED software. 136

Figure 12.6 (A), (B), (C), (D), and (E) 3D structure predictions of human HTN using Robetta software. 136

Figure 12.7 Structure predictions of human HTN by PSIPRED software. 137

Figure 12.8 Mean zeta potential measurements of peptides in combination at 100 µmol/l , where (M) is the measured mean zeta potential by DLS, and (E) is the expected (calculated) mean zeta potential of the peptide when in combination at 100 μmol/l. The error bars represent the ±SE of the mean. 139

Figure 12.9 Fraction of folding of the secondary structure components present in peptides when in combination using CONTINLL SP43 fit, (A)STN+HTN, (B)STN+HTN21, (C)STN21+HTN, and (D)STN21+HTN21 in (Solid blue) at a total concentration of 200 μmol/l. The expected (calculated) fraction of folding of the secondary structural components of the peptides when in combination if simply mixed in solution without interaction (diagonal blue stripes). Error bars represent the RMSD. The RMSD calculated by the CD apps software is STN+HTN-0.023, STN+HTN21-0.03, STN21+HTN-0.04, STN21+HTN21-0.023. 140

Figure 12.10 Amino acid sequence of STN, indicating polar (○) and non-polar (●) residues. 144

Figure 12.11 Amino acid sequence of HTN, indicating polar (○) and non-polar (●) residues. 146

Figure 12.12 Amino acid sequence of HTN21 and HTN-5, indicating polar (○) and non-polar (●) residue. 147

Figure 12.13 An illustration showing a possible aggregate structure of the peptides when in combination (peptide 1 in blue, peptide 2 in orange), where the surface of the aggregate is charged with the net charge of the N-terminal fragment of peptides (negative), while the core is formed by hydrophobic interactions. 150

Figure 13.1 HA disc mounted in SMR polymethyl methacrylate cell. 157

Figure 13.2 Area scan of an SMR cell with HA (A) or enamel sample (B) located centrally. X and Y axes represent coordinates of HA position on the SMR stage. 157

Figure 13.3 Mean percent reduction in the rate of mineral loss of HA discs (solid blue) and enamel blocks (blue diagonal stripes) exposed to 100, or 200 µmol/l of STN and STN21. The error bars represent the standard error of the means. No statistical difference between the PRRML of STN and STN21 for HA samples at either 100 or 200 µmol/l. Also, no statistical difference in the MPRRML of enamel treated with STN and STN21 at both concentrations. 161

Figure 13.4 Mean percent reduction in the rate of mineral loss of HA discs (solid blue) and enamel blocks (blue diagonal stripes) exposed to 100, or 200 µmol/l of HTN and HTN21.The error bars represent the standard error of the means. Statistical difference between the PRRML of HTN and HTN21 for HA samples at both 100 or 200 µmol/l (n=3, $p < 0.05$ *, $p< 0.01$ **). No statistical difference in the MPRRML of enamel treated with HTN and HTN21 at both concentrations. 162

Figure 13.5 SMR results of HA treatment with peptides in combination. (A) Comparing MPRRML of HA samples after treatment with STN at 100 and 200 µmol/l and combined with HTN or HTN21 (B) Comparing MPRRML of HA samples after treatment with STN21 at 100 and 200 µmol/l and combined with HTN or HTN21. (C) MPRRML of HA samples after treatment with HTN at 100 and 200 µmol/l and combined with STN or STN21. (D) MPRRML of HA samples after treatment with HTN21 at 100 and 200 µmol/l and combined with STN or STN21. Strong significant differences were found between HA samples treated with 100 and 200 µmol/l ($ρ< 0.01$). Significant differences were also found between HA samples treated with individual peptide at 100 µmol/l and HA treated with peptide mixture. (n=3, $ρ< 0.05$*, $ρ< 0.01$** and $ρ< 0.001$***). 164

Figure 13.6 SMR results of enamel treatment with peptides in combination. (A) Comparing MPRRML of enamel samples after treatment with STN at 100 and 200 µmol/l and combined with HTN or HTN21. (B) Comparing MPRRML of enamel samples after treatment with STN21 at 100 and 200 µmol/l and combined with HTN or HTN21. (C) MPRRML of enamel samples after treatment with HTN at 100 and 200 µmol/l and combined with STN or STN21. (4D) MPRRML of enamel samples after treatment with HTN21 at 100 and 200 µmol/l and combined with STN or STN21. Significant differences, $ρ< 0.05$* and, $ρ< 0.01$**, n=3..... 167

Figure 14.1 Correlation of the percent of adsorption of STN, HTN, STN21 and HTN21 individually at 100 and 200 µmol/l onto (A) HA discs, and (B) enamel, with the effect on the rate of demineralisation. 179

Figure 14.2 Correlation of the $T_{0.5}$ of STN, HTN, STN21 and HTN21 individually at 100 and 200 µmol/l onto HA with the effect on the demineralisation rates. 181

Figure 15.1(A) Mean amounts of non-human STN21 adsorbed at 200 µmol/l onto 1 mg of HA and (B) the mean time during which half of the peptide adsorb onto HA beads. The error bars represent the standard error of the means. The MAPA value and $T_{0.5}$ for C-STN21 were statistically different than the MAPA values and $T_{0.5}$ for human STN21, M-STN21, P-STN21 and S-STN21 ($p < 0.05$). 191

Figure 15.2 Mean percent reduction in the rate of mineral loss of HA discs after exposure to 200 µmol/l of human and non-human STN21 peptides for 24 hrs. Cattle-STN21 MPRRML value was the highest ($p < 0.05$), while Sheep-STN21 MPRRML was the lowest ($p < 0.05$). 192

Figure 15.3 (A), (B), (C), (D), and (E) 3D secondary structure predictions of Macaque-STN41 using Robetta software. 193

Figure 15.4 Secondary structure predictions of the Macaque-STN21 result by PSIPRED software. 193

Figure 15.5 Amino acid sequences for human and Macaque-STN21, showing polar (○) and non-polar (●) residues. 194

Figure 15.6 (A), (B), (C), (D), and (E) 3D secondary structure predictions of Pig-STN42 using Robetta software. 195

Figure 15.7 Secondary structure predictions of Pig-STN21 using PSIPRED software. 195

Figure 15.8 Amino acid sequences for human and Pig-STN21 sequences, showing polar (○) and non-polar (●) residues. 196

Figure 15.9 (A), (B), (C), (D), and (E) 3D secondary structure predictions of Sheep-STN37 using Robetta software. 197

Figure 15.10 Secondary structure prediction result for Sheep-STN21 using PSIPRED software. 198

Figure 15.11 Amino acid sequences for human and Sheep-STN21 sequences, showing polar (○) and non-polar (●) residues. 198

Figure 15.12 (A), (B), (C), (D), and (E) 3D secondary structure predictions of Cattle-STN40 using Robetta software. 199

Figure 15.13 Secondary structure prediction of Cattle-STN21 using PSIPRED software. 200

Figure 15.14 Amino acid sequence for human and Cattle-STN21 sequences, showing polar (○) and non-polar (●) residues. 200

Figure 15.15 Correlation of adsorption (MAPA) of STN21, Sheep-STN21, Macacaque-STN21, Pig-STN21 and Cattle-STN21 Individually 200 µmol/l onto HA beads with the effect on the rate of demineralisation (MPRRML). 203

Figure 15.16 Correlation of the $T_{0.5}$ of human and non-human STN21 at 200 µmol/l onto HA with the effect on the rate of demineralisation (MPRRML). 204

Table Index

Table 3.1 Inorganic composition of whole saliva (Ferguson, 1999). 24

Table 3.2 Organic composition and concentrations of salivary proteins/peptides and glycoproteins in human parotid and submandibular-sublingual saliva (Huq et al.,2007). 25

Table 3.3 Variation among individuals and within the same person in calcium and phosphate concentration, critical pH and flow rate of saliva (Anderson et al., 2001). 30

Table 4.1 Amino acid one letter abbreviation. 34

Table 4.2 STN primary sequence and the three variants, purified from submandibular/sublingual derived pellicle Jensen et al., (1991). The digits on the right for STN and SV2 are the accession no. from UniProt database (http://www.uniprot.org). 34

Table 4.3 Amino acid sequences of human salivary histatins, showing the alignment of amino acids of the three main forms 1,3, 5 and their 9 proteolytic peptides (Tsai and Bobek 1998). Reference digit was acquired from UniProt database. 39

Table 5.1 Hydrophobic (positive) and Hydrophilic (negative) hydropathy scores of amino acids side chains by Kyte and Doolittle, (1982). Green: hydrophobic, black: hydrophilic, red: hydrophilic and electronegative, and blue: hydrophilic and electropositive. 47

Table 11.1 Molecular weight of HTN, STN, HTN21 and STN21. 93

Table 12.1 Mean hydrodynamic radius of the peptide, individually at 100 and 200 μmol/l and the standard error of the mean. MR_H values of individual peptides at 100 μmol/l were statistically different than MR_H at 200μmol/l (n=3, $p < 0.001$). 130

Table 12.2 Mean hydrodynamic radius of peptides in combinations and the standard error of the mean. 138

Table 15.1 The 21 N-terminal amino acid sequences of the non-human peptides used in this study and the database references from UniProt (http://www.uniprot.org). 188

Table 15.2 The molecular weight of synthetic non-human 21 N-terminal STN. 189

List of Abbreviations

STN	statherin
STN21	statherin 21 N-terminal peptide
HTN	Histatin-1
HTN21	Histatins 21 N-terminal peptide
A-PRPs	Acidic proline-rich proteins
SMR	Scanning microradiography
DLS	Dynamic light scattering
CD	Circular dichroism
CPP	Casein phosphopeptide
DCPD	Dicalcium diphosphate dihydrate
DSHA	Degree of saturation with respect to hydroxyapatite
EDJ	Enamel-dentine junction
EMP	Enamel matrix protein
FTIR	Fourier transfer infrared spectroscopy
HA	Hydroxyapatite
NMR	Nuclear magnetic resonance
PP II	Helix polyproline II helix
RD	Rate of demineralisation
MPRRML	Mean percent reduction in the rate of mineral loss
MAPA	Mean amount of peptide adsorbed
R_H	Hydrodynamic radios
SDS	Sodium-dodecyl sulphate
XRD	X-ray diffraction
WHO	World Health Organisation
RML	Rate of mineral loss
MPRRML	Mean percent reduction in the rate of mineral loss
APR	Amount of peptide remaining
MAPA	Mean amount of peptide adsorption
MPPA	Mean percent peptide adsorbed

Acknowledgements

I would like to thank my supervisors Prof Paul Anderson and Dr Maisoon Al-Jawad who have supported and encouraged me throughout the last few years.

I am grateful for Dr Tony Williams for sharing his knowledge and helping me to develop my skills and confidence as a researcher, and above all for believing in me, my sincere thanks and appreciation.

I would like to thank all my colleagues at the Dental Physical Science Unit at the Institute of Dentistry at QMUL

I wish to thank my friends for their uplifting messages and unconditional support.

Finally, to my parents, to my family thank you for supporting me spiritually throughout my life, for your support and patience, I am forever thankful.

Abstract

Salivary proteins such as statherin (STN) are known to be involved in enamel de/remineralisation, the inhibition of crystal growth, and spontaneous precipitation of calcium phosphate salts. The active N-terminal of STN (STN21) is involved in binding with Ca^{2+} and in reducing HA demineralisation. In addition, salivary Histatin-1 (HTN) inhibits crystal growth of calcium phosphate salts but does not inhibit their spontaneous precipitation. These salivary peptides do not occur as individual molecules in saliva, they are part of a complex salivary system.

The aims were to investigate the effect of salivary STN, HTN and their 21 N-terminal peptides (STN21, and HTN21) individually and when in combination on the demineralisation rates of HA and enamel using scanning microradiography. In addition, to understand their effect on HA and enamel demineralisation, peptide adsorption onto HA and enamel was measured spectrophotometrically. Also, peptide aggregation, surface charge and, conformation in solution were investigated. The adsorption and demineralisation reduction of non-human STN was also investigated.

STN, HTN and STN21 individually showed similar adsorption and demineralisation reduction efficacy in HA but not in enamel. HTN21 showed the lowest demineralisation reduction of all peptides. STN21 when in combination with either HTN, or HTN21, showed the greatest demineralisation reduction of all peptides.

The increase in peptides demineralisation reduction efficacy when in combination suggests co-operative efficacy, which is further increased with

the removal of the C-terminal. All individual peptides were found to adopt an α-helical conformation at the N-terminal, which is important in peptide adsorption onto HA surfaces. When in combination conformational changes led to peptide interaction and caused an increase in their net negative charges. In conclusion, it was found that the degree to which demineralisation is reduced by peptides is correlated with the amount of peptide adsorbed.

Chapter 1. General Introduction

Saliva has a role in the defence against chemical, mechanical and microbial attacks in the oral cavity (Lendenmann *et al.,* 2000). The acquired enamel pellicle is formed on the tooth surface by selective adsorption of salivary components (Siqueira *et al*., 2012). Understanding the role of the pellicle requires knowledge of its composition, structure and mechanism of formation. Peptides and proteins are important in the inhibition of calcium phosphate crystallisation (Moreno *et al.,* 1979; Richardson *et al.,* 1993; *Salih et al.,* 2010), control of microbial adherence (Liljemark and Bloomquist 1981; Gibbons and Hay, 1988; Cannon *et al.,* 1995; Dawes *et al.,* 2015), and possibly calculus formation.

Salivary peptides such as STN and HTNs stabilise saliva which is supersaturated with calcium and phosphate salts. Acidification of saliva below the critical pH causes demineralisation of dental enamel of which hydroxyapatite (HA) $Ca_{10}(PO_4)_6(OH)_2$ is the main constituent (Margolis and Moreno, 1992).

Studies with single native or synthetic peptides provided physical parameters such as binding affinity and the number of binding sites for STN and HTNs (Moreno *et al.,* 1978; Yin *et al.,* 2003). However, the complexity of peptides and proteins forming pellicles *in vivo* requires complex experimental designs to understand not only the significant individual components but also the interactions. It is hoped that such data may be

used to help to synthesise models that mimic and optimise the oral environment protective function.

While many studies focus on the affinity of these peptides to HA, there are very few that accurately measure the direct physical effect of STN and HTNs (or truncated versions of them) on enamel and HA demineralisation in addition to providing kinetic data.

1.1 Aims and Objectives

The overall aim was to investigate and understand the demineralisation reduction efficacy of statherin and histatin both individually, and when in combination, and to correlate the amounts of individual peptides adsorbed with their effect on demineralisation of HA and enamel.

An additional aim was to study the effect of statherin interspecies amino acid sequence variations on binding and demineralisation reduction. This information could be used as a peptide engineering approach to develop statherin-like peptides with improved binding and therefore improved demineralisation reduction.

The first objective was to study the adsorption, desorption, and the binding rates characteristics of STN, HTN, STN21 and HTN21 individually, and when in combination, onto HA and enamel.

-Spectrophotometry was used to measure the adsorption, and desorption amount, and the binding rate of all these peptides, at two different concentrations individually, and when in combination, onto HA beads used as a chemical analogue of enamel.

-Spectrophotometry was used to measure the relative percent of individual peptides adsorption at two different concentrations, onto demineralised HA discs and enamel.

The second objective was to understand the underlying physico-chemical properties of these peptides in solution that contributes to their adsorption onto mineralised surfaces.

-Dynamic light scattering (DLS) was used to determine the net charge of STN, HTN, STN21 and HTN21 individually, and when in combination, and examine their possible interaction in solution at different concentrations.

-Circular Dichroism (CD) was used to determine the secondary structure of STN, HTN, STN21 and HTN21 individually, and when in combination in solution.

- Two protein structural prediction software systems, Robetta and PSIPRED Protein Sequence Analysis Workbench (Bioinformatics Group UCL) were used to further determine the secondary structure of all the peptides studied.

The third objective was to investigate the effect of STN, HTN, STN21 and HTN21 individually, and when in combination, on HA and enamel demineralisation rates *in vitro* under caries mimicking conditions.

- Scanning Microradiography (SMR) was used to directly measure the real-time effect of these peptides in two different concentrations individually, and when in combination, on HA and enamel demineralisation rates.

- The correlation of the percent adsorption (measured spectrophotometrically) of human STN, HTN, STN21 and HTN21 individually, at two different concentrations, onto HA discs and enamel blocks used in the demineralisation study, with the percent reduction of demineralisation (measured by the SMR) for the same HA discs and enamel blocks was also achieved.

The fourth objective was to use STN interspecies sequence variations to investigate the effect of the 21 N-terminal sequence, and α-helical structure on the adsorption of peptides onto HA, and HA demineralisation rates.

- Spectrophotometry was used to measure the adsorption of the 21 N-terminal STN from pig, cattle, macaque, and sheep onto HA beads.

- Scanning Microradiography (SMR) was used to directly measure real-time effects of the non-human peptides on HA demineralisation rate.

- Finally, the correlation of the amount of non-human peptides adsorbed onto HA beads (measured spectrophotometrically) with the percent reduction of demineralisation (measured by the SMR) was also achieved.

Chapter 2. Enamel and Enamel Demineralisation

2.1 Dental Hard Tissues

Physiological functions of teeth are possible due to different tissues involved in their composition. Teeth go through various chemical and physical processes; they are prone to compressive forces, wear, and chemical acidic attacks from food, and bacteria. Therefore, the tooth is protected by an exterior layer of dental hard tissue called enamel that shields the crown by a 2 mm thick layer occlusally and more in analogy to the cusps, while, the layer reduces cervically at the collar to just a few micrometres (Nanci, 2017). Underneath the enamel layer, dentine is present, and dentine is positioned beneath cementum in the root of the tooth. While ameloblasts produce enamel, odontoblasts produce dentine and cementoblasts produce cementum.

2.2 Enamel

Enamel is a translucent layer of calcified thin hard tissue, covering the anatomic crown of the tooth. It is the most mineralised tissue within the entire human body, particularly hard since it is primarily comprised of inorganic materials. Dental enamel consists of 95% calcium hydroxyapatite (Fincham and Belcourt, 1981). Trace minerals are found in the apatite crystal lattice making the mineral of enamel commonly referred to as substituted apatite or biological apatite. (Marthaler, 2003). The solubility of the enamel is affected by the concentration of these trace minerals. For

instance, the crystal structure becomes stronger with the presence of fluoride and the solubility decreases, whereas, the solubility increases by incorporating carbonate which disturbs the lattice (Nanci, 2017). Enamel hydroxyapatite crystals contain less carbonate and more fluoride in the outer layer as compared to the crystals in the inner layer. Therefore, the outer surface becomes less soluble in contrast to the deeper layers of the enamel (Fincham and Moradian, 1999).

Organic molecules form almost 1 to 2 % of enamel, in particular, the enamel-specific proteins enamelins, and amelogenins that have a high potential of binding hydroxyapatite crystals (Lussi and Hellwig, 2001). Enamel contains approximately 4 % water. All the components of enamel (water, organic, and inorganic) are highly organised.

The enamel prisms are aligned in thin and long structures (rods), with a diameter of about 4 to 8μm (Boyde, 1997). These rods appear as key-hole shaped structures when viewed in cross section. The number of rods in a tooth varies depending on the tooth type; the number differs from 5 million to 12 million in the lower lateral incisor and upper first molar, respectively.

The rods extend from the enamel-dentine junction (EDJ) to the surface of the tooth at right angles. A sheath made of protein matrix is around each developing rod (Nanci, 2017). Spaces exist between rods where crystals are not formed, which are typically called pores (diameter 1-10 nm) and account for 1-5 volume% of enamel. These pores allow the occurrence of fluid movement and diffusion making the enamel permeable. Also, they contribute to the hardness of the tooth and variations in the

density causing the formation of zones that are more vulnerable to demineralisation (Robinson and Briggs, 1981).

Enamel is generated through ectodermal derived ameloblast cells that go through a series of discrete differentiation phases that are associated with the different stages of enamel development. Ameloblasts are made from the ectodermal epithelium when the dental lamina is formed. Proliferation takes place as a result of invasion of the underlying mesenchyme by the neural crest cells. The ameloblasts are positioned at the base of the dental papilla around specific mesenchymal cells that secrets the dentinal matrix. In the pre-secretory phase, ameloblasts are separated from the odontoblasts by the basement membrane that is removed later when the ameloblasts go into their secretory stage. At this stage, an organic matrix is secreted by the ameloblasts, which is an enamel extracellular matrix, comprising 90% of amelogenin. Whereas, the remaining 10% of its constituents include non-amelogenin proteins such as enamelin, ameloblastin, and tuftelin, serum proteins, such as albumin, along with the protease enzymes like kallikrein-4 (KLK4) and, enamelysin (Smith, 1998; Smith *et al.,* 2017). Amelogenins have an internal hydrophobic core, and a hydrophilic mineral binding domain which permits self-assembly into nanospheres and adhesion onto the c-axis of HA crystals. The nanospheres act as spacers between forming HA crystals, defining their dimensions by preventing lateral crystal growth (Fincham and Moradian, 1999).

Figure 2.1 shows enamel extracellular matrix proteins and their possible functions. Amelogenin functions as mineral ion binding precursor,

and crystal growth controller. Ameloblastine functions as a determiner and a maintainer of prismatic structure, while enamelin controls and support crystal growth (Moradian-Oldak, 2012).

Protein and proteinases	Human gene chromosomal localization	Knock out (KO) mousegross enamel phynotype	Proposed function in enamel
Amelogenin	*AMELX*; Xp22.3-p22.1, AMELY; Yp11	Hypoplastic Disorganized (prismless)	Stabilization of amorphous Ca-P phase, control of apatite crystal morphology and organization, control of enamel thickness
Ameloblastin	*AMBN*;4q21	Thin dysplastic mineralized layer is formed on top of dentin	Cell adhesion protein, controls cell differentiation, maintains rod integrity
Enamelin	*ENAM*; 4q21	No true enamel but focal areas of pathological calcified material	Cooperates with amelogenin to control mineral nucleation and elongated growth
Amelotin	*AMTN*;4q13.3	-------	---
KLK-4[1]	*KLK4*;19q13	Delayed maturation and defects at the DEJ	Digests enamel proteins during the maturation stage facilitating their removal and hardening the final layer of enamel
Mmp-20[2]	*MMP-20*; 11q22.3	Hypoplastic and hypomineralized enamel with decreased hardness that separates from dentin	Cleaves amelogenin, ameloblastin, and enamelin at the secretory stage to produce stable intermediates with defined functions
Ctrc[3]	*CTRC; 1p36.1*	---	----

Figure 2.1 Enamel extracellular matrix proteins and proteinases, gene localisation and suggested role (Moradian-Oldak, 2012).

When the ameloblasts go through their maturation phase, the organic matrix is fully degraded by proteolytic enzymes, Matrix metalloproteinase 20 (MMP20), and kallikrein-4 (KLK4) (Bartlett, 2013). Amelogenin proteolysis by MMP20 and KLK4 was studied by Zhu *et al.,* (2014). They observed preferential and selective degradation of amelogenin when adsorbed to HA than when in solution. They proposed that amelogenin proteins go through structural conformation upon adsorption onto HA crystals. These structural changes induce proteolytic

degradation by MMP20 and KLK4, which leaves space for HA crystals to grow in both length and width until the crystal surfaces contact the surrounding amelogenin proteins within the enamel matrix. This enables the secondary growth of the HA crystals that will eventually fill the spaces that have been occupied earlier by the proteins of the enamel extracellular matrix. Subsequently, the mature erupted tissue completely loses the ameloblasts (Smith *et al.,* 2017).

Dental enamel is not completely mineralised at the time of eruption, phosphorous, calcium and fluoride ions from saliva, form a covering sheath 10 to 100µm in thickness on enamel in order to fully mineralise the tooth (Elliott *et al.,* 1998; Bartlett, 2013).

2.3 Enamel Mineral Composition

Enamel is mainly hydroxyapatite (HA) that contains calcium and phosphate. In general, minor constituents of whole enamel include typically 3.0 wt. % CO_2, 0.4 wt. % Cl, 0.2 wt. % Mg, 0.01 wt. % F and many trace elements (Elliott 1994; Dowker and Anderson, 1999). Enamel contains hydroxyapatite that is carbonated at different levels varying from 4% to 6%. In hypo-mineralised enamel, the distribution of carbonate is usually higher (Jalevik *et al.,* 2001). In healthy teeth, the overall distribution of fluoride occurs along a gradient increasing from the core towards the outer layers (Anderson *et al.,* 1996a).

Elements like magnesium and potassium are higher in concentration in regions that are hypo-mineralised. Whereas, the concentration of sodium has been reported to be higher in regions where the enamel is defective

(Downer *et al.,* 2005). The concentration of chlorine and strontium are not directly related to the level of mineralisation. Traces of elements such as iron, zinc, and barium were found in the enamel of children living in polluted regions or as a result of specific nutrition regimes among children.

2.4 Enamel Caries

According to the WHO, dental caries is the most common oral disease. Sixty to ninety percent of school children and nearly 100% of adults have dental cavities that lead to pain and discomfort (WHO, 2012). Regardless of its impact on eating, speech and self-confidence, the impact on mortality rates is not high. However, the cost of dental caries treatment is more than the cost of treatment for cardiovascular disease and cancer combined (Moynihan and Petersen, 2004).

Caries is a complex and dynamic process that involves chemical demineralisation of dental hard tissue due to bacterial acidic product over a period of time (Kidd and Fejerskov, 2004). Bacteria metabolise sucrose from the diet and then produces acid which lowers the pH and demineralises hydroxyapatite (Featherstone, 2000). The range of pH of saliva is from 6.5 to 7.5 (Robinson and Shore, 2000). Dental caries is formed when the oral pH falls below the threshold value which is at pH 5.5 (Marsh and Nyvad, 2008). Prolonged exposure and/or frequent cyclic exposure below the critical pH increase the likelihoods of enamel demineralisation, which occurs at occlusal surfaces specifically during eruption and interproximal beneath the contact points when dental biofilm (plaque) is left intact (Aoba, 2004). When the balance between

demineralisation (mineral loss) and remineralisation (mineral gain) is disrupted, demineralisation of mineral surfaces will occur over time (Fejerskov *et al.,* 1990).

Despite the multifactorial aetiology that involves acids (of both extrinsic and intrinsic origin), dietary habits, social and physical factors, it is clear after various studies that prevention is possible (Fejerskov and Kidd, 2004).

2.4.1 Histological Changes in Caries Enamel

A dental carious lesion is categorised histologically into four zones, starting from enamel outer surface until the enamel dentine junction (EDJ) by Silverstone, (1981) (Figure 2.2).

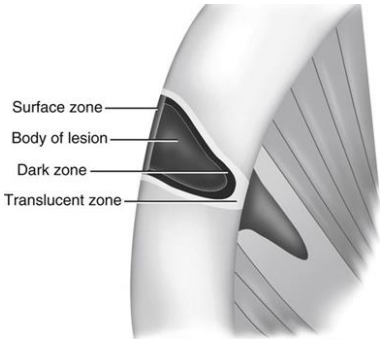

Figure 2.2 Enamel and (part of dentine) caries zones and as classified by Silverstone (Sapp et al., 2004). When the caries process spread along the EDJ, rapid involvement of the dentinal tubules occurs and act as tract leading to the pulp.

2.4.1.1 Surface Zone

As the pH is reduced an active demineralisation site is created by protonation (addition of a proton H^+) of phosphates (PO_4^{3-}) forming hydrogen phosphates (HPO_4^{2-}), creating an unstable crystal apatite. Due to

this instability, calcium ions are freed from the apatite crystals forming a 40 µm thick subsurface layer that is undersaturated.

The enamel outer surface remains apparently intact while subsurface demineralisation continues allowing inward acidic ion diffusion, and an outward mineral ion exchange. In the literature, subsurface demineralisation is mainly due to enamel structure anomalies, chemical enamel irregularities such as the presence of organic matrix in dental enamel or the presence of a supersaturated dental plaque layer in regards of calcium (Zahradnik and Moreno, 1977).

2.4.1.2 Body Zone

It represents the main part of the enamel caries lesion with a mineral mass loss of about 25-50 %, 5% appear near the periphery of the zone and 25% occur in the centre of the zone (Shellis and Wahab, 1993). The pores size is the largest in this zone (volume 5 to 25%) and will eventually form carious cavity following the breakdown of the surface layer.

2.4.1.3 Dark Zone

Adjacent to translucent zone, similar to the translucent zone large pores are present as well as small pores (1-10 nm diameter). When an enamel caries section is viewed under polarised light after being perfused with quinoline the lesion appears dark, as small pores cause the reversal of birefringence from negative to positive, since they are filled with air and not with histological medium (Kidd, 2005).

In the dark zone, the mineral mass loss is up to 2-4%. When exposed to artificial saliva or synthetic mineralisation solutions, the small pores show

partial remineralisation and an overall reduction of pore volume. This suggests that a simultaneous dynamic action of both demineralisation and remineralisation nature happens in this zone (Silverstone, 1981; Robinson and Shore, 2000).

2.4.1.4 Translucent Zone

In an advanced caries lesion, it represents the deepest zone, and 1% of the total mineral loss (Robinson and Shore, 2000). When viewed under light microscope perfused with quinoline there is an increase in porosity (up to ten-folds in volume), the zone appears structureless and therefore the zone looks translucent.

2.4.2 Dissolution Models

Models of calcium apatite dissolution in acid indicated important factors involved in enamel dissolution: apatite surface (adsorbed ions, and surface defect), substance bulk (composition, and particle size) and solution (composition, and pH). However, there are still missing factors that are involved in the overall explanation of the dissolution process. It would therefore be more insightful and informative to study all dissolution models available to gain a more complete and general overview of the enamel dissolution process from all aspects.

2.4.2.1 Diffusion and Kinetic Models

The chemical transport interaction between the reagents in the solution (H^+ and anions of acid) and the apatite elements (Ca^{2+} and F^-) mediates these dissolution models (Figure 2.3) (Higuchi *et al.,* 1984;

Thomann *et al.,* 1990; Brahim *et al.,* 2008). While the kinetic model emphasizes surface chemical interaction, the diffusion model is mediated by the dissolution rates of either chemical component and/or the products of the interactions (Ehrlich *et al.,* 2009). In the diffusion model, the solution adjacent to the apatite is saturated and the driving forces of dissolution are the concentration gradient within the diffusion layer. While in the kinetic model, the solution adjacent to the apatite is undersaturated and the gradient of ionic potential between the apatite surface and the solution is the driving force behind this process (Nancollas, 1974; Guidry and Mackenzie, 2003).

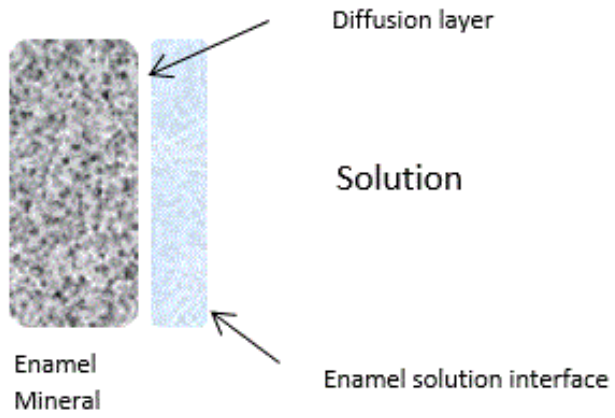

Figure 2.3 Dissolution model according to diffusion theory. Enamel minerals are dissolved according to their building units and their subsequent and transported to the bulk solution through the diffusion layer.

2.4.2.2 Mono- and Poly-nuclear Models

Mononuclear surface dissolution starts from a central detachment that leads to further breakdown. In polynuclear dissolution, the detachment can take place in multiple centres that may develop to multiple steps of break down as shown in Figure 2.4 (Ehrlich *et al.,* 2009).

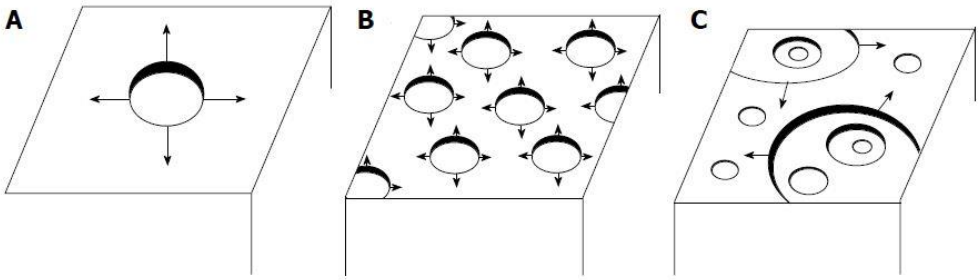

Figure 2.4 Mono- and polynuclear dissolution models. A: Mononuclear model; B: Polynuclear model; C: Polynuclear model with multiple steps (Ehrlich et al., 2009).

2.4.2.3 Self-inhibiting Layer Model

A self-inhibiting layer model refers to the formation of a calcium-rich layer on the surface of the apatite during dissolution (pH range 3.7-6.9) (Schaad *et al.,* 1997). At the early stages of dissolution, calcium release is observed to be lower than H^+ intake. As the process continues, the overall calcium release increases while H^+ intake decreases. As the process continues, dissolution overall rate decreases until the equivalence level is reached (2 H^+ and 1 Ca^{2+}) (Mafe *et al.,* 1992; Schaad *et al.,* 1997).

According to this model, after an initial dissolution of apatite, calcium cations in the solution adsorb on apatite surface (probably interacting with anionic counter ions or with negatively charged residues of proteins) forming a calcium rich layer. This layer is observed to be semi-permeable and positively charged (Thomann *et al.,* 1993).

2.4.2.4 Stoichiometric/non-stoichiometric Model

This model is determined by the measurement of ionic concentrations in solution or surface composition of the apatite throughout dissolution. In stoichiometric dissolution (congruent dissolution) the ions

dissolve at the same time and the dissolution rate is proportional to their molar concentrations in solution. Whereas in the non-stoichiometric dissolution model (incongruent) the ions dissolve independently, and the dissolution rates differ for each ion (Brown and Martin, 1999).

Studies of the effect of pH on HA dissolution have shown that the non- stoichiometric model is observed in solutions within 4.5 < pH < 8.2. While a stoichiometric dissolution of HA was found in solutions pH < 4.5 (Bengtsson *et al.,* 2009).

2.4.2.5 Chemical Model

According to this model, H^+ in solution interacts directly with the apatite crystal surface and reacts with PO_4^{3-} and OH^- producing HPO_4^{2-} and H_2O which causes a disruption of lattice bonds and the release of ions into solution (Equation 2.1):

$$Ca_{10}(PO_4)_6(OH)_2 = 10Ca^{2+} + H_2PO_4^- + H_2O \qquad \text{Equation 2.1}$$

According to Robinson *et al.,* (1995), the phosphate ion is probably the most important component of HA stability and/or dissolution. As the pH decreases, PO_4^{3-} ions, located at the accessible surfaces of the crystals, becomes protonated to form HPO_4^{2-}. This causes the mineral's surface to adopt properties of the more soluble calcium phosphate phase, dicalcium phosphate dihydrate (DCPD, $CaHPO_4.2H_2O$) (Elliott, 1994). Additionally, the Ca^{2+} in the lattice structure are held by the PO_4^{3-} ions and the change of some PO_4^{3-} to HPO_4^{2-} will weaken this bond, which results in some Ca^{2+} release from the apatite structure. This will further promote solubility of DCPD and dissolution of mineral. Protonation of some of the OH^- ions to

H_2O has minimal effect on the nature of the lattice since the OH^- ion is small and not such an integral part of the structure.

In conclusion, the suppositions made by each model are based on experimental methodology used to observe dissolution. Therefore, such models are particular to the parameters of each trial.

2.5 Erosion

Bacterial digestion of carbohydrates like sucrose and fructose creates acidic by-products in the dental biofilm that usually lower the salivary pH causing enamels degradation (Zero, 1996).

The irreversible and usually painless progression of losing dental hard tissue as a result of a chemical reaction like demineralisation or chelation that does not involve micro-organisms is called dental erosion (Marsh, 1999).

Susceptibility to dental erosion between people differs according to oral factors like oral pH value, buffering capacity of saliva, flow of the saliva, and formation of the pellicle. Nonetheless, it has been recognised that the ingestion of soft drinks and citrus fruits that form citric acid may be a major cause behind the progress of erosion (Littman, 2005; Chu *et al.,* 2010). Erosion prevalence is age related, about 28% and 52% between age groups of 7-10 and 11-14 years respectively. This could be explained by the change in the diet (Lussi*,* 2006). Carbonated soft drinks of a quite low pH value and the presence of sugar and various other additives contribute to the acid demineralisation and/or erosion of the dental enamel.

At the histological/microscopical level, it was thought that early stages of dental erosion are characterised with a softening of the enamel surface to a depth of 1-10 μm, whereas the enamel structure is still intact at this initial stage (Pindborg, 1970). However, Meureman and ten Cate (1996), and Imfeld, (1996) showed that erosion lesions show signs of subsurface loss and demonstrated hypo-mineralisation of a surface layer. Therefore, erosion is similar to the carious process with the important exception of the acid origin and a lack of dark zone. The absence of the dark zone may be explained by the much lower pH that is required to cause erosion-like lesion (pH 2-4), and the possibility that a precipitation of a more stable calcium phosphate phase is essentially made difficult if not totally prevented in this low pH range. The solubility of HA at pH 3 is about 100 times greater than at pH 5, but fortunately, exposure time to the extrinsic, or intrinsic acids is much shorter, allowing the buffering action of saliva.

Under controlled demineralisation conditions, caries lesions can be reproduced. Lesions of induced enamel caries are more homogeneously reproducible in contrast to natural caries (Kidd, 2005). Acetic acid has been used as demineralisation agent in many studies. It was found that acetic acid exhibits the same demineralisation effect as lactic acid (Anderson *et al.,* 2004).

At the initial stage of enamel demineralisation, microscopic studies showed the development of etch pits in the enamel rods (Featherstone *et al.*, 1979; Takuma, 1980). Enamel exposure to prolonged periods of acidic solution causes hollowing of enamel rods. In enamel crystal central areas, a preferential demineralisation was observed by Yanagisawa and Miake

(2003). This was described by Poole and Johnson, (1967) as keyhole shape of the enamel rod which is made up of a round head and narrow tail. Hydroxyapatite hexagonal crystals demonstrated similar demineralisation behaviour (Arends and Jongebloed, 1979). At the crystallite tip (or end) an etch pit is formed in a demineralisation spot (active site), successively a longitudinal demineralisation trail parallel to the c-axis is formed.

In enamel, the inter-prismatic spacing filled by organic matter separates crystallites. The space is between 16-40 Å and can be considered as a pathway for acidic diffusion. Acid penetration between crystallites in one rod was reported by Johnson *et al*., (1971), they found that it forms narrow clefts, particularly near rod junctions. Interestingly, crystals show similar morphological effect, therefore this observation cannot be accredited merely to the organic component in the enamel mineral.

At an atomic level irregularity such as “dislocations” present at apatite crystal are thought to be points where acidic demineralisation starts (Voegel and Frank, 1977). Active sites are thought to emerge from these dislocation points where chemical reactivity generally increases. In enamel apatite, these dislocations are parallel to the crystal c-axis which can explain the progress of core lesions in the course of enamel demineralisation.

It is believed that carbonated apatite might create straining fields around dislocation lines. Dark lines that run parallel to the c-axis were associated with preferential crystal demineralisation and were thought to form due to the increase in CO_3 content (Marshall and Lawless, 1981).

2.6 Hydroxyapatite as a Model System for Dental Enamel

There are some debates whether HA can be used as a good representative of dental enamel. Since HA has a constant chemical composition $Ca_{10}(PO_4)_6(OH)_2$, and the enamel chemical composition varies (as mentioned in Section 2.3). Also, owing to the different chemical composition HA has a higher mineral density (3.15 g/cm^3), when equated to enamel mineral density (2.99-3.02 g/cm^3). Additionally, the crystallographic studies of enamel and HA show different crystal lattice spacing between both; dental enamel, a= 9.455 Å and c= 6.881 Å while for HA, a= 9.418 Å and c= 6.881 Å (Pezzotti *et al.,* 2015). Figure 2.5 shows HA mineral crystal parameter and crystal structure (also called crystallite) comprised of millions of HA unit cells.

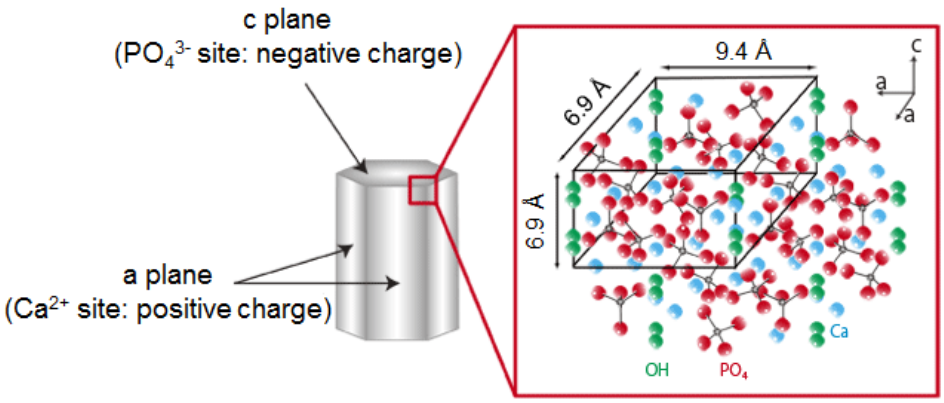

Figure 2.5 Unit cell of HA crystallite

Although there are differences between HA and enamel minerals, HA is generally acknowledged as an enamel analogue. This is mainly because HA is easier to attain, and no ethical approval is required. Also, the well-known and characterised chemical composition of HA and the

chemical adaptability of the composition by the addition of impurities such as fluoride mark it as a good representative of enamel.

To conclude, HA is structurally and chemically homogeneous when compared with enamel. However, the demineralisation kinetics is believed to be similar, making it a possible model for caries and erosion *in vitro* studies (Shellis *et al.,* 2010).

Chapter 3. Saliva and Dental Health

3.1 Saliva

Saliva is the oral fluid that covers oral hard and soft tissue and lubricates of food. It is a mixed secretion from both major, minor salivary glands and contains leakage from the gingival sulcus. Ten percent is secreted by minor salivary glands. While 90% is secreted by three paired glands (*i.e.* parotid, submandibular, and sublingual). Normally 0.5 to 1.0 litres of saliva are secreted per day (Khurshid *et al.,* 2016a). The stimulated flow rate is 2.5-5.0 ml/min, decreasing to 0.05-1.8 ml/min when not stimulated and less than 0.01 ml/min during sleeping (Siqueira *et al.,* 2008; Carneiro et al., 2014).

Salivary epithelial cells that are highly differentiated can produce oral fluid with a specific function. The secretary unit of salivary glands (the acinus) produce initial saliva containing 85 % of the total protein secretions (Baum, 1993). The acinar fluid is modified in the salivary ducts where Na^+ and Cl^- are reabsorbed and HCO_3^- and K^+ are secreted. The product has a low osmotic pressure compared with plasma and interstitial fluid (Smith, 1992). Some salivary proteins such as lysozyme and lactoferrin are secreted directly by ductal cells. Serum albumin and immunoglobulins are secreted by intercellular diffusion from blood.

The salivary secretion is controlled by the autonomic nervous system. While salivary fluid secretion is stimulated by the parasympathetic nerves, protein secretion is stimulated by sympathetic nerves (Smith, 1992).

Nevertheless, it is more probable that salivary secretion is controlled by numerous transmitters and overlapping stimulation of both para- and sympathetic nerves (Garrett, 1999). A powerful fluid stimulant is Pilocarpine and other parasympathomimetics drugs (e.g. Sialogogues), while, mastication and taste receptors stimulate both proteins and fluid secretion. An effective chemical stimulus of proteins secretion in saliva is citric acid. It is particularly found to enhance the secretion of STN and histatins (Hector & Linden, 1999; Proctor, 1999).

3.2 Salivary Secretion

The inorganic and organic contents of saliva and their functions are listed in Table 3.1 and Table 3.2. The unstimulated saliva contains 99% water. This hypotonic secretion (compared to plasma) permits higher taste sensitivity and contributes to hydration of mucins. This allows saliva to cover soft and hard oral tissue as a thin biofilm which contributes to tissue lubrication and protection (Humphrey and Williamson, 2001). The water content of saliva helps to dilute and clear the acid produced by dental plaque. Areas in the oral cavity that are close to the ducts of salivary glands show variation in the formation of the salivary film. Consequently, faster rates of food debris removal and acid neutralisation are observed (Dawes *et al.,* 1989). Even though, this may influence enamel demineralisation prevention, salivary fluid is much more complex in its capability to interact with dental plaque and tooth surface in other ways than just acting as a diluent.

When salivary secretion is stimulated, ductal cells have a narrow time to modify acini fluid which results in salivary secretion with ranges of ionic concentrations listed in Table 3.1 (Smith, 1992). Salivary secretion may be affected by drug intake, hydration, olfactory, gustatory, and visual stimuli. Lee and linden, (1992) reported that an olfactory-submandibular salivary reflex does exist in humans, however there is no olfactory-parotid salivary reflex in humans (Lee & Linden, 1991).

The salivary flow rate affects the final composition of saliva (Dawes, 1996). While acini produce aqueous fluid, 85% of the proteins are secreted and modified by ductal cells and infiltrated from blood (Proctor *et al.,* 2005). The concentration of salivary protein is also affected by local acidic challenges in the acquired enamel pellicle as it was found that the amount of protein (i.e. statherin) on eroded enamel surfaces was lower compared to the total protein on non-eroded enamel (Carpenter *et al.,* 2014; Mutahar *et al.,* 2017a).

Component	Unstimulated (mmol/l)		Stimulated(mmol/l)	
	Mean +/-SD	Range	Mean+/-SD	Range
Sodium	7.7+/-3	2-26	32+/-20	13-80
Potassium	21+/-4	13-40	22+/-12	13-38
Calcium	1.35+/-0.45	0.5-2.8	1.7+/-1	0.2-4.7
Magnesium	0.31+/-0.22	0.15-0.6	0.18+/-0.15	0.2-0.6
Chloride	24+/-8	8-40	25+/-18	10-56
Bicarbonate	2.9+/-2.4	0.1-8	20+/-8	4-40
Phosphate	5.5	2-22	10	1.5-25
Thiocyanate	2.5	0.4-5	1.2	0.4-3
Iodide(µmol/l)	5.5+/-4.2	2-22	10+/-7	2-30
Fluoride(µmol/)	1.5	0.2-2.8	5	0.8-6.3

Table 3.1 Inorganic composition of whole saliva (Ferguson, 1999).

Component	Range of concentrations in saliva (µg/ml)		
	Whole saliva	Parotid	SM-SL
Albumin	29–238	–	–
Amylase	380–500	650–2,600	-
Cystatin	240–280	1.6–4	92–280
Fibronectin	0.2–2	2–6	0.3–2.0
Histatins	2–30	30–55	13–70
IgG	0.4–14.4	–	–
Lactoferrin	194	12	13
Lysozyme	-	7	21
MG1	1 80–500	–	80–560
MG2	10–200	–	5–243
β-2-Microglobulin	-	0.2-0.9	0.3-0.4
Statherin	2-12	16-147	20-150
Proline-rich proteins	90–180	230–1,251	270–1,335
sIgA	19–439	20–230	41–56
Amino acids (mg/l)	-	40	-

Table 3.2 Organic composition and concentrations of salivary proteins/peptides and glycoproteins in human parotid and submandibular-sublingual saliva (Huq et al.,2007).

3.3 General Function of Saliva

The function of saliva can be divided into specific roles depending on the composition. The components may have more than one role (multi-functionality) as shown in Figure 3.3.

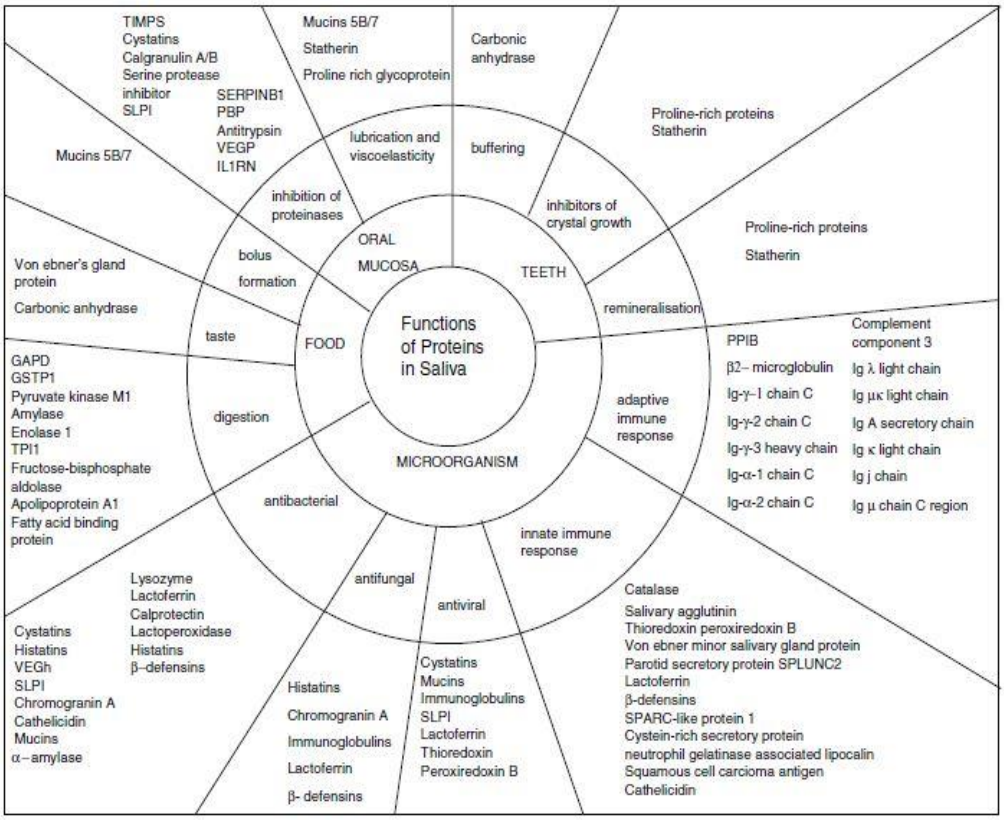

Figure 3.3 A diagram of the key functions of salivary peptides and proteins in relation to its components (Huq et al.,2007).

3.3.1 Food Taste, Clearance and Digestion

Mucins aid in food lubrication and improve the taste sensation due to their viscosity, adhesiveness, and low solubility (Dodds *et al.,* 2004). Since mucin is glycosylated and hydrophilic, it binds with water and food molecules and facilitates swallowing (Dawes, 2008). Mucins can also interact with reactive groups on bacterial cells and prevent their adhesion.

Alpha-amylase is a digestive salivary enzyme produced mostly by the parotid gland. It initiates starch digestion which is completed in the intestine by pancreatic amylase.

3.3.2 Lubrication

Lubrication of the hard and soft oral tissues is important for speech, mastication, swallowing and the overall integrity of the oral tissue. Glycoproteins, such as mucins, have sugars constituting from 50% up to 90% of the dry weight of the molecules. They help to form a mucosal barrier along the tissue so reducing irritation caused by plaque, enzymes and external and internal forms of chemicals (Berkovitz *et al.,* 2010).

3.3.3 Buffering

Saliva protects the dentition by forming a protective layer around the tooth surfaces exposed to the oral environment. The pellicle layer contains protein and peptides capable of shielding the teeth from microorganisms and also keeping the surrounding environment supersaturated with minerals (Hannig *et al.,* 2005). Proteolysis of peptides (e.g. histatins) to basic amino acids, such as lysine, histidine, and arginine can metabolise into amines and contribute to the buffering abilities of the pellicle (Edgar and O'Mullane, 1990).

In addition, saliva protects the dentition from acid attacks by rapid acid neutralisation and increasing salivary pH. The presence of bicarbonate (HCO_3^-) with pKa of 6.0 in stimulated saliva, secreted mainly by the salivary gland cells (containing enzyme carbonic anhydrase) and partly from plasma, increases the buffering capability when compared to unstimulated

saliva. The concentration of bicarbonate ion rises from 10 to 50 times at high flow rates (Humphrey and Williamson, 2001). At high salivary flow rate, the metabolism in the salivary gland cells increases and thereby, the bicarbonate concentration increases from 1.3 mmol/l to 30.1 mmol/l. This increase in bicarbonate concertation aids in increasing salivary pH back to 7.5-7.7 within a short time period (Ferguson, 1999).

When there is a drop in pH below 6.0 in unstimulated saliva, the phosphate buffering system aids in reversing the pH level to a neutral value. This is accomplished when HPO_4^{2-} is converted to $H_2PO_4^-$ by binding to a proton (H^+) (pKa 6.7 and 7.2) (Cole and Eastoe, 1988a). The phosphate buffering system is as effective as the bicarbonate buffering system at low salivary flow as both have a similar concentration in unstimulated saliva (Dawes, 1996).

3.3.4 Antimicrobial Effects

Immunoglobulin proteins such as IgA, IgG and IgM in saliva function as a local immune system, particularly IgA. They work via adhering to microorganisms and ensuring their wash by reducing their adherence ability (Diaz-Arnold and Marek, 2002). Also, some non-immunological peptides such as histatins disturb the fungal activity by attaching to them and preventing their adherence to oral tissue (Dodds *et al.,* 2004). Saliva also contains hydrogen peroxide that restricts the growth of microorganisms such as Gram-positive cocci, Actinomyces and Lactobacilli (Cole and Eastoe, 1988b). Also, antimicrobial enzymes such as lysozyme present in

saliva have a specific hydrolytic activity against the peptidoglycans in the cell wall of bacteria.

3.3.5 Preservation of Tooth Integrity

The balance between demineralisation and remineralisation relies on salivary pH, and mineral saturation. One of the key roles of saliva is to help maintain the integrity of the dental hard tissue by being a source of calcium and phosphate (Anderson *et al.,* 2001). The concentrations of these ions and their degree of saturation with respect to enamel influence the thermodynamic forces driving enamel demineralisation and remineralisation (Larsen and Pearce, 2003). At salivary pH 6.0-7.5, 50% of calcium is present in complexes formed using proteins or other salivary constitutes such as $Ca(HCO_3)_2$ (Hay and Moreno, 1989; Matsuo and Lagerlof, 1991). STN is a peptide that is known to bind to tooth surfaces and keep the surrounding tooth environment supersaturated with minerals (Margolis and Moreno, 1992; Margolis *et al.,* 2014). However, it should be noted that only free ions contribute to the degree of saturation with respect to enamel and its stability (Anderson *et al.,* 2001). The degree of saturation of saliva depends on the stability of these calcium constitutes at different pH levels (Hay *et al.,* 1982; Gao *et al.,* 1991), which will result in a variation of ion concentrations of individual ions as observed by the range of values shown in Table 3.3.

In addition, the presence of ions in saliva such as fluoride leads to remineralisation of the tooth and formation of acid resistant apatite such as fluorapatite. During acidic challenges, in the pH range of 4.5-5.5, low

concentration of F^- in saliva will cause a simultaneous supersaturation with respect to FA. Thereby, demineralisation of enamel will compete with simultaneously forming FA (Larden and Thorsen, 1974). Furthermore, the presence of fluoride enhances the remineralization process by adsorbing to enamel crystal surface and attracting calcium ions from saliva, so that the newly formed apatite is concentrated in fluoride and rejects carbonate (Featherstone, 2008).

	Children (n=15)				Adults (n=15)			
(mmol l^{-1})	Resting	Range	Stimul.	Range	Resting	Range	Stimul.	Range
Ca^{2+}	0.31 (0.12)	0.18-0.63	0.28 (0.05)	0.18-0.37	0.53 (0.23)	0.25-1.07	0.48 (0.19)	0.21-0.61
phosphates	4.4 (1.1)	2.54-6.41	3.53 (0.9)	2.15-4.87	4.62 (0.69)	3.06-5.64	3.68 (0.74)	2.48-5.37
Critical pH	6.19 (0.12)	6-6.14	6.27 (0.08)	6.1-6.4	5.97 (0.12)	5.7-6.1	6.07 (0.11)	5.9-6.3
Flow rate (ml/min)	0.44 (0.34)	0.05-0.99	0.88 (0.52)	0.28-1.89	0.39 (0.23)	0.08-0.81	3.05 (1.11)	1.92-6.06

Table 3.3 Variation among individuals and within the same person in calcium and phosphate concentration, critical pH and flow rate of saliva (Anderson et al., 2001).

3.4 Acquired Enamel Pellicle

Enamel mineral loss occurs at the interface between the enamel surface and the acquired enamel pellicle (AEP). Saliva covering the soft tissue and (dental) hard tissue forms a mucosal pellicle and an enamel pellicle respectively. It is mostly developed by molecules derived from saliva, such as STN, histatins and proline-rich glycoproteins (Hicks *et al.*, 2003). The enamel pellicle has an outer surface that is 100 nm thick and an inner deeper layer that is approximately 40 µm thick (Hannig, 1999). It protects the dental hard tissue by slowing calcium and phosphate diffusion

away from mineralised surface. Also, it hydrates the tissue and acts as a lubricant layer that assists mastication.

According to Waterman *et al.,* (1988), STN forms the majority of the surface layer with a Ca^{2+} concentration that is 500 times higher than that is present in bulk saliva. Calcium present in that layer increases the strength (viscoelasticity) of the biofilm (Waterman *et al.,* 1988). This layer on the surface of teeth provides a high calcium concentration that aids the mineralization of teeth, without undesirable secondary precipitation of minerals on to the tooth surface (Hay, 1995).

Proteins such A-PRP, STN, cystatins, and α-amylase, have high affinity to the enamel surface, their adsorption to enamel is a very fast process. After 1 min from the removal of the enamel pellicle a dense basal layer forms and grows to a maximum thickness of 1.0 μm after 1.5-2 hrs. (Hannig and Balz, M. 2001). Lamkin *et al.,* (1996) showed that although individual salivary proteins adsorb in different patterns, the highest protein incorporation is reached within 30-60 min. These salivary proteins allow bacterial adhesion, that acts as a base for dental plaque formation in the acquired enamel pellicle (Bakaletz, 2004; Marsh, 2004).

There are about 500 microorganisms that are present in the oral flora. Adhesion and early colonization of bacteria such as Actinomyces, Prevotella, and, Veillonella of which 60-90 % are Streptococci, is an important stage in the formation of dental plaque. Enhancement of the adhesion of these bacteria is associated with either a change in protein conformation upon adsorption onto mineral surfaces or by promotion of the initial microbial binding (Xie *et al.,* 1991; Gmür *et al.,* 1999). Therefore, the

enamel pellicle can act as a foundation for receptors which are recognisable by early bacterial colonisers, formed by salivary proteins such as proline-rich proteins, mucins, STN, histatins-1-3-5, and α-amylase (Gibbons *et al.,* 1991).

Chapter 4. Salivary Statherin and Histatin

More than 130 salivary proteins are identified from acquired enamel pellicle (AEP) so far (Hara and Zero, 2010). They function as tissue-coating molecules; proteins and peptides maintain enamel homeostasis by binding calcium ions, inhibiting primary and secondary precipitation, and acting as a pH buffer (Khurshid *et al.,* 2016a).

Within minutes of exposure to saliva, a 10-20 nm thick enamel pellicle is formed. This is initiated by salivary proteins and peptides referred to as pellicle precursors that have high an affinity for hydroxyapatite and bind to it through electrostatic interactions (Lendenmann *et al.,* 2000). STN, HTN, and aPRPs are amongst the first to adsorb to HA. A rapid surge in acquired enamel pellicle thickness to 100-1000 nm follows due to adsorption of protein and peptide aggregates (Hannig, 1999).

The protective role of the AEP appears to apply only to enamel since the pellicle formed on dentine affords minor protection against acid challenges (Hannig and Balz 2001; Hara *et al*., 2006; Siqueira *et al.,* 2010). There are multiple components that contribute to enamel overall protection including salivary flow, protein/peptides, and presence of ions such as Ca^{2+}.

This chapter will focus on STN and HTN as pellicle precursors among several peptides with the highest affinity for HA.

4.1 Salivary Human Statherin (STN)

Statherin (STN) is a multifunctional acidic phosphopeptide produced by the acinar cells of salivary glands, with a molecular weight of 5380 Da,

and contains 43 amino acids. STN concentration in saliva ranges between 16 and 200 µg/ml and constitutes ~0.7% of the enamel pellicle (Li *et al.*, 2004).

Table 4.1 shows the twenty-one amino acids found in proteins, each described with one letter abbreviation. Table 4.2 shows STN primary sequence using one letter abbreviation.

Amino Acid	One Letter Abbreviation
Isoleucine	I
Valine	V
Leucine	L
Phenylalanine	F
Cysteine	C
Alanine	A
Methionine	M
Proline	p
Glycine	G
Tryptophan	W
Threonine	T
Serine	S
Tyrosine	Y
Proline	P
Asparagine	N
Glutamine	Q
Glutamic acid	E
Aspartic acid	D
Lysine	K
Arginine	R
Histidine	H

Table 4.1 Amino acid one letter abbreviation.

Peptide Amino Acid Sequence		Refrance
DpSpSEEKFLRRIGRFGYGYGPYQPVPEQPLYPQPYQPQYQQYTF	(STN)	(P02808)
DpSpSEEKFLRRIGRFGYGYGPYQPVPEQPLYPQPYQPQYQQYT_	(SV1)	
DpSpSEE_____YGYGPYQPVPEQPLYPQPYQPQYQQYTF	(SV2)	(P02808-2)
DpSpSEE_____YGYGPYQPVPEQPLYPQPYQPQYQQYT_	(SV3)	

Table 4.2 STN primary sequence and the three variants, purified from submandibular/sublingual derived pellicle Jensen et al., (1991). The digits on the right for STN and SV2 are the accession no. from UniProt database (http://www.uniprot.org).

The gene coding evolution of proteins was investigated by Kawasaki and Weiss, (2003). They found that salivary proteins STN and HTN are involved in bio-mineralization and diverge from the evolution of single primordial enamel matrix protein (EMP).

HA growth in dental enamel is regulated via STN by preventing spontaneous calcium phosphate precipitation and inhibiting crystal growth (de Sousa-Pereira *et al.,* 2013). The negatively charged N-terminal fragment of STN is DpSpSEE (where the pS represents the phosphorylated serine residue) promotes binding of Ca^{2+} ions (Waite and Qin, 2001). The clustering of negative charges in the STN molecule in saliva and the peptide conformation was thought to form a “cape” on calcium and phosphate nuclei inhibiting them from primary precipitation (Moreno *et al.,* 1991; Hay and Bowen, 1996). This could explain the need for the complete STN sequence for the inhibition of primary precipitation, whereas preventing secondary precipitation (crystal growth) entails only the N-terminal.

Raj *et al.* (1992) established that an N-terminal 15-residue peptide of STN inhibits HA crystal growth as efficiently as the full-length STN. Exclusion of DpSpSEE motif from STN-like peptide reduces the HA binding affinity of this polymer (Shaw *et al.,* 2000). Also, alteration to synthetic non-phosphorylated peptide reduces the binding affinity to HA. Substitution of the phosphoserines by simple serine weakens HA binding but substitution of the serines by aspartic acid restores the binding affinity to 70%. This indicates that the phosphoserine residues and acidic amino acid side chains are important for binding of STN to HA.

Structural analysis of STN in solution using Nuclear Magnetic Resonance (NMR) or Circular Dichroism (CD) has shown an α-helix conformation at its N-terminal (D1-G15) (Naganagowda *et al.,* 1998). This result was confirmed by Long *et al.,* (2001), when STN N-terminus (pS2-G12) was bound to HA. Furthermore, the α-helix (K6-G12) binds weakly to HA surface when compared to the acidic N-terminal of the helix (D1-E5) (Long *et al.,* 2001). The lack of segment F6-G15 in SV2 and SV3 (sequence shown in Table 4.1) alter the secondary structure and hence the stability of the N-terminal helical structure compared to STN (Long *et al.,* 2001).

Protein secondary structure prediction can be obtained with Jpred4 software (*www.compbio.dundee.ac.uk/jpred/*) (Drozdetskiy *et al.,* 2015). This software gives a consensus of secondary structure prediction from Jnet algorithm that provides α-helix, β-sheet and coil prediction with an accuracy of 81.5% (Cole *et al.,* 2008). Figure 4.1 shows that STN N-terminal helix length is from residue 4 to 11, or possibly 12 or 13. No other significant secondary structure was predicted.

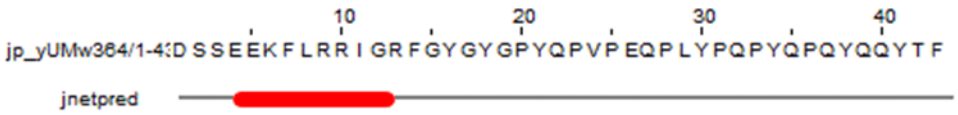

Figure 4.1 Jpred4 secondary structure prediction of STN, showing secondary helical confirmation confined mostly to the N-terminus (in red).

The C-terminus does not exhibit an ordered conformation but a more flexible structure that is not part of the α-helix. The proline-rich sequence present at the inner section at positions P20, P23, P25, P28, P31, P33 and P36 suggests a poly-L-proline II helix (PPII) in PBS (Raj *et al.,* 1992).

Naganagowda *et al.,* (1998) suggested that the hydrophobic C-terminal P36-F43 has a 3_{10} helical structure that is more flexible when compared to the N-terminal α-helix. The antimicrobial activity of STN is believed to be due to its C-terminus (Kochanska *et al.,* 2000). The middle PPII domain exposes sites that bind *A. Naeslundii gsp* 2 and *F. Nucleatum,* and the potential 3_{10} helical structures bind *A. Viscosus* and *P. Gingivalis* (Amano *et al.,* 1996; Niemi and Johansson 2004; Khurshid *et al.,* 2016b) (Figure 4.2).

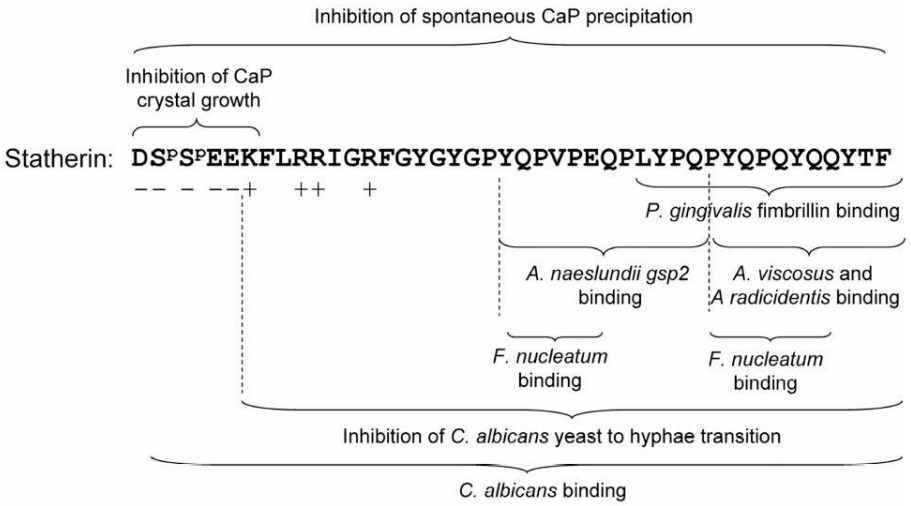

Figure 4.2 STN functional characteristics according to the amino acid sequence. (Helmerhorst et al., 2010).

The secondary structure conformation in the N-terminus α-helix (D1-Y16) and the PPII helix is thought of as a protective conformation for hydrophobic amino acids present at positions 7, 8, 11 and 14 which therefore allow a higher stability of the peptide in solution (Raj *et al.,* 1992).

Cyclo-STN has been detected as a minor component in the salivary proteome. It accounts for ≈1% of total STN. Cyclisation happens due to the reaction of lysine side chains with glutamine side chains in STN, catalysed

by transglutaminase. Such cyclisation could increase or reduce the activity of the peptide by introducing rigidity into what is a flexible molecule (Cabras *et al.,* 2006). Lysine positively charged amino groups transform into an amide bond after the reaction, losing the positively charged side chain. Therefore, it can be argued that this cyclisation may increase the adsorption of the peptide to HA.

Cossu *et al.,* (2011) found that STN is not exclusive to salivary glands but it is also expressed in human male sex glands (prostate and seminal vesicles). The binding capacity of STN to some microbial organisms could be beneficial in the defence of the genital tract against infection. Also, due to the high affinity of STN to hydroxyapatite, it binds to calculi that often grow in the prostatic duct to form a protective layer. This layer changes the calculi surface to be hydrophobic allowing the calculi to move through the duct (Cossu *et al.,* 2011).

A form of STN was also identified in the parotid secretion of pigs, indicating that it is not exclusive to primates (Manconi *et al.,* 2010). The structure of STN has been inferred from the gene sequences of primates but also cattle and sheep amongst a total of twelve animals.

4.2 Salivary Human Histatins

Histatins are present in different forms in saliva. Azen (1978) looked at HTN genetic polymorphism comprehensively. Similar to STN, the genes encoding these peptides are mapped on human chromosome 4. Three main forms of these peptides exist, histatin-1 (HTN), -3 (HTN-3), and -5

(HTN-5), which are 38, 32, and 24 residues long respectively (Table 4.3). They have low molecular weight (3000-4000 Da) and are basic in charge.

Histatin Peptide	Amino Acid Sequence	Reference
1	DpSHEKRHHGYRRKFHEKHHSHREFPFYGDYGSNYLYDN	(P15515)
2	RKFHEKHHSHREFPFYGDYGSNYLYDN	
3	D SHAKRHHGYKRKFHEKHHSHRGYR -------- SNYLDYN	(P15516)
4	RKFHEKHHSHRGYR ------- SNYLYDN	
5	D SHAKRHHGYKRKFHEKHHSHRGY	
6	SHAKRHHGYKRKFHEKHHSHRGYR	
7	RKFHEKHHSHRGY	
8	KFHEKHHSHRGY	
9	RKFHEKHHSHRGYR	
10	KRHEKHHSHRGYR	
11	KRHHGYKR	
12	KRHHGYK	

Table 4.3 Amino acid sequences of human salivary histatins, showing the alignment of amino acids of the three main forms 1,3, 5 and their 9 proteolytic peptides (Tsai and Bobek 1998). Reference digit was acquired from UniProt database.

Histatins are known to be produced by the ductal cells of the parotid and the submandibular salivary glands, at a concentration 50-425 µg/ml in healthy adults (de Sousa-Pereira *et al.,* 2013). According to Hardt *et al.,* (2005) these peptides are affected by diurnal variations, while STN concentration does not change. Histatin -1, - 3, and -5 are most abundant in the afternoon. Proteolysis of these three main members produces nine proteolytic peptides in saliva.

Histatins were first referred to as peptides that improve the glycolytic activity of microorganisms, later on, they were described as peptides that have fungicidal properties (De Smet and Contreras, 2005; de Sousa-Pereira *et al.,* 2013). They cross the membrane of the fungus by mobilization of K^+, and then they inhibit mitochondrial respiration by forming

reactive oxygen species causing cell death (Xu *et al.,* 1991). A C-terminal 25-mer of HTN was also revealed to assist wound healing *in vitro* by encouraging cell migration (Oudhoff *et al.,* 2008).

McDonald *et al.,* (2011) found *in vivo* an intact amount of full-length HTN, 3, and 5 in AEP that resists proteolysis. Siqueira *et al.,* (2010) observed that HTN binding to HA slows peptide resists degradation. The mechanism by which this action is achieved is not understood, however, it is proposed that when HTN is tightly bound to HA, the conformation of HTN while bound to HA may prevent the accessibility of tryptic-like proteolytic activity to preferred amino acid cleavage residues (i.e. arginine, and lysine). (McDonald *et al.,* 2011).

Driscoll *et al.,* (1995) reported that adsorbed HTN show a higher hydroxyapatite adsorption affinity than synthetic HTN which lacks the covalently linked phosphate at position 2. According to Kawasaki *et al.,* (2003) HTN3 and HTN5 do not have the SXE motif which is the phosphorylation site responsible for Ca^{2+} binding. Instead, they both have SXA motif that reduced their HA affinity but did not eliminate it.

There is little literature on HTN secondary structure in solution, Whereas, HTN-3 and HTN-5 have been studied structurally as major histatins present in saliva (Barsukov and Lian, 1993; Raj *et al*.1998; Tsai and Bobek, 1998). These studies were carried out using circular dichroism and two-dimensional NMR of HTN-3, and, -5. They reported HTN-5 exhibited random coil conformation in aqueous solution and conforms in an α-helical conformation at the N-terminal. Whereas HTN-3 has less tendency to form a helical structure in aqueous solution and becomes much more

ordered in a mixture of 50:50 H_2O–dimethyl sulfoxide (Brewer *et al.,* 1998; Tsai and Bobek, 1998).

The secondary structure prediction of HTN obtained with Jpred4 software indicates a helix extension from residue 6 to 11, or possibly 5 to 11 (Figure 4.3). No other significant secondary structure was predicted.

Figure 4.3 Jpred4 secondary structure prediction of HTN, showing secondary helical confirmation confined mostly to the N-terminus (in red).

Chapter 5. Salivary Proteins/Peptides and The Mineralised Tissue Affinity

5.1 Hydroxyapatite and Enamel as an Adsorbent Surface

Salivary peptides maintain the integrity of dental hard tissue by adsorption onto mineralised surfaces. HA can be used as an *in vitro* model of enamel to study selective protein/peptide binding affinity (Moreno *et al.,* 1987; Yin *et al.,* 2003). It has been found that the net charge at the HA surface boundary with any solvent is governed by the nature of ions in the solution, the ionic strength of the solution and its pH (Lagerlof, 1983). At high pH the phosphate ions on HA surface become gradually de-protonated as $H_2PO_4^-$ and HPO_4^{2-}. Also, the $CaOH_2^+$ decreases and CaOH increases (Koutsoukos and Valsami-Jones, 2004).

At a specific pH, a solid surface will reach a balance where the charge of surface anions and cations will be neutral. The point of zero charge (pI) for HA is at pH 8.15 and with the presence of CO_2, it shifts to pH 7.13 (Elliott, 1994). When the pH of a protein solution is close to the pI of the substrate it promotes protein adsorption (Norde, 1986; Norde *et al.,* 1986). Since enamel apatite contains 3.5 % CO_2, the pI point of enamel is lower compared to HA (LeGeros, 1994). Adsorption studies of synthetic protein (dendrimer) and human dentine phosphoprotein, confirmed that there is an association between surface charge domains of HA mineral crystals and protein binding (Wallwork *et al.,* 2002; Chen *et al.,* 2003,).

5.2 Role of Amino Acids and Their Functional Groups in Peptide/Protein and HA Adsorption

Proteins are chains of 50 amino acids or more, while a chain of fewer than 50 amino acids is labelled as peptide (Berg *et al.,* 2002). Investigating the amino acids and their functional groups as building blocks of peptides/proteins allows an understanding of the affinity of these amino acids and their importance in binding to HA. Figure 5.1 represents the general structure of an amino acid, where the amino end in a protein/peptide represents the N-terminal and the carboxyl group end of a protein/peptide represent the C-terminal. The R group is the functional group (side chain), which is different for each amino acid (Mann, 2001).

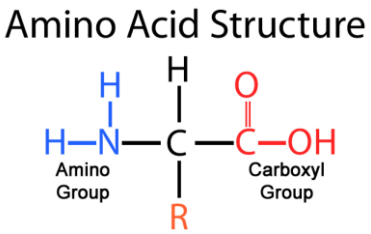

Figure 5.1 Typical chemical structure of an amino acid, R is the function group specific for each amino acid as shown in Figure 5.2.

Figure 5.2 shows the chemical structures, functional groups and abbreviations of the 21 amino acids that are directly encoded for protein synthesis.

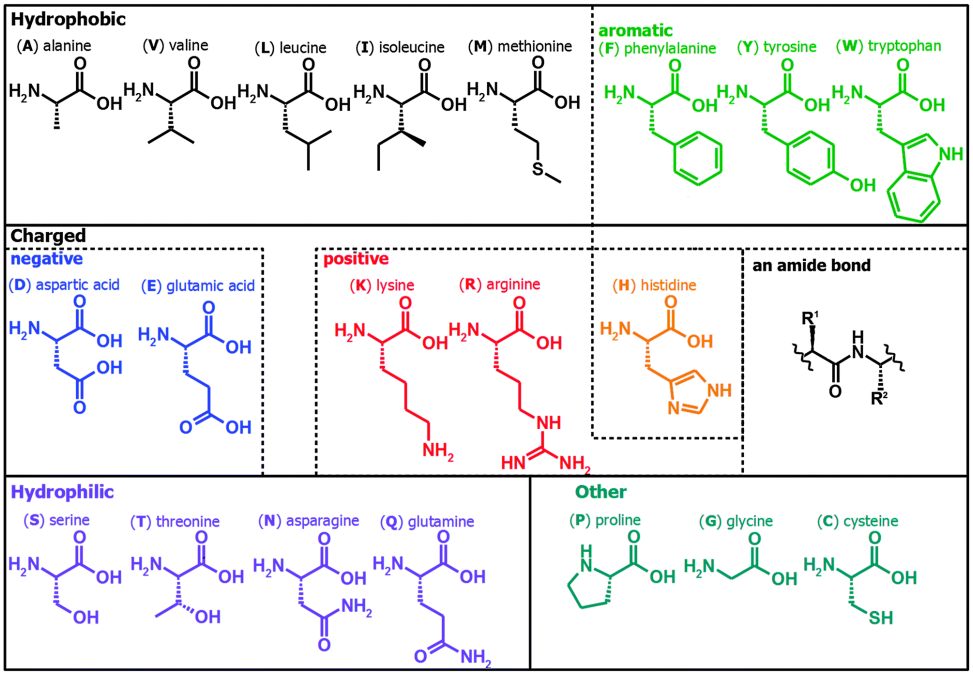

Figure 5.2 The twenty-one amino acids that appear in the genetic code; categorized according to their hydrophobicity, charge, and functional groups (Fleming and Ulijn, 2014).

Johnsson *et al*., (1993) studied HA binding domains in salivary proteins such as STN, PRPs, HTN, HTN5, cystatins. They found that the affinity of proteins to HA depends on the number and charge of the amino acids. Neutral or positive residues binds less strongly to HA, while proteins that contain several negative charges binds more readily to HA.

Post-transitional modification of peptides such as phosphorylation of serine has been proven to increase the adsorption of peptide to HA (Figure 5.3) (Moreno *et al.,* 1991; Spanos and Koutsoukos, 2001). Such improvement is evident by the greater adsorption affinity of HTN to HA compared to HTN5 which lacks the phosphorylation of serine (Johnsson *et al*., 1993).

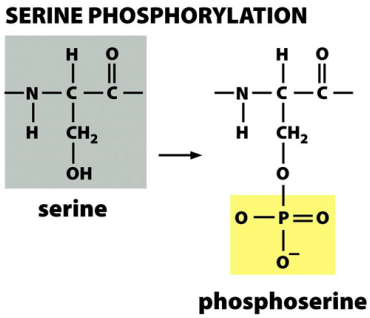

Figure 5.3 Structural change of phosphorylated serine. In peptides such as STN and HTN, a post-translational modification occurs in which the N-terminal serines are phosphorylated by a protein kinase by the addition of a covalently bound phosphate group (Moreno et al., 1991).

Romero *et al.,* (2015) compared casein (phosphopeptide) and dephosphorylated casein (Dcasein), effect on HA growth using Field Emission Scanning Electron Microscopy (FE-SEM) and Transmission Electron Microscopy (TEM). They found that at 100 µg/ml, Dcasein had a much lower inhibitory effect than casein. Casein inhibitory effect was mediated by the affinity of the phosphate groups of phosphoserines to calcium growth sites in HA, while Dcasein reduced effect was explained by the reduction of phosphate groups available to interact with HA. Therefore, different functional group existing in amino acids have specific binding to HA, which is based mainly on the charge of the functional groups.

In addition, it was found that pre-treatment of HA surface increases the adsorption affinity of amino acid residues. Either by creating adsorption sites of high affinity for certain amino acids or by non-specific improvement of HA surface (Kresak *et al.,* 1977). At pH 7.8, HA pre-treatment with Ca^{2+} increases the adsorption of aspartic acid while pre-treatment of HA with phosphate increased the adsorption of arginine (Hjerten *et al.,* 1965; Kresak *et al.,* 1977).

5.3 Sequences and Conformation of Peptide/Protein Accountable for the Adsorption onto HA

Protein primary structure is dictated by its sequence. Studies on individual amino acids provide knowledge on interaction onto HA. However, to further explain the adsorption of protein/peptide with mineral surfaces the whole molecule should be studied.

The SXE motif, which is a phosphorylation site, is responsible for the Ca^{2+} binding, this motif is found in STN, HTN, and A-PRP sequences (Huq *et al.,* 2000; Kawasaki and Weiss, 2003). Schlesinger and Hay (1977) and Raj *et al.,* (1992) suggested that the N-terminal amino acid sequence of STN is responsible for HA binding through electrostatic interaction. Substituting phosphoserine residues by aspartic acid has almost the same effect on the affinity for HA. This suggests that this interaction is mediated by the overall charge of the fragment. The removal of the phosphate group from the phosphoserine (pS2, and pS3) reduces the affinity of STN for HA significantly because of the charge reduction (Raj *et al.,* 1992).

The sequence of amino acids in peptides is important in determining secondary structure conformation, which contributes to the peptide adsorption onto HA. The most common secondary structure associated with the binding of proteins/peptides on HA surface is an α-helical structure (Moreno *et al.,* 1991; Raj *et al.,* 1992; Mann, 2001). The α-helix forms when a carboxyl group of one amino acid form a hydrogen bond with the amide group of an amino acid located 4 residues along the sequence (Dunitz, 2001). The hydrogen bond forms between two amino acids with either

similar hydrophobicity or hydrophilicity (Pace and Scholtz, 1998). Table 5.1 shows the hydropathy score for each amino acid according to Kyte and Doolittle, (1982), which could help in α- helix conformation prediction using the primary sequence of proteins. Pace and Scholtz, (1998) also reported that some amino acids have the tendency to form α-helices, including A, L, M, F, E, Q, H, K, and R, while other amino acids tend to disturb the formation of an α-helix either because the residue is too flexible, such as G, or the amino acid is too rigid, which is the case of P. Additionally, the presence of salt bridges between amino acids, such as E or D, and L, or K will further help to stabilise the helix, although they should be located three residues apart in a sequence (Kumar and Nussinov, 2002; Meuzelaar *et al.,* 2016).

Amino Acid	One Letter Abbreviation	Hydropathy Score
Isoleucine	I	4.5
Valine	V	4.2
Leucine	L	3.8
Phenylalanine	F	2.8
Cysteine	C	2.5
Alanine	A	1.8
Methionine	M	1.6
Proline	p	0.6
Glycine	G	-0.4
Tryptophan	W	-0.9
Threonine	T	-0.7
Serine	S	-0.8
Tyrosine	Y	-1.3
Proline	P	-1.6
Asparagine	N	-3.5
Glutamine	Q	-3.5
Glutamic acid	E	-3.5
Aspartic acid	D	-3.5
Lysine	K	-3.9
Arginine	R	-4.5
Histidine	H	-3.2

Table 5.1 Hydrophobic (positive) and Hydrophilic (negative) hydropathy scores of amino acids side chains by Kyte and Doolittle, (1982). Green: hydrophobic, black: hydrophilic, red: hydrophilic and electronegative, and blue: hydrophilic and electropositive.

NMR and CD studies have shown the presence of an α-helix conformation at the negative N-terminal in solution (α-helix forming sequence DpSpSEEKFLRRIGR) (Bennick *et al.,* 1979; Naganagowda *et al.,* 1998; Goobes *et al.,* 2007a). The α-helical conformation was found to orient the negative and positive charges of the STN on to HA surface (Goobes *et al.,* 2007a).

Therefore, the presence of specific amino acids in a sequence that leads to protein conformation is important in the adsorption affinity of proteins onto mineralised surfaces.

5.4 Thermodynamics of Peptide/Protein Adsorption to HA

Though electrostatic forces play an important role in protein binding, it is not the only factor driving it. Moreno *et al.,* (1982) showed that the thermodynamics of adsorption indicates that the process is endothermic; therefore, the driving force for adsorption must be entropic in nature. It was suggested that the conformation of protein and the dislodgment of H_2O molecules from the surface of protein and HA are accountable for adsorption energy (Moreno *et al.,* 1991). This might justify the higher affinity of salivary protein/peptides to fluorapatite (FA) compared to HA since HA surface has a high wettability (more hydration). In addition, a similar binding mechanism was proposed for STN, where STN gain more structural stability at the N-terminal when bound onto HA showing the importance of H_2O molecule exclusion that allows protein adaptation on HA surface (Stayton *et al.,* 2003).

Fourier Transfer Infrared Spectroscopy (FTIR) study of A-PRP showed that there is an increase in the α-helical and β-sheets conformation upon adsorption compared to A-PRP conformation in solution (Moreno *et al.,* 1991). Furthermore, certain microorganisms were found to bind only to A-PRPs, STN, and HTN after they adsorb onto enamel (Moreno *et al.,* 1991, Siqueira *et al.,* 2010). Which led to the conclusion that structural conformational changes happen to proteins upon adsorption.

Therefore, proteins that show structural changes upon adsorption have the highest adsorption affinity for mineral surface which is produced by maximizing their entropy (Moreno *et al.,* 1982).

5.5 Effect of Different Biological Molecules on Protein/Peptide Adsorption

The formation of enamel pellicle depends on the selective affinity of salivary proteins. Most studies of salivary protein were on the affinity of single components of saliva. However, the formation of the AEP *in vivo* occurs in the presence of different salivary proteins and is possibly influenced by the adsorption of more than one protein.

Rykke *et al.,* (1995) and Vitkov *et al.,* (2004) reported the formation of salivary supramolecular structure *i.e* salivary micelle-like structures, that pre-exists to adsorption. They reported that these micelle-like structures are hydrophobic in core with a surface negative net charge (Rykke *et al.,* 1996). Further studies showed that these structures exist in different sizes and shapes ranging from 150-200 nm in diameter globular structures to 20-40 nm raspberry-like structures (Soares *et al.,* 2004). They identified the

formation of three molecular complexes; i) large salivary micelles proteins complexes of MG2 and secretory IgA, ii) intermediate complexes of amylase-A-PRP-STN-HTN complexes, and iii) small soluble (lysozyme) complexes. These salivary micelle structures may contribute to the formation of enamel pellicle by helping the adsorption of protein present in the complexes, with less affinity to enamel. Thus, help in the maintenance of enamel homeostasis and the protection against microorganisms.

The complexity of the protein components of pellicle formed *in vivo* raises questions regarding the biological significance of the adsorption data gained from *in vitro* studies using a single protein and HA.

5.6 Affinity of Salivary Proteins/Peptides for HA/Enamel

Phosphorylated salivary STN, HTN, A-PRPs and cystatins are considered as enamel pellicle precursors (Lindh, 2002; Yao *et al.,* 2003). Adsorption of salivary proteins is selective, with STN showing the highest affinity to minerals (Hay, 2003). However, selective affinity is affected by the HA/protein ratio. At a ratio of 5 mg HA to 10 ml saliva STN was the only protein that adsorbed. At a higher ratio of 50 mg HA to 10 ml saliva the selectivity is reduced and STN, HTN and A-PRPs were adsorbed (Jensen *et al.,* 1992; Vitkov *et al.,* 2004,). Even though A-PRPs affinity is slightly higher than STN, the density of adsorbing sites on HA for STN is 4 times higher than A-PRPS (Moreno *et al.,* 1984). Similarly, cystatins adsorb more effectively than STN but to a lower density (Johnsson *et al.,* 1993).

Lamkin *et al.,* (1996) suggested that there are 3 time-dependent types of adsorption expressed in the binding capacity of individual salivary proteins:

1. The first group of salivary proteins bind instantly (e.g. STN, A-PRP 3, and A-PRP 4).
2. The second group that binds slower than the first group (e.g. α-amylase, glycosylated PRPs and cystatins). The difference in the rapidity of adsorption of these proteins might be due to the difference in their molecular weights and their flexibility.
3. The third group display an intricate pattern of adsorption. There is a rapid period of adsorption to HA and a slower period affected by protein-protein interaction (e.g. HTN, A-PRP1, and A-PRP 2).

Yin *et al.* (2006) studied HTN-5 binding to HA beads in a multi-component experimental system. They found that pre-treatment of HA with STN further enhanced the binding of HTN-5. This suggests that specific proteins with high adsorption affinity to HA can mediate the binding of other proteins with low affinity.

5.7 Salivary Proteins/Peptides and Enamel Homeostasis

5.7.1 Buffering Capacity

Bicarbonate buffer has the main role in the buffering capacity of saliva (Section 3.3.3). The concentration of enamel pellicle precursor proteins influences the buffering capacity (Hay and Moreno, 1989). In the AEP, the presence of proteolytic fragment and free basic amino can

increase the buffering capacity of enamel pellicle (Cole and Eastoe, 1988a). Basic amino acids, such as arginine and lysine can be metabolised into amines by the oral flora and contribute to the buffering capacity (Vitorino *et al*., 2005).

5.7.2 Inhibition of Calcium Phosphate Salts Precipitation

The supersaturation of saliva with calcium and phosphate ions result in the precipitate of calcium orthophosphate in the absence of salivary proteins such as STN and A-PRPs (Elliott, 1994). STN contains similar charged N-terminal as casein and enamel matrix proteins (Reynolds, 1987; Schlesinger *et al.,* 1989). Which suggest that the inhibition of Ca^{2+} and PO_4^{3-} precipitation by STN is due binding to Ca^{2+}. Similarly, A-PRPs prevent secondary precipitation by binding to Ca^{2+} through the 30 first N-terminal residues that contains two phosphorylated sites (Aoba *et al.,* 1984). Additionally, salivary proteins STN, A-PRP, and HTN were also found to adsorb on HA/enamel surfaces covering mineral surfaces that function as crystal growth sites (Kautsky and Featherstone, 1993).

5.7.3 Inhibition of Mineral Demineralisation

Both *in vitro* and *in vivo* studies have shown that the enamel pellicle decreases enamel demineralisation (Doebert *et al.,* 2002; Escamilla-García E *et al.,* 2017; Mutahar *et al.,* 2017b). It was also verified by Hannig, (2002) that the enamel pellicle basal layer is accountable for protection against acid and abrasion attacks. Margolis and Moreno, (1994) demonstrated that the mean Ca^{2+} concentration is higher (6.8 mmol/l) in individuals with no

caries and 5.5 mmol/l in individuals with caries. This increase in calcium concentration would lead to an increase in saturation and hence the dynamic force of enamel demineralisation would decrease. Since salivary proteins such as STN, HTN and A-PRP have an affinity for Ca^{2+}, they can affect the demineralisation of HA crystals by interacting with Ca^{2+} in solution or at the mineral surface (Tang *et al.,* 2003).

In vitro adsorption studies with a single native, or recombinant, proteins provide an understanding of physical parameters such as the binding affinity and the number of binding sites of salivary proteins (Moreno *et al.,* 1978; Yin *et al.,* 2003; Shaw, 2015). However, the complexity of proteins forming pellicle *in vivo* raises questions regarding the biological significance of the adsorption data obtained from *in vitro* studies using single protein and HA. The study of protein interactions with HA should include more than one constituent to better reflect the heterogeneity of proteins in saliva. While most studies focus on the affinity of these proteins for HA, there are very few which measure the direct physical effect of STN and/or HTN individually and also in combination.

TECHNIQUES USED IN THIS STUDY

Chapter 6. Scanning Microradiography (SMR)

6.1 Scanning Microradiography (SMR)

Elliott *et al.* (1981) developed Scanning Microradiography (SMR) as an X-ray attenuation technique to improve conventional microradiography. It allowed demineralisation studies with exact measurements in mineral mass observed in real-time physical and chemical changes. The SMR system consists of three main units: X-ray generator, X-Y scanning stage that holds the cells containing the samples under study, and an X-ray detector system (Figure.6.1).

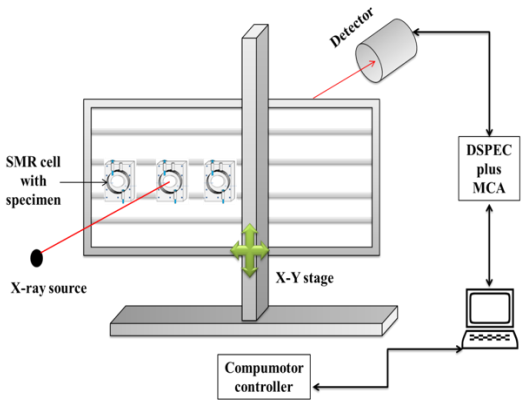

Figure 6.1 Schematic of SMR X-Y scanning stage with SMR cells, an X-ray beam is targeted on the specimen and the attenuated X-ray photon is detected by a photon counting detector.

6.1.1 Foundation of Electromagnetic Radiation

The conveyance of energy through space and matter is defined as radiation. Electromagnetic radiation is the movement of energy through space as a combination of electric and magnetic fields (Figure 6.2). Particulate radiation consists of atomic nuclei or subatomic particles moving

at a high velocity, such as α-particles and β-particles (White and Pharoah, 2008).

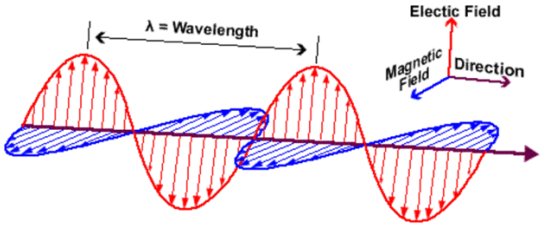

Figure 6.2 Electromagnetic radiation is a wave in space or through matter with the electric and magnetic field components perpendicular to each other and perpendicular to the direction of energy propagation (Seibert, 2004).

Radio-waves, microwaves, visible light, ultraviolet radiation, X-ray, and gamma rays are electromagnetic waves. Classified according to wave length where, radio waves have the longest wavelength and gamma rays have the shortest.

Electromagnetic radiation is a cyclic wave. The number of cycles per second (s^{-1}) is the frequency, f. Electromagnetic radiation travels at a velocity, C, of 3.0 x 10^8 ms^{-1} in a vacuum. Wavelength, λ, is the distance travelled by 1 cycle. C = λf describes the relationship between velocity, frequency and wavelength (Seibert, 2004).

6.1.2 X-ray Production

X-rays are generated when electrons from the cathode strike the target material in the anode inside an X-ray tube (Figure 6.3). To generate X-rays, a high voltage potential (between the anode and the cathode) is required to accelerate the electrons, this is achieved using high voltage, and a stabilised power supply.

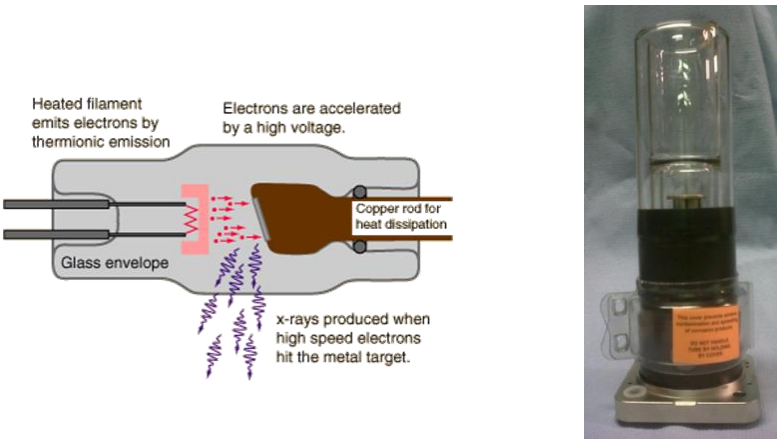

Figure 6.3 Schematic diagram showing basic components of an X-ray tube (A) and X-ray tube used in SMR machine with silver (Ag) target (B).

6.1.3 X-ray Tube

An X-ray tube is an air evacuated glass envelope that holds two metal electrodes, a heated tungsten filament (cathode) and a metallic target.

The cathode is a coil of tungsten wire about 2 mm in diameter and 1 cm in length. The heated filament is the source of free electrons that are produced due to heating by an electrical power supply. The cathode is also the source that is negatively charged.

The anode is the target, made up of a metal of high atomic number, high melting point and a low vapour pressure. The target is implanted in a copper block that is cooled and kept at a high positive potential in contrast with the filament.

When the tungsten wire is heated electrons are produced. Due to the potential difference between the anode and the cathode these electrons accelerate with a kinetic energy in keV equal to the applied tube voltage. When these high energy electrons hit the target, they transfer their kinetic

energy to X-ray photons. Not all the electrons' kinetic energy produces X-ray photons, 99% of this energy is converted to heat, hence the need for a high melting target. When X- rays are produced they leave the X-ray tube case through two or more windows, usually made from beryllium.

6.1.4 Micro-focus Tubes

These are usually removable X-ray tubes with a very small focal spot. The focal spot size regulates the size of the actual X-ray source. The tubes attain a high resolution and high magnification when a fine X-ray beam size is needed.

6.1.5 Electron Impact X-ray Source

Two types of radiation are produced when the accelerated electrons hit the target on the anode; continuous spectrum radiation (Bremsstrahlung radiation) and characteristic radiation (Figure 6.4).

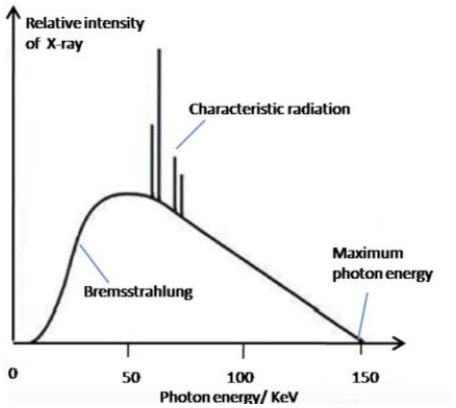

Figure 6.4 X-ray spectrum produced by a tube with tungsten target showing continuous and characteristic radiation.

6.1.5.1 Bremsstrahlung Radiation

When an electron from the filament is deflected by the nucleus or nuclear field of the target, the electron will decelerate and lose energy. The kinetic energy lost is transformed into a photon with equal energy. The closer the electron interacts with the nucleus the greater the deceleration. This results in higher X-ray photon energy.

6.1.5.2 Characteristic Radiation

This type of radiation occurs when an electron from the filament with enough energy interact and eject an orbital electron from the inner shell of the target atom (K, L or M). This outer shell electron then drops to the inner shell to fill the inner shell vacancy. The difference in energy between the two shells is released in the form of characteristic radiation.

6.2 X-ray Interaction with Matter

X-rays beam interact with the matter by three mechanisms:

- Penetrate matter without interaction.

- Interact with matter by depositing their energy.

- Interact and scatter from their original direction and deposit part of their energy.

X-rays interact with matter by elastic scattering (coherent), inelastic scattering (incoherent), or photoelectric absorption (Figure 6.5) (Seibert and Boone 2005).

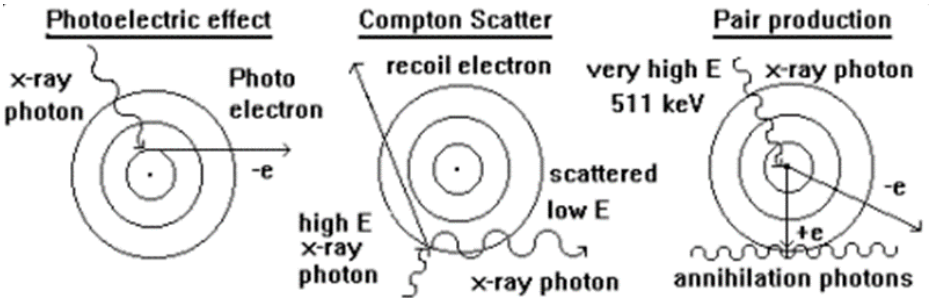

Figure 6.5 X-ray attenuation mechanisms

6.2.1 Photoelectric Absorption

This implicates the interaction of an X-ray photon and an inner orbital shell electron in the matter. When the energy of the inner shell electron is lower than the photon; the energy of the photon transfers to the electron ejecting the electron from the shell. When this happens an electron vacancy is created, this vacancy is then filled by an electron from an outer shell. This produces X-ray photon at characteristic energy due to the difference in energy between the two shells (White and Nancollas, 1977).

6.2.2 Compton Scattering

When an X-ray photon interacts with a loosely bound electron in the atom, only a part of the photon energy is used to eject the electron from the shell (usually in an outer shell). The interacted photon with reduced energy deflects in a different direction, and the electron recoil, and distributes its energy through ionisation.

6.2.3 Rayleigh Scattering

When an X-ray photon interacts with a strongly bonded electron (inner shell), it results in the re-emission of the photon with no loss in energy. This is due to the much lower energy of the photon compared to the binding energy of the electron. This type of scattering includes both coherent and elastic scattering.

6.2.4 Pair Scattering

When the X-ray photons energy is greater than 1.02 MeV, the interaction of the photon with the electronic field of the nucleus produces an electronic –positron pair (e^- -positron e^+ charged particles). This interaction is not relevant to this study.

The energy of the X-ray photon and the nature of the target material influence the occurrence of these mechanisms.

In the SMR studies, the incident photon energy is predominantly AgKα (22.1 keV) and the specimen is either enamel or HA. Under these conditions, the predominant interaction will be photoelectric absorption.

6.2.5 X-ray Attenuation: Beer's law

An X-ray beam is attenuated exponentially as it passes through a homogeneous substance. The X-ray attenuation depends on:

-The energy of X-ray photons

-The density of the attenuating substance

-The atomic number of the substance

The relation for monochromatic radiation is expressed by Beer's law as:

$$I = I_o e^{-\mu x} \qquad \textbf{Equation 6.1}$$

where I is the intensity of the attenuated (transmitted) beam, I_o is the incident beam intensity or photon count per unit area, X is the thickness of the substance, μ is the linear attenuation coefficient (LAC) in cm^{-1} and LAC refers to the absorption or scattering of the X-ray photon of a given energy per unit thickness of the substance expressed in units of cm^{-1}.

If the substance exhibits a difference in physical density the LAC can vary significantly at a given photon energy. The mass attenuation coefficient (MAC), μ_ρ compensates for these variations by normalizing the linear attenuation per unit area density of the substance. It is expressed in units of $cm^2\ g^{-1}$.

$$\mu_\rho = \frac{\mu}{\rho} \qquad \textbf{Equation 6.2}$$

Where:

μ is the linear attenuation coefficient (cm^{-1})

ρ is the density ($g\ cm^{-3}$)

μ_ρ is the mass attenuation coefficient (MAC)

MAC for HA is the weighted average of mass absorption coefficients of its constitutional elements. In HA $(\mu/\rho)_{Ca}$, $(\mu/\rho)_P$, etc. If we consider the weight fractions of Ca, P, as w_1, w_2, then the mass absorption coefficient of HA can be given by:

$$\frac{\mu}{\rho} = \boldsymbol{w1}\left(\frac{\mu}{\rho}\right)\mathrm{Ca} + \boldsymbol{w2}\left(\frac{\mu}{\rho}\right)\mathrm{p}+..$$ **Equation 6.3**

The values for MAC for several characteristic wavelengths are reported in the International Table for Crystallography (Creagh and Hubbell, 1992). The reported MAC for stoichiometric HA is 4.69 g/cm^2 calculated for AgKα radiation (22.1 keV).

6.3 X-ray Detection

6.3.1 Semiconductor Detectors

Solid state semiconductor detectors, gas detectors, scintillation detectors and X-ray films are different types of X-ray detection systems. The detector material is the main element that affects the efficacy of an X-ray detector. In addition, other factors such as the detector distance, geometry, physical thickness in the direction of the incident beam and the energy of the incident beam could affect the X-ray detector.

The SMR system uses semiconductor detector. The semiconductor generates pulses proportional to the adsorbed X-ray energy. An example of these solid-state semiconductor materials in detectors is high purity germanium (HPGe) which is used in this study and lithium drifted silicon detectors (Si(Li)).

To avoid thermally generated charge, the germanium detectors are cooled to liquid nitrogen temperature (77 ^{o}K =-196 ^{o}C). The counter should not be allowed to warm to room temperature since the electronic noise increases with temperature and reduces the resolution of the technique.

6.4 Multi-channel Analyser (MCA)

The X-rays are converted into pulsating electric current by X-ray photon counters. In SMR, the preamplifier converts the charge into a voltage pulse, and a Multi-Channel Analyser (MCA) is used to convert the voltage pulses from the detector preamplifier into digital pulses. The amount of charge in the pulse produced by the detector is proportional to the energy of the photon.

The MCA sorts the pulses electronically according to their amplitude into channels that correspond to specific narrow amplitude range. A spectrum is produced, and the MCA uses an analogue amplifier to digitize the pulses into memory and puts the pulse distribution in a histogram. In the histogram, the X-axis is the pulse height and the Y-axis represent the number of counts.

MAESTRO software runs the MCA which has an Analog-to-Digital Converter (ADC) and a histogram for display. The digital resolution is affected by the ADC's number of channels, which should be chosen to match the detector type and energy range.

In this study, a DSPEC Plus (EG & G ORTEC, TN, USA) is used as both amplifier and digital MCA. Signal processing does take time and the time the system is available to receive a signal is considered "live time" while all the time consumed with signal processing is "dead time". MCA systems use logic signals to determine this "dead time" in order to ensure any quantitative data is correct.

6.5 SMR Apparatus

The SMR allows measurement of an approximately 15 µm transmitted x-ray beam. It measures the attenuated beam as it passes through the specimen mounted on a moving cell holder stage. This stage is controlled by a computer and moves a distance of 600 mm horizontally in the X-axis and 200 mm vertically in the Y-axis with an accuracy of approximately 0.1 µm (Anderson *et al.,* 2003). A high purity Germanium detector is used to detect transmitted X-ray photons which eliminates the necessity for close contact between the sample and the detector. For this reason, each sample cell chemical environment can be modified independently of other cells. The measurement of changes in mineral mass can be monitored.

SMR can be carried out in either parallel or a perpendicular mode. When the acid demineralisation is perpendicular to the X-ray beam it is called perpendicular mode. When the acid demineralisation is parallel to the X-ray beam it is called parallel mode, which was used in this study (Anderson and Elliott, 2000).

6.5.1 X-ray Generator

An Enraf-Nonius® FR590 X-ray microfocus generator was used with a PANalytical ® X-ray tube with a silver (Ag) target which gives a characteristic Kα peak at 22.1 keV. A 15 µm aperture made from 90% gold and 10% platinum is used to produce an X-ray beam of ~15 µm diameter.

6.5.2 X-ray Detector

A high purity germanium detector (Ametek, PA, USA) combined with a digital spectrometer and multichannel analyser DSPEC PLUS™ (Digital Gamma-Ray Spectrometer, ORTEC®, Ametec, PA, USA) are used as X-ray count detector. A photon voltage pulse detected by the detector is converted to a digital value by an analogue digital converter.

6.5.3 SMR Stage

The stage is connected to a computer and controlled by software written by Prof P. Anderson (Queen Mary University of London). The software allows the stage to implement up to 30 experiments simultaneously with different parameters (time, number of steps, step size, and standards).

6.5.4 SMR Cell

Cells are made of polymethyl methacrylate (PMMA), with dimensions of 40.0 mm x 50.0 mm. Each cell has a centrally located chamber of 20.0 mm diameter and 6.0 mm depth, and a cover made up of the same material as the cell itself, with the same dimensions but with 2.0 mm thickness (Figure 6.6). An HA disc is securely placed in the centre of the SMR cell chamber and the cover securely sealed with silicon and screws.

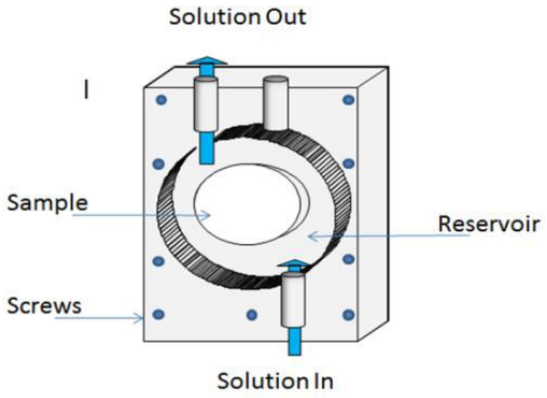

Figure 6.6 Schematic diagram of SMR cell containing HA disc. Water or acidic solutions are circulated through the cell by introducing the solutions through the bottom input (solution in) and then removed by the upper output (solution out). A third output is used to de-pressure the cell (Lingawi, 2012).

6.6 Data Analysis at a Scanning Position

Data analysis was done by standardising the counts at a chosen point against the standard HA measurement in order to correct for variations in X-ray generation.

By introducing the density of a material ρ, the Beer's law (Section 6.2.5) can be written as:

$$I = I_o\, e^{-\mu_\rho\, m} \qquad \textbf{Equation 6.4}$$

Where I is the intensity of the transmitted beam, I_o is the incident beam intensity, m is the mass per unit area of material (g/cm^2). The mass is calculated by multiplying the thickness (t) by the density (ρ), i.e., m = ρt.

Can also be written as:

$$m = \frac{1}{\mu_\rho}\left[ln\frac{N_0}{N}\right] \qquad \textbf{Equation 6.5}$$

Where, N is the number of transmitted photons and N_0 is the number of incident X-ray photons from measurements taken from the HA standard. From Equation 6.5 the integrated mass per unit, at a point can be calculated for a material of a known MAC, by measuring the intensity of the incidence and transmitted beam for monochromatic radiation.

Differentiating this gives the error in the measurement of m as

$$\delta m = \frac{1}{\mu_\rho}\left[\frac{1}{\sqrt{N}} + \frac{1}{\sqrt{N_\circ}}\right] \qquad \textbf{Equation 6.6}$$

$\frac{1}{\sqrt{N_\circ}}$ can be neglected as the number of incident X-ray photons, (N_0) is very high (≈500,000). N, the number of transmitted X-ray photons, is typically about 50,000 which give a fractional error in m of ±0.5 %

Using Equation 6.5 the projected mass of HA per unit area (g /cm^2) can be calculated by using the mass attenuation coefficient of HA (4.69 g/cm^2) calculated for AgKα radiation (22.1 KeV). Therefore, at a scan position the X-ray attenuation value can be changed to a mass value for enamel per unit area.

6.7 Calculation of The Mineral Mass loss

Figure 6.7 is an example of SMR raw data showing a linear change in mineral mass loss per unit area plotted against time (≈48 h) during exposure to an acidic environment (pH 4.0). The rate of mineral loss for HA (RML_{HA}) is determined by linear regression fitting of the slope (y = a + bx), 2.27x 10^{-4} g cm^{-2} h^{-1}, SE = 5.3420x 10^{-6} g cm^{-2} h^{-1}) using SigmaPlot 10.0

(Systat Software, California, USA). The standard error in the gradient is decreased by increasing the number of observations made.

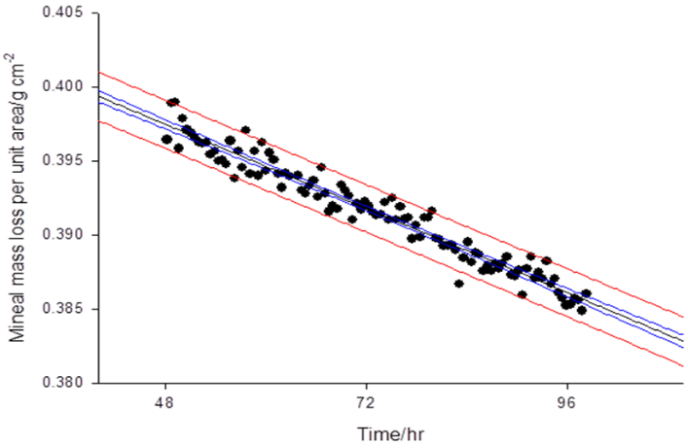

Figure 6.7 SMR raw data showing a linear change in mineral mass loss per unit area plotted against time (≈48 h) during exposure to an acidic environment (pH 4.0) at a single scan position on a HA sample. RML_{HA} was determined by linear regression fitting of the slope and the number of data points, (y = a + bx), 2.27Ex 10^{-4} g cm^{-2} h^{-1}, SE = 5.3420x 10^{-6} g cm^{-2} h^{-1}).

6.7.1 Percent Reduction in the Rate of Mineral Loss (PRRML)

The rate of mineral loss (RML) measurement of each sample after the exposure to the peptides is compared with that during the initial acidic demineralisation prior to exposure to the tested solution (the peptide) using paired t-test. The percentage reduction in the rate of mineral loss between, prior to exposure to peptide and after exposure to test peptide, were calculated by:

$$PRRML_{SUBTRATE} = \frac{Control\ RML_{SUBSTRATE} - Test\ RML_{SUBSTRATE}}{Control\ RML_{SUBSTRATE}} x100$$

Figure 6.8 compares the RML_{HA} before and after exposure to 200 nmol/ml of HTN at a single scan position. The change in the gradient of the

lines validates that the exposure to 200 µmol/l of this peptide significantly reduced the RML_{HA}.

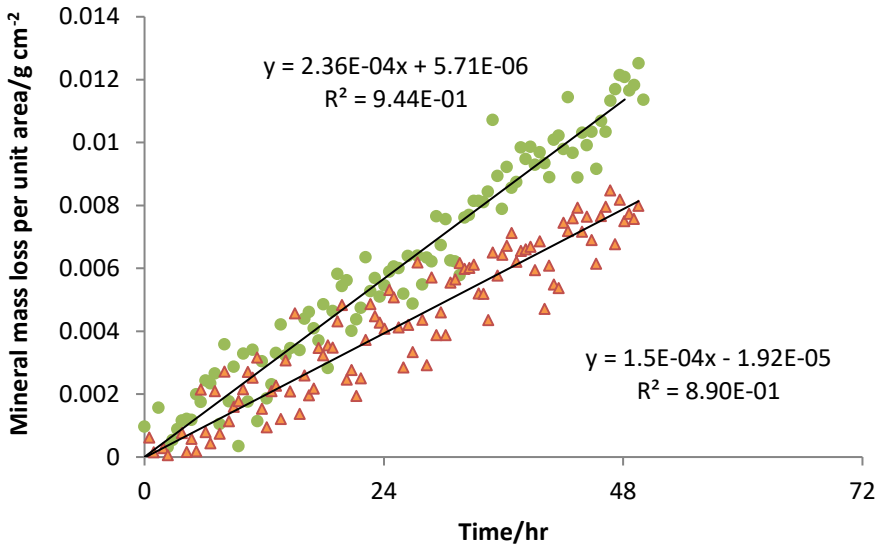

Figure 6.8 The gradient of the measured slops before (circles) and after exposure to HTN (triangles) measured at a single scan position on a HA sample. Exposure to 200 µmol/l of HTN reduced the mineral loss rate by 36.4%. The SE of the rates before and after the exposure to the peptide were $2.45x10^{-6}$ g cm^{-2} s^{-1} and $2.59x10^{-6}$ g cm^{-2} s^{-1} respectively.

6.8 Responsiveness of SMR

SMR measurement response to the changes in the cell environment is immediate (Figure 6.9). This is an indication of the sensitivity of SMR to very small changes in the cell environment and/or mineral density.

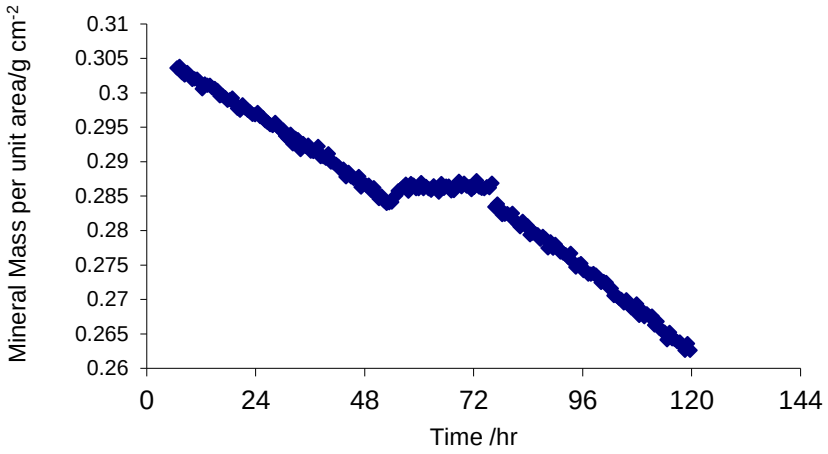

Figure 6.9 Mineral mass changes in a scan position in a HA sample during exposure to in vitro acidic solution. After the first 29 hrs of demineralisation, the enamel block was exposed to PBS (negative control) for 24 hr. Demineralisation was noted to halt immediately and the mineral density measurement changed accordingly. The demineralisation continued when the acidic solution was reintroduced to the cell and mineral loss was measured again. The gap noted in the data after the introduction of the acidic solution represents the X-ray halting time needed for the removal of PBS and sample wash with distal water (±15 min).

6.9 Advantages of SMR

SMR overcomes the conventional microradiography techniques that uses photographic emulsions. The disadvantage of the conventional technique includes the inhomogeneity of the film emulsion due to manufacturing variations, saturation of the film and noise at low X-ray exposures. On the other hand, the advantages of SMR include:

- The sample used in SMR does not need to be in close contact with the x-ray detector and can be located within environmental cells.

- The SMR method is quantitative and the accuracy is only limited by counting statistics.

- The photon counting can be selected to only a certain energy range, thus allowing electronic monochromatisation of the X-ray beam.

- Each cell can maintain a different environment for the sample it contains, for example, different pH conditions, and degree of saturation, chemical composition and circulating rate of the solution.

- Real-time measurement of mineral mass of the physical and chemical changes in enamel and HA demineralization (Anderson and Elliott, 2000; Shah *et al.,* 2011).

Chapter 7. Nano-Spectrophotometry

7.1 Introduction

Chemical analysis before 1940 was a lengthy procedure requiring skill and care. Arnold J. Beckman invented the U.V. and visible spectrophotometer in 1940. The technique was used to quantitate the reflection or transmission of a substance at a particular wavelength. Chemical analysis was then greatly simplified taking less time while achieving an accuracy of up to 99%. From then the ease of use was improved by the addition of a double beam version. In the 1990s, the addition of PC control and onscreen spectra display was added (Simoni *et al.,* 2003).

Visible and ultraviolet (UV) lights of the electromagnetic spectrum have energy that excites electrons (150–400 kJ mol^{-1}). When light absorption is measured as a function of wavelength a spectrum is attained (Harris and Bashford, 1987). Electrons in aromatic rings absorb UV light between 150-400 nm and 400-800 regions in visible light. For absorbance measurement, the chemical substance (nucleic acids, peptides or proteins) should be dissolved in a clear solvent such as buffer or water. The intensity of absorbance and the wavelength of absorbance depend on the chemical nature of the solvent and the molecular chromophores tags if present. (Pace *et al.,* 1995)

A spectrophotometer contains a source of light and passed through a monochromator (optical filter). The monochromatic light passes through

the cuvette and what is not absorbed is detected by a photomultiplier. Modern spectrophotometers contain double beams; a beam that passes through a cuvette that has the solvent (blank) as a reference, its absorbance is deducted from the absorbance of the tested sample.

Spectrophotometers may serve specific purposes:

-Standard spectrophotometer with standard cuvettes holders that accept a sample of 0.5 ml. The cuvettes have a 1 cm light path with thickened walls. This is a step towards a micro-spectrophotometer (e.g. Implen Spectrophotometers)

-Molecular biology spectrophotometers with a fixed wavelength of 200 and 280 nm to measure nucleic acids.

-Thermo-spectrophotometers: they have heated cuvettes holders that take 0.5 ml quartz cells with tight stopper and allow the temperature to rise to 100°C. These are used to follow conformational changes especially the melting of DNA (e.g. Gilford Spectrophotometers).

7.2 Beer-Lambert Law

Protein and nucleic acid concentrations can be measured in solution. According to the Beer-Lambert law, the absorbance is linear with the concentration; therefore, it is suited for quantitative measurements. Absorbance of light depends on the intensity of light before and after passing through a solution.

$$A = \log(I_0/I) \qquad \textbf{Equation 7.1}$$

Where A is the absorbance, (I_0) is the intensity of light before passing through solution. (I) is the intensity of light after passing through the solution.

Therefore, the concentration of a material can be calculated from the absorbance using:

$$A = \varepsilon cl \qquad \textbf{Equation 7.2}$$

Where Ɛ is the molar absorbance coefficient (L mol^{-1} cm^{-1}), c is the molar concentration, and l is the path-length in centimetres.

7.3 Protein Absorption

Peptide bonds absorb light in the range of 180 to 230 nm (ultraviolet). Also, the disulfide bonds in proteins containing two cysteine residues sidechains show absorbance near 260nm (Schmid, 1997)

In addition, proteins display absorption between 275-280 nm due to the presence of aromatic amino acids (Figure 7.1 A and B). Phenylalanine which is one of the aromatic amino acids contributes to a much smaller absorption compared to tyrosine or tryptophan. If protein primary sequence includes no aromatic amino acids, or few, the error in measurement will be high unless high concentrations can be used (Schmid, 2001).

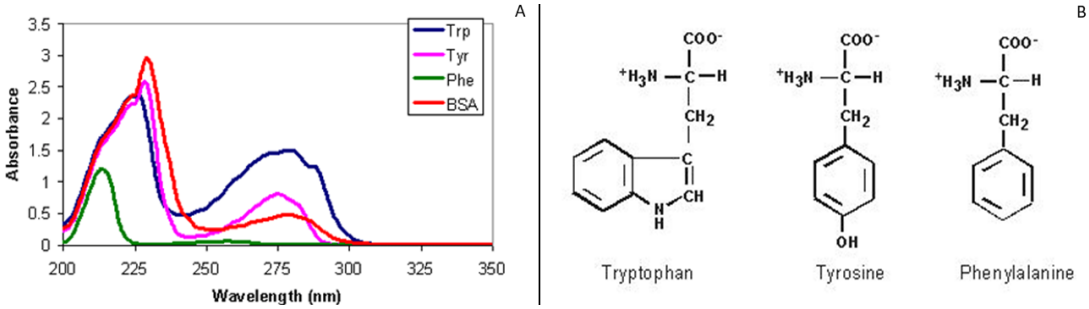

Figure 7.1(A) Spectra scan of aromatic amino acids. (B) The three aromatic amino acids that give absorbance between 275 and 280 nm: tryptophan (W), tyrosine (Y) and phenylalanine (F) (Held, 2003).

7.4 Advantages of Nano-Spectrophotometry

-Sample volume: the use of microplate instead of cuvettes uses a volume 100-200 µl. It also reduces the light path from 1cm to 0.5 cm or less. Also, the addition of tags can greatly increase U.V. absorbance.

-Sample recovery: for limited samples a non-destructive method such as spectrophotometry is useful, the technique is also quick and easy to use.

-Absorbance analysis is highly reproducible (Noble *et al.*, 2007).

- Protein absorbance modification: it is difficult to measure the UV absorbance of proteins that lack the presence of aromatic amino acids in their sequence. However, spectrophotometry permits the measurement of tags that could enhance the absorbance of proteins and hence their quantification e.g. fluorescein isothiocyanate tags (McKinney *et al.*, 1966).

Chapter 8. Dynamic Light Scattering (DLS)

Understanding of light, electromagnetic radiation and how molecules scatter light in the 19th and 20th century enabled the development of an understanding of the phenomena. In the last quarter of the 20th century, multiple forms of spectroscopy were developed. Photon Correlation Spectroscopy, or as it is more commonly known as, Dynamic Light Scattering, is one form of spectroscopy.

Lord Rayleigh developed an understanding of light scattering by particles between 1871 and 1899. Today commercial instruments allow the phenomenon to be applied for several purposes including estimating the size aggregation of particles in solution or suspension (Berne and Pecora, 2000; Pecora, 2000).

Rayleigh's work and Gans (1925) was limited in theory to gases where molecules are spherical in shape and refractive indexes were similar (Pecora, 2000). Biological structures such as proteins or larger molecules scatter light. Due to their motion, fluctuation in the scattered light occurs, which is the part we are interested in analysing.

8.1 Particle Size Measurement

The DLS technique depends on (A) an illuminating light, a laser beam typically, (B) scattering light by particles (due to Brownian motion), and (C) a detector.

Particle size measurement is given by DLS as a hydrodynamic radius (R_H), which can be defined as the radius of a hypothetical sphere that diffuses at the same rate as particle under investigation.

When a monochromatic beam of light encounters solution containing molecules, light scatters in all directions as a function of the size of the molecule. In DLS, the intensity of scattered light is analysed as time-averaged intensity, if the intensity fluctuations (caused due to Brownian motion of molecules in solution) of scattered light is analysed, the diffusion coefficient (D) that is related to the hydrodynamic size of molecules can be obtained.

The diffusion coefficient describes the motion of light emitting particles. It is specified by Einstein-Stokes equation of the diffusion coefficient (Smith, 2007):

$$\boldsymbol{D = \frac{k_B T}{6\pi n R_H}} \qquad \textbf{Equation 8.1}$$

where T is the temperature in Kelvin, k_B is the Boltzmann constant (1.380×10^{-23} $kg.m^2.s^{-2}.K^{-1}$), R_H is the hydrodynamic radius, and n is the viscosity of the solvent. Therefore, the hydrodynamic radius can be calculated by auto-correlating the particle diffusion coefficient to scattered light signal.

The detector position in DLS experiments is either at 90° or at 175° (backscatter). The advantages of using backscatter detection which is used in this work are:

-The incidence beam does not need to travel through the whole sample. Therefore, samples with high concentration can be used.

-It reduces mutable scattering, where the light that is scattered from one molecule is scattered again from another molecule (Amin *et al.,* 2014).

8.2 Zeta Potential

Charged particles will attract towards an electrode of opposite charge when an electrical field is applied.

During electrophoresis, a moving particle scatters an incident laser. As the particles move they scatter laser at a different frequency than the original incident beam. The shift in frequency is proportional to particle velocity (Ito *et al.,* 2004). The electrophoretic mobility U_E is calculated first

$$U_E = \frac{V}{E} \qquad \textbf{Equation 8.2}$$

where V is the velocity (µm/s), and E is the electrical field strength (Volt/cm). Then the zeta potential can be calculated from Henry equation;

$$U_E = \frac{2\varepsilon\, z\, f(ka)}{3n} \qquad \textbf{Equation 8.3}$$

where Ɛ is the dielectric constant of the solution, z is zeta potential, f(ka) is Henry's function (1.5), n is the viscosity and U_E is the electrophoretic mobility of a particle.

8.3 Advantages of DLS

The advantages of using DLS compared to other techniques include:

- DLS has a smaller limit while detecting particle size (e.g.<50 nm), While laser diffraction has a better detection for larger particles (e.g. > 1 µm) (Ziegler and Wachtel, 2005).

- Measurement of small oscillations that are very sensitive to particle size change or disturbance. While particle size determination by sedimentation (X-ray disc centrifuge and DCS/differential centrifugal sedimentation) measures particles size based on their density. Therefore, it is unable to differentiate between two particle sizes with the same density (Fielding *et al.,* 2012).

- Provides superior size distribution compared to Atomic force microscopy (AFM) (Lamprecht *et al.,* 2014).

Chapter 9. Circular Dichroism (CD)

Circular dichroism is a technique used for rapid characterization of protein secondary structure and folding properties. It measures the difference in absorbance between the left and right circular polarised light.

9.1 Background

In the 18th century, Jaen-Baptist Biot reported that light polarisation plane is altered when it passes through liquids (Fasman, 1996). Since then the alteration in the polarisation was related to the asymmetrical organization of the saturated carbon atom. This was the foundation of chemical stereochemistry that helped with explaining the properties of organic compounds. The technique was later developed to include optical rotatory dispersion (ORD) and circular dichroism spectroscopy.

Conventional CD measures spectra down to 180nm and provides information on excitation bands in near and far UV. Proteins change CD spectra due to the presence of peptide bond, aromatic side groups and disulphide bridges (Calero and Gasset, 2005).

9.2 Theory

Light has a time-dependent electrical and magnetic fields. When the light is polarised, the electric field will oscillate in a single plane wave. This wave is the result of 2 component of equal magnitude. One rotates clockwise (E_R), and the other rotates anticlockwise (E_L). Biomolecules are

mostly chiral (asymmetric). A chiral molecule interacts differently to right circularly polarised light and the left circularly polarised light (Oakley *et al.,* 2006).

The difference in absorbance between the left and right circular polarised light is defined as

$$\Delta A = A_L - A_r \qquad \textbf{Equation 9.1}$$

where, A_l and A_r are the absorbance of the left and right circularly polarised lights, respectively. Preferential absorption of left and right circularly polarised lights results in elliptical polarised light. Circular dichroism is represented in terms of ellipticity (θ). A plot between the wavelength against ΔA or θ represents CD spectra.

9.3 CD Data Analysis

The CD data is given in ellipticity values (θ); they are converted to mean residue ellipticity (MRE) through the equation:

$$MRE = \frac{\theta}{(10 \times Cr \times l)} \qquad \textbf{Equation 9.2}$$

where l is the path-length (cm) and C_r is the mean residue molar concentration known from:

$$Cr = n \times \frac{1000 \times n \times C_g}{M_r} \qquad \textbf{Equation 9.3}$$

where n is the number of peptide bonds, C_g is protein concentration (g/ml) and M_r is the molecular weight of the residue.

9.4 Deconvolution of the CD Spectra

Deconvolution analysis was carried out to compare the contributions of each secondary structure components in the measured CD spectra of a given sample. Results were reported using CONTIN/LL programme and analysed using the CD software Diamond Light Source (Benning, 2014). The CONTIN/LL programme operate using a basic data set of 43 soluble proteins whose crystal structures are known (SP43) (Sreerama and Woody, 2000). The reference set of proteins includes those with helical content, β-strand, Turns and Unordered. Based on the comparison between the spectra of the reference set of proteins and the CD spectra of the sample being tested, a fraction of folding of α helix, β strands, turn and disordered conformation in the protein under study is obtained. The CONTIN/LL program uses the spectra range between 190 nm and 240 nm.

9.5 CD of Proteins

All amino acids apart from glycine are chiral. This chirality is reflected further in the structural component that the proteins adopt. When circular polarised light passes through a protein, the structure of the protein gives characteristic bands in particular regions of the CD spectrum. Secondary structure conformation such as α-helix, β-strands, β-turns and random coil structure give bands of different shapes and magnitude in the far UV (190-250 nm) (Figure 9.1).

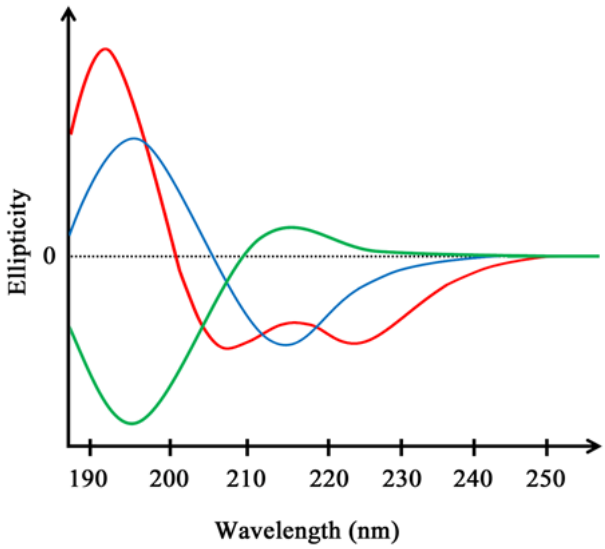

Figure 9.1 Secondary structure conformations, shown in a characteristic CD spectrum, α-helix (referred to in red), β-strand (blue), and random coil (green) (Correa and Ramos, 2009).

An alpha helix shows a (-) bands at 222 and 208 nm and a (+) band at 190 nm. β-strand has a (-) band at 218 nm and a (+) at 196 nm. While random coil conformation shows a (-) band at 195 nm and a (+) band at 212 nm. Beta turn in proteins are made from a motif that contains 4 amino acid residues with a backbone that turns approximately 180°; therefore, it is difficult to define it. However, a typical β-turn has a week (-) band at 225 nm and a strong (+) band at 200 nm (Louis-Jeune *et al.,* 2012).

It has been suggested that the ellipticity ratio between the two negative ellipticity peaks (as seen in Figure 9.1) at 222:208 nm (R2) is an indication that the sequence contains isolated helix, or several helices (Naganagowda *et al.,* 1998). An ellipticity ratio of 1.10 is evidence of coiled-coil structure. An ellipticity ratio of 0.9 (or smaller) is evidence of single helix, including 3_{10} helices. However, according to Anderson *et al.,* (1996b) and Zheng *et al.,* (2015) the 3_{10} helices cannot be distinguished from α-helices

by CD measurements and the R2<1.10 simply reflects the presence of short helices seen commonly in NMR structures of peptides and proteins.

9.6 Application of CD in biology

The CD structural analysis has different applications in biological studies including:

-Determination of protein secondary structure; far UV CD analysis provides information about proteins secondary structure. Proteins with a mixture of secondary structures spectra can be deconvoluted to acquire the fraction of different structures present (Goobes *et al.,* 2006).

-Studying the stability of proteins or denaturation due to heat. Circular dichroism band shifts at certain wavelengths, usually at 220 nm, which can provide denaturation curves for proteins in solution (Micsonai *et al., 2015)*.

Chapter 10. Secondary Structure Prediction of Individual Peptides

Several protein secondary structure prediction methods were used to locate the position and the length of the helix revealed by the CD experiments.

10.1 Protein Secondary Structure Prediction Using Robetta software

The Robetta full-chain protein structure prediction server facility (http://robetta.bakerlab.org/) provides protein structure prediction and analysis for proteins with sequence length between 27 and 1000 residues (Kim *et al.,* 2004). Secondary structure prediction is calculated from 'Ginzu' method, (shown in Figure 10.1), that uses the primary sequence of the peptide, in order to resolve separate protein structural components of putative domain (Kim *et al.,* 2004). These domains are used in comparative modelling of homologous experimentally determined structures (Chivian *et al.,* 2003).

Figure 10.1 An example of online Robetta software structure prediction submission web page, showing the method for secondary structure prediction (Ginzu), target name, and analysis using the primary sequence (AA).

The method always generates five models where each conformational model is equally probable (Figure 10.2). If these models contain similar secondary structural prediction, then there is a higher probability that this structure occur.

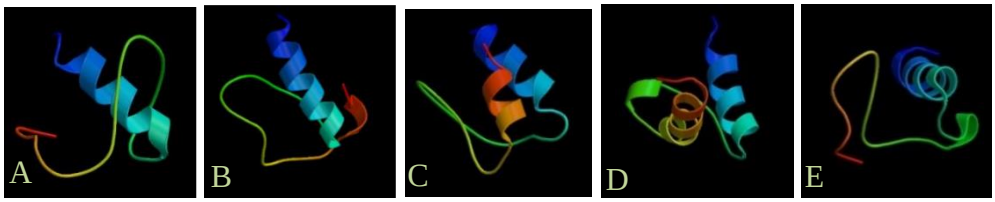

Figure 10.2 Typical 3D structure predictions using Robetta software. Where the N-terminals are shown in blue, while the C-terminals are shown in orange. Each model A), (B), (C), (D), and (E) is possible to occur. The presence of a repeated conformation in each model such as the helical conformation in the N-terminal indicates that it is more probable to occur in the secondary conformation of a peptide.

10.2 Protein Secondary Structure Prediction Using PSIPRED (Bioinformatics Group)

The Bioinformatics Group at University College London has developed a secondary structure prediction software using (PSIPRED) method *(http://bioinf.cs.ucl.ac.uk/introduction/)* shown in Figure 10.3 (Buchan *et al.*, 2013). The method gives ''a consensus'' of the secondary structure prediction by comparing the input primary sequence intra-residue contacts with a library of contact maps of known structures (Jones, 1999).

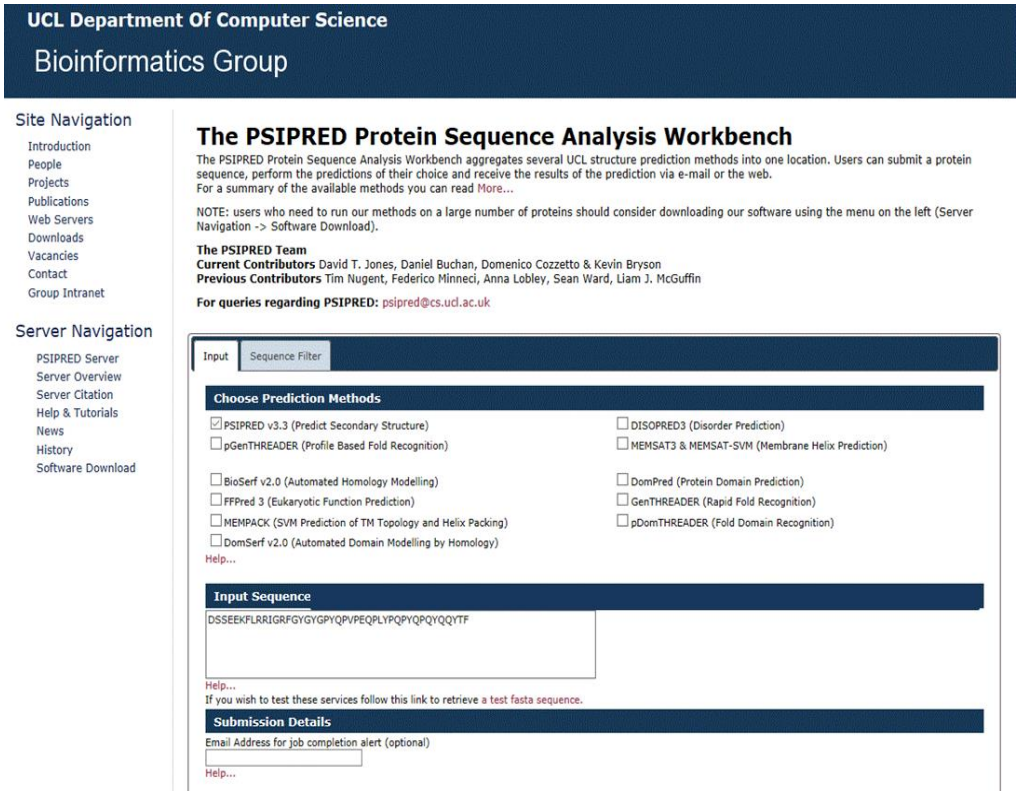

Figure 10.3 An example of UCL Bioinformatics Group server structure prediction submission web page, showing the method for secondary structure prediction (PSIPRED), and analysis using the primary sequence (Input Sequence).

The featured secondary structure prediction is generated in a diagram, as shown in Figure 10.4. The diagrams show the secondary structures in a sequence through a cartoon that is colour coded according

to the secondary structure predicted (pink: helical structure, Yellow arrow: β-sheet, black line: Random coil) and also an abbreviation of the secondary structure matching with the amino acid sequence (H: helical structure, E: β-strands, and C: random coil).

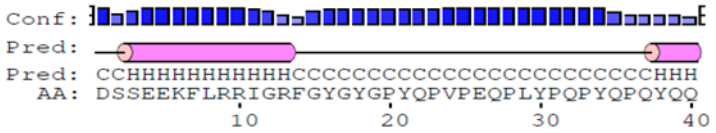

Figure 10.4 Typical structural prediction diagram using PSIPRED. Where Conf. represent the confidence value at each position in the alignment, given as a series of blue bar graphs. Pred. is the predicted secondary structure, and AA is the target sequence.

EXPERIMENTAL STUDIES

Chapter 11. Spectrophotometric Characterisation of the Adsorption of Statherin, Histatin-1 and Their 21 N-terminal Peptides Individually and When in Combination onto HA Beads, HA Discs and Enamel

11.1 Introduction

The acquired enamel pellicle (AEP) is formed by selective adsorption of salivary organic, and inorganic molecules onto enamel surface *in vivo*. The protein composition of the AEP is important in the inhibition of calcium and phosphate precipitation, crystallisation, and control of microbial adhesion (Jensen *et al.,* 1992). Understanding the biological importance of the pellicle entails the clarification of its composition, structure and mechanism of formation. With regards to the function of the pellicle, proteins/peptides are important for calcium phosphate regulation, control of microbial adherence, and possibly calculus formation.

Selective adsorption of salivary proteins studies had led to the conclusion that specific proteins are pellicle precursors and bind according to their affinity to HA (Moreno *et al.,* 1987; Yin *et al.,* 2003). Adsorption of salivary peptide mixtures can vary considerably from individual peptides. After adsorption of a single peptide at a specific binding site, a further peptide binding will be affected by peptide-peptide interactions. These specific peptide-peptide interactions play an important role in pellicle function and formation *in vivo* (Vitkov *et al.,* 2004).

Apart from peptide-peptide interactions, peptides are subjected to the modification of the dynamics oral environment. That exposes these peptides to proteolytic cleavage and acidic settings (Helmerhorst and Oppenheim, 2007). These oral environment modifications may alter the structure and the function of these peptides.

The aim of the studies described in this chapter was to investigate the adsorption characteristics of salivary peptides STN, HTN, STN21 and HTN21 individually, and, also when in combination onto; HA beads, HA discs, and enamel.

The first objective was to spectrophotometrically measure the mean amount of STN, HTN, STN21, and, HTN21 adsorption (MAPA), desorption and binding rates onto HA beads individually, (at 100 and 200 nmol/ml) and, when in combination. The second objective was to calculate the mean percentage of peptide adsorbed (MPPA) for STN, HTN, STN21, and, HTN1 individually onto HA discs, and enamel blocks (used in the SMR study, Chapter 13), to investigate whether these peptides behave differently upon adsorption onto HA discs or enamel blocks.

11.2 Materials

11.2.1 Chemical Solutions and Peptide Samples

Phosphate buffered saline powder (Sigma-Aldrich, UK) was dissolved in deionised water to prepare 10 mmol/l phosphate buffered saline containing 0.138 mol/l NaCl, and 0.0027 mol/l KCl at pH 7.4.

Full-length phosphorylated STN, HTN, STN21 and HTN21 were synthesised by Fmoc solid-phase peptide synthesis (SPPS) and purified (98% pure) by HPLC as trifluoroacetate salts (TFA), (Peptide Protein Research Ltd, United Kingdom).

Trifluoroacetic acid is frequently used in the synthesis of peptides (Table 11.1). It cleaves synthesized peptides from solid-phase resins and is also used to improve High-performance liquid chromatography (HPLC) performance in peptide purification step.

Peptide	Molecular weight
HTN	5760 Da
HTN21	3371 Da
STN	5785 Da
STN21	3223 Da

Table 11.1 Molecular weight of HTN, STN, HTN21 and STN21.

The 21-mers of both peptides have fewer tyrosine residues than STN (3 in STN21) and HTN (1 in HTN21). Therefore, the 21 N-terminal peptides were each labelled with absorbance tags to enhance the absorbance measurement of peptides individually. Different absorbance tags for STN21 and HTN21 were used in order to measure the change in absorbance of each peptide individually and when in combination with other peptides. STN-21 was tagged with fluorescein isothiocyanate (F-STN21), and HTN21 was tagged with Coumarin (C-HTN21) (Peptide Protein Research Ltd, United Kingdom). Both were tagged at the C-terminal end to reduce the possible interference at the N-terminal binding motif. Fluorescein has a spectral peak wavelength at approximately 495 nm, and Coumarin at 352 nm, therefore each peptide is identifiable individually as shown in Figure 11.1.

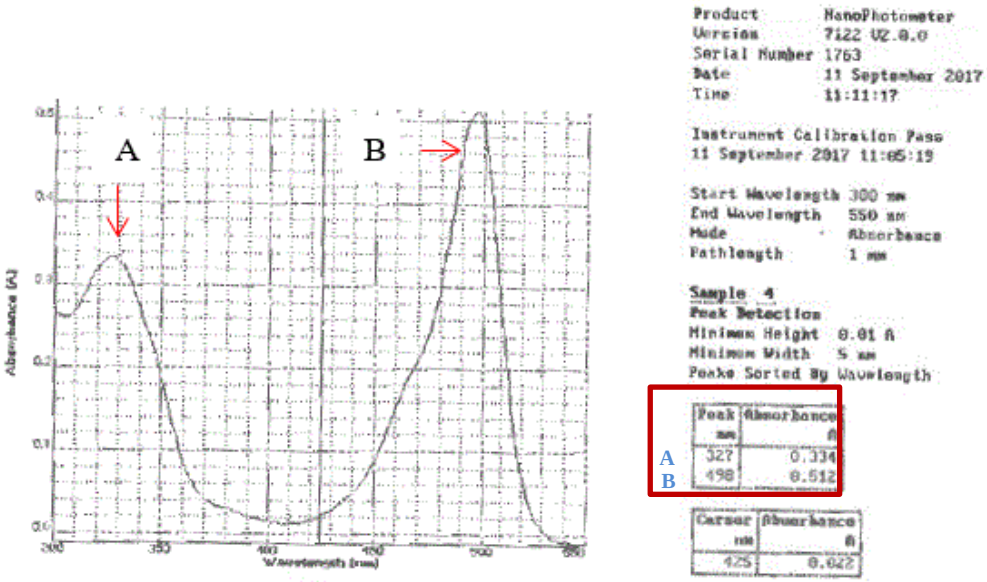

Figure 11.1 Instrumental absorbance plot of F-STN21 and C-HTN21 combined. (A) Absorbance peak of C-HTN21 at 327 nm. (B) Absorbance peak of F-STN21 at 498 nm. STN21 was synthesised with fluorescein at the C-terminus and HTN21 with Coumarin for two reasons. These tags increased the absorbance and allowed the peptides to be measured separately while in combination.

Peptides were weighed with an UMX2 Ultra-microbalance (Mettler Toledo, UK). Peptides were dissolved in PBS, at a concentration of 100 and 200 nmol/ml when used individually, and 100 nmol/ml of each when in combination. These concentrations were selected from the range of statherin concentrations used by Kosoric *et al.,* (2007) to test the effect of up to 10 times greater concentration of STN than the concentration in saliva on the demineralisation of HA. Therefore, HTN was also used at a concentration of 100 and 200 nmol/ml as a form of comparison.

For the purpose of this chapter units for concentration are expressed as nmol/ml, However, elsewhere within the thesis peptide concentration units are expressed in µmol/l as seen in Sugiyama and Ogata, (1993) and Kosoric *et al.,* (2007).

11.2.2 Particle Size Analysis of HA Beads

Ceramic HA beads (CHT Type I) sintered at 400°C were used (Bio-Rad Laboratories. Inc) to study peptide adsorption. These HA beads are spherical with a diameter of 80 ±8 µm according to the manufacturer information. Particle size analysis was carried out using a Mastersizer 3000E (Malvern Instruments Ltd, UK). SEM was also carried out to measure HA bead particle size and surface characteristics. Particle size analysis, and SEM images of the HA beads taken at 400 µm magnification (typical example shown in Figure 11.2) showed a large size distribution range from 80-110 µm and surface inconsistencies, which could produce variability in the results. Therefore, peptide adsorption per unit volume (mg/ml) rather than per unit surface area was used.

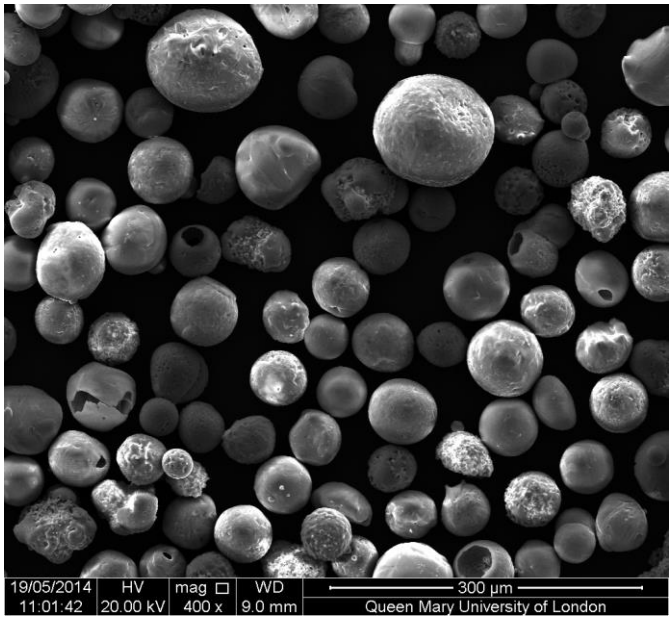

Figure 11.2 Scanning electron microscopy of the Bio-Rad ceramic HA beads (CHT Type I), demonstrating the HA particle size variation and surface discrepancy.

11.2.3 Spectrophotometric Calibration of STN, HTN, F-STN21, and C-HTN21 Absorbance

Calibration was done to confirm the instrumental response for concentration changes, and to calibrate the absorbance with the concentration of peptide in solutions after HA exposure to the tested peptide. The calibration curves were made for full-length peptides based on tyrosine absorbance at 278 nm, whereas the absorbances for the truncated peptides, were based on the fluorescein tag at 498 nm, and coumarin tag at 357 nm.

Dilutions of the peptide solutions were made with the same solvent used to dissolve the peptide. A blank was prepared of the solvent alone.

The spectrophotometer (NanoPhotometer, Implen GmbH) was turned on 30 min prior to the measurements to ensure stabilisation. The wavelength range selected was between 200-400 nm for STN and HTN, while the wavelength range used for F-STN21 and C-HTN21 was between 250-500 nm. The optical pathway length was set at a 1 mm light path length. This pathway required up to 5 µl of solution, which was recovered after measurement. A solvent blank was used to zero the instrument with each batch of samples. Figure 11.3 shows the calibration plots for STN, HTN, F-STN21, and C-HTN21.

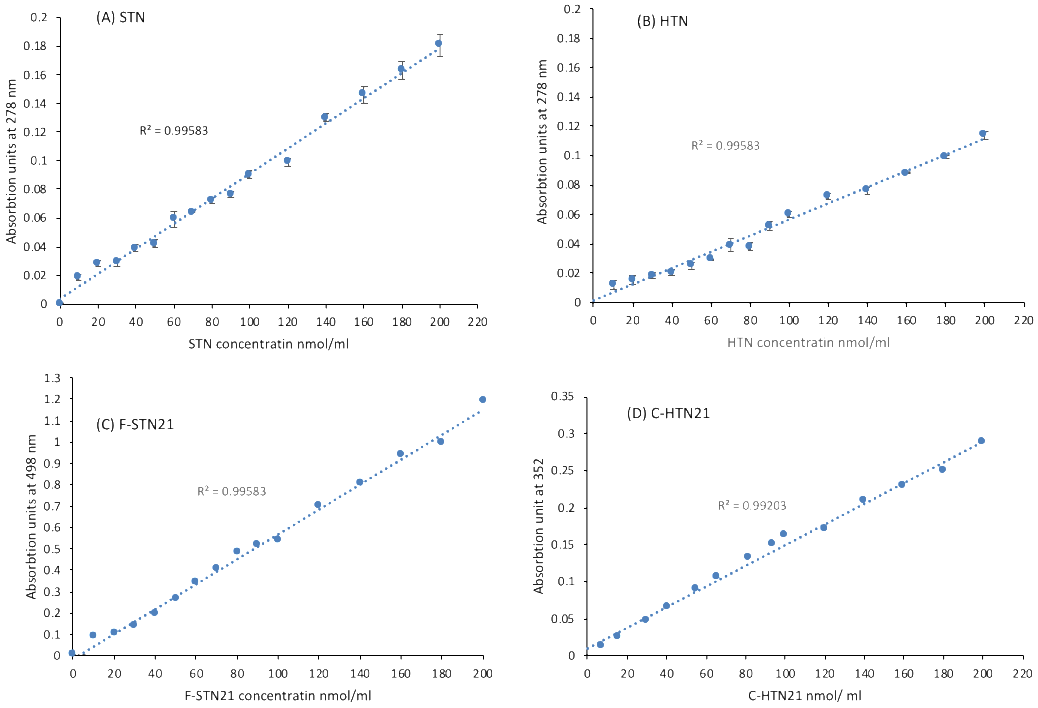

Figure 11.3 Peptides calibration plots. (A) STN standard solution concentration and its dilutions plotted versus absorbance at 278 nm. (B) HTN standard solution concentration and its dilutions plotted versus absorbance at 278 nm. (C) F-STN21 standard solution concentration and its dilutions plotted versus absorbance at 498 nm. (D) C-HTN21 standard solution concentration and its dilutions plotted versus the absorbance of coumarin at 352 nm. All peptides showed a linear relation between the absorbance and the changes in concentration.

11.3 Spectrophotometric Methods

11.3.1 Adsorption of STN, HTN, F-STN21, and C-HTN21 Individually onto HA Beads

All peptides were dissolved in 1.0 ml solution in Eppendorf tubes. The initial absorbance measurement was taken for each peptide solution. Each peptide solution was then exposed to 1.0 mg of HA. The suspensions of beads in peptide solution were mounted on a rocking shaker (See-saw rockers - SSM4) operated at a 60 oscillation/minute at an angle of 7°. Further absorbance measurements of the peptide solutions were taken after time intervals of, 1, 3, 5, 10, 15, 20, 25, 35, 45, 60, 120 min and after

further 24 hrs at 25 ±2 °C. After each time point measurement, the suspensions were centrifuged for 30 sec at 6,000 rpm (Micro-centrifuge micro-spin 24S). The time course of adsorption of peptides onto HA beads was followed until saturation of HA beads was reached. Each experiment was repeated four times for each peptide.

A control solution without HA beads was made for each peptide to confirm that the reduction in absorbance was due to peptide adsorption onto HA beads rather than the Eppendorf tubes.

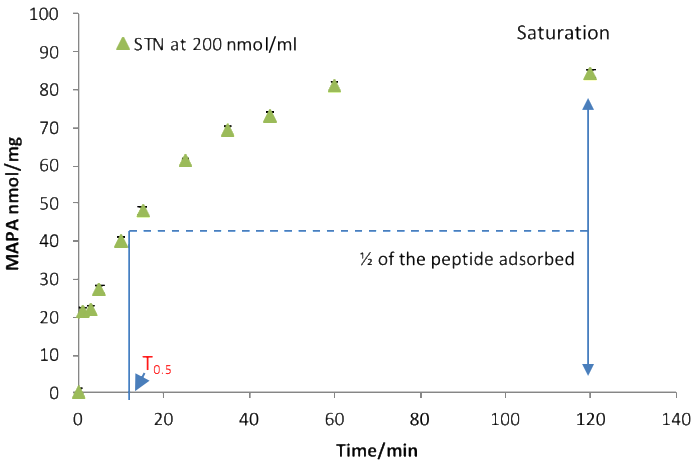

Figure 11.4 Examples of a saturation plot calculated from the spectrometric absorbance. The plots show the MAPA (at 200 nmol/ml) after exposure to 1.0 mg of HA beads for 120 min. The MAPA was obtained at saturation. $T_{0.5}$ was determent from the curve when half-saturation was achieved.

Figure 11.4 shows a typical saturation plot of a peptide with time. The mean amount of peptide adsorbed (MAPA) (nmol/mg) was obtained at saturation. The rates of binding were determined from the saturation curves by measuring the half-time to saturation ($T_{0.5}$) (as shown in Figure 11.4).

Data was analysed using GraphPad Prism 7.0d (GraphPad Software Inc., La Jolla, USA) statistical software for normality using Shapiro-Wilks test. After confirming data was normally distributed analysis of variance (ANOVA) with post hoc Bonferroni test was used to identify which means were significantly different from each other. Significance was predetermined at $\alpha=0.05$. Results are expressed as mean and standard error (±SE).

11.3.2 Adsorption of Peptides When in Combination onto HA Beads

11.3.2.1 Adsorption of STN, HTN, F-STN21, and C-HTN21 When in Combination onto HA Beads

The spectrophotometric absorbance of each individual peptide when in combination was carried out:

- STN when in combination with C-HTN21.
- HTN when in combination with F-STN21.
- F-STN21 when in combination with either HTN or C-HTN21.
- C-HTN21 when in combination with either STN or STN21.

The absorbance of individual full-length peptides when in combination was based on tyrosine absorbance, while the absorbance for the individual truncated peptides in combination, was based on the fluorescein and coumarin tags, which enabled the measurement of absorbance for each peptide individually when in combination. This was possible since tyrosine, fluorescein and coumarin have distinct absorbance peaks at different wavelengths, as discussed in Section 11.2.1. Each experiment was repeated four times for each peptide when in combination.

11.3.2.2 Sequential Adsorption of STN and HTN onto HA Beads

The absorbance data for full-length STN and HTN in combination cannot show which (of the two peptides) is binding since both of their absorbances is based on tyrosine absorbance. Full-length peptides tagged with fluorescein and coumarin tag were unavailable within the time limits for this project. Therefore, a modified method to measure the sequential adsorption of each peptide onto HA beads was developed. This protocol required exposing HA beads to one of the full-length peptides dissolved at a concentration of 100 nmol/ml for 2 hrs. The beads were then centrifuged for 30 sec at 6,000 rpm, dried, and then exposed to the solution containing the second full-length peptide (also at a concentration of 100 nmol/ml). Absorbance measurements of the 2nd solution were taken at time intervals of 1, 3, 5, 10, 15, 20, 25, 35, 45, 60, 120 min. The experiment was repeated four times, and data analysis was carried out the same way as described in Section 11.3.1.

This sequential adsorption of STN after exposing HA beads to HTN and the adsorption of HTN after exposing HA beads to STN was used as a model for STN and HTN when in combination in solution.

11.3.3 Desorption of STN, HTN, F-STN21, and C-HTN21 Individually or When in Combination from HA Beads

The HA beads from each adsorption experiment were collected by centrifuging the suspensions. The desorption experiments were carried out by exposing the HA beads to i) 1.0 ml of acetic acid pH 4.0, ii) and to 2 M NaCl for 48 hours (Gorbunoff, 1985). The absorbance of the desorbed

peptide was measured spectrophotometrically after time intervals of 1, 3, 10, 15, 30, 60, 120 min at 25 ±2 °C. Each experiment was repeated twice for each peptide.

11.3.4 Adsorption of STN, HTN, F-STN21, and, C-HTN21 Individually onto HA Discs, and Enamel

In the SMR demineralisation study (Chapter 13), 12 mm diameter HA discs and 4 mm x 4 mm enamel blocks were exposed to peptide solutions for 24 hrs. Analysis of these solutions spectrophotometrically was done in order to calculate the mean percent of peptides adsorbed (MPPA) individually onto HA discs and enamel blocks.

The MPPA onto HA discs and enamel was calculated from the change in absorbance of each individual peptide in the solution used in the SMR experiment. Spectrophotometric absorbance measurements were obtained for each peptide solution before the exposure to HA discs or enamel blocks, and after 24 hrs exposure to the peptide solution. The concentration of peptide remaining in solution was then determined from the calibration curves. The difference between the initial concentration of peptides before the exposure to HA discs or enamel ($C_\circ$), and, the concentration of peptide in solution after the exposure to HA discs or enamel (C_i) was used to calculate MPPA,

$$MPPA = \frac{C_\circ - C_i}{C_\circ} x100 \qquad \text{Equation 11.1}$$

The spectrophotometer settings were similar to those described in Section 11.2.3.

Coumarin and fluorescein were added to improve the absorbance measurement and distinguish between HTN21 and STN21 and the other peptides adsorption while in combination. Although it is realised that these tags might affect the adsorption of the peptides we have assumed that this is minimal. The SMR demineralisation results of peptides with and without these labels were not significantly different.

The SMR experiments (Chapter 13) of peptides in combination were done only with untagged peptides. It was not possible to distinguish the absorbance of each peptide when in combination, and therefore the MPPA onto HA discs, and enamel were obtained only for the individual peptides.

11.4 Results

11.4.1 Adsorption of STN, HTN, F-STN21, and C-HTN21 Individually onto HA Beads

Figure 11.5A and B shows saturation plots for STN and F-STN21 after the exposure to 1.0 mg HA.

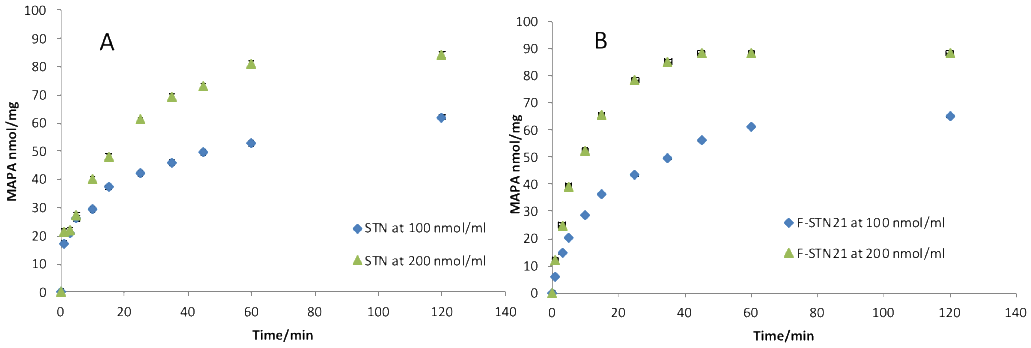

Figure 11.5 Saturation plots of STN(A) and F-STN21(B) showing the MAPA vs. time when exposed to 1.0 mg of HA. Changes in the MAPA was measured until a plateau was achieved.

The MAPA values, and the $T_{0.5}$ were obtained for STN at 100 nmol/ml, and, at 200 nmol/ml from Figure 11.5A. The MAPA values, and the $T_{0.5}$ were obtained for F-STN21 at 100 nmol/ml, and, at 200 nmol/ml from Figure 11.5B.

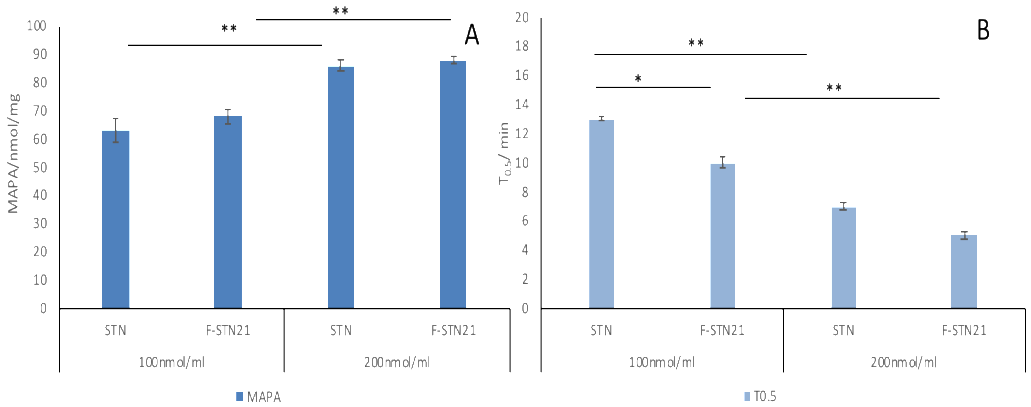

Figure 11.6 (A) Mean amounts of STN and F-STN21 adsorbed (MAPA) at two different concentrations to 1 mg of HA beads (B) The mean time during which half of the peptide adsorbed onto HA beads. The error bars represent the standard errors of the means (n=4, p< 0.05, p< 0.01**)*

Figure 11.6A shows that the MAPA value of both STN and F-STN21 were statistically similar at 100 nmol/ml, and, at 200 nmol/ml. Doubling the concentration of STN and F-STN21 increased the MAPA value of both similarly but did not double it ($p < 0.01$).

Figure 11.6B shows that the binding rate for STN was slower than the F-STN21 at 100 nmol/ml ($p < 0.05$). The binding rates for STN and F-STN21 were faster when the concentration was doubled ($p< 0.01$). F-STN21 binding rate was twice as fast when the concentration was doubled compared to F-STN21 at 100 nmol/ml.

Figure 11.7A and B shows that saturation plot for HTN and C-HTN21 after the exposure to 1.0 mg HA.

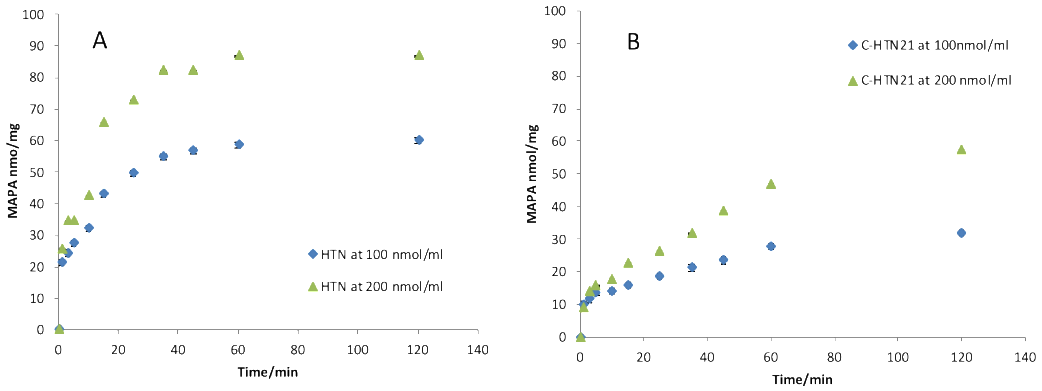

Figure 11.7 Saturation plots of HTN(A) and C-HTN21(B) showing the MAPA vs. time when exposed to 1.0 mg of HA. Changes in the MAPA was measured until a plateau was achieved

The MAPA values, and the $T_{0.5}$ were obtained for HTN at 100 nmol/ml, and, at 200 nmol/ml from Figure 11.7A. The MAPA values, and the $T_{0.5}$ were obtained for C-HTN21 at 100 nmol/ml, and, at 200 nmol/ml from Figure 11.7B.

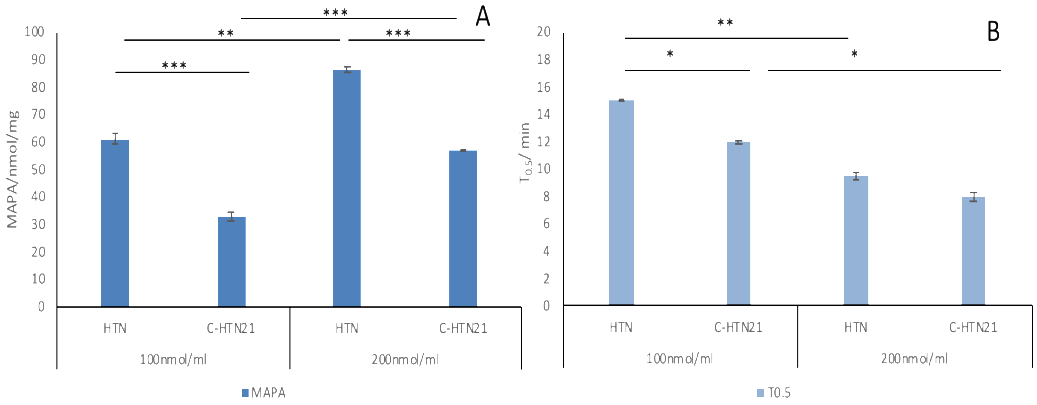

Figure 11.8 (A) Mean amounts of HTN and C-HTN21 adsorbed (MAPA) at two different concentrations to 1 mg of HA bead. (B) The time during which half of the peptide adsorbed onto HA beads. The error bars represent the standard error of the means (n=4, p< 0.05, p< 0.01**, p < 0.001 ***)*

Figure 11.8A shows that the MAPA value of C-HTN21 was statistically lower than the MAPA value of HTN at both 100 nmol/ml, and 200 nmol/ml (by 52% and 33% respectively) (ρ< 0.001). Doubling the

concentration of HTN and C-HTN21 increased the MAPA value for both peptides (up to 86% and 57% respectively) ($\rho < 0.01$, and $\rho < 0.001$).

Figure 11.8B shows that the binding rate for HTN was slower than the C-HTN21 at 100 nmol/ml ($\rho < 0.05$). The binding rates for HTN and C-HTN21 were faster when the concentration was doubled ($\rho < 0.001$ and $\rho < 0.05$ respectively).

Comparison of Figures 11.6A and 11.8A shows that the MAPA values for STN, HTN, and STN21 were similar at 100 nmol/ml, and at 200 nmol/ml. C-HTN21 had the lowest MAPA value of individual peptides at 100 nmol/ml, and, at 200 nmol/ml ($\rho < 0.001$).

Comparison of Figures 11.6B and 11.8B shows that the binding rates for both STN and F-STN21 were faster than HTN and C-HTN2 ($\rho < 0.05$) at 100 nmol/ml, and 200 nmol/ml. Furthermore, full-length peptides (STN and HTN) had slower binding rates than their truncated 21 N-terminal peptides (STN21 and HTN21) at 100 nmol/ml ($\rho < 0.05$).

11.4.2 Adsorption of STN, HTN, F-STN21, and C-HTN21 When in Combination onto HA Beads

Figures 11.9, 11.10, and 11.11 show the saturation plots of individual peptides when in combination with a 2nd peptide after the exposure to 1.0 mg HA.

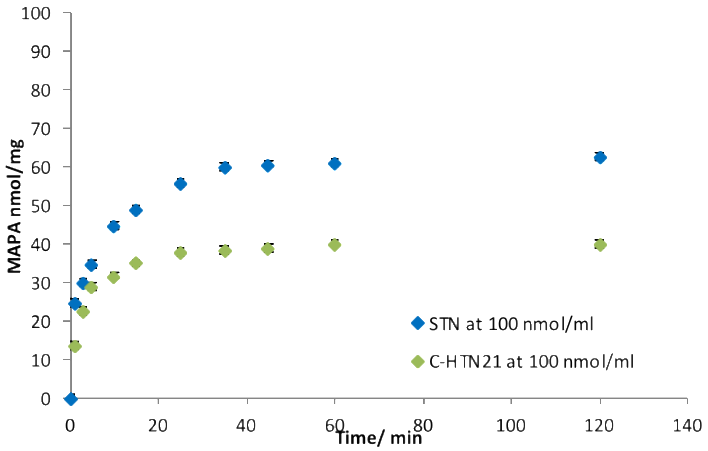

Figure 11.9 Saturation plot of STN measured at 278 nm and, C-HTN21 measured at 327 nm, when in combination at 100 nmol/ml of each, after the exposure to 1.0 mg of HA.

Figure 11.9 shows the simultaneous increase of MAPA values for both STN measured at 278 nm, and C-HTN21 measured at 327 nm when in combination. The MAPA values, and the $T_{0.5}$ were obtained for STN and HTN at 100 nmol/ml.

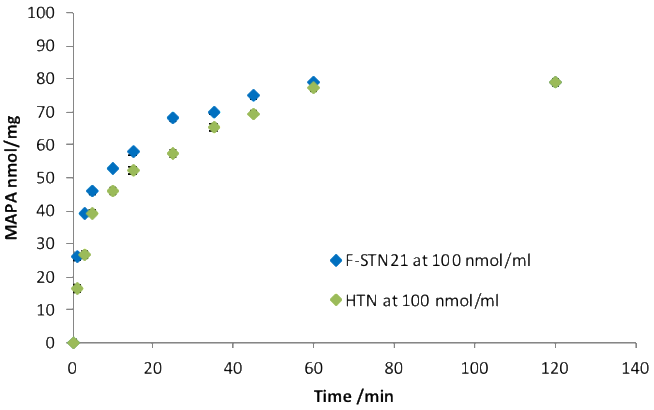

Figure 11.10 Saturation plot of F-STN21 measured at 498 nm and, HTN measured at 278 nm, when in combination at 100 nmol/ml of each, after the exposure to 1.0 mg of HA.

Figure 11.10 shows the simultaneous increase of MAPA value for both F-STN21 measured at 498 nm, and HTN measured at 278 nm when in combination. The MAPA values, and the $T_{0.5}$ were obtained for F-STN21 and HTN at 100 nmol/ml.

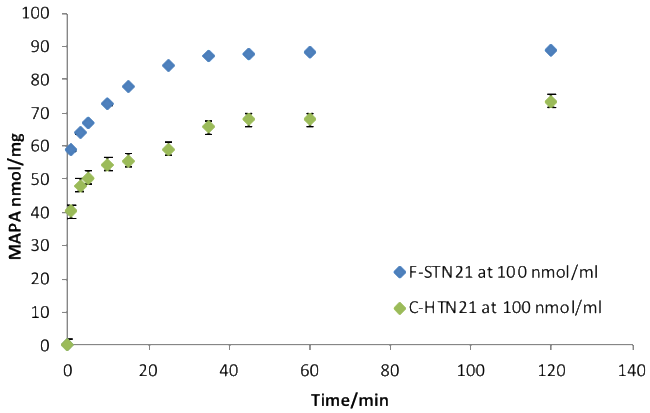

Figure 11.11 Saturation plot of F-STN21 measured at 498 nm and, C-HTN21 measured at 327 nm, when in combination at 100 nmol/ml of each, after the exposure to 1.0 mg of HA.

Figure 11.11 shows the simultaneous increase of MAPA value for both F-STN21 measured at 498 nm, and C-HTN21 measured at 327nm when in combination. The MAPA values, and the $T_{0.5}$ were obtained for F-STN21 and C-HTN21 at 100 nmol/ml,

Figure 11.12 shows the saturation plots of STN and HTN when added sequentially.

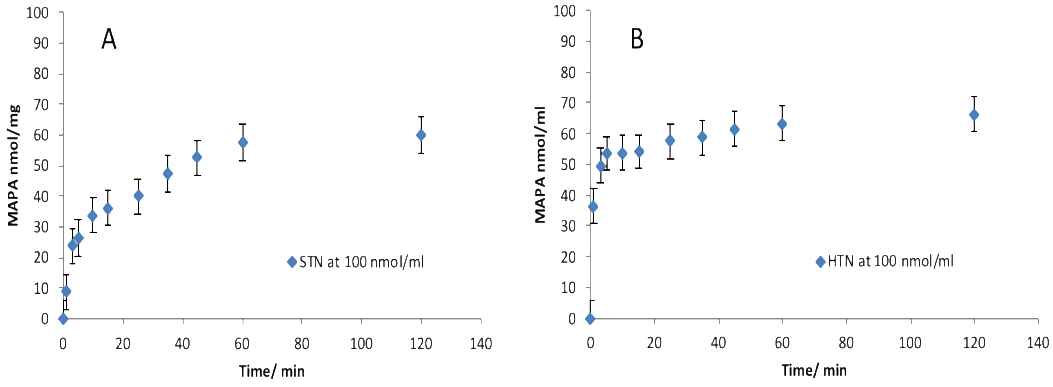

Figure 11.12 Saturation plot for STN and HTN when added sequentially to 1 mg of HA. (A) The MAPA of STN after the exposure of 1.0 mg of HA to 100 nmol/ml of HTN. (B) The MAPA of HTN after the exposure of 1.0 mg HA to 100 nmol/ml of STN.

The MAPA values, and the $T_{0.5}$ for both sequential combination of STN and HTN were obtained after the exposure to 1.0 mg of HA from Figure 11.12A and B.

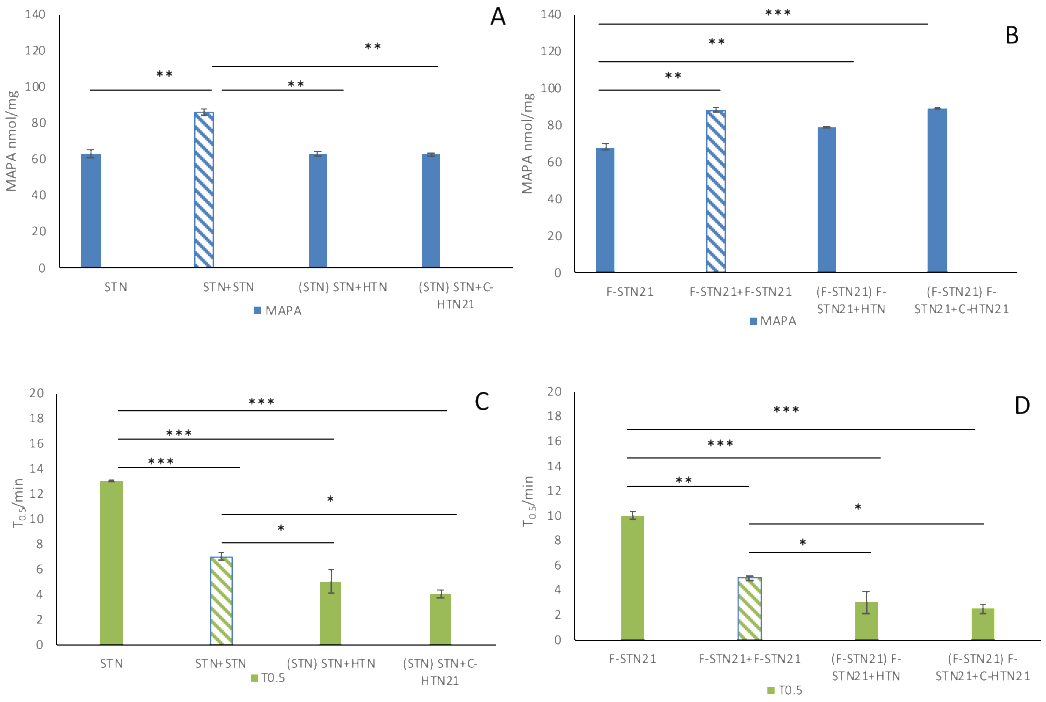

*Figure 11.13 MAPA individually and when in combination onto 1.0 mg of HA beads and the time during which half of the peptide adsorbed onto HA beads. (A) MAPA for STN at 100 nmol/ml, and, at 200 nmol/ml (blue stripes), and when combined with HTN or C-HTN21(B) MAPA for F-STN21 at 100 nmol/ml, and, at 200 nmol/ml (blue stripes), and when combined with HTN or HTN21(C) $T_{0.5}$, for STN individually and when in combination (D)$T_{0.5}$, for F-STN21 individually and when combined. The error bars represent the standard error of the means (n=4, p < 0.05 *, p< 0.01 **, p < 0.001 ***).*

Figure 11.13A shows that no change was detected in the MAPA value for STN at 100 nmol/ml when in combination with either, HTN or C-HTN21. However, at 200 nmol/ml (STN+STN), the MAPA value for STN was lower when in combination with either, HTN or C-HTN21 (28.5 % reduction) (P< 0.01).

Figure 11.13B shows that the MAPA value for F-STN21 at 100 nmol/ml increased when in combination with either HTN (p<0.01) or HTN21

(p<0.001), (by 17 and 25.6% respectively). The MAPA values for F-STN21 when in combination with either HTN or C-HTN21 were similar.

Figures 11.13C, and D show that the binding rates were faster for the STN and for F-STN21 when in combination than individually (at both 100 nmol/ml and 200 nmol/ml). The binding rates were twice as fast when STN and F-STN21 were combined with either HTN or C-HTN21 compared to STN and F-STN21 at 100 nmol/ml.

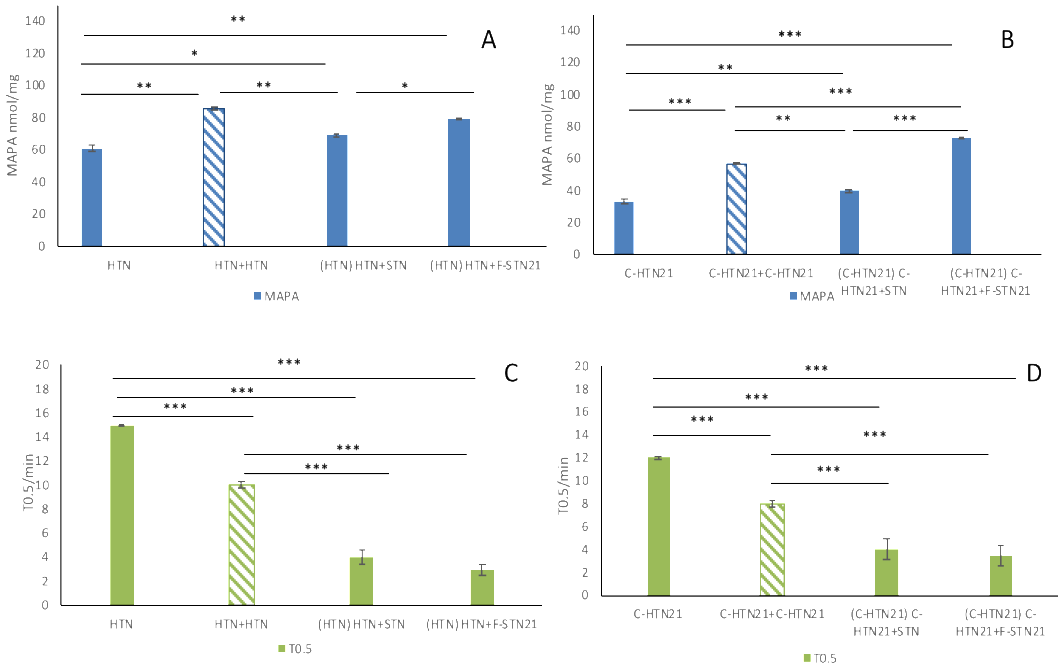

*Figure 11.14 MAPA individually and when in combination onto 1.0 mg of HA beads and the time during which half of the peptide adsorbed onto HA beads. (A) MAPA for HTN individually at 100 nmol/ml, and, at 200 nmol/ml (blue stripes), and individually when combined with STN or F-STN21(B) MAPA for C-HTN21 individually at 100 nmol/ml, and, at 200 nmol/ml (blue stripes), and individually when combined with STN or F-STN21(C) $T_{0.5}$, for HTN individually and when in combination (D)$T_{0.5}$, for C-HTN21 individually and when combined. The error bars represent the standard error of the means (n=4, p < 0.05 *, p< 0.01 **, p < 0.001 ***).*

Figure 11.14A shows that the MAPA value for HTN at 100 nmol/ml increased when in combination with F-STN21 (by 24%) (p< 0.01) more than when in combination with STN (increased by 13%) (p< 0.05). However, at

200 nmol/ml (HTN+HTN) the MAPA value for HTN was lower when in combination with STN (19.7 %) ($p< 0.01$). The MAPA values for HTN when in combination with STN (HTN+STN) was lower than the MAPA value for HTN when in combination with F-STN21(HTN+F-STN21) (by 12.5%) ($p< 0.05$).

Figure 11.14B shows that the MAPA value for C-HTN21 increased when in combination with F-STN21 (54%) ($p < 0.001$) more than when in combination with STN (17.5%) ($p< 0.01$). At 200 nmol/ml (C-HTN21+C-HTN21) the MAPA value for C-HTN21 decreased when in combination with STN (by 29.8%) ($p< 0.01$), however, the MAPA value for HTN21 increased when combined with F-STN21 (by 28.5 %) ($p< 0.001$). The MAPA value for C-HTN21 when in combination with F-STN21 (C-HTN21+F-STN21) increased more than (C-HTN21+STN) combination (by 45.2 %) ($p< 0.001$).

Figures 11.14C and D show that the binding rates were faster for HTN and for C-HTN21 when in combination than individually (at both 100 nmol/ml and 200 nmol/ml). The binding rates were twice as fast when HTN and C-HTN21 were combined with either STN or F-STN21 compared to HTN, and C-HTN21 at 100 nmol/ml.

11.4.3 Desorption of STN, HTN, F-STN21, and, C-HTN21 Individually and When in Combination from HA Beads

Figures 11.15A and B show examples of desorption plots of peptides exposed to different solutions. STN did not show any desorption from HA beads after the exposure to either 1 ml of acetic acid at pH 4.0, or 1 ml of 2.0 M of NaCl.

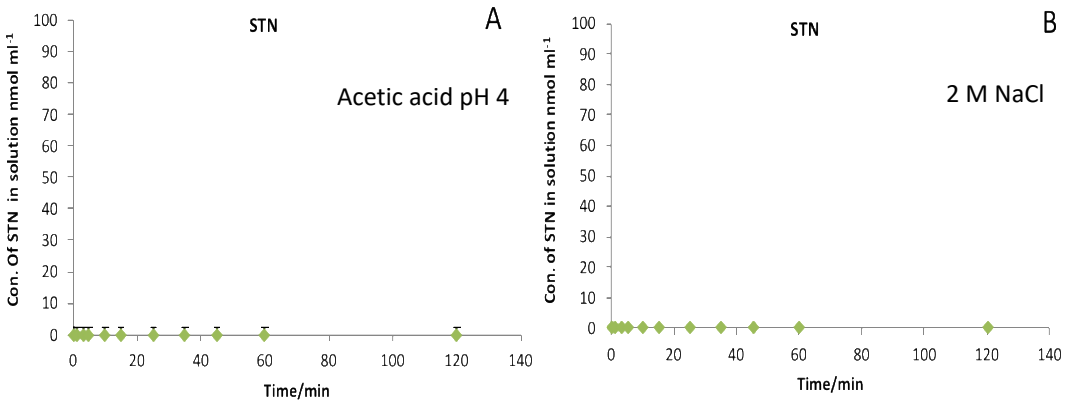

Figure 11.15 Typical desorption plots of peptides. (A) Desorption plot of STN after the exposure to 1ml of acetic acid pH 4.0. (B) Desorption plot of STN after the exposure to 1 ml of 2M of NaCl. STN did not show any desorption from HA bead when exposed to either of the desorption solutions.

All of the desorption experiments for STN, HTN, F-STN21, and C-HTN21 individually or when in combination did not show any desorption from HA beads when exposed to 1 ml of acetic solution at pH 4.0 or 1 ml of 2.0 M NaCl pH 7.0 for 48 hrs.

11.4.4 Adsorption of STN, HTN, F-STN21, and, C-HTN21 Individually onto HA Discs, and Enamel

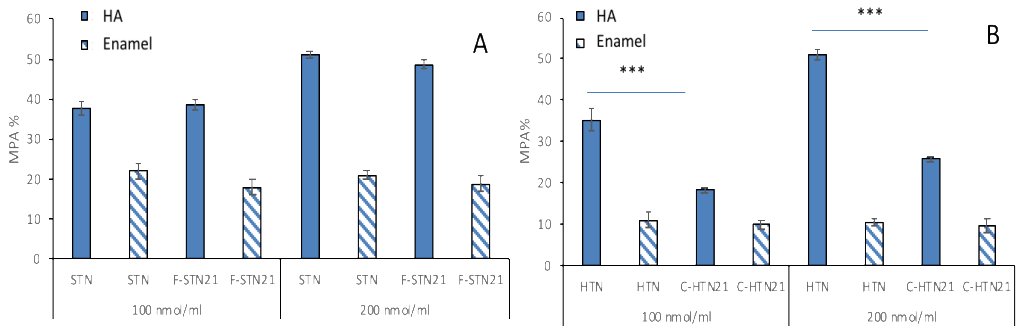

*Figure 11.16 Mean percent of peptides adsorbed onto HA discs and enamel samples used in SMR demineralisation study at 100 and 200 nmol/ml. (A) MPPA of STN and F-STN21, (B) MPPA of HTN and C-HTN21. The error bars represent the standard error of the means (n=3, $p < 0.001$ ***).*

Figure 11.16 shows the MPPA values for STN, HTN, F-STN21, and, C-HTN21 individually onto HA discs, and enamel blocks (used in the SMR study) at 100, and 200 nmol/ml.

Figure 11.16A shows that the MPPA value for STN and F-STN21 onto HA discs were similar at both 100 nmol/ml, and 200 nmol/ml. Doubling the concentration of STN and F-STN21 increased the MPPA value ($p< 0.01$). Similarly, Figure 11.16A shows that the MPPA values for STN and F-STN21 onto enamel were similar at both 100 nmol/ml, and 200 nmol/ml. Doubling the concentration of STN and F-STN21 did not increase the MPPA values.

Figure 11.16B shows that the MPPA value for C-HTN21 onto HA discs was lower than the MPPA value for HTN at 100 nmol/ml, and, at 200 nmol/ml (48% and 49* respectively) ($ρ< 0.001$). Doubling the concentration of HTN and C-HTN21 increased the MPPA value ($p< 0.01$).

Figure 11.16B also shows that the MPPA values for HTN and C-HTN21 onto enamel were similar at both 100 nmol/ml, and 200 nmol/ml. Doubling the concentration of HTN and C-HTN21 did not increase the MPPA values.

The results of MPPA for individual peptide onto HA discs and the results of MAPA of the individual peptide onto HA beads in Sections 11.4.1 show similar adsorption behaviour onto HA beads and discs. However, the adsorption of individual peptides onto enamel show different behaviour as shown by the MPPA results.

11.5 Discussion

11.5.1 Adsorption of STN, HTN, STN21, and HTN21 Individually onto HA Beads

The results in this study show that STN and STN21 had similar adsorption amounts onto HA beads. This suggests that the truncation of STN C-terminal does not alter the adsorption of STN onto HA beads. Schlesinger and Hay, (1977) suggested that the N-terminus of STN may be responsible for HA binding. Raj *et al.,* (1992) suggest that the main forces responsible for HA binding are electrostatic interactions of the charged residues at the N-terminus of STN onto HA surface. These authors also suggested a role of the N-terminal helical structure in adsorption phenomena. They speculated that the possible role of the α-helix present at the N-terminus of STN is to position negatively and positively charged residues at the best possible positions for interactions with HA surface. Raj *et al.,* (1992) also reported that the first 15 N-terminal residues are as effective as full-length STN in binding to HA. Therefore, STN21 adsorb onto HA beads as efficient as STN through the electrostatic interaction between the N-terminal negative residues (DpSpSEE) and Ca^{2+} present in HA, and through positive residues (K6, R9, R10, and R13) interaction with PO_4^{2-} present in HA. Also, possibly through the N-terminal α-helical conformation which might help in the adsorption of the peptide onto HA surfaces. The conformation of STN21 and the presence of the N-terminal α-helix will be investigated in chapter 13.

In this study, HTN and HTN21 did not show similar adsorption amounts on HA beads. The truncation of the HTN C-terminal altered the

adsorption of HTN onto HA beads. Driscoll *et al.,* (1995) investigated the adsorption of HTN and a recombinant peptide of HTN that lacks the phosphorylation at the N-terminus second residue (S2) onto HA beads. They found that HTN adsorbed 80% more than the recombinant peptide. This signifies the importance of phosphorylation at the N-terminal for HTN adsorption onto HA beads. However, they observed that the recombinant HTN did adsorb onto HA, even though to a lesser extent (10%), which indicated that the phosphorylated serine at position 2 is not the only contributing factor to the adsorption of HTN onto HA. The C-terminal has been found to contribute to hydrogen bonding with the HA surface (Santos *et al.,* 2008). This is in agreement with this current study, which showed that even though HTN21 is phosphorylated, the absence of the C-terminal (which contributes to hydrogen bonds with HA), reduces the adsorption amount of HTN21 onto HA.

In this study, the amount of HTN adsorbed onto HA beads was similar to that of STN at 100 nmol/ml, and, at 200 nmol/ml. HTN has 3 negative residues at the N-terminal, whereas, STN has 5 negatively charged residues in the N-terminal sequence, as shown in Figure 11.17A and B. Therefore, the lack of 2 negatively charged residues, one of which is phosphorylated at the N-terminal of HTN does not affect HTN adsorption onto HA beads.

(A) STN

1	2	3	4	5	6	7	8	9	10	11	12	13	14	15	16	17	18	19	20	21	22	23	24
D	pS	pS	E	E	K	F	L	R	R	I	G	R	F	G	Y	G	T	G	P	Y	Q	P	V
25	26	27	28	29	30	31	32	33	34	35	36	37	38	39	40	41	42	43					
P	E	Q	P	L	Y	P	Q	P	Y	Q	P	Q	Y	Q	Q	Y	T	F					

(B) HTN

1	2	3	4	5	6	7	8	9	10	11	12	13	14	15	16	17	18	19	20	21	22	23	24
D	pS	H	E	K	R	H	H	G	Y	R	R	K	F	H	E	K	H	H	S	H	R	E	F
25	26	27	28	29	30	31	32	33	34	35	36	37	38										
P	F	Y	G	D	Y	G	S	N	Y	L	Y	D	N										

Figure 11.17 Amino acid sequence starting from the N-terminus. (A) STN, (B)HTN.

Shimotoyodome *et al.,* (2006) studied the adhesion of S. mutans to HA, which was promoted by high-molecular weight glycoproteins. They found that the presence of STN or HTN reduced the adsorption of these microorganisms onto HA equally. They proposed that there is a similar preventive behaviour of HTN or STN and glycoproteins, which shows that both STN and HTN adsorb onto the similar or even the same HA adsorption sites, and therefore their adsorbing amount should be comparable.

The results of this study showed that there is an increase in the amount of peptides adsorption onto HA when the concentration was doubled. Proteins go through conformational changes when adsorbing onto mineral surfaces (Sharma *et al.,* 2010). The free energy (internal energy) of proteins in solution (a closed system) changes on adsorption on to a surface. Upon adsorption proteins gain free energy; therefore, the adsorbing molecules tend to increase their “footprint” (i.e. the area covered by a unit of peptide) by structural conformation (Sharma *et al.,* 2010). However, protein chains can also adsorb in a side-on or an end-on manner (Dee *et al.,* 2002). On initial adsorption, proteins adopt an orientation that

favours protein-surface interaction. Neighbouring proteins with similar charges repel (unfavourable repulsion). At low peptide surface density, the repulsive charges are not significant. However high peptide surface density requires a smaller distance between the molecules. This might orient the peptide molecules in a way to form less repulsive forces and so increases the surface peptide uptake (as shown in Figure 11.18). Therefore, at higher concentrations, non-specific binding promoted by molecule-molecule interaction of the same peptide, might increase the surface peptide uptake/adsorption.

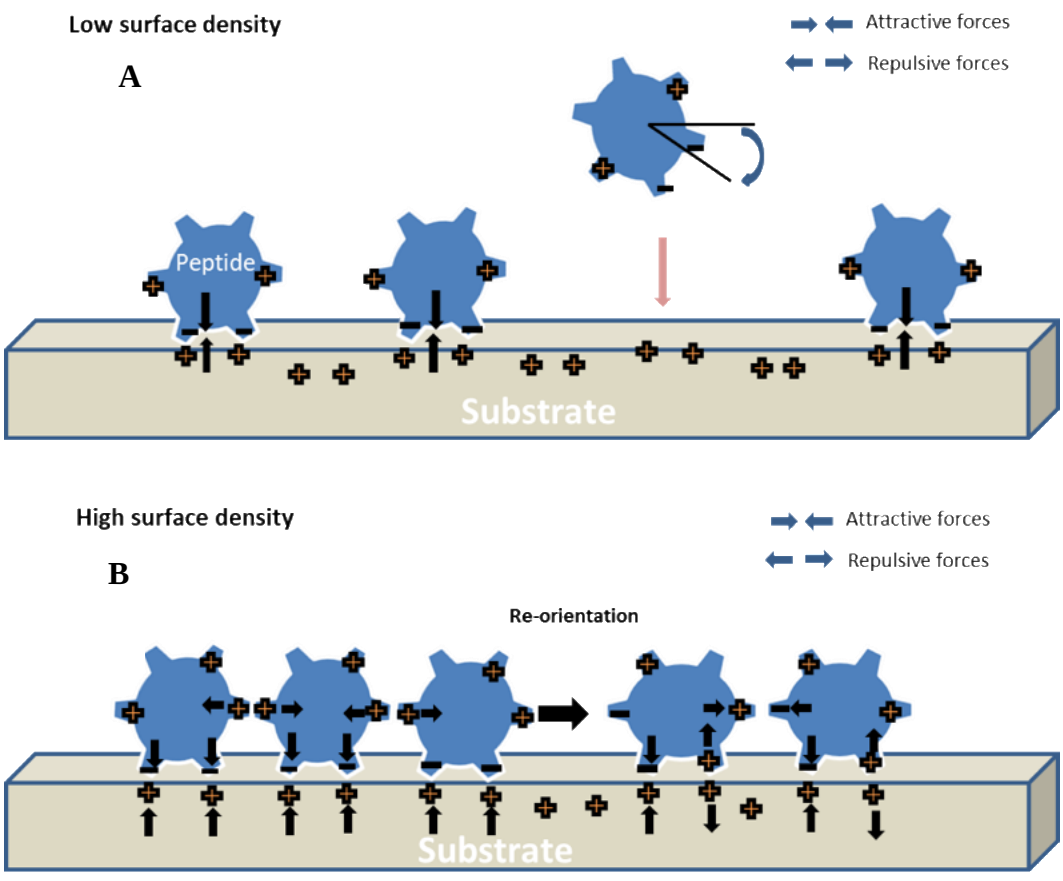

Figure 11.18 Schematic illustrations of proteins adsorption and orientation changes. (A) At low concentration, surface density is dependent on peptide-surface interaction. (B) At higher concentration the peptide surface density is partially dependent on peptide-peptide interactions that affect surface interactions.

In this study, both STN and STN21 had faster binding rates than HTN or HTN21 at 100 nmol/ml, and, at 200 nmol/ml, as shown in Figure 11.6B and 11.8B. Lamkin *et al.,* (1996) suggested that STN is one of the enamel pellicle precursor proteins that adsorbs rapidly onto HA mineral surfaces. The rate of adsorption is dependent on the highly negative motif at the N-terminus that both STN and STN21 possess (one D, two pS, and two E), whereas, HTN and HTN21 have fewer negative residues at the N-terminus (one D, one pS, and one E). Consequently, STN and STN21 adsorb faster than HTN and HTN21.

In this study individual peptides had faster binding rates at 200 nmol/ml compared to 100 nmol/ml. Also, STN21 and HTN21 had faster binding rates than those of STN and HTN, suggesting that “shorter” and hence smaller peptide adsorb faster. Variables such as concentration and/or molecular size are important in determining a molecule rate of adsorption onto the surface (diffusion) (Dee *et al.,* 2002). Therefore, a higher concentration and/or smaller protein molecular size (which is inversely associated with the diffusion coefficients), results in a larger number of molecules arriving at the surface and hence a faster rate of binding.

11.5.2 Adsorption of STN, HTN, F-STN21, and C-HTN21 When in Combination onto HA Beads

In this study, there was an increase in the amount of both HTN and HTN21, adsorption onto HA when in combination with either STN or STN21. The co-operative adsorption of proteins facilitated by a pre-adsorbed

protein has been debated in the literature (Kurrat *et al.,* 1994; Striolo *et al.,* 2005; Vasina *et al.,* 2005). For example, Kurrat *et al.,* (1994) suggested that there is a catalysis of desorption that occurs between neighbouring proteins. A pre-adsorbing protein may repulse a protein approaching the surface to adsorb. From a theoretical respect, big proteins can repel smaller ones from the adsorbent surface (Fang and Szleifer 2003; Striolo *et al.,* 2005). However, this was not the case in this study, which showed that combining shorter peptides with full-length ones improved their adsorption affinity to HA. Ball *et al.,* (2000) and Vasina and Déjardin, (2004) suggested that the attractive forces that operate in positive co-operative adsorption are induced by an electrostatic self-reorientation and assembly by adsorbed proteins, which in turn increases protein uptake/adsorption. This means that a peptide could adsorb on a specific binding site as a single molecule or, as clusters onto nonspecific mineral binding sites, promoted by a preferred adsorption to a vacancy, guided by pre-adsorbed peptide. Figure 11.19 schematically illustrates such a situation where co-operative peptide-peptide adsorption occurs.

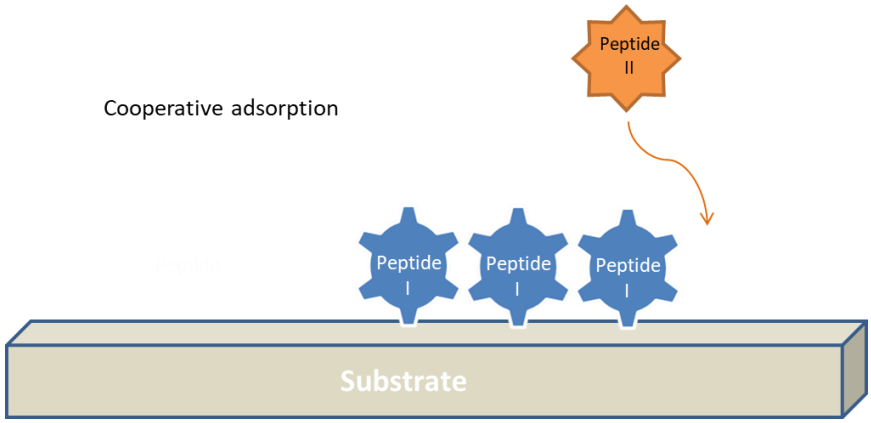

Figure 11.19 Schematic illustration of co-operative peptide-peptide adsorption, in this co-operative adsorption the incoming peptide (orange) diffuse to the adsorbent surface at the same time it is repelled horizontally (guided) by another adjacent peptide (blue).

The amount of STN adsorbed onto HA did not increase when in combination with either HTN or HTN21, however, STN21 adsorption onto HA increased when in combination with either HTN or HTN21. Hydrogen bonds were suggested to play a role in the intermolecular adsorption of STN onto HA through polar uncharged residue (Santos *et al.,* 2008). The C-terminus of STN contains 12 polar uncharged residues (seven Q, four Y, and one T). This suggests that the uncharged polar residue present in larger quantity in STN might affect the adsorption of peptides when in combination. The competitive adsorption of STN C-terminus, onto HA, is possible by masking nonspecific mineral binding sites, that were promoted by peptide-surface and/or peptide-peptide interaction when STN is in combination. The loss of the C-terminus of STN21 increased the adsorption amounts while in combination with either, HTN or HTN21, which further point out the competitive adsorption behaviour of the full-length peptide STN, due to its C-terminal.

There was an increase in the amount of HTN adsorption observed when HA beads were pre-coated with STN. Yin *et al.,* (2006) investigated HTN-5 (HTN-5) binding affinity to HA beads at pH 6.0—7.5 by pre-coating HA beads with either STN or its truncated 10 N-terminal amino acid peptide (STN10). They found that there was an increase in HTN-5 uptake when HA beads were pre-coated with STN, but not with STN10. Their results suggested that amino acid residues present in bound STN (but not in STN10) may be important for the increase in HTN-5 uptake. They suggested that these residues are hydrophobic in nature and consist of P, and V, L, I and F. Therefore, it is reasonable to infer that the pre-coating of

STN onto HA supports the adsorption of HTN through hydrophobic interactions between STN and HTN. This hydrophobic interaction occurs while the charged hydrophilic fragment of STN is bound to the HA surface through its negative N-terminus. It has also been suggested by Raj *et al.,* (1992), that the reduction of HTN-5 binding onto HA, is due to the loss of α-helix conformation in STN10 which is important in the electrostatic interactions and binding affinity to HA.

The results of the rate of binding demonstrated that each peptide when in combination had faster binding rates compared to the individual peptide. Suggesting that there is a co-operative interaction between the peptides when combined, that affect either their molecular structure, surface charges or both, which could contribute to their affinity to HA measured by their binding rates. This is further discussed in Chapter 14.

11.5.3 Desorption of Peptides individually and When in Combination from HA Beads

All the desorption results showed that the STN, HTN, F-STN21, and C-HTN21 individually, or when in combination, remained bound to the HA beads, after exposure to either acetic solution at pH 4.0 or 2.0 M NaCl, for 48 hrs.

This shows that these peptides, either individually or in combination, when exposed to acidic conditions in the oral environment, or strong salting solution (2 M NaCl) (that is used in chromatography column decontamination of HA) (Gorbunoff, 1985), they remain bound onto HA. STN and HTN are subjected to be degraded in the whole mouth saliva

(Helmerhorst and Oppenheim, 2007). Therefore, the desorption of the peptides from the mineral surface in the oral environment might be secondary to the proteolytic process of oral proteases. Such protease activities might negatively impact the adsorption of these peptides onto a mineralised surface by truncating the peptides at specific cleavage sites effecting their adsorbing stability.

After a period of exposing peptides to a solid substrate, all of the adsorption curves should plateau (equilibrium). At equilibrium, the number of adsorbing molecules equals those desorbing (according to the Langmuir adsorption isotherm). The adsorption of protein onto specific binding sites onto HA surfaces is reversible, though in many studies this has been questioned (Moreno *et al.,* 1982; Poumier *et al.,* 1996). Moreno *et al.,* (1982) suggested that reason for such (irreversible adsorption) is due to a much slower desorbing process compared to adsorption.

Therefore, the time period that the HA beads were exposed to acetic acid or 2 M NaCl might not be long enough for desorption to occur, or that the peptides are strongly bound to HA and therefore the only way for desorption to occur would be through proteolytic processes. Hence, future work should be done on salivary peptide desorption using longer exposure time and perhaps in different environments.

11.5.4 Adsorption of STN, HTN, F-STN21, and, C-HTN21 Individually onto HA Discs, and Enamel

The results of individual peptide adsorption onto HA discs (represented in the MPPA Section 11.4.4) and the results of individual

peptides adsorption onto HA beads (represented by the MAPA Section 11.4.1) show similar adsorption behaviour. This confirms that the peptides adsorption onto HA beads is similar to peptides adsorption HA discs (used in the SMR experiments section 13.3.1) showing the similarity of these mineral surfaces in terms of mineral surface influence on peptide adsorption.

Also, STN and STN21 adsorbed similarly onto both enamel and HA. However, HTN and HTN21 adsorbed similarly onto enamel but not onto HA. Masica *et al.,* (2010) and Roehrich and Dorbeny, (2013), studied the binding of STN onto each crystal face. They reported that the basis of STN adsorption onto HA surfaces is a complementarity between the amino acids side chains in the N-terminal α-helix and HA crystal faces. The STN (STN21), pS2, pS3, E4, E5, K6, R9, and R10 residues bind best to the 001 faces of HA crystal lattice. Whereas, the binding of basic and negative residues is not preferred onto 100 and 010 face of HA crystal lattice. The separation of the two phosphate and glutamate anions in space by 4.6- 6.2 Å in STN (STN21) N- terminal helical conformation closely matches the interatomic distance, 5.45 Å between calcium ions in the 001 faces of the hydroxyapatite crystal (Masica *et al.,* 2010). Figure 11.20 shows HA crystal faces. The 001 face of the crystal represents the face that STN has the highest adsorption affinity too (Masica *et al.,* 2010). Interestingly, this is also the crystal face of enamel that is naturally exposed to the oral environment (exposed to acidic attacks) (Tsuda and Arends, 1994; Pezzotti *et al.,* 2015). Therefore, STN (STN21) adsorption is biologically relevant to its function of demineralisation reduction.

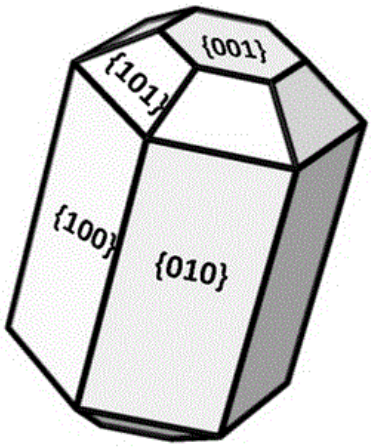

Figure 11.20 Schematic HA model showing the four crystal faces that proteins adsorb on (Masica et al.*, 2010).*

Similarly, HTN may have specific binding to HA crystal faces which are biologically relevant for HTN (HTN21) adsorption. In enamel, the 001 HA crystal face is present in an ordered manner in highly oriented enamel crystallites (Tsuda and Arends, 1994). Whereas, in HA beads and discs, the crystals are unordered and with random face orientations. Therefore, unlike STN the adsorption amount HTN and HTN21 may differ for HA and enamel.

Additionally, the percentage of peptides adsorbed were higher in HA discs compared to enamel. Meureman and ten Cate, (1996) reported that enamel erosion lesions show hypo-mineralisation of the surface layer. The reduction of the mineral content of enamel surface layer, and/or the mineral substitution by other ionic species (e.g. carbonate) in enamel, may further reduce the availability of peptide adsorption sites and therefore reduce the amount of peptide adsorbed on eroded enamel.

11.6 Conclusions

- The absence of residues 22 onwards in STN does not affect STN adsorption to HA or enamel. This suggests that the C-terminal of STN is not involved in individual peptide adsorption onto HA or enamel.

- The absence of residues 22 onwards in HTN reduces the adsorption of HTN onto HA but not enamel. This suggests that the C-terminal of HTN is involved in individual peptide adsorption onto HA through hydrogen bonds but not for enamel.

- The binding of STN and HTN is HA crystal face specific, this is also seen in amelogenin, which has a role in enamel formation that is also HA crystal face specific (Iijima and Moradian-Oldak, 2004).

- Combinations of STN, HTN and their 21 N-terminal peptides increased the binding of individual peptides while in combination onto HA, indicating a co-operative binding efficacy. The absence of residues 22 onwards in STN improved the co-operative adoption when in combination with HTN and HTN21, suggesting the contribution of C-terminal to the competitive binding of STN when in mixtures.

- In this study it has been shown that both STN and HTN bound to HA beads did not desorb, however one other possible scenario remains If peptides are added sequentially. It is possible that the second added peptide replaces the first peptide. The absorbance measurements of the peptides, when added sequentially, does not distinguish between each peptide. Further experiments using these peptides could succeed using labelled HTN and STN.

- The binding affinity of peptides to HA mineral surface (measured by the rate of adsorption) is affected by the density of negative charges present in the N-terminal fragment, peptides size, concentration, and peptides combination in solution.

- The major driving forces of peptide adsorption (of both amount, and speed of binding) are peptide concentration, structural rearrangements due to peptide-surface interactions, and peptide-peptide interactions.

- Peptide adsorption onto HA is concentration dependent but could be irreversible.

- The difference in the individual peptides adsorption behaviour onto HA beads, discs and enamel question the further use of HA as chemical and structural equivalent for enamel when using biomolecules.

Chapter 12. Aggregation, Surface Charge and Secondary Structure of Statherin, Histatin-1 and Their 21 N-terminal Peptides Individually and When in Combination in Solution

12.1 Introduction

Salivary STN, HTN, A-PRPs and cystatins show the highest affinity for enamel and HA (Johnsson *et al.,* 1993; Yin *et al.,* 2003). These studies have provided knowledge of the affinity and surface characteristics of single proteins. However, they did not take in consideration the influence of protein aggregation, protein-protein interactions and whether these interactions, occur prior to or after adsorption in the form of supramolecular salivary precursors (Vitkov *et al.,* 2004).

The aims of this chapter were to:

- Investigate the degree to which salivary STN, HTN, STN21, and, HTN21 aggregate in solution at the concentrations used, individually and in combination.

- To measure the zeta potential (ZP) of STN, HTN, STN21, and, HTN21 individually (at 100 and 200 μmol/l) and in combination, which is indicative evidence towards the nature of their surface charge (positive/negative).

- To characterise the secondary structure of STN, HTN, STN21 and HTN21 in solution, individually (at 100 and 200 μmol/l) and in combination, this would be a step towards understanding how they interact and function on the surface of mineralised dental tissue.

12.2 Materials and Method

12.2.1 Aggregation and Surface Charges of STN, HTN, STN21, and HTN21 Individually and When in Combination

12.2.1.1 Peptide Solution Preparation

All peptides were dissolved in PBS (Sigma-Aldrich, UK) at concentrations of 100, and, 200 μmol/l when studied individually, and 100 μmol/l of each when studied in combination. Contamination filters of 0.25 microns were used (Millex®-GS units, Millipore™) since the DLS technique is sensitive to dust. Air bubbles were removed by ultra-sonication for 15 sec. The samples were clean, transparent and without precipitation. Prior to DLS measurements samples were centrifuged for 20 min 45,000 rpm at 4°C.

For particle size and surface charge measurements, 1ml of each peptide solutions were placed in clean and scratch-free folded capillary cell (DTS1070) made of polycarbonate.

12.2.1.2 Size and Surface Charge Measurement

Size and surface charge measurements were done using DLS, Zetasizer Nano ZS system that uses Laser Doppler Micro-Electrophoresis (Malvern Instruments Ltd. UK). The measurements were controlled by Malvern Zetasizer software.

The peptide solutions were illuminated by a laser 4 mW He-Ne, λ_0 = 633 nm. The intensity of the light scattered at an angle of 175° was measured by a photodiode. Each size and zeta potential measurement was repeated 3 times for each peptide at 25°C. For zeta potential measurements a constant voltage of 40 mV was used, values of the solution viscosity and

dielectric constant were set at 0.8872 cP and 79.0 respectively. Particle size result given by the DLS software is given as hydrodynamic radii (R_H).

Data was analysed using GraphPad Prism 7.0d (GraphPad Software Inc., La Jolla, USA) statistical software for normality using Shapiro-Wilks test. After confirming data was normally distributed. Analysis of variance (ANOVA) with post hoc Bonferroni test was used to identify which means were significantly different from each other. Significance was predetermined at $\alpha=0.05$. Results are expressed as mean and standard error (±SE).

12.2.2 CD Investigation of the Secondary Structures of STN, HTN, STN21, and HTN21 Individually, and When in Combination

12.2.2.1 Peptide Solution Preparation

The peptides were dissolved in phosphate-buffered saline at 100 and 200 µmol/l when used individually, and 100 µmol/l of each when in combination.

12.2.2.2 CD Measurements

The CD measurement of STN, HTN and their 21 N-terminal peptides individually and when in combination, was carried out using Chirascan Spectrometer (Photophysics, Leatherhead, Surrey, UK). Each spectrum was recorded at 1-nm wavelength intervals using a quartz cell with a path length of 0.1 cm, in the wavelength range 190 to 260 nm. Each CD measurement was repeated 3 times for each peptide both individually, and when in combination, at 25°C and pH 7.0. Baseline spectra measurements

were obtained for PBS solution without the peptides in the same manner at 25°C.

12.2.2.3 CD Data Analysis

After each CD measurement, the data was analysed as described in Section 9.3.

12.2.2.4 Deconvolution Analysis of CD Data

Deconvolution analysis was done to compare the contributions of each secondary structure components in the measured CD spectra of a given sample. Analysis of the CD data yields CD curves of the main secondary structural elements (helical structures, β-strands, or unordered conformation). Therefore, the CD measurements were deconvoluted for each peptide, individually (at 100 and 200 µmol/l), and when in combination.

Deconvolution was carried out as described in Section 9.4, using CD software Diamond Light Source (Benning, 2014). The software gives a root mean square deviation (RMSD) of each fit. The RMSD is a quantitative calculation of how well a submitted secondary structure matches the known target structure (Armougom *et al.,* 2006). Therefore, the lower the RMSD, the better the fit of the peptide secondary structure is in comparison to the target structure.

12.2.3 Secondary Structure Predictions of STN and HTN Individually

Two secondary structure prediction software were used to locate the position and the length of the α-helix revealed by the CD experiments. The

sequences of full-length STN and HTN were submitted to the Robetta and the PSIPRED website for secondary structural prediction (Section 10.1, and 10.2).

The Robetta secondary structure predictions were done using full-length sequences of STN and HTN since the software does not accept less than 27 residues in a sequence.

The PSIPRED secondary structure predictions were carried out using the full-length and the 21 N-terminal sequence of each peptide. The secondary structural prediction of the N-terminal α-helical length were the same in the full-length and the 21 N-terminal. Therefore, the secondary structural prediction results by PSIPRED are only shown for the full-length sequences.

Both secondary structural prediction software used do not allow for modified amino acids side chains such as phosphoserine to be used in the sequence. Therefore, the helices length predictions maybe short.

12.3 Results

12.3.1 Particle Size, Surface Charge and Secondary Structure of STN, HTN, STN21, and HTN21 Individually

12.3.1.1 Particle Size of STN, HTN, STN21, and HTN21 Individually

Peptides	MR_H (nm) at 100 µmol/l (±SE)		MR_H (nm) at 200 µmol/l	(±SE)
STN	1.82	(±0.82)	110	(±19)
HTN	1.3	(±0.28)	102	(±13)
STN21	0.9	(±0.30)	95	(±12)
HTN21	1.0	(±0.22)	100	(±18)

Table 12.1 Mean hydrodynamic radius of the peptide, individually at 100 and 200 µmol/l and the standard error of the mean. MR_H values of individual peptides at 100 µmol/l were statistically different than MR_H at 200µmol/l (n=3, p< 0.001).

Table 12.1 shows the MR_H of all peptides studied at 100 and 200 µmol/l. At 100 µmol/l STN had the largest MR_H value, followed by HTN, HTN21, while STN21 had the smallest MR_H, however, there were no statistical differences in the peptides MR_H at 100 µmol/l. At 200 µmol/l, there was a significant increase in the MR_H of all peptides compared to the peptides individually at 100 µmol/l ($\rho<0.001$). Although STN had the largest MR_H, followed by STN21, HTN21 and HTN respectively, statistical analysis showed there was no statistical significance in the MR_H of the peptides at 200 µmol/l.

The increase in the MR_H resulting from the increase in concentration suggests that the peptides form aggregates.

12.3.1.2 Surface Charge of STN, HTN, STN21, and HTN21 Individually

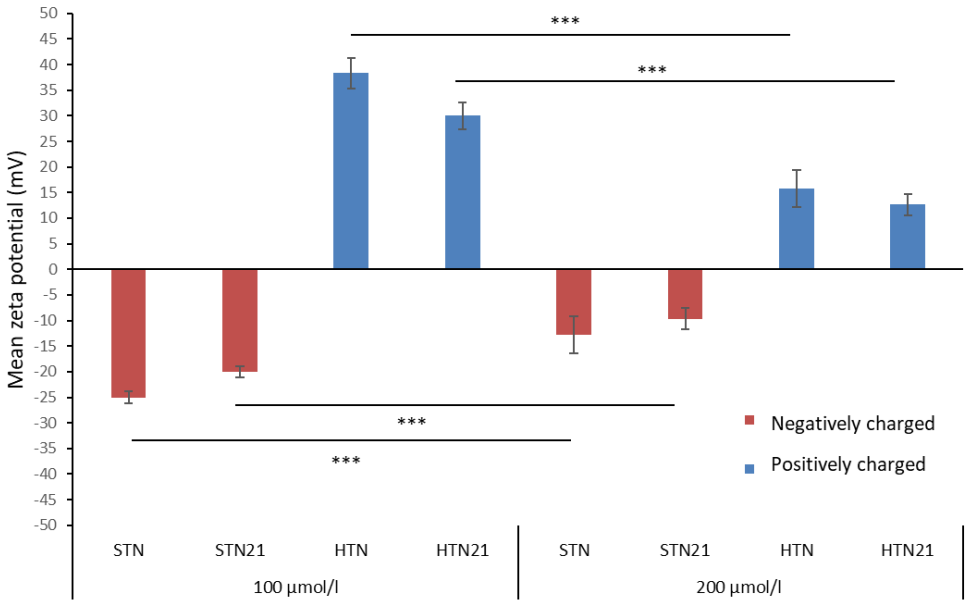

*Figure 12.1 Mean zeta-potential measurements of STN, HTN, STN21 and HTN21 individually at 100 and 200 µmol/l, and the standard error of the mean (n=3, p< 0.001***).*

Figure 12.1 shows the mean surface net charge of peptides individually at 100 µmol/l, and 200 µmol/l. Both STN and STN21 demonstrated net negative charges at 100 and, at 200 µmol/l. STN21 net negative charge was reduced by 20 % and 23 % compared to STN at 100 and 200 µmol/l respectively ($p< 0.05$). Both HTN and HTN21 demonstrated net positive charges at 100 and, at 200 µmol/l. HTN21 net negative charge was reduced by 21 % and 19 % compared to HTN at 100 and 200 µmol/l respectively ($p< 0.05$). The surface net charge of each peptide significantly decreased when the concentration of peptide was increased ($p< 0.001$).

12.3.1.3 Secondary Structure Conformation of STN, HTN, STN21, and HTN21 Individually

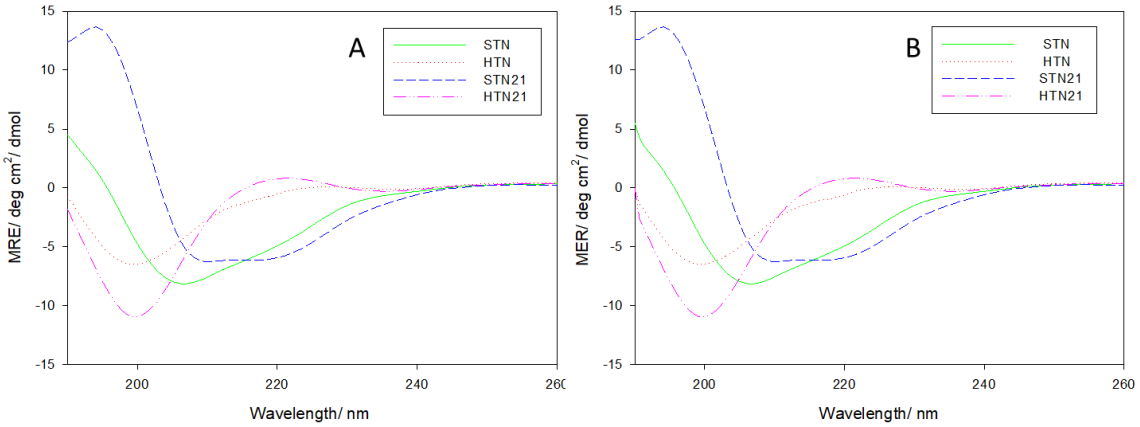

Figure 12.2 Mean residue ellipticity vs wavelength of individual peptides at 100 µmol/l and at 200 µmol/l, measurements were taken at 37 °C and pH 7. Fitting of the spectra was done using SigmaPlot 10.0 (Systat Software, CA, USA).

Figures 12.2A and B show the CD MRE spectra of STN, HTN, STN21, and HTN21 at 100 µmol/l and at 200 µmol/l. STN and STN21 showed two negative absorption bands, at 206-208 nm, and at 216-220 nm, and a positive band between 195-190 nm at both 100 µmol/l and at 200 µmol/l. The spectra suggest α-helix structures as shown in Figure 9.1. The

strong negative band at 206-208 and the week negative band at 216-220 in STN is a characteristic of poly-L-proline type II helical structure (Woody, 2010).

At 100 µmol/l, and at 200 µmol/l, HTN CD spectra showed a weak negative band at 200 nm which is characteristic of a β-strand. HTN21 showed a strong negative band at the same wavelength (200 nm) and a positive band at 210-225 which is characteristic of random coil (unordered) conformation at 100 µmol/l, and at 200 µmol/l.

Figure 12.3 shows the CD spectra deconvoluted data, showing fraction of folding for the secondary structural components of individual peptides at 100, and at 200 µmol/l.

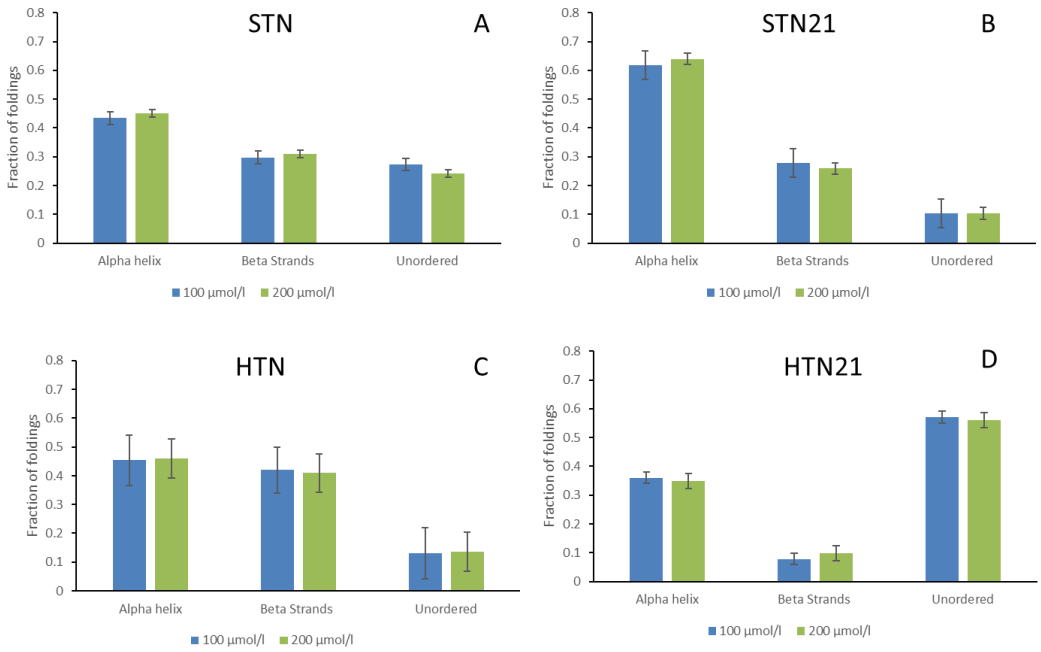

Figure 12.3 Fraction of folding of the structural components present in (A) STN, and (B) STN21, both at 100 and 200 µmol/l. (C) HTN, and (D)HTN21 both at 100 and 200 µmol/l, using CONTINLL SP43 fit. Error bars represent the RMSD. The RMSD calculated by the CD apps software at 100 µmol/l, STN-0.022, STN21-0.05, HTN-0.094, HTN21-0.022. At 200 µmol/l STN-0.0.21, STN21-0.023, HTN-0.088, HTN21-0.023.

Figures 12.3A and B show that for both STN and STN21 the highest fraction of folding is for α-helical conformation followed by the fraction of folding for β-strand conformation and lastly, the fraction for unordered conformation. Doubling the concentration of both STN and STN21 had no significant effect on the relative fraction of folding of secondary structure conformation.

Figure 12.3C shows that HTN had similar fraction of folding for α-helix conformation, and β-strand conformation, followed by the fraction for unordered conformation. Doubling the concentration of HTN had no significant effect on the secondary structure conformation.

Figure 12.3D shows that HTN21 had the highest fraction of folding for unordered conformation followed by the fraction of folding for α-helix conformation, and lastly β- strand conformation. Doubling the concentration of HTN21 had no significant effect on the secondary structure conformation.

12.3.1.4 Secondary Structure Prediction of STN and HTN Individually

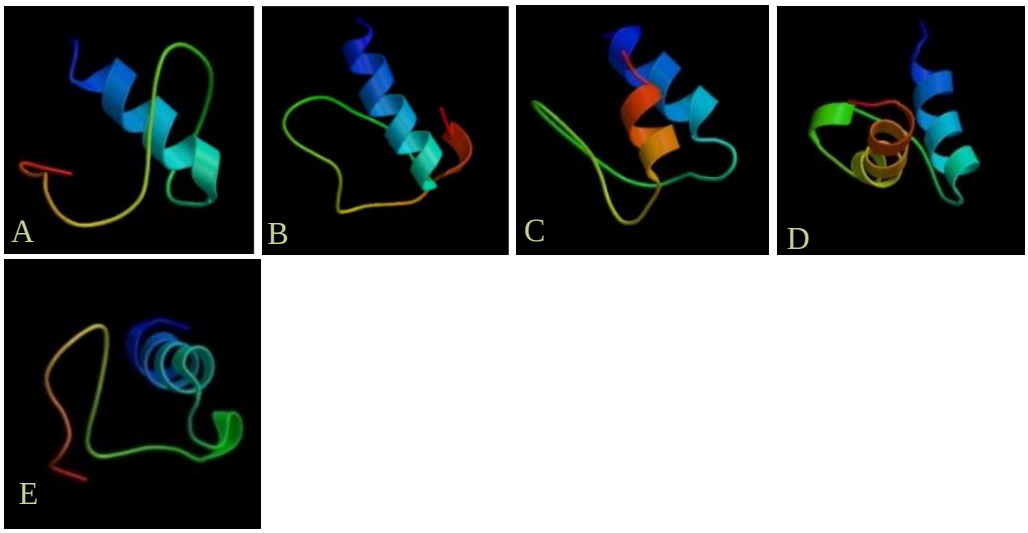

*Figure 12.4 (*A), (B), (C), (D), and (E) 3D structural predictions of human STN using Robetta software.

Figure 12.4 shows the five structural predictions of STN by Robetta. All predictions showed an α-helix structure at the N-terminal, the difference in prediction is mainly in the sequence after the amino acid 21. Figure 12.4A showed possible unordered conformation at the C-terminal. Figure 12.4B showed possible short helical conformation at the C-terminal. Figure 12.4C showed possible 2 turn helical conformation at the C-terminal. Figure 12.4D showed possible short helical formation at the middle sequence and a helical conformation at the C-terminal. Figure 12.4E showed possible short helical conformation at the middle sequence and unordered conformation at the C-terminal.

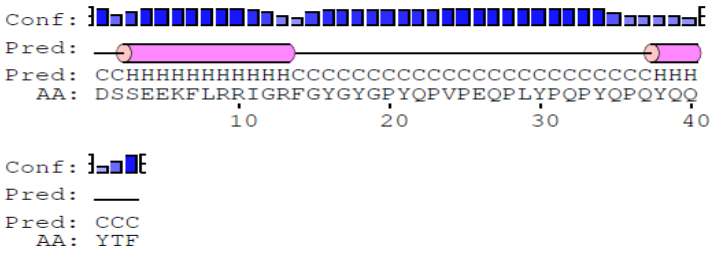

Figure 12.5 Secondary structure prediction of STN by PSIPRED software.

Figure 12.5 shows secondary structure prediction of STN by PSIPRED software, showing a possible α-helical secondary structure conformation between S3-R13 at the N-terminal, and Y38-Q40 at the C-terminal while the rest of the sequence is unordered.

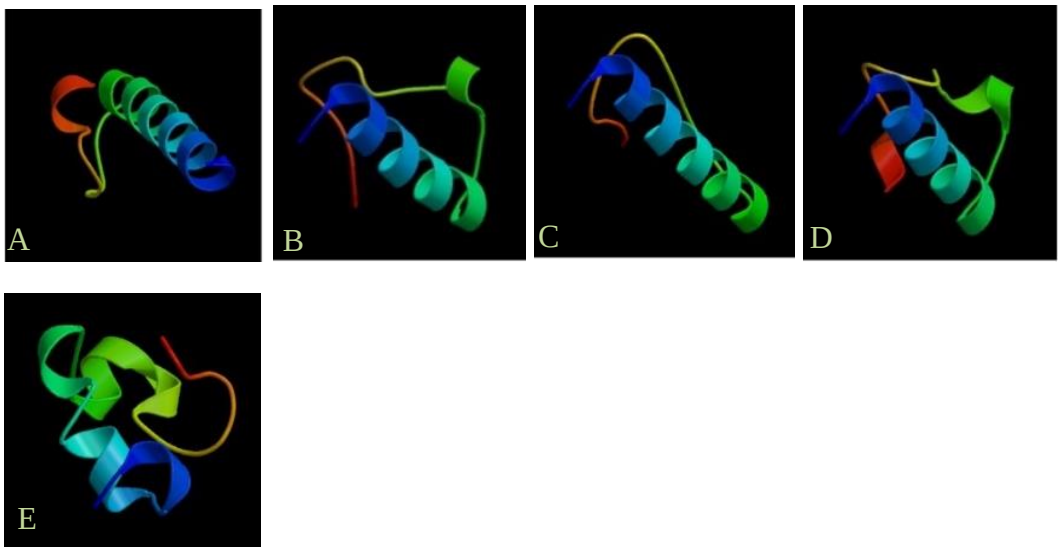

Figure 12.6 (A), (B), (C), (D), and (E) 3D structure predictions of human HTN using Robetta software.

Figure 12.6 shows the five structural predictions of HTN by Robetta software. All predictions showed an α-helix structure at the N-terminal (except for Figure 12.6E). The difference in prediction is mainly in the sequence after the amino acid 21. Figure 12.6A showed possible unordered

conformation in the middle sequence and a possible short helical conformation at the C-terminal. Figure12.6B showed possible short helical conformation at the middle sequence and an unordered conformation at the C-terminal. Figure 12.6C showed possible unordered structure following the N-terminal helix. Figure 12.6D showed possible short helical conformation at the middle sequence and C-terminal. Figure 12.6E showed that following a short α-helix structure at the N-terminal the middle fragment showed multiple short helical conformations followed by an unordered conformation at the C-terminal.

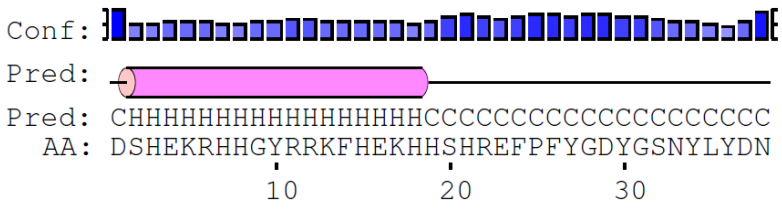

Figure 12.7 Structure predictions of human HTN by PSIPRED software.

Figure 12.7 shows secondary structure prediction of HTN by PSIPRED software, also showing a possible α-helical secondary structure conformation between S2-H18 at the N-terminal while the rest of the peptide is unordered.

All the secondary structural predictions of STN and HTN by Robetta shown in Figure 12.4 and 12.6 (A, B, C, D, and E) show an α-helical conformation at the N-terminal. However, the middle and C-terminal differ in each prediction. In short peptides, the conformation is very variable because of the lack of extensive bonding between amino acids in different parts of the sequence. This results in the software making a series of

different possible conformations that may occur. Therefore, the N-terminal α-helix is confirmed by Robetta software for both STN and HTN.

12.3.2 Particle Size, Surface Charge and Secondary Structure of STN, HTN, STN21, and HTN21 when in Combination

12.3.2.1 Particle Size of STN, HTN, STN21, and HTN21 when in Combination

Peptides combined	MR_H (nm)	(±SE)
STN+HTN	101	(±13)
STN+HTN21	114	(±10)
STN21+HTN	105	(±61)
STN21+HTN21	91	(±17)

Table 12.2 Mean hydrodynamic radius of peptides in combinations and the standard error of the mean.

Table 12.2 shows the MR_H of STN, HTN, STN21, and HTN21 when in combination at 100 µmol/l of each. Statistical analysis showed that there was no significant difference in the MR_H for the peptide when in combinations.

Table 12.1 and Table 12.2 shows that there was a significant increase in the MR_H caused by the combination of peptides in solution compared to individual peptides at 100 µmol/l ($\rho<0.001$), suggesting the formation of aggregates. However, there was no statistical difference in the MR_H of peptides at 200 µmol/l and the peptides when in combination at a total concentration of 200 µmol/l.

12.3.2.2 Surface Charge of STN, HTN, STN21, and HTN21 When in Combination

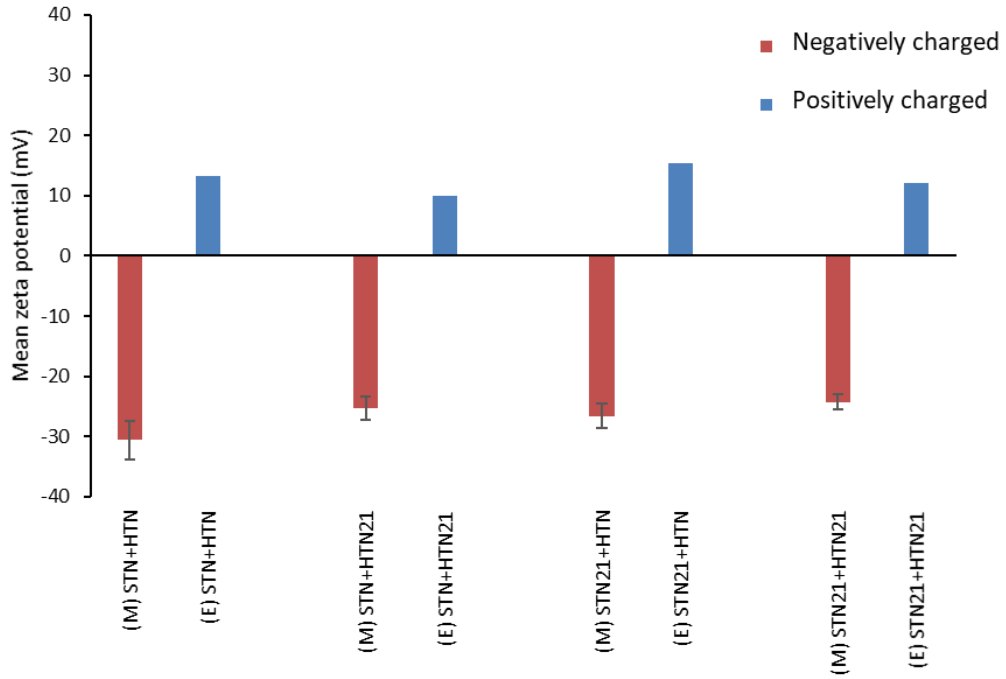

Figure 12.8 Mean zeta potential measurements of peptides in combination at 100 µmol/l , where (M) is the measured mean zeta potential by DLS, and (E) is the expected (calculated) mean zeta potential of the peptide when in combination at 100 µmol/l*. The error bars represent the ±SE of the mean.*

Figure 12.8 shows the measured and expected mean net charges of the peptides when in combination. All peptides when in combination demonstrated net negative charges, despite the fact that individual HTN and HTN21 were positively charged. There were no statistical differences in the net charges of peptides when in combination.

12.3.2.3 Secondary Structure Conformation of STN, HTN, STN21, and HTN21 when in Combination

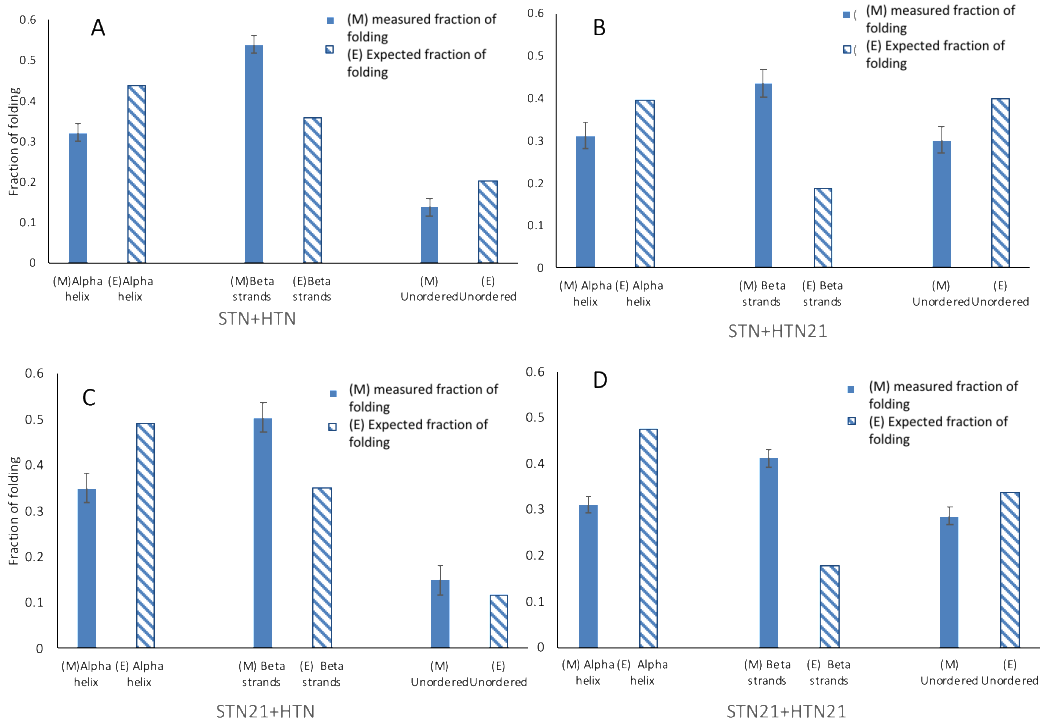

Figure 12.9 Fraction of folding of the secondary structure components present in peptides when in combination using CONTINLL SP43 fit, (A)STN+HTN, (B)STN+HTN21, (C)STN21+HTN, and (D)STN21+HTN21 in (Solid blue) at a total concentration of 200 µmol/l*. The expected (calculated) fraction of folding of the secondary structural components of the peptides when in combination if simply mixed in solution without interaction* (diagonal blue stripes). *Error bars represent the RMSD. The RMSD calculated by the CD apps software is STN+HTN-0.023, STN+HTN21-0.03, STN21+HTN-0.04, STN21+HTN21-0.023.*

Figure 12.9 shows the fraction of folding of conformation of peptide when in combination at a total concentration of 200 µmol/l. All combinations showed a reduction in the fraction of folding for α-helical conformation and much higher fractions of folding for β-strand conformation than would have been expected if simply mixed in solution, indicating possible partial unfolding of individual peptides and possible interaction between the peptides resulting in structural changes. The fraction of folding for

unordered conformation did not change for the peptides when in combination.

12.4 Discussion

12.4.1 Aggregation, and Surface Charge of STN, HTN, STN21, and HTN21 Individually

In this study, individual peptides showed small MR_H and high net charges at 100 µmol/l. Increasing the concentration of individual peptides to 200 µmol/l resulted in the reduction of the net charge, but, significantly increased the peptide size, suggesting the formation of large aggregates. Peptide surface charge forms a long-ranged repulsion, electrostatic in cause, mainly in dilute solution (Weiss *et al.,* 2009). This is because the distance between each peptide particle is large. Therefore, low peptide concentration and high surface net charges of STN, HTN, STN21, and HTN21 individually will cause an electrostatic repulsion between each peptide molecule to occur and consequently, peptides do not aggregate. However, in solutions with higher concentration, particles are closer together. Both Brummitt *et al.,* (2011) and Kim *et al.,* (2013) examined the factors that contribute to aggregation of proteins and found that aggregation is initiated by the addition of a single molecule of protein or by the combination of clusters. Initially, single molecules are governed by electrostatic forces. If the repulsions between the molecules are large, molecules do not aggregate. However, if the molecules are adequately attracted, they will form dimer or oligomer or aggregates. Therefore, by increasing the concentration of peptides, close range interactions

(governed by van der Waals interaction) are increased, and therefore proteins will tend to aggregate (Weiss *et al.,* 2009).

In this study, Table 12.1 and Figure 12.3 showed that increasing the concentration from 100 to 200 µmol/l for the individual peptides resulted in peptide aggregation, with no significant change in the secondary structures. Wang *et al.,* (2010) studied peptide aggregation pathways and the possible aspects that could control their aggregation. These authors suggested that proteins could aggregate through direct association (aggregation through self-association). They suggested that increasing the concentration would increase the chances of self-association facilitated by van der Waals forces. The van der Waals forces between the peptides used in this study occur due to short-range attractive forces between the peptides enabled by uncharged residues (Y, G, P, N, S, Q, and T). The authors also suggested that such aggregation may be accompanied by subtle structural changes, which was also observed in the current study.

In this study, STN and STN21 showed net negative charges while HTN and HTN21 showed net positive charges at 100 and 200 µmol/l. Truncation of both the peptides reduced their surface net charge. STN21 contain 5 negatively charged residues in its N-terminal sequence, STN contains an additional negative residue at E26. HTN and HTN21 contain positively charged residues, 13 in HTN (six H, three K, and four R), while HTN21 contain 12 positively charged residues. Therefore, the presence of the negative residues in STN and STN21 or positive residues in HTN and HTN21 attribute to the surface net charges of these peptides in solution.

The reduction of the surface net charge in the truncated peptide is possibly due to the loss of the C-terminal. In this current study, individual peptides net charges decreased with increasing the concentration. The aggregation of the peptides at 200 μmol/l seems to affect the net charges of these aggregates possibly by concealing parts of the charged molecule in the aggregate. However, this study does not give details on how aggregation occur and consequently how aggregation may affect the net charge. Therefore, further work should be done to investigate peptides aggregation and the effect on the net charges.

12.4.2 Secondary Structure Conformation of STN, HTN, STN21, and HTN21 Individually

12.4.2.1 Secondary Structure Conformation of STN, and STN21

The CD results (shown in Figure 12.3A and B) of the deconvoluted data showed that both STN and STN21 displayed higher fractions of helical conformation, compared to β-strands, or unordered conformation. Even though the CD deconvoluted data yields the fraction of folding of the secondary structure of proteins, it does not provide information about the location of those secondary structures within the overall modelled structure. Analysing the primary structure and comparing it with the CD data and the secondary structure predictions is a way to further explain the results obtained for peptide secondary structure conformation. Primary sequence analysis is possible by looking at the hydropathicity of amino acids that favours α-helical conformation according to Pace and Scholtz, (1998) (discussed in Section 5.3), and the distribution pattern of polar, and non-

polar residues in a sequence reported by Bradley *et al.,* (2006). Bradley *et al.*, (2006) related the secondary structure of proteins to the Binary patterning of polar and nonpolar amino acids residues in their sequences. They reported that a pattern of polar (○) and nonpolar (●) amino acids arranged with an alternating periodicity of (○●●○○●●○) is present in an α-helical conformation, and an alternating periodicity of (○●○●○●○) is an indicator for β-strand structure. Figure 12.10 shows the primary amino acid sequence of human STN, and the polar and nonpolar patterning.

○	○	○	○	○	○	●	●	○	○	●	●	○	●	●	○	●	○	●	●	○	○	●	●
1	**2**	**3**	**4**	**5**	**6**	**7**	**8**	**9**	**10**	**11**	**12**	**13**	**14**	**15**	**16**	**17**	**18**	**19**	**20**	**21**	**22**	**23**	**24**
D	pS	pS	E	E	K	F	L	R	R	I	G	R	F	G	Y	G	Y	G	P	Y	Q	P	V
●	○	○	●	●	○	●	○	●	○	○	●	○	○	○	○	○	○	●					
25	**26**	**27**	**28**	**29**	**30**	**31**	**32**	**33**	**34**	**35**	**36**	**37**	**38**	**39**	**40**	**41**	**42**	**43**					
P	E	Q	P	L	Y	P	Q	P	Y	Q	P	Q	Y	Q	Q	Y	T	F					

Figure 12.10 Amino acid sequence of STN, indicating polar (○) and non-polar (●) residues.

Human STN structure is asymmetrical in terms of charge distribution similar to A-PRP (Aoba *et al.,* 1984), with most of the charged residues at the N-terminus (D1-R13), whereas the C-terminal is less polar.

Analysis of the primary sequence of STN and STN21 based on the hydropathicity of amino acids, and the alternation of polar and non-polar amino acids, shows an α-helix promoting interaction between K6 and R9, R10 and R13, L8 and I11 is probable. The helix is further stabilised by a salt bridge between pS3-K6. The presence of G12 will increase the flexibility of the helix and favour an extended conformation (Pace and Scholtz, 1998). Based on the β-strand pattern the G15-T18 and L29-Q37 fragments show a likelihood of STN to adopt a β-strand conformation. A polyproline II helix

conformation in STN is possible between G19-P28, similar to that adopted by the collagen pattern motif, G-P-X (where X is any other amino acid) (Barnes *et al.,* 1996). Residues between Y38-F43 do not show any structural disposition and therefore, this region is likely to be unordered.

The secondary structure predictions by Robetta software (Figure 12.4) all show an α-helical conformation at the N-terminal of STN. The secondary structure prediction by PSIPRED of STN (Figure 12.5) also suggests the presence of an α-helical conformation in STN and STN21 (the length of the α-helix is from S3-R13) which also agrees with the polar and nonpolar analysis of the primary sequence of STN and STN21.

The CD results of STN in this study also confirms Gururaja and Levine, (1996), and Naganagowda *et al.,* (1998) who reported an α-helical conformation at the N-terminal, linked to an extended β-strand, which in turn is linked to a L-proline type II helix. Further, the N-terminal of STN also showed an α-helical conformation, according to structural predictions (Chou and Fasman, 1974) and CD measurements of the 15 N-terminal peptide (Raj *et al.,* 1992).

12.4.2.2 Secondary Structure Conformation of HTN, and HTN21

The deconvoluted CD results shown in Figure 12.3C showed that HTN had a higher fraction of folding for α-helix, and β-strands compared to unordered conformation. Figure 12.11 shows the primary amino acid sequence of human HTN, and the polar and nonpolar patterning.

○	○	○	○	○	○	○	○	●	○	○	○	○	●	○	○	○	○	○	○	○	○	○	●
1	**2**	**3**	**4**	**5**	**6**	**7**	**8**	**9**	**10**	**11**	**12**	**13**	**14**	**15**	**16**	**17**	**18**	**19**	**20**	**21**	**22**	**23**	**24**
D	pS	H	E	K	R	H	H	G	Y	R	R	K	F	H	E	K	H	H	S	H	R	E	F
●	●	○	●	○	○	●	○	○	○	●	○	○	○										
25	**26**	**27**	**28**	**29**	**30**	**31**	**32**	**33**	**34**	**35**	**36**	**37**	**38**										
P	F	Y	G	D	Y	G	S	N	Y	L	Y	D	N										

Figure 12.11 Amino acid sequence of HTN, indicating polar (○) and non-polar (●) residues.

Human HTN structure is not as structurally asymmetrical in terms of charge distribution as human STN. Apart from D29 and 37, the charged residues in the N-terminus are from D1 to E23.

Analysis of the primary sequence HTN based on its primary sequence hydropathicity of amino acids and the pattern of polar and non-polar is carried out to further explain the results of the CD data. The primary sequence (shown in Figure 12.11) suggest an α-helix formation supported by salt bridges between S2 and K5, and E4 and R6 or H7. The presence of a flexible G at position 9 affect the extension of the helix (Pace and Scholtz, 1998). A hydrophilic link might give rise to a helix from R12 to H15. A possible salt bridge between K13 and E16 could occur. There is no secondary structural tendency for the sequence between K17 and P25 and therefore, it is highly possible that this region is unordered. Residues between F26-D29, Y30-S32, and Y34-Y36 might promote β-strands conformation.

The secondary structure prediction by Robetta software for HTN confirms the presence of an N-terminal α-helix. This is confirmed further by the polar and non-polar analysis. Therefore, the whole α-helix would extend

from S3-E16, similar to the secondary structure prediction by PSIPRED software shown in Figure 12.7.

The deconvoluted CD results shown in Figure 12.3D suggest that HTN21 adapts a slightly different conformation than HTN. HTN21 had the highest fraction of unordered conformation followed by α-helical conformation and lastly β-strand conformation. The reduction of the β-strand conformation observed between HTN and HTN21 could be due to the loss β-strands inducing fragment (F26-D29, Y30-S32, and Y34-Y36). The CD result of the α-helix conformation confirms the presence of an α-helix however, contrary to the secondary structure prediction by PISPRED software, the CD deconvolution results show shorter α-helix conformation than what is expected.

There is little literature on HTN or HTN21 secondary structure in solution to use for comparison purposes. Whereas, the structure of histatin-5 (HTN-5) which is an un-phosphorylated peptide of 24 residues, 7 of which are histidine has been studied. Therefore HTN-5 could be used as a model for HTN21 conformation comparison purposes, as shown in Figure 12.12.

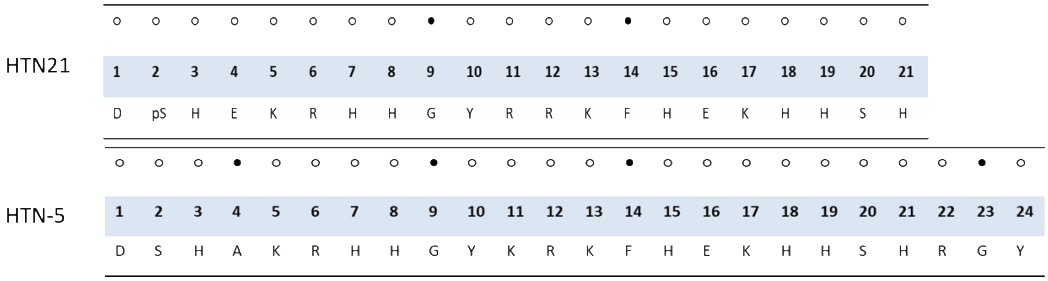

Figure 12.12 Amino acid sequence of HTN21 and HTN-5, indicating polar (○) and non-polar (●) residue.

The HTN-5 sequence resembles HTN21 sequence except for two substitutions, one is a substitution of hydrophilic negative residue E4, with a hydrophobic nonpolar A4, which could affect the stability of the helix formation in HTN-5. The second is the substitution of polar positive residue R11, with another polar positive residue K11, which is structurally not significant. In addition, HTN21 lacks the RGY fragment present at the end of HTN-5.

The CD and NMR structure analysis showed that HTN-5 exhibits mostly an unordered conformation with a tendency to form α-helical conformation at its N-terminal (Raj *et al.,*1998; Barsukov and Lian, 1993). Nuclear magnetic resonance on HTN-5 also showed that it has characteristic of β-strand structure, but it is very transient in nature (Barsukov and Lian, 1993). By comparison with HTN-5, it can be suggested that HTN21 adopt an α-helical conformation at the N-terminal, and a possible β-strand while the rest of the peptide is unordered.

12.4.3 Aggregation, Surface Charge and Structural Conformation of STN, HTN, STN21, and HTN21 when in Combination

In this study peptides in combination formed aggregates, that had net negative charges, and tendencies to form β-strands. Folded peptid molecules can form weak reversible bonds, usually through van der Waals forces (Sung, 2015), and form dimers or minor oligomers. Alternatively, peptides can unfold partially or completely, and then refold while in solution (Sung, 2015). The partially unfolded molecule reveals more hydrophobic residues (Wang *et al.,* 2010). Aggregation of peptides occurs when

hydrophobic surfaces interact (Wang *et al.,* 2010). Initial stages of peptides aggregation involve the interaction of specific residues in a surface with a matching hydrophobic surface residue in a neighbouring molecule (Fink, 1995). As the aggregation continue, there will be an increase in size. Ultimately as more peptide fragments unfold, they form more hydrophobic interactions and hydrogen bonds, which will give rise to new conformations (Fink, 1995). It could be argued that this type of aggregation could also occur in peptide-peptide interactions as seen in the peptide when in combination in this study. Where part of the α-helical structure unfolds and form hydrophobic link with a neighbouring peptide molecule, which contributes to the formation of aggregates.

In this study, there was a marked change in the surface net charge of HTN and of HTN21, from a net positive charge (individually) to a net negative charge when in combination with either STN or STN21. STN contains fourteen hydrophobic residues compared to only five in STN21. Whereas HTN contains five hydrophobic residues in its sequence compared to one in HTN21. Iontcheva *et al.,* (1997) and Vitkov *et al.,* (2004), reported the presence of salivary supramolecular globular aggregations that exist prior to mineral surface adsorption. They suggested that these aggregates have hydrophobic cores, and charged groups located on the surface. Therefore, it is possible that the peptides when in combination aggregate into larger size molecules hydrophobic in core, which changes the net charge towards a more negative value.

The CD deconvolution data of the peptides when in combination showed that the formation of β-aggregates appears to be the principal

mechanism driving the process of aggregates formation as shown in Figure 12.9. FTIR studies on proteins by Oberg *et al.,* (1994) and Fink, (1995) showed that up to 70% of aggregated proteins exhibit new secondary structural conformation (i.e. additional new β- structures form). In the case of small proteins, there is often a marked increase of β-structure when there is protein-protein interaction. Linding *et al.,* (2004) suggested that in addition to hydrophobic attractions, hydrogen bonds between two neighbouring β-strand give rise to β-aggregates. Therefore, hydrogen bonds between the side chains of neighbouring β-strands present in STN, HTN, STN21 or HTN21 can further stabilise the conformation by forming possible β-sheets between peptides, which will cause the formation of β-aggregates. This type of aggregation is also common in proteins such as amyloid (Roberts, 2014). Figure 12.13 is a possible illustration of the β-aggregates structure where the core is hydrophobic while the surfaces would be the hydrophilic charged with the net charge of the hydrophilic N-terminal, which is negatively charged in STN, HTN, STN21, and HTN21.

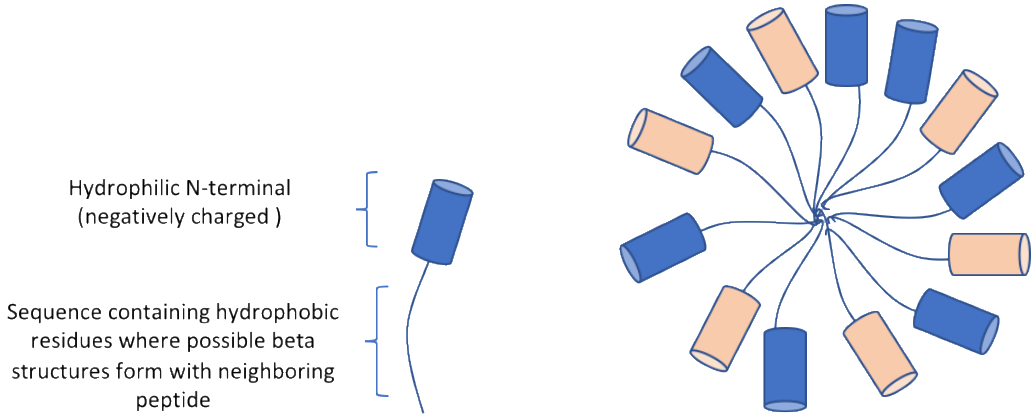

Figure 12.13 An illustration showing a possible aggregate structure of the peptides when in combination (peptide 1 in blue, peptide 2 in orange), where the surface of the aggregate is charged with the net charge of the N-terminal fragment of peptides (negative), while the core is formed by hydrophobic interactions.

Peptide aggregation is more complex than the simple α-helix → aggregated β-structure transitions. CD spectra of proteins in the near-UV spectral region (250 and above) can be sensitive to specific aspects of the tertiary structure. At the near UV region, the chromophores are the aromatic amino acids (Rahman et al., 2013). If a peptide does not have a defined tertiary structure while maintaining its secondary structure, the signals in the near-UV region will be nearly zero. In this study, the CD spectra were unable to give detailed insight into the tertiary and quaternary structures of proteins since CD measurements were not done in the near-UV light.

Peptide-peptide interaction is not yet fully understood and needs further investigation to determine what initiates peptide-peptide aggregation, and what are the factors that determine the kinetics of aggregation, which could be the basis for future work.

12.5 Conclusions

- This study shows that at a concentration where individual peptides do not aggregate, STN and STN21 demonstrate net negative charges while HTN and HTN21 demonstrate net positive charges. Truncation of both peptides reduced their surface net charges.

- The results from particle size analysis of individual peptides at 200 μmol/l suggest that individual peptides aggregation is concentration dependent.

- Secondary structural analysis of STN, HTN, STN21, and HTN21 showed that the N-terminal of each peptide adopts an α-helical

conformation. Truncation of STN C-terminal doesn't alter STN21 N-terminal α-helix length. However, Truncation of HTN C-terminal reduced the N-terminal α-helix while increasing the unordered conformation for HTN21.

- When in combination STN, HTN, STN21, and HTN21 aggregate. The driving force of aggregation is partial peptide unfolding and β-conformational changes driven by hydrophobic residues interaction and hydrogen bonds between neighbouring β-strands. The aggregate of peptides in combination demonstrate a net negative surface charge, which could contribute to mineral surface affinity.

Chapter 13. The Effect of Statherin, Histatin-1 and Their 21 N-terminal Peptides Individually and When in Combination on HA and Enamel Demineralisation Rates

13.1 Introduction

Dental caries is a major public health issue worldwide and is the most prevalent non-communicable disease (Listl *et al.,* 2015). Despite the multifactorial aetiology of caries that involves acids (extrinsic and intrinsic origin), dietary habits, social and physical factors, it is clear that after many studies that prevention is possible (Fejerskov and Kidd, 2004; Public Health England, 2016). However, saliva constituents have a major role in the defence against chemical, mechanical and microbial attacks in the oral cavity (Lendenmann *et al.,* 2000).

STN and HTN are salivary phosphopeptides. The phosphorylation of their serine residues by a kinase within the salivary glands contributes to the adsorption of these peptides onto HA (Shaw, 2015).

Previous demineralisation studies on the cariostatic effect of STN and the N-terminal peptide STN21, have provided information on the effects of these peptides in the protection against HA demineralisation but not enamel (Kosoric *et al.,* 2007; Shah *et al.,* 2011). In addition, there are no similar studies that consider the effect of phosphorylated HTN on HA and enamel demineralisation. Furthermore, most of such studies investigate the effect of single salivary protein component on HA demineralisation.

However, to understand the complexity and anti-demineralisation function of the acquired enamel pellicle *in vivo* requires using combinations of salivary peptides to understand the importance of peptide-peptide interactions. This includes aggregation, proteolysis, cross-linking, truncation and possibly cyclisation all of which could influence the function of AEP (Yao *et al.,* 1999 and 2000).

The aim of this study was to directly measure the demineralisation reduction efficacy (using HA discs and enamel) after the exposure to human salivary peptides.

The objective was to measure the changes in mineral loss rates of HA discs and enamel, after the exposure to human STN, HTN, STN21 and HTN21 individually (at 100 µmol/l, and 200 µmol/l), and when in combination using SMR**.**

13.2 Materials and Method

13.2.1 Hydroxyapatite Discs and Enamel Block Preparation

Hydroxyapatite discs (Plasma Biotal Ltd, UK) made from sintered HA powder by uniaxial pressing (20 % porosity) with a thickness of ~2 mm were used as enamel model in this artificial demineralisation study. Three discs were used for each tested peptide at each concentration. All sides of each HA disc were protected with acid resistant nail varnish expect a circular area of 132.7 mm^2, where exposure of peptide was carried out on.

Caries free permanent molars extracted for orthodontic purposes (stored in normal saline) were randomly selected for each peptide

experiment. Ethical approval was obtained from Queen Mary Research Ethics Committee (QMREC 2011/99). The buccal and lingual surfaces of the teeth were cut into blocks approximately 4 mm x 4 mm with a thickness of ~ 2 mm using a Micro-slice 2 (Malvern Instruments Ltd., UK). Any dentine present was polished off using a P600 grit silicon carbide paper. Three enamel blocks were used for each test peptide.

13.2.2 Chemical Solutions and Peptide Samples

A stock solution of 100 mmol/L acetic acid (AnalaR VWR) was prepared with deionized water and buffered to pH 4.0 using 1000 mmol/L NaOH (Sigma-Aldrich, UK), and divided into six flasks of 1000 ml for each tested peptide. The pH of each acetic solutions during the whole course of the experiments was measured every day to check for changes.

Phosphate buffered saline powder (Sigma-Aldrich, UK) was dissolved in deionised water to prepare 10 mmol/l phosphate buffered saline containing 0.138 mol/l NaCl, 0.0027 mol/l KCl at pH 7.4.

Full-length phosphorylated STN, HTN, and their truncated 21 N-terminal peptides were synthesised by Fmoc solid-phase peptide synthesis (SPPS) and purified (98% pure) by HPLC as trifluoroacetate salts (TFA), (Peptide Protein Research Ltd, United Kingdom) as discussed in Section 11.2.1.

Peptides were weighed with UMX2 Ultra-microbalance (Mettler Toledo, Richmond scientific limited, Lancashire) and were dissolved in PBS at a concentration 100 µmol/l and 200 µmol/l when they were tested

individually. The peptides when in combination were dissolved at a concentration of 100 µmol/l of each.

13.2.3 SMR Experimental Method

The SMR technique has been described in Chapter 6. Enamel blocks and HA discs were mounted in SMR cells individually, as shown in Figure. 13.1. Each cell had two drain inputs one at the top to limit the volume of solution in the cell and one input at the bottom to deliver the deionised water or acidic solution. A butterfly needle is connected to the top hole and another to the hole at the bottom of the SMR cell, to allow the solution to be pumped in and out, maintaining its circulation throughout the experiment. The butterfly needles are SURFLO® winged butterfly (TERUMO EUROPEN N.V.,3002 LEUVEN, BELGIUM, needle length 19.0 mm, and diameter of 0.8 mm). These inputs were connected to a two-way peristaltic pump to circulate the solution at a flow rate of 0.4ml/min. The second top hole was also fitted with a needle to allow the escape of air to prevent building up of internal pressure within the cell and leakage in case of pump failure. Once the cell was securely sealed with silicone rubber compound (Geocel Ltd, Western Wood Way, Plymouth, UK, product # 12125388) to prevent leakage and tightened up with a 9-6 screw. The cell is then mounted on the SMR stage.

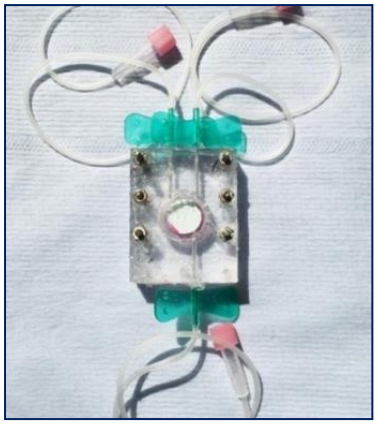

Figure 13.1 HA disc mounted in SMR polymethyl methacrylate cell.

13.2.3.1 SMR Area Scanning

Before each main experiment, an area scanning of each HA disc and enamel block was performed to give an indication of the status of the specimen and its exact location coordinates on the SMR scanning stage as shown in Figure 13.2.

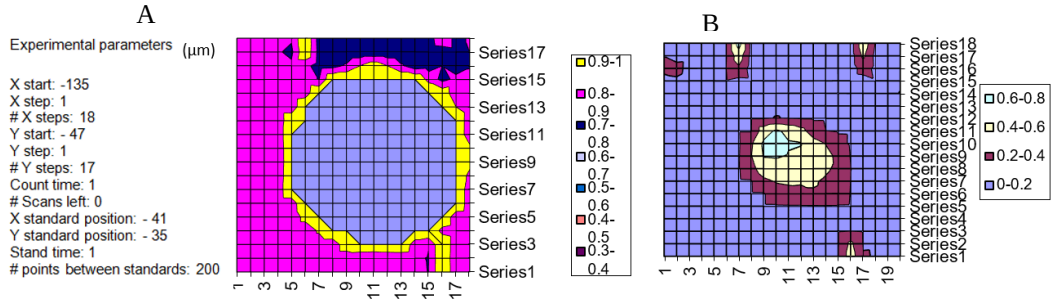

Figure 13.2 Area scan of an SMR cell with HA (A) or enamel sample (B) located centrally. X and Y axes represent coordinates of HA position on the SMR stage.

Two scanning positions were selected on each sample for the measurement of the rate of mineral loss. For the first 24 hrs, deionised water was circulated to work as an individual control for each sample. The samples were exposed to acidic solutions (pH 4.0 100 mmol/L acetic acid) for 2 days. After this preliminary acidic exposure, the samples were rinsed

thoroughly with distilled water and then exposed to 2.0 ml of the test peptide solution containing the peptides dissolved in PBS at a concentration of 100 or 200 µmol/l. After 24 hrs, the peptide solutions were recovered from the cell using 5 ml needles for further analysis. The blocks were then re-exposed to the acidic solution for a further 2 days. In addition, two enamel blocks and HA discs were exposed to PBS and used as negative controls. All measurements were carried out at 25.0 ±2.0 ^{o}C.

13.2.3.2 SMR Mineral Mass Measurement at a Scan Position

At each scan position, the transmitted photon counts were measured repeatedly for 60 seconds and were standardized against a standard measurement. The standard measurement was taken at a position on a homogenous and unaffected HA disc located in a SMR cell adjacent to SMR cells containing the samples. The scanning time for the standard was 60 seconds which allowed large number of data points (≈ 100 - 1000) to be obtained resulting in good statistical accuracy.

Two scanning positions on each sample were continuously scanned and real-time counts were detected by the detector during the experiment. At the selected point the X-ray attenuation value can be then converted to a value of projected mass of HA per unit area (g/cm^2) (as described in Section 6.6).

13.2.3.3 Data Processing

Projected mineral mass loss of enamel and HA per unit area was plotted against time on the assumption that the mineral loss is linear with time (Anderson and Elliott, 2000), demineralisation rate can then be calculated as:

$$y = bx \qquad \textbf{Equation 13.1}$$

where y is the projected mass loss of HA per unit area, x is the time, b is the rate of demineralisation.

The rate of mineral loss and associated statistical errors were calculated from the slope and the number of points used by linear regression fitting using SigmaPlot 10.0 (Systat Software, CA, USA). The standard error (SE) of each rate was the SE of the slope coefficient of the fitted straight line. The accuracy of the linear regression fitting was increased by using large number of data points measured at each scan position (as shown in Section 6.7, Figure 6.7).

The $RML_{enamel/HA}$ measurements of each sample after the exposure to the peptides were compared with those during the initial acidic demineralisation (prior to exposure to peptides). All samples showed significant difference in the RML after treatment with peptide. The differences in the demineralisation rates between control (prior to exposure to peptide) and each test RML value (after exposure to test peptide) was then calculated as a percentage reduction in the rate of mineral loss (PRRML) (as discussed in Section 6.7.1). For reproducibility, 2 different scan positions were measured on each HA and enamel sample.

Results are expressed as mean percentage reduction in the rate of mineral loss (MPRRML) and standard error. Data was analysed using GraphPad Prism 7.0d (GraphPad Software Inc., La Jolla, USA) statistical software for normality using Shapiro-Wilks test. After confirming data was normally distributed. Analysis of variance (ANOVA) with post hoc Bonferroni test was used to identify which means were significantly different from each other. Significance was predetermined at $\alpha=0.05$.

The $RML_{HA/enamel}$ values and associated errors at each scan position are presented in Appendix 3, for peptides individually, and Appendix 4 for peptides when in combination.

13.3 SMR Results

13.3.1 Effect of STN, HTN, STN21 and HTN21 Individually on HA and Enamel Demineralisation Rates

13.3.1.1 Effect of STN, and STN21 Individually on HA and Enamel Demineralisation Rates

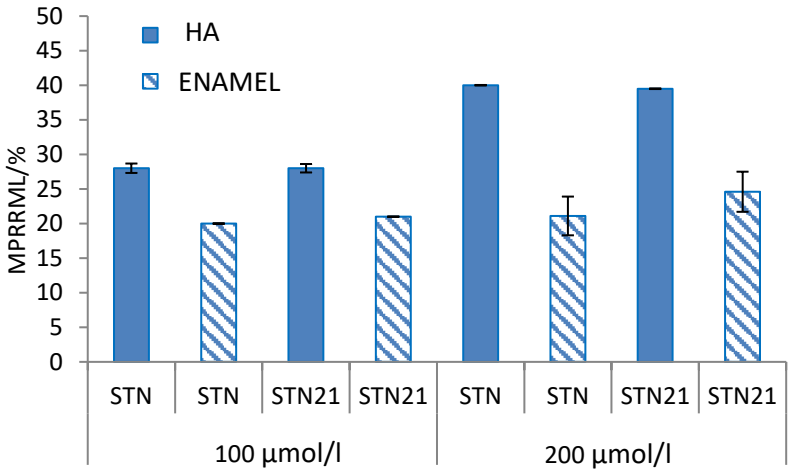

Figure 13.3 Mean percent reduction in the rate of mineral loss of HA discs (solid blue) and enamel blocks (blue diagonal stripes) exposed to 100, or 200 µmol/l of STN and STN21. The error bars represent the standard error of the means. No statistical difference between the PRRML of STN and STN21 for HA samples at either 100 or 200 µmol/l. Also, no statistical difference in the MPRRML of enamel treated with STN and STN21 at both concentrations.

Figure 13.3 shows the SMR results of the MPRRML values for HA and enamel samples after treatment with STN and STN21 at 100, and 200 µmol/l. Both STN and STN21 reduced the demineralisation rates in HA and enamel. Truncating the length of STN to its 21 N-terminal peptide did not affect the MPRRML value at 100 µmol/l for both HA and enamel, or at 200 µmol/l, for both HA and enamel.

Doubling the concentration of both STN and STN21, increased the MPRRML value for HA ($p < 0.01$), but not for the enamel.

13.3.1.2 Effect of HTN, and HTN21 Individually on HA and Enamel Demineralisation Rates

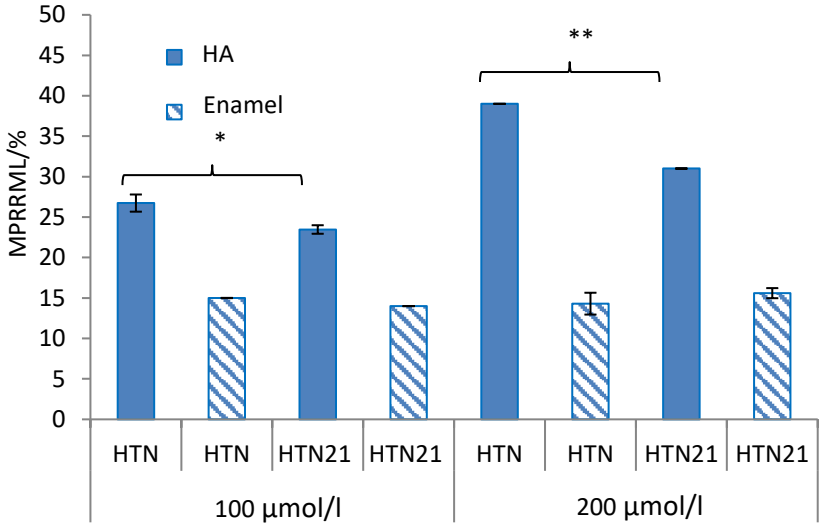

*Figure 13.4 Mean percent reduction in the rate of mineral loss of HA discs (solid blue) and enamel blocks (blue diagonal stripes) exposed to 100, or 200 µmol/l of HTN and HTN21.The error bars represent the standard error of the means. Statistical difference between the PRRML of HTN and HTN21 for HA samples at both 100 or 200 µmol/l (n=3, p < 0.05 *, p< 0.01 **). No statistical difference in the MPRRML of enamel treated with HTN and HTN21 at both concentrations.*

Figure 13.4 shows the SMR results of the MPRRML values for HA and enamel samples after the treatment with HTN and HTN21 at 100, and 200 µmol/l. Both HTN and HTN21 reduced the demineralisation rates in both HA and enamel. Truncating HTN length to its 21 N-terminal peptide did not affect the MPRRML value for enamel, however, it reduced the MPRRML value for HA at 100, and at 200 µmol/l (14% and 20% reduction, respectively) ($p< 0.05$, $p< 0.01$).

Doubling the concentration of HTN and HTN2, increased the MPRRML value in HA ($p< 0.01$ and $p< 0.05$ respectively), but not enamel.

13.3.1.3 Comparing the Effect of STN, and STN21 with HTN, and HTN21 on HA and Enamel Demineralisation Rates

Figures 13.3 and 13.4, also show that STN, STN21, and HTN are similarly effective in reducing HA demineralisation rates at 100, and at 200 µmol/l.

However, HTN MPRRML value was lower in enamel samples compared to STN and STN21 at both concentrations (25% reduction in the MPRRML value at both concentrations) ($\rho < 0.05$).

Truncating HTN length to the 21 N-terminal peptide reduced the value of MPRRML for HA samples but not for the enamel samples.

All samples exposed to individual peptides showed a significant increase in the MPRRML value compared to the control ($\rho < 0.001$). However, all the values of MPRRML were lower in enamel compared to HA.

13.3.2 Effect of STN, HTN, STN21, HTN21 When in Combination on HA and Enamel Demineralisation Rates

13.3.2.1 Effect of STN, HTN, STN21, HTN21 When in Combination on HA Demineralisation Rates

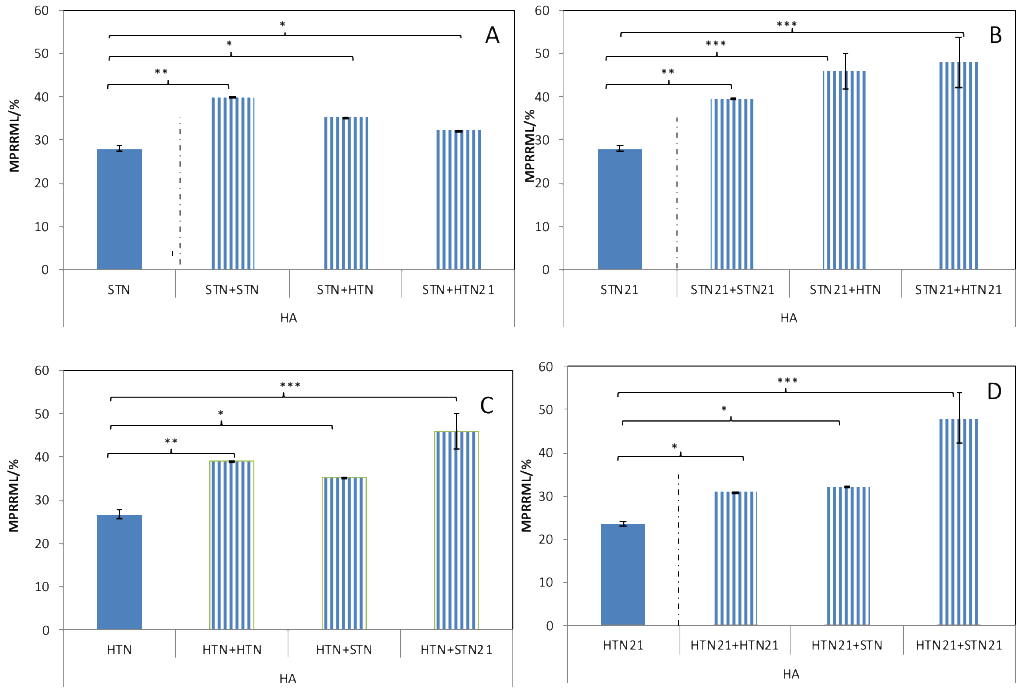

Figure 13.5 SMR results of HA treatment with peptides in combination. (A) Comparing MPRRML of HA samples after treatment with STN at 100 and 200 µmol/l and combined with HTN or HTN21 (B) Comparing MPRRML of HA samples after treatment with STN21 at 100 and 200 µmol/l and combined with HTN or HTN21. (C) MPRRML of HA samples after treatment with HTN at 100 and 200 µmol/l and combined with STN or STN21. (D) MPRRML of HA samples after treatment with HTN21 at 100 and 200 µmol/l and combined with STN or STN21. Strong significant differences were found between HA samples treated with 100 and 200 µmol/l (ρ< 0.01). Significant differences were also found between HA samples treated with individual peptide at 100 µmol/l and HA treated with peptide mixture. (n=3, ρ< 0.05, ρ< 0.01** and ρ< 0.001***).*

Figure 13.5 shows the SMR results of the MPRRML values of HA when treated with peptides when in combination.

Figure 13.5A shows that MPRRML value for STN increased when in combination with either HTN or HTN21, compared to the MPRRML value for STN individually at 100 µmol/l (p <0.05). However, the MPRRML value

for STN was lower when in combination with both HTN and HTN21 compared to MPRRML value for STN individually at 200 µmol/l (18.8 and 18 % reduction, respectively). No statistical difference in the MPRRML values for STN when in combination with HTN and HTN21.

Figure 13.5B shows that MPRRML values for STN21 increased when in combination with both HTN and HTN21 compared to the MPRRML value of STN21 individually at 100 µmol/l (increased 39.1% and 41.6% respectively) (ρ<0.001). STN21 MPRRML value increased when in combination with both HTN and HTN21 compared to the MPRRML value for STN21 individually at 200 µmol/l (14.1% and 17.7% respectively) (ρ< 0.05). No statistical difference in the MPRRML values for STN21 when in combination with HTN and HTN21.

Figure 13.5C shows that MPRRML values for HTN increased when in combination with both STN and STN21 compared to the MPRRML of HTN individually at 100 µmol/l (*p*<0.05 and *p*<0.001 respectively). HTN MPRRML value increased when in combination with STN21(15%) (*ρ*< 0.05), but not when in combination with STN, compared to the MPRRML value for HTN individually at 200 µmol/l. There was a statistical difference in the MPRRML value for HTN when in combination with STN and STN21 (*ρ*< 0.05). HTN MPRRML value when in combination with STN21 increased (23%) compared to the MPRRML value for HTN when in combination with STN.

Figure 13.5D shows that MPRRML values for HTN21 increased when in combination with both STN and STN21 compared to the MPRRML value for HTN21 individually at 100 µmol/l (*p*<0.05 and *p*<0.001

respectively). HTN21 MPRRML value increased when in combination with STN21 more than when in combination with STN in solution. HTN21 MPRRML value was more than doubled when in combination with STN21 compared to HTN21 individually at 100 µmol/l (from 23% to 48%). HTN21 MPRRML value increased when in combination with STN21 (35.4%) ($\rho <$ 0.01), but not when in combination with STN, compared to the MPRRML value for HTN21 individually at 200 µmol/l. There was a statistical difference in the MPRRML values for HTN21 combination with STN and STN21($\rho<0.001$). HTN21 MPRRML value when in combination with STN21 increased (32%) compared to the MPRRML value for HTN when in combination with STN.

Figure 13.5 A, B, C and D shows that increasing the concentration of STN, HTN or the 21 N-terminal peptides from 100 µmol/l to 200 µmol/l, increased the MPRRML values for HA samples (as shown previously in Sections 13.3.1, and 13.3.2).

13.3.2.2 Effect of STN, HTN, STN21, HTN21 When in Combination on Enamel Demineralisation Rates

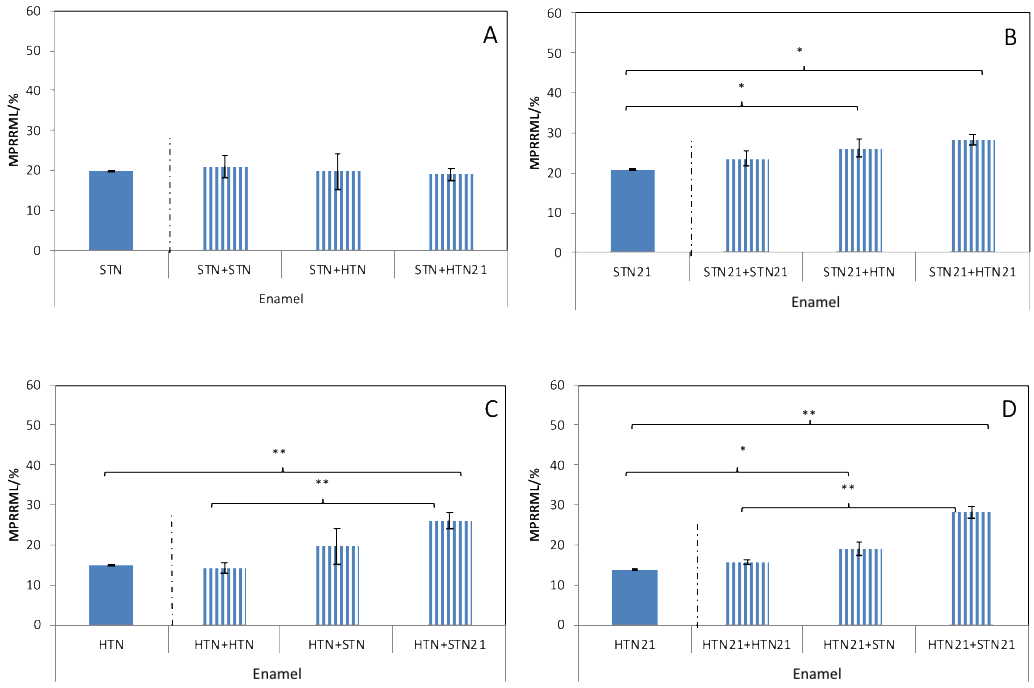

Figure 13.6 SMR results of enamel treatment with peptides in combination. (A) Comparing MPRRML of enamel samples after treatment with STN at 100 and 200 µmol/l and combined with HTN or HTN21. (B) Comparing MPRRML of enamel samples after treatment with STN21 at 100 and 200 µmol/l and combined with HTN or HTN21. (C) MPRRML of enamel samples after treatment with HTN at 100 and 200 µmol/l and combined with STN or STN21. (4D) MPRRML of enamel samples after treatment with HTN21 at 100 and 200 µmol/l and combined with STN or STN21. Significant differences, ρ< 0.05 and, ρ< 0.01**, n=3.*

Figure 13.6 shows the SMR results of the MPRRML values for enamel when treated with peptides in combination. Figure 13.6A shows that the MPRRML value for STN was not statistically different when in combinations compared to the MPRRML value for STN individually at 100 µmol/l or at 200 µmol/l. No statistical difference in the MPRRML values for STN when in combination with HTN and HTN21.

Figure 13.6B shows that the MPRRML values for STN21 were statistically higher when in combination with both HTN and HTN21 compared to the MPRRML value for STN21 individually at 100 µmol/l (ρ<

0.05). However, STN21 MPRRML values were not statistically different when in combination with both HTN and HTN21 compared to the MPRRML value for STN21 individually at 200 µmol/l. No statistical difference in the MPRRML values for STN21 when in combination with HTN and HTN21.

Figure 13.6C shows that the MPRRML value for HTN was statistically higher when in combination with STN21 ($\rho < 0.05$), but not when in combination with STN compared to the MPRRML value for HTN individually at 100 µmol/l. HTN MPRRML value was statistically higher when in combination with STN21($\rho < 0.05$), but not when in combination with STN, compared to the MPRRML value for HTN individually at 200 µmol/l. There was a statistical difference in the MPRRML values for HTN when in combination with STN and STN21($\rho < 0.05$). HTN MPRRML value when in combination with STN21 increased (24%) compared to the MPRRML value for HTN when in combination with STN.

Figure 13.6D shows that the MPRRML values for HTN21 increased when in combination with both STN and STN21 compared to the MPRRML value of HTN21 individually at 100 µmol/l ($\rho < 0.05$ and $\rho < 0.01$ respectively). HTN21 MPRRML value increased when in combination with STN21 (35%) ($\rho < 0.01$), but not when in combination with STN, compared to MPRRML value for HTN21 individually at 200 µmol/l. There was a statistical difference in the MPRRML values for HTN21 when in combination with STN and STN21($\rho < 0.05$). HTN21 MPRRML value when in combination with STN21 increased (21%) compared to the MPRRML value for HTN21 when in combination with STN.

All samples showed a significant increase in the MPRRML values compared to the control ($\rho < 0.001$). However, all the values of MPRRML for the peptides when in combination were lower in enamel compared to HA.

13.4 Discussion

13.4.1 The Effect of STN and STN21 Individually on Reducing HA and Enamel Demineralisation Rates

In this study both STN and STN21 reduced the rates of demineralisation of both HA and enamel. Also, truncating the length of STN to its 21 N-terminus peptide STN21 did not negatively affect the MPRRML value of the peptide, as previously shown (Kosoric *et al.,* 2007, Shah *et al.,* 2011). Peptides/proteins are complex polymers made from 20 naturally occurring amino acids with potential for the addition of side chains such as phosphate and many other derivatives by post-transitional modification. The demineralisation reduction role of STN is reportedly due to its N-terminal hexa-peptide, whereas lubrication and bacterial adhesion are associated with its C-terminal (Gibbons *et al.,* 1988; Fejerskov and Kidd, 2004). Mineral binding is facilitated by the electrostatic interaction of the negative residues at the N-terminal of the peptide and the positive charges on the HA surface. Among the negative groups, the phosphates in the phosphoserine at the 2nd and 3rd positions forms bonds with HA, 20 times stronger than carboxyl bonds (Moreno *et al.,* 1984; Raj *et al.,* 1992; Long *et al.,* 2001).

Kosoric *et al.,* (2007) and Shah *et al.,* 2011 studied the effect of both STN and STN21 on demineralisation rates of HA pellets (20% porosity, by weight). They showed that at 190 µmol/l the efficacy of STN and STN21

(individually) reduced the demineralisation rates by 40%, similar to the results obtained in the current study. Wikiel *et al.,* (1994) also studied the effect of full-length STN on HA demineralisation and showed reductions of up to 70% in the demineralisation rates. The difference in the demineralisation rates between this current study (and Kosoric *et al.,2007;* Shah *et al.,* 2011 studies), and the previous study (Wikiel *et al.,* 1994) might be due to the degree of saturation (DS) of the demineralising solutions in terms of calcium and phosphate. In the present study, Ca^{2+} or PO_4^{3-} were not added to the demineralising solution (DS=0), whereas the DS was 0.59 in the study done by Wikiel *et al.,* (1994).

Therefore, the presence of Ca^{2+} or PO_4^{3-} could help maintain a high calcium concentration adjacent to the tooth and maybe reduce enamel demineralisation, however, this study confirms that the presence of STN or STN21 individually bound onto the surface of mineral reduced the demineralisation rates efficiently either by forming a barrier or a membrane that regulates the demineralisation process.

13.4.2 The Effect of HTN and HTN21 Individually on HA and Enamel Demineralisation Rates

In this study, both HTN and HTN21 reduced the rates of demineralisation for both HA and enamel. However, HTN21 was not as effective in increasing the MPRRML as full-length HTN for HA samples.

The variety of the different amino acid residues in HTN and HTN21 peptides makes predicting their efficacy in preventing demineralisation and adsorption behaviour difficult. Different regions of their

structure show different affinities to surfaces. Positively charged, negatively charged, hydrophobic or hydrophilic regions are all involved in mineral binding. Therefore, apart from structural considerations, the phosphorylated serine at position 2 and the acidic amino acids in positions 1 and 4 in HTN (and in HTN21), suggest that the peptides can prevent demineralisation by binding to mineral surface, which was also suggested by Siqueira *et al.,* (2010), and Khurshid *et al.,* (2017).

13.4.3 Comparing the Effect of STN, and STN21 with HTN, and HTN21 on HA and Enamel Demineralisation Rates

Comparison of the SMR results of STN (Section 13.3.1) and HTN (Section 13.3.2), showed that the MPRRML of HTN was similar to that of STN and of STN21. The lack of one phosphoserine at the N-terminus of HTN compared with STN (and STN21), which has two, did not reduce the MPRRML of HTN.

The removal of the C-terminus of HTN reduced HTN21 MPRRML for HA samples but not for enamel samples. This truncation of the C-terminal affected HTN but not STN. Hydrogen bonds play a role in peptide adsorption (Santos *et al.,* 2008). The C-terminal of STN contains 12 uncharged polar residues (7 Q, 4 Y, and 1 T), the C-terminal of HTN contains only 6 polar uncharged residues (4 Y and 2 N). STN adsorption onto HA has been studied in terms of basic amino acids within STN sequence by Goobes *et al.,* (2007b). They found that STN-mineral interactions were due to the N-terminal five acidic residues and the three basics residues of STN. The exclusion of one basic amino acid does not

affect STN-mineral interaction. However, the removal of two or more basic residues from STN sequence negatively affected STN-mineral interaction. Therefore, it can be argued that the lack of;

1) 6 uncharged polar residues in HTN21 compared to HTN (that contribute to hydrogen bonds),

2) 1 basic residue in HTN21 compared to HTN,

3) the presence of only one phosphoserine at the N- terminal,

maybe the reasons why HTN21 demineralisation reduction for HA is reduced compared to HTN, STN, and STN21.

However, the removal of the C-terminal did not affect the enamel results. This result question the use of HA discs as a model system in studies involving biomolecular interactions.

13.4.4 The Effect of Peptides When in Combination on HA and Enamel Demineralisation Rates

Section 13.3.2 shows that there is a further increase in the MPRRML of HTN and HTN21 when combined with STN and STN21 compared to individual peptides at 100 µmol/l. This suggests an enhanced co-operative action. The increase in the MPRRML was more evident with STN21 combinations. Chatelier and Minton, (1996) first used the terms “positive co-operative adsorption” and “negative cooperativity”. These terms refer to protein-protein interactions which occur away from the primary binding site on the mineral surface. Positive co-operative adsorption implies that there

is an enhancement in protein adsorption kinetics when combined. The adsorption rates and amounts bound are generally higher than those of single component systems. The kinetics of adsorption would be the opposite in the case of negative co-operative adsorption. Lamkin *et al.,* (1996) proposed that proteins and/or peptides can directly adsorb onto HA or can adsorb indirectly via protein-protein interactions. Protein-protein interactions are governed by the net charge proteins (Bremer *et al.,* 2004; Demaneche *et al.,* 2009). Also, protein-protein interactions are governed by the buffer pH. For pH values higher or lower than the pI of the protein, the packing density is lower than if pH=pI, due to electrostatic repulsion between proteins (Demaneche *et al.,* 2009). In this study, the pH value of the buffer is 7.4, while the pI values are 8.32 for HTN and 6.25 for STN. When the pH=pI of a peptide, the number of negative and positive charges are in balance resulting in a net neutral molecule. At pH<pI, which is the case for HTN and HTN21, peptides are positively charged. Whereas, at pH>pI conditions peptides are negatively charged (STN and STN21). Therefore, instead of being repulsed by equal net charges, they interact due to electrostatic binding and aggregate.

The presence of seven H, three K and four R residues give HTN a high net positive charge. A strong electrostatic interaction between its positive charges and the negative charges of the N-terminal fragment of STN has been reported (Schlesinger and Hay, 1977; Norde, 1986). It is possible that this electrostatic interaction helps stabilise the adsorption of peptides, and hence improve the demineralisation reduction efficacy for the peptides when in combination.

Long *et al.,* (2001) suggested that the hydrophobic segment of STN supports the adsorption of HTN when its hydrophilic segment is strongly adsorbed to the mineral surface. However, Goobes *et al.* (2006) concluded that upon STN adsorption onto HA, the hydrophobic residues of the middle and C-terminal of STN are associated with HA surface. Therefore, even with the stabilising electrostatic interactions at the N-terminal between STN and HTN, the hydrophobic segment of STN upon binding to HA could act as a competitive binding segment to HTN and HTN21 when combined, and therefore affect the adsorption and demineralisation reduction efficacy for the peptides when in combination. This could also explain why STN demineralisation reduction efficacy did not increase when combined with HTN or HTN21 as much as STN21 combinations did. The observed increase in STN21 efficacy when in combination with both HTN and HTN21 could be that there is formation of specific protein binding sites on the mineral surface mediated by peptide-peptide interactions. These specific peptide binding sites could be occupied by hydrogen bonds of uncharged polar amino acids of STN C-terminal if present, which means that the C-terminus of STN could contribute to the competitive binding affinity of STN in a mixture.

In this study, there were differences in the MPRRML values for HA when exposed to different concentrations of peptides. The difference in the demineralisation reduction might be due to the difference in the amount of peptide available for adsorption that is able to contribute to demineralisation reduction and/or adsorption dynamics. Low protein concentration means slower adsorption, which allows structural conformation, and orientation

changes on the mineral surfaces. This permits the protein to increase its "footprint" (i.e. the area covered by a unit of the peptide) on the mineral surface. Whereas, at high protein concentration, there is a rapid adsorption, so structural changes of each molecule would be hindered on the mineral surface, and therefore the surfaces are covered more rapidly and densely by other molecules (Brynda *et al.,* 1990) as discussed in Section 11.5.1.

13.4.5 Differences in Demineralisation Rates Between Hydroxyapatite and Enamel

This study showed differences in the MPRRML values for HA and enamel. In the HA diffusion demineralisation model of Nancollas, (1974), "demineralisation pits" are formed by first removing a single ion (Ca^{2+}) which diffuses away from its detachment site and then into the bulk solution (Dorozhkin, 2012). Peptide adsorption onto the mineral surface may affect the demineralisation of enamel and HA crystals by inhibiting such Ca^{2+} loss at the "demineralisation pits". The difference in the availability of adsorption sites between HA and enamel might be the cause of the different peptide demineralisation reduction values observed between enamel and HA. The HA discs used in this study were 20% porous, whereas enamel is much less porous (4% by weight) (Shellis and Dibdin, 2000). Therefore, the availability of adsorbing sites for peptides is less in enamel compared to HA.

In the 1960s, it was believed that the chemical composition of enamel was identical to HA and consequently, the unit cell density of enamel would be the same as HA. However, Elliott, (1997) showed that enamel composition contains impurities such as the carbonate ions

substituting some of the phosphate group, which increases the unit cell dimensions of enamel (Xu *et al.,* 2012). These substitutions in the mineral crystal lattice disturb the structure, and therefore the apatite in enamel is much more acid soluble than stoichiometric HA. Also, enamel crystals possess intermolecular distances specific for each crystal face, which contribute to face-selective binding of peptides/proteins onto enamel surface (Yuwei *et al.,* 2009). These various substitutions may affect the intermolecular distances and therefore disturb the binding affinity of peptides onto specific enamel crystal faces. This, in turn, will reduce the demineralisation reduction efficacy of the peptides. Furthermore, enamel crystallites are highly organized, compared to synthetic HA, and therefore random binding will occur onto HA crystal faces compared to enamel crystal faces, which will increase the overall peptide uptake.

In addition, there is a high positive and a low negative charge distribution on the surface of enamel crystal (Kirkham *et al.,* 2000). Consequently, there is an association between surface charge domains of mineral crystals and protein/peptide binding.

13.5 Conclusions

- STN, HTN, STN21 and HTN21 provide protective efficacy against demineralisation. These phosphorylated peptides are effective in preventing mineral loss in both HA and enamel during acidic caries attacks.

- The absence of residues 22 onwards in STN did not alter the protective efficacy against demineralisation in HA and in enamel. Whereas,

the absence of residues 22 onwards in HTN did not alter the protective efficacy against demineralisation in enamel but did reduce the protective efficacy against demineralisation in HA. This suggests that the C-terminal of STN is not involved in the protective efficacy against demineralisation in both HA and enamel, whereas the C-terminal of HTN is involved in the protective efficacy against demineralisation of HA but not enamel. This signifies the importance of the electrostatic interaction of the negatively charged N-terminus and the mineral surface. Additionally, the presence of hydrogen bonds between the nonpolar amino acids and the mineral surfaces may help to further stabilise the peptide.

- Combinations of STN, HTN and their 21 N-terminal peptides increased the efficacy against demineralisation in HA and in enamel thus indicating a co-operative action. The absence of residues 22 onwards in STN21 improved the co-operative protective efficacy against demineralisation when in combination, suggesting the contribution of STN C-terminal to the competitive binding affinity of STN in mixtures.

- The differences in the demineralisation reduction values observed between HA and enamel samples challenges the usefulness of hydroxyapatite discs as an analogue system for enamel in demineralisation studies. Therefore, peptides/protein interaction with minerals should be in conjunction with both synthetic and natural occurring apatite.

Chapter 14. Overall Discussion

The protein composition of the AEP is important in the inhibition of calcium and phosphate precipitation, crystallisation, and control of microbial adhesion (Hay and Moreno, 1989; Jensen *et al.,* 1992; Hay, 1995). Salivary STN and HTN are known to be salivary proteins precursors of the AEP (Lamkin and Oppenheim, 1993). While both STN and HTN are capable of inhibiting crystal growth by binding to HA, STN alone can inhibit spontaneous precipitation (Lamkin *et al.,* 1996; Hay and Bowen, 1996).

Both STN and HTN affinity to HA have been studied (Moreno *et al.,* 1987; Yin *et al.,* 2003; Shimotoyodome *et al.,* 2006; Siqueira *et al.,* 2010). However, the influence of STN, STN21 and HTN on HA and/or enamel demineralisation has been the topic of fewer studies (Chin *et al.,*1993; Wikiel *et al.,* 1994; Kosoric *et al.,* 2007; Shah *et al.,* 2011). Since the demineralisation of both HA and enamel is reported to be a surface mediated process (Zahradnik *et al.,* 1976), it is probable that this process will be affected by macromolecules generated by the protein-protein interactions of the acquired enamel pellicle precursors that have an adsorption affinity onto HA surfaces (Zahradnik *et al.,* 1976; Vitkov *et al.,* 2004).

14.1 Overall Discussion of the Studies of STN, HTN, STN21, and HTN21 Individually

One of the aims of this thesis was to correlate the amounts of peptides adsorbed individually at 100 µmol/l and 200 µmol/l with the observed effect on demineralisation.

Figure 14.1 shows the correlation of the MPPA calculated in Section 11.4.4 with the MPRRML measured in Section 13.3.1.1 and 13.3.1.2 of individual peptides at either 100 µmol/l or at 200 µmol/l for HA discs and enamel blocks.

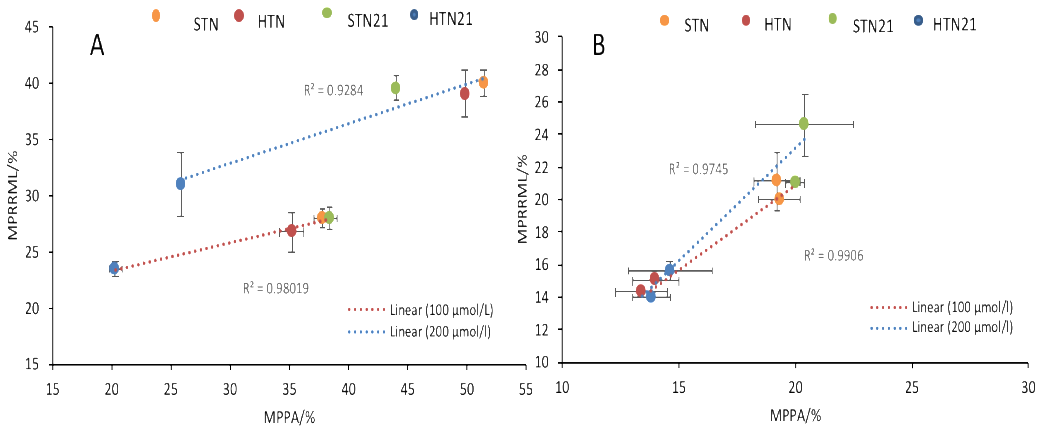

Figure 14.1 Correlation of the percent of adsorption of STN, HTN, STN21 and HTN21 individually at 100 and 200 µmol/l onto (A) HA discs, and (B) enamel, with the effect on the rate of demineralisation.

Both substrates show there was a positive linear correlation between the demineralisation reduction efficacy and the amount of peptide adsorbed. However, the results suggest that at 100 µmol/l the adsorption characteristics of individual peptides are different than their adsorption at 200 µmol/l. At a concentration where the substrate surface is sufficiently covered by a monolayer, demineralisation reduction is achieved through an ion semipermeable membrane that acts to control the diffusion of ions from

the apatite lattice into the solution and vice versa (Zahradnik *et al.,* 1976; Mutahar *et al.,* 2017b). As shown in Section 12.3.1. individual peptides aggregation at 200 µmol/l might lead to an increase in the thickness of the adsorbed layer, and hence an increase in demineralisation reduction efficacy. This peptide adsorption concentration dependence has been also reported by Santos *et al.,* (2008).

The results obtained from the effect of STN, HTN, and their 21 N-terminal peptides individually, on enamel adsorption and demineralisation rates showed that the negative N-terminal of these peptides is involved in peptide adsorption and demineralisation efficacy. HTN and HTN21 showed a decrease in enamel adsorption and demineralisation reduction efficacy compared to STN and STN21. By comparison with STN, HTN adsorbed onto enamel and reduced demineralisation rates (in a lesser amount and lower efficacy) even though STN has a net negative surface charge while HTN has a net positive surface charge. The reduction in efficacy could be attributed to localised factors within peptide sequences, such as the reduction in the number of the N-terminal acidic residues (5 acidic residues in STN compared to 3 acidic residues in HTN), which also affected the adsorption affinity to HA as measured by the rate of binding (Lamkin *et al.,* 1996) (Section 11.4.1). The truncation of the peptides further confirms that the density of the negative N-terminal charges is what contributes to the electrostatic interaction with mineral surfaces rather than the overall surface charge of the peptides. Since, STN21 and HTN21 had similar adsorption and demineralisation reduction rate for enamel samples as their full-length

peptides even though their net surface charges were reduced compared to the full-length peptides.

Figure 14.2 shows the correlation of the $T_{0.5}$ measured in Section 11.4.1 with the MPRRML measured in Section 13.3.1 of individual peptides at either 100 µmol/l or at 200 µmol/l for HA.

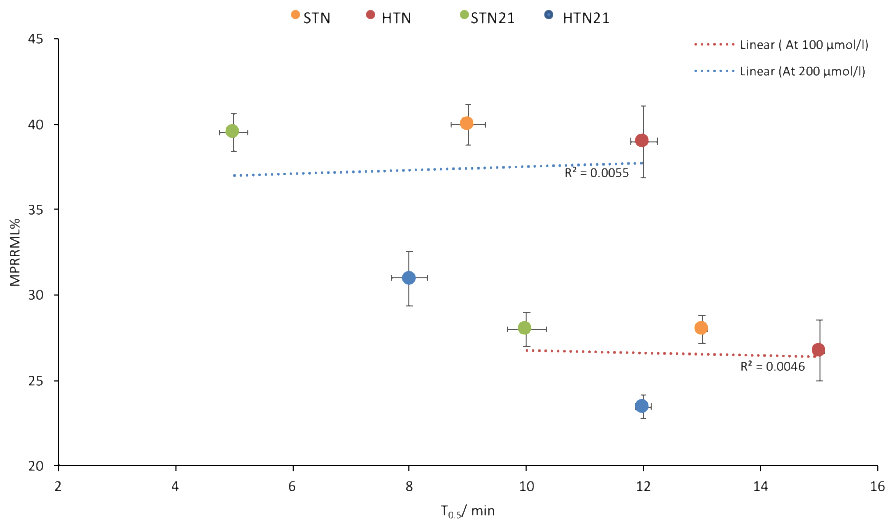

Figure 14.2 Correlation of the $T_{0.5}$ of STN, HTN, STN21 and HTN21 individually at 100 and 200 µmol/l onto HA with the effect on the demineralisation rates.

Figure 14.2 shows that there is no correlation between the demineralisation reduction observed in HA samples and the rate of binding. At 200 µmol/l truncated peptides, STN21 and HTN21 bind faster than full-length peptides, however, their demineralisation reduction efficacy was not related to their binding rates. STN21 reduced HA demineralisation rate up to 39.5% while HTN21 MPRRML was up to 31%. HTN was the slowest to bind onto HA compared to the other peptides, however, MPRRML was higher than HTN21 (up to 39%). Similar behaviour was observed when peptides are tested at 100 µmol/l.

Secondary structural analysis of individual peptides showed that STN, HTN, STN21, and HTN21 adopt α-helical conformations at their N-terminal. The α-helix conformation is longer in HTN compared to STN and STN21, while HTN21 adopted a shorter α-helix compared to HTN (Section 12.3.1.3). The α-helix has been previously suggested as a general structural mechanism for aligning acidic side chain residues with HA (Raj *et al.,* 1992) either by HA lattice matching, or by a more overall electrostatic complementarity. The results in Chapter 11 and 13 also agree with the proposed mechanism of α-helix matching of acidic side chain residues with HA surfaces. Additionally, the reduction in the α-helix length in HTN21 N-terminal compared to HTN could be one of the reasons to the observed reduction in HTN21 adsorption amount to HA beads and discs, and to the reduction in the MPRRML value for HA discs.

However, the results obtained from the effect of STN, HTN, and their 21 N-terminal peptides individually, at 100 µmol/l, and, at 200 µmol/l, on HA demineralisation rates and adsorption, also showed that the peptides adsorb differently onto HA than enamel. Hence their demineralisation reduction efficacy was affected by the different adsorption dynamics. The adsorption affinity of individual peptides measured by MPPA (Section 11.4.4) and the demineralisation reduction efficacy of the peptides individually and when in combination measured by MPRRML (Section 13.3.1, and 13.3.2) were more evident for HA samples compared to enamel samples (also shown in Figure 14.1). As discussed in Chapter 11, and Chapter 13, the difference could be attributed to various reasons;

1) the difference in the availability of adsorption sites in HA and enamel (HA is 20% pores, while enamel is 4 % pores by weight) (Shellis and Dibdin, 2000). As well, the difference in the availability of specific binding crystal faces in HA which could be biologically relevant for peptide adsorption,
2) also, due to the substitution of the phosphate group by some carbonate in enamel, the structure of the crystal lattice is disturbed (Xu *et al.,* 2012), and therefore might disturb the adsorption affinity of the peptides to enamel.
3) additionally, on enamel surface, there is a high positive and a low negative charge distribution compared to HA surface (Kirkham *et al.,* 2000) which affect the electrostatic affinity of the peptides to the mineral surfaces.

14.2 Overall Discussion of the Studies of STN, HTN, STN21, and HTN21 When in Combination

Results obtained from the adsorption of individual peptide when combined (Section 11.4.2), showed an increase in the individual peptide adsorption onto HA when in combination. The increase in the adsorption onto HA was more evident in STN21 combination with either, HTN or HTN21. Suggesting that STN C-terminal contributes to competitive adsorption with either HTN or HTN21 when in combination. Therefore, the loss of the C-terminal creates a co-operative adsorption effect where one peptide assists the adsorption of another. This co-operative and competitive

adsorption effect was also evident in the demineralisation reduction efficacy of peptides when in combination (Section 13.3.2).

The results of peptides adsorption when in combination (Section 11.4.2) and the results of peptides aggregation when in combination (Section 12.3.2.3) suggest two possible outcomes:

- the adsorption of peptides when in combination depends on the composition of each aggregating unit (amount of each peptide in an aggregate unit), for example when STN is in combination with HTN21, more STN is adsorbing onto HA compared to HTN21, implying that each aggregate unit contains more STN than HTN21, therefore enabling more STN to adsorb compared to HTN21.

- the adsorption of peptides when in combination does not depend on the amount of each peptide in an aggregating unit, as the aggregates could dissociate upon adsorption, increasing one peptide adsorption over the other. The increase of the amount of peptide adsorbing would depend on the affinity of each peptide to HA, or/and the side of each aggregate adjacent to the mineral surface while adsorbing, which could give a higher probability of one peptide to adsorb first over the other.

In both possibilities, the peptide that adsorbs first could either have a co-operative or a competitive effect on the adsorption of the second peptide.

To further understand the effect of aggregation on each peptide adsorption when in combination, the amount of each peptide in an aggregate and also the adsorption kinetics of these aggregates need to be investigated.

The results in Section 12.3.2 showed that peptides in combination formed aggregates that exhibited net negative charges, and tendencies to form β-structures. Rykke *et al.,* (1995, 1996) were the first to demonstrate the presence of globular structures present in parotid saliva and the presence of similar globular structures in the enamel pellicle. Vitkov *et al.,* (2004) further reported that these structures contain hydrophobic cores, and charged groups located on the surface and that they exist prior to the attachment onto the mineral surface. Therefore, the aggregation of peptides when in combination and the increase in the net negative surface charge compared to the individual peptides increases the binding rates of peptides when in combination onto HA.

The results presented in this thesis, and the results reported by these authors further indicates that enamel pellicle formation does not occur only as a result of a single peptide adsorption, but also as a consequence of the adsorption of supramolecular aggregates of pellicle precursors, that could further add to the protective ability of the enamel pellicle against acidic demineralisation.

Chapter 15. Using Non-Human STN21 Sequences to Investigate the N-terminal Sequence Features Needed for the Adsorption onto HA and Demineralisation Reduction

15.1 Rationale Behind Using Non-human Statherin Sequences

Much speculation has taken place over the role of the helical zone of the N-terminal of STN in the adsorption onto HA. Secondary structure software can reveal the probability that helices exist within protein sequences. However, the helical secondary structure is most certain where its formation is reinforced by tertiary and even quaternary conformation (Muirhead and Perutz, 1963; Kurivan *et al.,* 2012). Unfortunately for STN, these studies are less readily available.

The role of peptide helices and the impact of amino acid side chains in the adsorption of human STN and STN21 onto HA has been the subject of several studies (Long *et al.,* 2001; Goobes *et al.,* 2006; Ndao *et al.,* 2010). One way to investigate this would be to systematically replace certain amino acids one at a time in the synthetic manufacture of peptides by e.g. Fmoc solid-phase peptide chemistry. For example, R10 is considered important in the helical formation in human STN, and in its adsorption onto HA surfaces (Ndao *et al.,* 2010), this residue could be replaced in a synthetic statherin peptide. However, we have found that selectively replacing amino acids in STN by another amino acid with similar hydropathicity causes peptide insolubility. Such behaviour is not uncommon according to the staff

at Peptide Protein Research, possibly because of molecule “clumping”. Therefore, this approach is not possible.

An alternative approach is to look at non-human (across species) for homologues for human STN that may have slightly different amino acids sequences. In order for these non-human homologues to function, they must of course be soluble. As far as we are aware STN sequences are available for a number of non-human species. In most cases these sequences are derived, not by direct sequencing of purified proteins, but by inferences made from genomic DNA sequences of the animals (Belford *et al.*, 1984; Rijnkels *et al.,* 2003; Patamia *et al.,* 2005; Manconi *et al.,* 2010). For example, Pig-STN42, Cattle-STN40, Sheep-STN37 and Macacque-STN41 are “putative” proteins that may behave in the same way as STN in man and primates. It is not known whether these putative proteins are phosphorylated (as it is in humans), however, it seems reasonable to hypothesise that they are. A kinase from pig salivary gland certainly does phosphorylate the pig peptide sequence. Manconi *et al.,* (2010) proposes that the casein kinase of the Golgi apparatus of the salivary gland strictly identifies the SXE sequence in target peptides. For this study, in order to have these putative peptides to resemble the STN used in the current study, it is necessary that they all bisphosphorylated. That allows any differences in adsorption and effect on demineralisation reduction to be attributed to the remaining peptide sequence.

The aim of this chapter was to compare the adsorption characteristics and demineralisation reduction efficacy of non-human STN

with human STN in ordered to investigate the effect of substitutions in the N-terminal sequence.

The first objective was to measure the adsorption of a selected set non-human STN21 onto HA at 200 μmol/l using spectrophotometry. The second objective was to measure the effect of the non-human STN21 peptides at 200 μmol/l on HA demineralisation rates using SMR. The third objective was to characterise the N-terminal α-helix of these 21 N-terminal peptides and compare them with the result from human STN21 to further understand the effect of structure on the function of the peptides.

15.2 Materials and Methods

Table 15.1. Shows the 21 N-terminal sequences of the four selected non-human peptides used in this study.

Common Name	Scientific Name	Amino Acid Sequence	Database Reference
Macaque	Macaca arctoides	DSSEEKFLRRLRRFDEGRYGP	P14709
Pig	Sus scrofa	DSSDEKHHRKWQNREREHYR	D8WUT6
Sheep	Ovis aries	DSSEEVRHFPSLEKRPYPIQQ	W5PLL6
Cattle	Bos taurus	DSSEEEHRLRFNPRFYYPNQQ	Q8HY86

Table 15.1 The 21 N-terminal amino acid sequences of the non-human peptides used in this study and the database references from UniProt (http://www.uniprot.org).

The 21 N-terminal peptide of each non-human STN was synthesised by Fmoc solid-phase peptide synthesis (SPPS) and purified (98% pure) by HPLC as trifluoroacetate salts (TFA), (Peptide Protein Research Ltd, UK), with MW, as shown in Table15.2.

Each peptide was tagged with fluorescein isothiocyanate to improve the spectrophotometric quantification of the peptides. The tags were at the C-terminal of the peptides to reduce possible interference with the N-terminal.

Peptide	Molecular Weight
Macaque-STN21, (M-STN21)	3365 Da
Pig-STN21, (P-STN21)	3350 Da
Sheep-STN21, (S-STN21)	3294 Da
Cattle-STN21, (C-STN21)	3380 Da

Table 15.2 The molecular weight of synthetic non-human 21 N-terminal STN.

Each peptide was weighed with a UMX2 Ultra-microbalance and was dissolved at a concentration of 200 µmol/l in PBS.

Spectrophotometric calibration of non-human STN21 absorbance was carried out as described in Section 11.2.3. For the adsorption experiments, 1 ml of each peptide solution was thoroughly mixed with 1 mg of HA beads and their absorbance changes over time were recorded as previously described in Section 11.3.1. The MAPA values and the rate of binding were then calculated as described in Section 11.3.1. Each experiment was repeated four times for each peptide.

The effect of the peptides on HA discs demineralisation rates were investigated at a concentration of 200 µmol/l using SMR. The experiments were carried out in a similar way to the study described in Section 13.2. Three discs were used for each tested peptide.

The results for adsorption amounts, binding rates, and demineralisation rates are expressed as mean, and standard error (±SE). Data was analysed using GraphPad Prism 7.0d (GraphPad Software Inc.,

La Jolla, USA) statistical software for normality using Shapiro-Wilks test. After confirming the data was normally distributed. Analysis of variance (ANOVA) with post hoc Bonferroni test was used to determine which mean was significantly different from each other. Significance was predetermined at $\alpha=0.05$.

Secondary structure predictions by Robetta and PISPRED software for Macaque-STN41, Pig-STN42, Sheep-STN37 and Cattle-STN40 were carried out as described in Section 12.2.3.

Robetta secondary structure predictions were done using full-length sequences of the non-human peptides since the software does not accept less than 27 residues in a sequence.

PISPRED software secondary structure predictions were done using the full-length and the 21 N-terminal sequence of each peptide.

Both structural prediction software used do not allow for modified amino acids side chains such as phosphoserine to be used in the sequence. Therefore, the helices predicted by the software maybe shorter.

15.3 Results

15.3.1 Adsorption of the 21 N-terminal Non-Human Peptides onto HA Beads

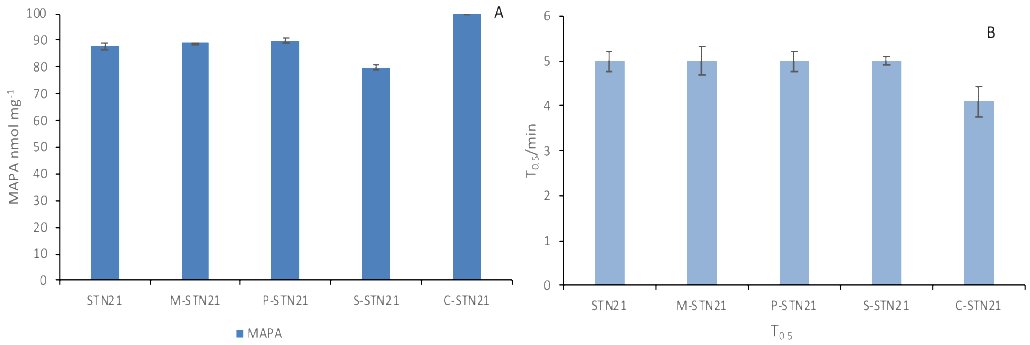

Figure 15.1(A) Mean amounts of non-human STN21 adsorbed at 200 µmol/l onto 1 mg of HA and (B) the mean time during which half of the peptide adsorb onto HA beads. The error bars represent the standard error of the means. The MAPA value and $T_{0.5}$ for C-STN21 were statistically different than the MAPA values and $T_{0.5}$ for human STN21, M-STN21, P-STN21 and S-STN21 ($p < 0.05$).

Figure 15.1 shows the MAPA values, and the half-time to saturation for 1.0 mg HA beads with 200 µmol/l of human and non-human STN21 peptides. Figure 15.1A shows that the MAPA values for STN21, Macaque-STN21, and Pig-STN21 are similar with no significant differences. Whereas, the MAPA value for Sheep-STN21 was lower ($p < 0.05$), and the MAPA value for Cattle-STN21 was higher ($p < 0.05$).

Figure 15.1B show that the rate of binding was similar for all STN 21 N-terminal peptides ($T_{0.5}$ = 5 min) but Cattle-STN21 had a statistically faster binding rate ($p < 0.05$).

15.3.2 Effect of the 21 N-terminal Non-Human Peptides on HA Discs Demineralisation Rate

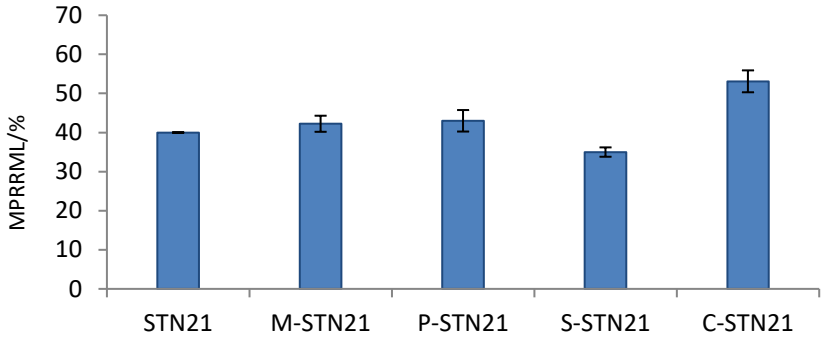

Figure 15.2 Mean percent reduction in the rate of mineral loss of HA discs after exposure to 200 µmol/l of human and non-human STN21 peptides for 24 hrs. Cattle-STN21 MPRRML value was the highest ($p< 0.05$), while Sheep-STN21 MPRRML was the lowest ($p< 0.05$).

Figure 15.2 shows the SMR results of the MPRRML values for HA discs after the treatment with the human and non-human STN21 peptides at 200 µmol/l. The MPRRML values for STN21, Macaque-STN21, and Pig-STN21 were statistically similar. The MPRRML value was the lowest for Sheep-STN21 (35%) ($p<0.05$) and was the highest for Cattle-STN21 (53%) ($p<0.05$).

15.3.3 Secondary Structure Prediction of the Non-human STN Peptides

Robetta secondary structure predictions for Macaque-STN41, Pig-STN42, Sheep-STN37 and Cattle-STN40 were used as a confirmation of the presence of the N-terminal α-helix.

Predictions of the N-terminal helical sequence length was the same for each non-human full-length peptide and its 21 N-terminal peptide. Therefore, secondary structural predictions result by the PISPRED software are only shown for the 21 N-terminal sequences.

15.3.3.1 Structural Prediction for Macaque-STN

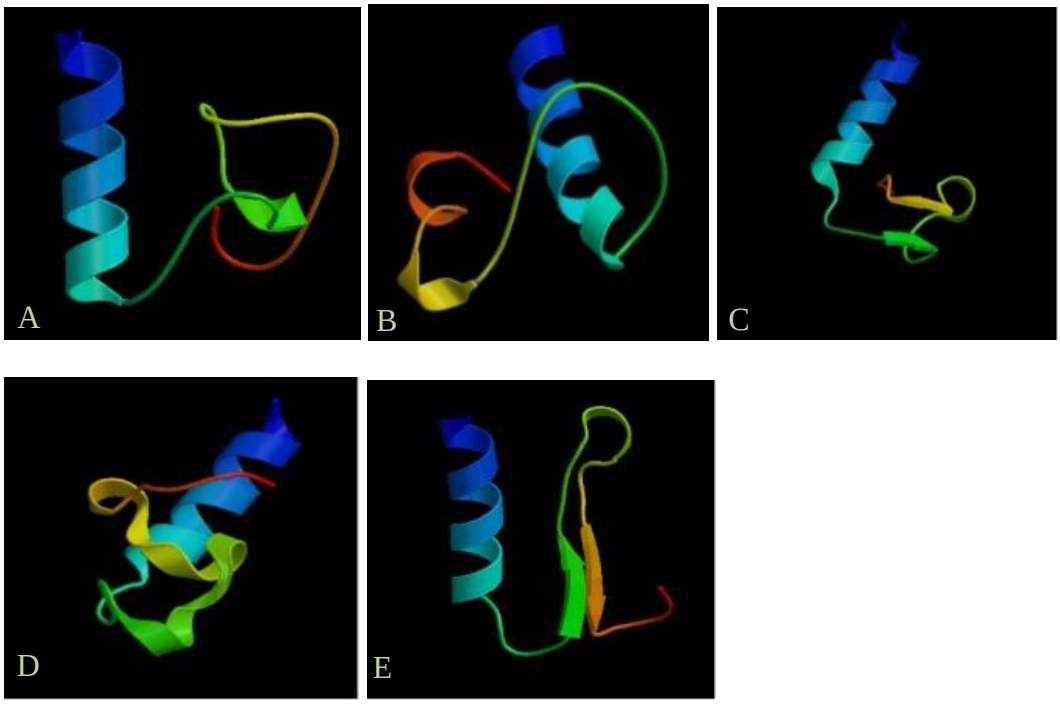

Figure 15.3 (A), (B), (C), (D), and (E) 3D secondary structure predictions of Macaque-STN41 using Robetta software.

Figure 15.3 shows the secondary structural predictions of Macaque-STN41 using Robetta software. All five predictions showed an α-helix structure at the N-terminal before residue 21. The differences in predictions are mainly after amino acid 21.

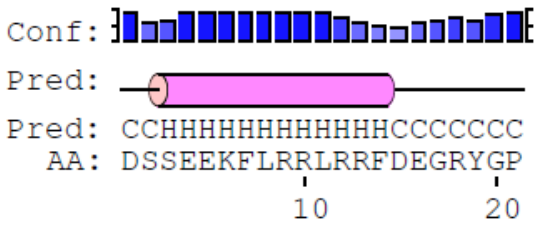

Figure 15.4 Secondary structure predictions of the Macaque-STN21 result by PSIPRED software.

Figure 15.4 shows secondary structure prediction result for Macaque-STN21 using the PSIPRED software, showing an α-helix secondary structure between S3-F14.

○	○	○	○	○	○	●	●	○	○	●	●	○	●	●	○	●	○	●	●	○	
1	2	3	4	5	6	7	8	9	10	11	12	13	14	15	16	17	18	19	20	21	Homo sapiens STN21
D	pS	pS	E	E	K	F	L	R	R	I	G	R	F	G	Y	G	Y	G	P	Y	
○	○	○	○	○	○	●	●	○	○	●	○	○	●	○	○	●	○	○	●	●	
1	2	3	4	5	6	7	8	9	10	11	12	13	14	15	16	17	18	19	20	21	Macaca arctoides STN21
D	pS	pS	E	E	K	F	L	R	R	L	R	R	F	D	E	G	R	Y	G	P	

Figure 15.5 Amino acid sequences for human and Macaque-STN21, showing polar (○) and non-polar (●) residues.

Comparison of human STN21 and Macaque-STN21 using the hydropathicity of amino acids and the alternation of polar and non-polar amino acids as shown in Figure 15.5, shows that the first ten residues are identical. The substitution at I11 to L11 in Macaque-STN21 is not significant structurally. The G12 to R12 substitution should increase helix forming potential in Maqcaque-21. The G15 to D15 replacement and Y16 to E16 introduce acidic amino acids, resulting in a possible salt bridge between R12-D15 and R12-E16. This suggests a N-terminal α-helix length from S3-E16, similar to the secondary structure prediction result for Macaque-STN21 using the PSIPRED software as shown in Figure 15.4.

15.3.3.2 Structural Prediction for Pig-STN

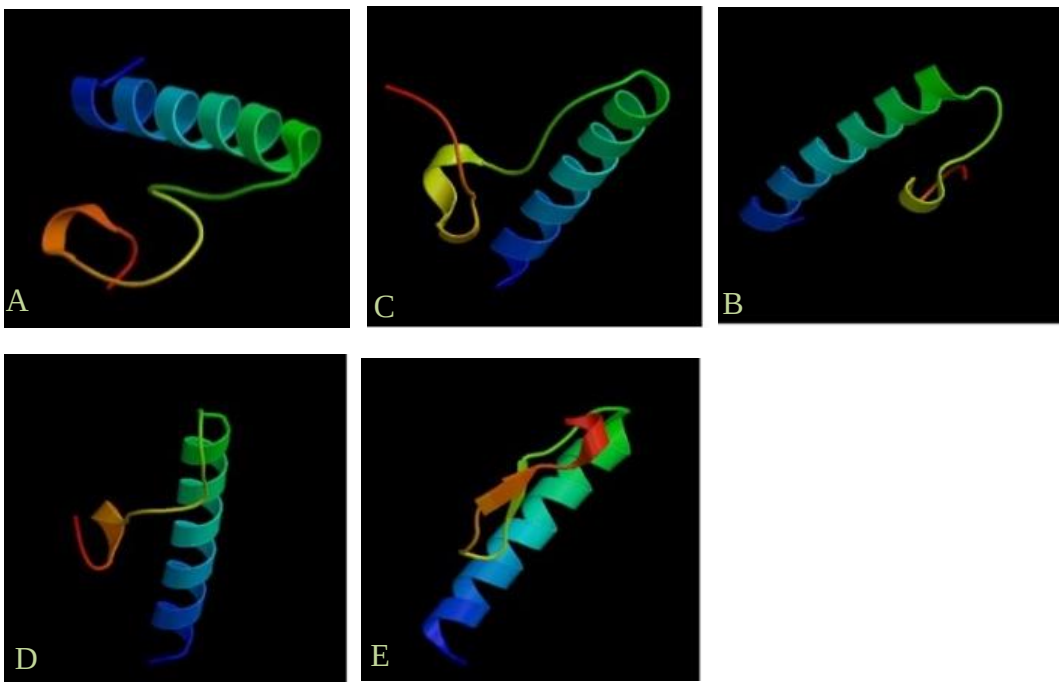

Figure 15.6 (A), (B), (C), (D), and (E) 3D secondary structure predictions of Pig-STN42 using Robetta software.

Figure 15.6 shows the secondary structural predictions of Pig-STN42 using Robetta software. All predictions showed an α-helix structure at the N-terminal, the difference in prediction is mainly in the sequence after the amino acid 21 and again these representations differ and are unlikely to exist in any permanent way.

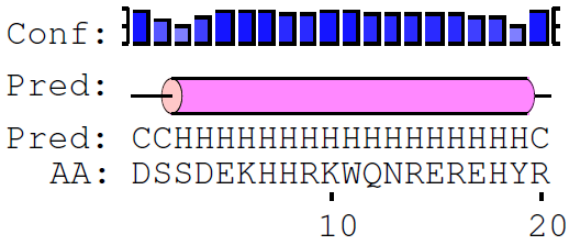

Figure 15.7 Secondary structure predictions of Pig-STN21 using PSIPRED software.

Figure 15.7 shows the secondary structure prediction result for Pig-STN21 using PSIPRED software showing a long possible α-helix secondary structure between S3-Y20.

When the human STN21 sequence is compared with the Pig-STN21 the dissimilarity is more extreme than with other non-human peptides except the Sheep-STN21, as shown in Figure 15.8. There is no F residue in the sequence and it is highly hydrophilic. The Pig-STN21 contains one W and Y, both of which are hydrophilic, but no proline at all.

○	○	○	○	○	○	●	●	○	○	●	●	○	●	●	○	●	○	●	●	○	
1	2	3	4	5	6	7	8	9	10	11	12	13	14	15	16	17	18	19	20	21	Homo sapiens STN21
D	pS	pS	E	E	K	F	L	R	R	I	G	R	F	G	Y	G	Y	G	P	Y	
○	○	○	○	○	○	○	○	○	○	●	○	○	○	○	○	○	○	○	●	○	
1	**2**	**3**	**4**	**5**	**6**	**7**	**8**	**9**	**10**	**11**	**12**	**13**	**14**	**15**	**16**	**17**	**18**	**19**	**20**	**21**	**Sus scrofa STN21**
D	pS	pS	D	E	K	H	H	R	K	W	Q	N	R	E	R	E	H	Y	G	R	

Figure 15.8 Amino acid sequences for human and Pig-STN21 sequences, showing polar (○) and non-polar (●) residues.

Figure 15.8 shows a comparison of human and Pig-STN21 sequences. The first six residues are virtually identical. After residue six only two positions, 9 and 10, have an identity or near identity. The E4 to D4 substitution is a minimal change of like for like. The F7 and L8, two hydrophobic non-polar residues, are replaced by hydrophilic polar H. The R10 to K10 substitution is not significant because they are both similar. The residues I11 and W11 in the two sequences are (hydrophobic, I) in the human but (hydrophilic, W) in the pig. Significantly, three G in the human sequence are substituted by G12 to Q12, G15 to E15 and G17 to E17. Those changes will reduce the flexibility of the pig sequence and tend to

increase the length of the helix. The R14 to E17 in the pig sequence might give a salt bridge in a helical structure. Therefore, the whole helix would extend from S3-E17, similar the secondary structure prediction using the PSIPRED software.

15.3.3.3 Structural Prediction for Sheep-STN37

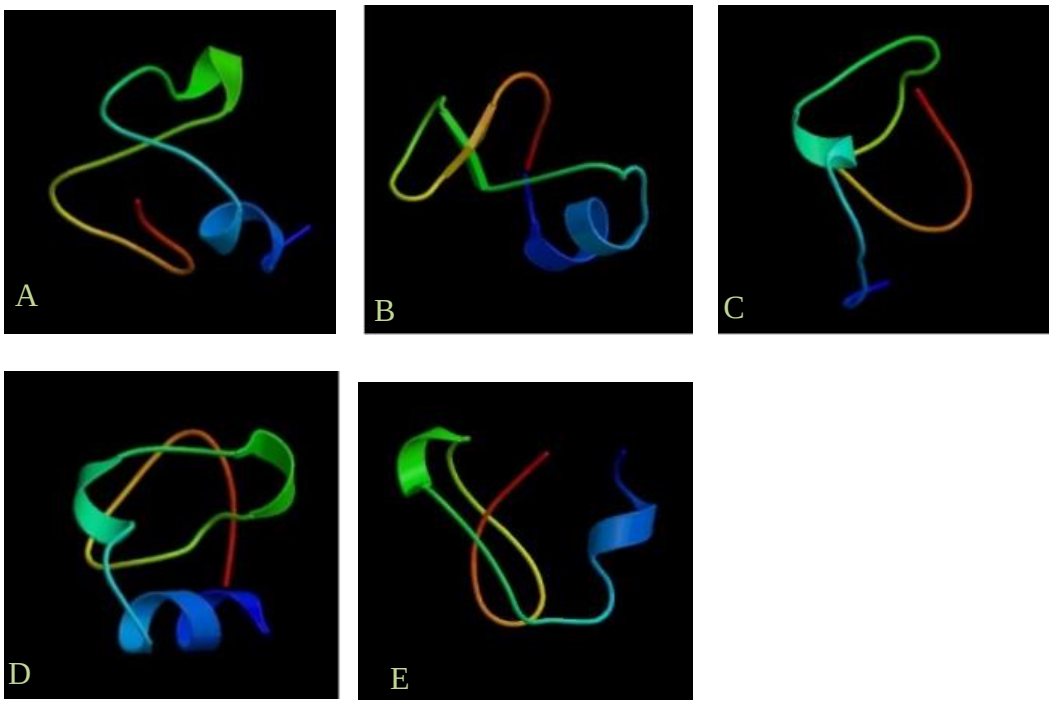

Figure 15.9 (A), (B), (C), (D), and (E) 3D secondary structure predictions of Sheep-STN37 using Robetta software.

Figure 15.9 shows 3D secondary structure predictions of Sheep-STN37 using Robetta. The helix revealed at the N-terminus is the shortest found in all the mammalian peptides tested. A helix only appears in four of the five representations. Again, the possibilities for secondary structure outside the 21-mer seem unlikely to persist.

Figure 15.10 Secondary structure prediction result for Sheep-STN21 using PSIPRED software.

Figure 15.10 shows secondary structure prediction result for Sheep-STN21 using PSIPRED software showing an α-helix secondary structure between S3-R7. This is only one turn of an α-helix and is unlikely to be stable. A critical factor in terminating the helix is the P10 (rigidity of structure) (Pace and Scholtz, 1998).

○	○	○	○	○	○	●	●	○	○	●	●	○	●	●	○	●	○	●	●	○
1	2	3	4	5	6	7	8	9	10	11	12	13	14	15	16	17	18	19	20	21
D	pS	pS	E	E	K	F	L	R	R	I	G	R	F	G	Y	G	Y	G	P	Y
○	○	○	○	○	●	○	○	●	●	●	●	○	○	○	●	○	●	○	●	●
1	2	3	4	5	6	7	8	9	10	11	12	13	14	15	16	17	18	19	20	21
D	pS	pS	E	E	V	R	H	F	P	S	L	E	K	R	P	Y	P	I	Q	Q

Homo sapiens STN21

Ovis aries STN21

Figure 15.11 Amino acid sequences for human and Sheep-STN21 sequences, showing polar (○) and non-polar (●) residues.

Figure 15.11 shows a comparison of human and Sheep-STN21. The first five residues are identical to Human STN. The K6 to V6 is replacing hydrophilic polar with hydrophobic non-polar residue. The F7 and L8 hydrophobic non-polar residues are replaced by hydrophilic polar R7 and H8 in Sheep-STN21. There is a potential salt bridge from E4 to R7, E5 to H8 in Sheep-STN21. Two hydrophilic polar R9 and R10 are replaced by hydrophobic non-polar F9 and low hydrophilic non-polar P10 which is also a helix breaker in the Sheep-STN21 sequence. A hydrophobic link might

give rise to a helix from V6 to F9 in the Sheep-STN21 sequence, but the one from F9 to L12 may be disturbed by P10. Three prolines present at position 10, 16, and 18 in the Sheep-STN21 will decrease the helix possibility of the sheep sequence. If a helix did exist, it might extend from S3-F9 at the N-terminal, which is indicated in the secondary structure prediction using the PSIPRED software.

15.3.3.4 Structural Prediction for Cattle-STN40

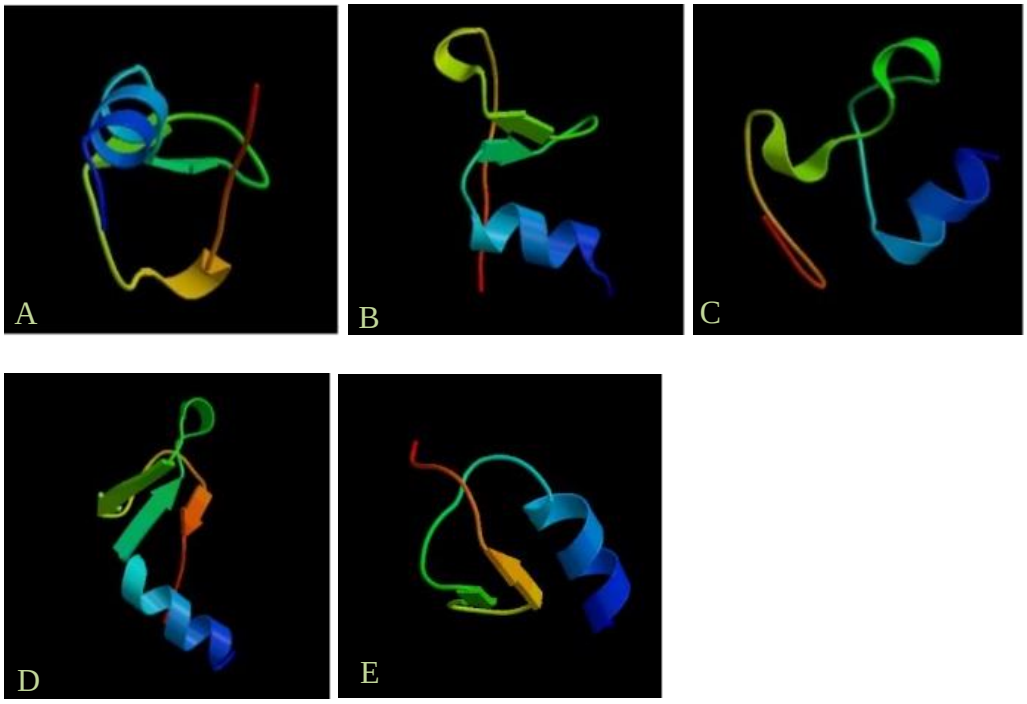

Figure 15.12 (A), (B), (C), (D), and (E) 3D secondary structure predictions of Cattle-STN40 using Robetta software.

Figure 15.12 shows secondary structural predictions of Cattle-STN40 using Robetta software. All predictions showed an α-helix structure at the N-terminus. The differences in prediction are mainly in the sequence after residue 21.

Figure 15.13 Secondary structure prediction of Cattle-STN21 using PSIPRED software.

Figure 15.13 shows the secondary structure prediction result for the Cattle-STN21 using the PSIPRED software showing an α-helix secondary structure from S3 to R10, while the rest of the sequence is unordered.

Human STN21 has little identity with Cattle-STN21 as shown in Figure 15.14.

○	○	○	○	○	○	●	●	○	○	●	●	○	●	●	○	●	○	●	●	○	
1	2	3	4	5	6	7	8	9	10	11	12	13	14	15	16	17	18	19	20	21	Homo sapiens STN21
D	pS	pS	E	E	K	F	L	R	R	I	G	R	F	G	Y	G	Y	G	P	Y	
○	○	○	○	○	○	○	○	●	○	●	○	●	○	●	○	○	●	○	○	○	
1	2	3	4	5	6	7	8	9	10	11	12	13	14	15	16	17	18	19	20	21	Bos taurus STN21
D	pS	pS	E	E	E	H	R	L	R	F	N	P	R	F	Y	Y	P	N	Q	Q	

Figure 15.14 Amino acid sequence for human and Cattle-STN21 sequences, showing polar (○) and non-polar (●) residues.

Figure 15.14 shows a comparison of human and Cattle-STN21. The sequences differ from the human STN21 from E6 to Q21 except for R10 and Y16. Similarities include the occurrence of L and R in the two sequences at position 8 and 9, although in reverse order. An R14 in Cattle-STN21 rather than R13 in human STN21 and the Y17 rather than Y16 are identical in the sequence but one residue displaced. If salt bridges contribute to helix formation in Cattle-STN21, they could be between E4

and H7 and E5 and R8. Probably significant is the loss of all four G residues which are replaced by N12, F15, Y17 and N19 in the cattle sequence. These changes would decrease the flexibility in the cattle sequence compared to human and promote helix formation. Despite this, the helix breaking P13 might limit the helix sequence to S3-R10 in the cattle sequence, as suggested by in the secondary structure prediction using the PSIPRED software.

15.4 Discussion

In this study, the MAPA values for human STN, Macaque-STN21, and Pig-STN21 were not statistically different and had an equal effect on demineralisation reduction. Raj *et al.,* (1992) suggested that the N-terminal amino acid sequence of human STN is responsible for HA adsorption through electrostatic interaction. The presence of 5 acidic amino acids, 2 of which are phosphorylated at the N-terminal of human STN, Macaque-STN21 and Pig-STN21, as shown in Figure 15.5 and 15.8, creates an equal adsorption affinity to HA. Also, the predicted conformation of the N-terminal is an α-helical structure in STN21, Macaque-STN21 and Pig-STN21. This might allow the helical structure of the adsorbing peptide to match with the HA mineral lattice, further stabilising the adsorbing peptide onto HA, as previously suggested by Raj *et al.,* (1992) and hence reduces the demineralisation rates to an equal extent for each peptide.

Pig-STN21 has D at position 4 instead of E, as shown in Figure 15.8. Tavafoghi, and Cerruti, (2016), suggested that HA surface coverage ability

by an adsorbed amino acid depends on the amino acid side chains extension. The side chain of aspartic acid (D) is shorter than that of glutamic acid (E), and therefore, E can cover a larger fraction of HA surface than the D. However, the substitution of E4 with D4 in Pig-STN21 does not affect the adsorption amount to HA nor the demineralisation reduction efficacy, which suggests that the surface coverage ability of the D and E residue is not important in HA surfaces interaction.

In this study, Sheep-STN21 had the least adsorption amount, and, was the least effective in demineralisation reduction. Although human STN21, Sheep-STN21, Macaque-STN21, and Pig-STN21 all have similar number of acidic residues at the N-terminal, the predicted short helix at the N-terminal of Sheep-STN21, as shown in Figure 15.10, compared to the other peptides, may affect (reduce) the structural stability of the helix while adsorbing onto HA. This would suggest that the demineralisation reduction efficacy maybe also reduced.

Whereas the Cattle-STN21 adsorbed onto HA the most and was also the most effective in demineralisation reduction. Although the α-helix was not the longest, the additional acidic residue E6 in Cattle-STN21 N-terminal α-helix maybe the explanation for the high adsorption and therefore higher demineralisation reduction. Such an importance of an extra acidic amino acid for the optimum adsorption of STN onto HA was suggested by Raj *et al.,* (1992).

Also, Cattle-STN21 had faster rates of binding than STN21, Macaque-STN21, Pig-STN21, and Sheep-STN21. As previously discussed in Chapter 11, the rate of binding of STN and HTN are dependent on the

highly negative motif at the N-terminus (Lamkin *et al.,* 1996). The additional negatively charged amino acid (E6) in Cattle-STN21 may cause this faster rate of binding.

Figure 15.15 shows the correlation of the MAPA of the non-human STN21 peptides with the MPRRML.

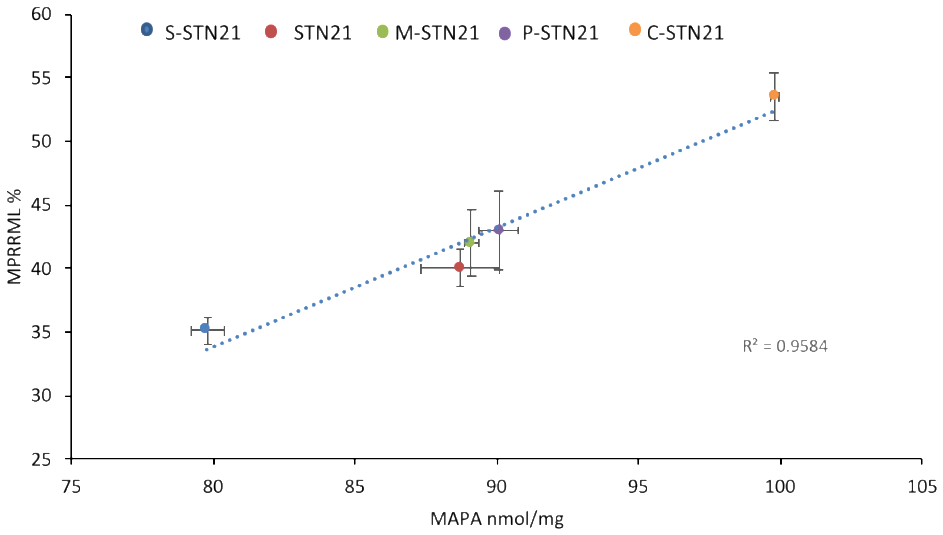

Figure 15.15 Correlation of adsorption (MAPA) of STN21, Sheep-STN21, Macacaque-STN21, Pig-STN21 and Cattle-STN21 Individually 200 µmol/l onto HA beads with the effect on the rate of demineralisation (MPRRML).

This shows a positive linear correlation between the demineralisation reduction efficacy and the amount of peptide adsorbed. Sheep-STN21 had the least adsorption and had the least demineralisation reduction efficacy. Human STN21, Macaque-STN21, and Pig-STN21 had similar adsorption amounts and showed similar demineralisation reduction efficacy. The Cattle-STN21 had the highest amount of peptide adsorbed and the highest demineralisation reduction efficacy.

The observed correlation between the amounts of peptides adsorbed and the demineralisation reduction is similar to that seen in human peptides shown in Section 14.1, Figure 14.1.

Figure 15.16 shows the correlation of the $T_{0.5}$ with the MPRRML of human and non-human STN21 at 200 µmol/l for HA.

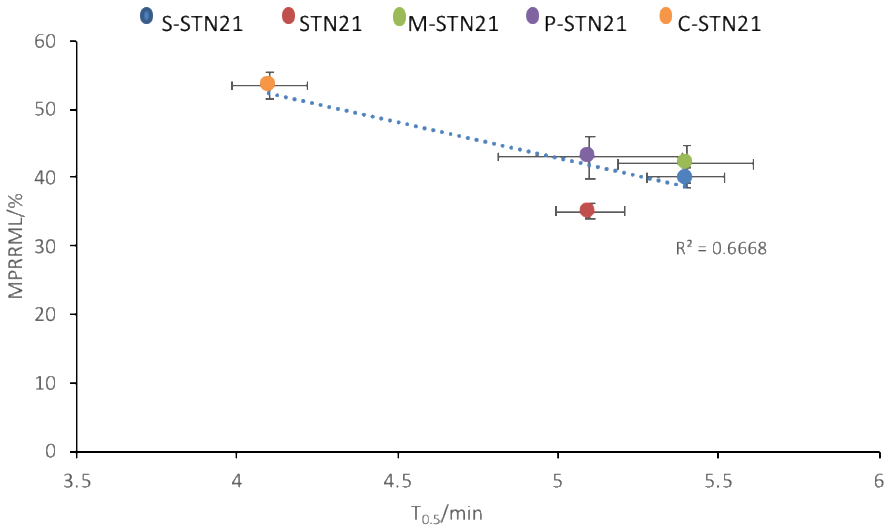

Figure 15.16 Correlation of the $T_{0.5}$ of human and non-human STN21 at 200 µmol/l onto HA with the effect on the rate of demineralisation (MPRRML).

Figure 14.2 shows that there is no correlation between the rate of binding and the demineralisation reduction observed in HA samples. The observed correlation between the rate of binding of non-human peptides and demineralisation reduction is similar to the seen in human peptides shown in Section 14.1 Figure 14.2.

Even though cattle enamel is used as an analogue for human enamel studies (Oesterle *et al.,* 1998; De Oliveira *et al.,* 2017), this current study specifically investigated the molecular interaction of the peptide with HA surfaces and the effect on adsorption and demineralisation reduction.

This investigation was not meant to compare STN with diet and dentition, although this could be part of future studies.

15.5 Conclusions

- The effect of peptides on demineralisation reduction of HA is dependent on the amounts of peptide adsorbed. However, demineralisation reduction does not depend on the rate of binding.

- The adsorption affinity to HA shown by the MAPA, and the binding rates, and demineralisation reduction depend on the density of the acidic residues at the N-terminus that provide the electrostatic interaction with the HA surface. The cattle peptide, that is most effective, has one more acidic residue than the others.

- Although the Sheep-STN21 has an acidic N-terminus identical to those of all peptides except the Cattle-STN21 it is the least effective in adsorption and demineralisation reduction. That may well be caused by its shorter helix, which only includes 5 amino acids residues.

- The original speculation was that the amino acid sequences of this set of STNs might cause different effects. This is not true for three of them: namely the human, macaque, and pig. The properties of the Pig-STN21 show that similar results can come from different sequences although the pattern of acidic amino acids is closely similar in human and the macaque. For the sheep variant, the feature that causes the difference from the other three is not as clear. It seems that further work could selectively modify sheep STN. That might throw light on the reasons for its effect being lesser

than the human, macaque, pig, and cattle. Substitution of amino acids between residue nine and fifteen might produce an extended helix. Its adsorption and its effect on demineralisation would be of interest.

Chapter 16. Conclusions, Clinical Implications and Future Work

16.1 Conclusions

- There is a co-operative efficacy in adsorption and in demineralisation reduction when STN, HTN, STN21, and HN21 are present in combination. This cooperativity is further improved by the removal of the C-terminal.

- Salivary peptide like STN and HTN are important for oral health. By engineering novel peptides with diverse amino acid sequences and testing those for adsorption to HA and demineralisation reduction, the understanding of the requirements for interaction between peptides and mineral surfaces maybe improved.

- The ability of STN, HTN, STN21, and HTN21 to reduce HA and enamel demineralisation in vitro caries simulating condition was demonstrated using SMR.

- The 21 N-terminus of STN (STN21) and HTN (HTN21), reduces the demineralisation of enamel as effectively as the full-length peptides.

- The degree to which demineralisation is reduced by individual peptides depends on the density of the N-terminal negative charges (number of negatively charged residues) and the amount of peptide adsorbed. However, demineralisation reduction does not depend on the rate of binding.

- The mechanism by which peptides individually and in combination adsorb and hence reduce the rate of demineralisation is complex. It involves peptides secondary structure conformation, surface charge, peptide concentration and the aggregation of peptides in solution which might later influence their adsorption characteristics.

- The importance of α-helical conformation in the matching of acidic side chain residues with HA surfaces is further confirmed in this study. The reduction of the N-terminal α-helical length as seen in Sheep-STN21 effect peptide adsorption onto HA surfaces and therefore reduces the demineralisation reduction efficacy.

- The difference in the adsorption and demineralisation reduction results of peptides for HA and enamel challenges the chemical and structural suitability of hydroxyapatite as an analogue system for enamel in sophisticated demineralisation and adsorption studies.

16.2 Clinical Implications

The prevention and management of caries lesion is an ongoing challenge in dentistry. Currently, caries preventive measures focus mainly on delivering fluoride in order to reduce enamel demineralisation as

fluorapatite is less soluble than HA. However, the results of this study suggest that peptides such as STN, HTN, STN21 and HTN21 individually and combined have protective qualities that reduce demineralisation rates.

Xerostomia or dry mouth syndrome is the reduction of salivary flow or changes in salivary composition. Salivary duct obstruction, medications (e.g. Doxepin, Prazosin), cancer therapy such as radiation therapy that involve salivary glands or chemotherapy and ageing can be causative factors. Dry month syndrome could also have an unidentifiable cause (Sjogren syndrome). The complication of developing dry mouth syndrome is that there would be an increase in tooth decay and yeast infection among other health complication. The treatment would depend on the cause, such as the removal of the salivary duct obstruction, and changing the causative medication, or in the cases of severe dry mouth the prescription of medication that stimulate salivary secretion such pilocarpine. Another treatment option would be the use of palliative measures such as salivary substitute of neutral pH and containing ions (including calcium, fluoride) to correspond approximately to the composition of saliva. The acidic pH of some artificial saliva products is proved to be damaging to the tooth surface (Kielbassa *et al.*, 2001). These options do not concede the application of proteins. From this study, STN21 when in combination with HTN21 showed higher demineralisation reduction efficacy compared to full-length peptides. Treatment options using STN21 and HTN21 is more concise and targeted. Therefore, modification of existing saliva substitution containing surface active polymers such as STN21 and HTN21 in combination could be beneficial in the reduction of demineralisation.

The biomimetic method aims to develop nano-biomaterials that can be used in different products to promote oral health care. Tooth Mousse (Recaldent™) is a product that can help in the reduction of demineralisation. This product contains milk protein, casein, which was proven to have demineralisation protective effect (Reynolds et al., 1999). The casein protein contains Casein Phosphopeptide (CPP). The CPP binds to forming clusters of amorphous calcium phosphate (ACP) in the AEP. Therefore, maintaining an environment that is supersaturated with respect to tooth enamel, which decreases demineralisation (Reynolds, 1998). Similar to ACP, STN contains the phosphorylated sequence needed for the affinity for calcium phosphate. Consequently, incorporating STN and HTN peptides in combination into topical treatments such as dentifrices, varnishes and mouthwashes could offer an alternative protective product. Although further work needs to be done to assess their stability within the media they are delivered in.

16.3 Future Work

Chapter 11: To investigate the adsorption affinity of HTN, and HTN21 individually onto different HA crystal faces which will enable the correlation of their amount bound with the observed function. This will further help in the understanding of the co-operative and competitive adsorption of peptides when in combination.

Additionally, the dynamics of adsorption of peptides onto HA and enamel needs to be further investigated in terms of adsorption as a

monolayer or multilayer which could contribute to the demineralisation reduction efficacy of the peptides. An effort was made to measure the kinetics of peptides adsorption onto HA using quartz crystal microbalance (QCM), and ellipsometry, however, due to the instability of the HA substrate, the reproducibility was affected and therefore peptide adsorption (as layers) could not be measured accurately.

The time period that the HA beads were exposed to acetic acid or 2 M NaCl might not be long enough for desorption to occur. future work should be done on peptide desorption using different exposure times and if possible in different conditions where dynamic movement of the desorbing solution occurs to better mimic the oral environment.

Chapter 12: Individual peptides net charges decreased when they aggregated at 200 µmol/l compared to 100 µmol/l. The critical point where aggregation occur needs to be investigated, also further investigation on the effect of particle size (aggregation) on the net charge is needed. The suggested method is to measure the net charges of the peptide at different ranges of concentration in solution and correlate them with particle size (aggregation) changes.

CD spectroscopy is a fast method for assessing the secondary structure of proteins, however, the spectral range where the peptide secondary structure was tested at is unable to give detailed information about the tertiary structures, therefore measurement of tertiary structures near-UV light for the peptides should be done.

Campbell *et al.,* (1989) suggested that peptides go through structural conformation upon adsorption, which could affect their function. Therefore,

to further understand the contribution of these structural changes on the observed demineralisation reduction of peptides individually and in combination, a comparison between the secondary structure of peptides in solution (CD results) with NMR study of peptides structural conformation upon adsorption is important.

There is a need to further investigate the interaction of STN and HTN in solution that gives rise to aggregates, which have similarities with supramolecular pellicle precursors observed by (Vitkov *et al.,* 2004). A technique such as Surface Plasmon Resonance can be used for identifying molecular interactions by binding of a mobile molecule to a molecule immobilized on a thin metal film (Schuck, 1997). Additionally, NMR could help also in the verification of the amount of each peptide present in an aggregating unit when in combination. This could be achieved by labelling each peptide with different tags. In addition, the use of SRCD could provide novel information on the kinetics folding and unfolding nature of protein macromolecular interactions (Clarke *et al.,* 1999; Chang *et al.,* 1999).

Chapter 13: The focus of this thesis was to measure and compare the effect of salivary STN and HTN (known to have an affinity to HA) individually and in combination on the demineralisation rates of enamel and HA. The period of HA and enamel exposure with peptides presented in this study was 24 hrs. it was reported that HTN concentration is affected by diurnal variations, while STN concentration does not change (Hardt *et al.,* 2005), therefore to better mimic the oral environment, demineralisation of enamel and HA study through the exposure to peptide at various time points would give a better representation of what is happening *in vivo*. Additionally,

repeating the experiments with different de/remineralisation conditions would provide more information about the biological function of peptides in different settings.

Also, investigation of the effect of STN, HTN on the kinetics of demineralisation using other techniques would be useful in comparing the results (e.g. AFM, surface micro-hardness (SMH).

References

Amano A, Kataoka K, Raj PA, Genco RJ, Shizukuishi S. 1996. Binding sites of salivary statherin for Porphyromonas gingivalis recombinant fimbrillin. Infect. Immun. 64:4249–4254.

Amin S, Barnett GV, Pathak JA, Roberts CJ, Sarangapani PS. 2014. Protein aggregation, particle formation, characterization and rheology. Curr. Opin. Colloid Interface Sci. 19, 438–449.

Anderson NH, Liu Z, Prickett KS. 1996b. Efforts toward deriving the CD spectrum of a 3_{10} helix in aqueous medium. FEBS Lett. 399, 47.

Anderson P, Bollet-Quivogne FRG, Dowker SEP, Elliott JC. 2004. Demineralization in enamel and hydroxyapatite aggregates at increasing ionic strengths. Archives of Oral Biology (49), 3:199–207

Anderson P, Elliott JC, Bose U, Jones SJ. 1996a. A Comparison of the Mineral Content of Enamel and Dentine in Human Premolars and Enamel Pearls Measured by X-Ray Microtomography. Archives of Oral Biology, 41: 281-290.

Anderson P, Elliott JC, Dowker SEP, Bollet-Quivogne F. 2003. “Scanning Microradiography, a digital 2D X-Ray Imagining Techinque” G.I.T. Imaging & Microscopy 02: 22-24.

Anderson P, Elliott JC. 2000. Rates of mineral loss in human enamel during in vitro demineralization perpendicular and parallel to the natural surface. Caries Res. 34:33–40.

Anderson P, Hector MP, Rampersad MA. 2001. Critical pH in resting and stimulated whole saliva in groups of children and adults, Int J Paed Dent, 11: 266-273.

Aoba T, Moreno EC, Hay DI. 1984. Inhibition of apatite crystal growth by the amino-terminal segment of human salivary acidic proline-rich proteins, Calcif Tissue Int, 36(6):651-8.

Aoba T. 2004. Solubility properties of human tooth mineral and pathogenesis of dental caries, Ora. Dis, volume10, page 249-257.

Arends J, Jongebloed WL. 1979. Ultrastructural Studies of Synthetic Apatite Crystals. Journal of Dental Research, 58, 837-843.

Armougom F, Moretti S, Keduas V, Notredame C. 2006. The iRMSD: a local measure of sequence alignment accuracy using structural information. Bioinformatics. 22 (14): e35–39.

Azen EA. 1978. Genetic protein polymorphisms in human saliva: an interpretive review. Biochem Genet 16:79-99.

Bakaletz LO. 2004. Developing animal models for polymicrobial diseases. Nature Reviews Microbiology. 2, 552-568.

Ball V, Ramsden JJ. 2000. Analysis of hen egg white lysozyme adsorption on Si(Ti)O_2|aqueous solution interfaces at low ionic strength: a biphasic reaction related to solution self-association. Colloids Surf. B 17:81–94.

Barnes MJ, Knight CG, Farndale RW. 1996. The use of collagen-based model peptides to investigate platelet-reactive sequences in collagen. Biopolymers 1996; 40: 383–97.

Barsukov I, Lian L-Y. 1993. Structure determination from NMR data: I analysis of NMR data. In NMR of macromolecules: a practical approach. Edited by G. Roberts. Oxford University Press, New York. pp. 315–357.

Bartlett JD. 2013. Dental Enamel Development: Proteinases and Their Enamel Matrix Substrates. ISRN Dentistry, 684607.

Baum JB. 1993. Principles of Saliva Secretion, in Saliva as a diagnostic fluid, Annals of the New York Academy of Sciences, vol 694, pp 17-23, (eds. Malamud D, and Tabak L), New York.

Belford HS, Triffleman EG, Offner GD, Troxler RF, Oppenheim FG. 1984. Biosynthesis of salivary proteins in the parotid gland of the subhuman primate, Macaca fascicularis. Cell-free translation of the mRNA for a proline-rich glycoprotein and partial amino acid sequence and processing of its signal peptide. J Biol Chem. Mar 25;259(6):3977–3984.

Bengtsson Å, Shchukarev A, Persson P, Sjöberg S. 2009. A solubility and surface complexation study of a non-stoichiometric hydroxyapatite. Geochim Cosmochim Acta; 73: 257-267.

Bennick A, Cannon M, Madapallimattam G. 1979. The nature of the hydroxyapatite-binding site in salivary acidic proline-rich proteins, Biochem J, 1;183(1):115-26.

Benning K. 2014. CD Apps documentation. Available at: http://confluence.diamond.ac.uk/display/B23Tech/CD+Apps+documentation.

Berg JM, Tymoczko JL, Stryer L. 2002. Protein Structure and Function. In Biochemistry. 5th edition. New York: W H Freeman.

Berkovitz BKB, Moxham BJ, Linden RWA, Sloan AJ. 2010. Master Dentistry Volume 3 Oral Biology: Oral Anatomy, Histology, Physiology, Churchill Livingstone. Biomolecules, Springer, Berlin.

Berne BJ, Pecora R. 2000. Dynamic Light Scattering: with Applications to Chemistry, Biology, and Physics. Courier Dover Publications.

Boyde A. 1997. Microstructure of Enamel, in Dental Enamel-Proceedings of the Symposium on Dental Enamel, held at the Ciba Foundation, (eds. D. Chadwick and G. Cardew), pp 18-32, John Wiley&Sons Ltd, Chichester, England.

Bradley LH, Thumfort PP, Hecht MH. 2006. De novo proteins from binary-patterned combinatorial libraries. Methods Mol Biol 340:53–69.

Brahim K, Antar K, Khattech I, Jemal M. 2008. Effect of temperature on the attack of fluorapatite by a phosphoric acid solution. Scientific Research and Essays; 3: 035-039.

Bremer M, Duval J, Norde W, Lyklema J. 2004. Electrostatic interactions between immunoglobulin (IgG) molecules and a charged sorbent. J. Colloids and Surfaces, A: Physicochemical and Engineering Aspects, 250, 29-42.

Brewer D, Hunter H, Lajoie G. 1998. NMR Studies of the Antimicrobial Salivary Peptides Histatin 3 and Histatin 5 in Aqueous and Nonaqueous Solutions. Biochem Cell Biol.76:247–256.

Brown PW, Martin RI. 1999. An analysis of hydroxyapatite surface layer formation. J Phys Chem B; 103: 1671-1675.

Brummitt RK, Nesta DP, Chang L, Kroetsch AM, Roberts CJ. 2011. Nonnative aggregation of an igg1 antibody in acidic conditions, part 2: nucleation and growth kinetics with competing growth mechanisms. J Pharm Sci, 100 (6), pp. 2104-2119.

Brynda E, Hlady V, Andrade JD. 1990. Protein packing in adsorbed layers studied by excitation energy transfer. J. Coll. Int. Sci. 139, 374-380.

Buchan DWA, Minneci F, Nugent TCO, Bryson K, Jones DT. 2013. Scalable web services for the PSIPRED Protein Analysis Workbench. Nucleic Acids Research.41(W1): W340-W348. (http://bioinf.cs.ucl.ac.uk/introduction/). Accessed July. 10. 2016.

Cabras T, Inzitari R, Fanali C, et al. 2006. HPLC-MS characterization of cyclo-statherin Q-37, a specific cyclization product of human salivary statherin generated by transglutaminase 2. J Sep Sci.29:2600-8.

Calero M, Gasset M. 2005. Fourier Transform Infrared and Circular Dichroism Spectroscopies for Amyloid Studies," in Amyloid Proteins (New Jersey: Humana Press), 129–152.

Campbell AA, Ebrahimpour A, Perez L, Smesko SA, Nancollas GH. 1989. The dual role of polyelectrolytes and proteins as mineralization promoters and inhibitors of calcium oxalate monohydrate, Calcif Tissue Int, 45.

Cannon RD, Nand AK, Jenkinson HF. 1995. Adherence of Candida albicans to human salivary components adsorbed to hydroxyapatite. Microbiology 141, 213-219.

Carneiro LG, Nouh H, Salih E. 2014. Quantitative Gingival Crevicular Fluid Proteome in Health and Periodontal Disease Using Stable Isotope Chemistries and Mass Spectrometry. J. Clin. Periodontol.018448.

Carpenter G, Cotroneo E, Moazzez R, Rojas-Serrano M, Donaldson N, Austin R, Zaidel L, Bartlett D, Proctor G. 2014. Composition of enamel pellicle from dental erosion patients. Caries Res 48: 361–367.

Chang JF, Phillips K, Lundback T, Gstaiger M, Ladbury JE, Luisi B. 1999. Oct-1 POU and octamer DNA co-operate to recognise the Bob-1 transcription co-activator via induced folding. J Mol Biol, 288 :941-952.

Chatelier RC, Minton AP. 1996. Adsorption of globular proteins on locally planar surfaces: models for the effect of excluded surface area and aggregation of adsorbed protein on adsorption equilibria. Biophys J.;71(5):2367–2374.

Chen H, Banaszak Holl M, Orr BG, Majoros I, and Clarkson BH. 2003. Interaction of dendrimers (artificial proteins) with biological hydroxyapatite crystals, J Dent Res, 82(6):443-8.

Chin KOA, Johnsson M, Bergey EJ, Nancollas GH.1993. A constant composition kinetics study of the influence of salivary cystatins, statherin, amylase and human serum albumin on hydroxyapatite demineralisation, Colloids Surfaces A, 78, 229-34.

Chivian D, Kim DE, Malmstrom L, Bradley P, Robertson T, Murphy P. et al. 2003. Automated prediction of CASP-5 structures using the Robetta server. Proteins, 53 (Suppl. 6), 524–533.

Chou PY, Fasman GD. 1974. Conformational parameters for amino acids in helical, β-sheet, and random coil regions calculated from proteins. Biochemistry, 13 (2), 211-222.

Chu C, Pang K, LO E. 2010. Dietary behaviour and knowledge of dental erosion among Chinese adults; BMC Oral Health, 10, 13.

Clarke DT, Doig AJ, Stapeley BJ, Jones, GR. 1999. The alpha-helix folds on a millisecond time scale. Proc Natl Acad Sci USA, 96 :7232-7237.

Cole AS, Eastoe JE. 1988a. Plaque metabolism and dental disease, in Biochemisty and Oral biology 2nd ed. pp 502-520, Wright, Bristol.

Cole AS, Eastoe JE. 1988b. The oral environment, in Biochemistry and Oral biology 2nd ed. pp 475-490, Wright, Bristol.

Cole C, Barber JD, Barton GJ. 2008. The Jpred 3 secondary structure prediction server. Nucleic Acids Res. 36 (Web server issue): W197–W201.

Correa DHA, Ramos CHI. 2009. The use of circular dichroism spectroscopy to study protein folding, form and function. Afr J Biochem Res. 3:164–173.

Cossu M, Isola M, Solinas P, De Lisa A, Massa D, Lantini MS. 2011. Immunoreactivity of the Salivary Protein Statherin in Human Male Accessory Sex Glands. Prostate, 71 (6), pp.671 :674.

Creagh DC, Hubbell JH. 1992. X-Ray Absorption (or Attenuation) Coefficients, Sec. 4.2.4. In: Wilson AJC. (ed.) International Tables for Crystallography. Kluwer Academic Publishers,Dordrecht.

Dawes C, Pedersen AM, Villa A, Ekstrom J, Proctor GB, Vissink A, et al. 2015. The functions of human saliva: a review sponsored by the world workshop on oral medicine VI. Arch Oral Biol. 60:863–74.

Dawes C, Watanabe S, Biglow-Lecomte P, Dibdin GH. 1989. Estimation of the velocity of the salivary film at some different locations in the mouth, J Dent Res, 68(11):1479-82.

Dawes C. 1996. Factors influencing salivary flow rate and composition, in Saliva and Oral Health, pp 27-43, eds. Edgar WM, O'Mullane DM), British Dental Association, London.

Dawes C. 2008. Salivary flow patterns and the health of hard and soft oral tissues, JADA139:18S-24S.

De Oliveira GC, Tereza GPG, Boteon AP, Ferrairo BM, Gonçalves PSP, Silva TCd, et al. 2017. Susceptibility of bovine dental enamel with initial erosion lesion to new erosive challenges. PLoS ONE 12(8).

De Smet K, Contreras R. 2005. Human antimicrobial peptides: defensins, cathelicidins and histatins. Biotechnology Letters;27(18):1337–47.

de Sousa-Pereira P, Amado F, Abrantes J, Ferreira R, Esteves PJ, Vitorino R. 2013. An evolutionary perspective of mammal salivary peptide families: cystatins, histatins, statherin and PRPs. Arch. Oral Biol. 58 (5), 451–458.

Dee KC, Puleo DA, Bizios R.2002. Protein surface interactions. In Tissue-Biomaterials Inter- actions; John Wiley & Sons Inc.: Hoboken, NJ, Chap. 3, 45–51.

Demaneche S, Chapel JP, Monrozier LJ, Quiquampoix H. 2009. Dissimilar pH dependent adsorption features of bovine serum albumin and α-chymotrypsin onmica probed by AFM. Colloids Surf. B. 70, 226–231.

Diaz-Arnold AM, Mark CA. 2002. The impact of saliva on patient care: a literature review, J of Prosth Dent 88:337-43.

Dodds MW, Johnson DA, Yeh CK. 2004. Health benefits of saliva: a review. J.Dent.Res, vol 33, page 223-233.

Doebert A, Fiebigeri M, Guentzeri M, Zimehl R, Hannig M. 2002. Protective properties of the short-term in-situ formed salivary pellicle, J Dent Res, 81, 3261.

Dorozhkin SV. 2012. Demineralisation mechanism of calcium apatites in acids: a review of literature. World J Methodol 2:1–17.

Dowker S, Andreson P. 1999. Crystal Chemistry and Demineralisation of Calcium Phosphate in Dental Enamel; Mineralogical Magazine, 63(6): 791-800.

Downer MC, Drugan CS, Blinkhorn AS. 2005. Dental caries experience of British children in an international context, Community Dental Health, 22 (2): 86-93.

Driscoll J, Zuo Y, Xu T, Choi JR, Troxler RF, Oppenheim FG. 1995. Functional comparison of native and recombinant human salivary histatin 1. J Dent Res 74:1837-1844.

Drozdetskiy A, Cole C, Procter J, Barton GJ. 2015. JPred4: a protein secondary structure prediction server. Nucleic Acids Res., gkv332.www.compbio.dundee.ac.uk/jpred/. Accessed Jan.10 2018.

Dunitz J. 2001. Pauling's Left-Handed α-Helix. Angewandte Chemie International Edition. 40 (22): 4167–4173.

Edgar WM, O'Mullane DM. 1990. Effect of saliva on plaque pH, in Saliva and Dental Health, pp 55-68 (eds. Edgar WM, O'Mullane DM), British Dental Association, London.

Ehrlich H, Koutsoukos PG, Demadis KD, Pokrovsky OS. 2009. Principles of demineralization: modern strategies for the isolation of organic frameworks. Part II. Decalcification. Micron; 40: 169-193.

Elliott JC, Dowker SEP, Knight RD. 1981. Scanning X-ray microradiography of a section of a carious lesion in dental enamel, J Microscopy,123: 89-92 19.

Elliott JC, Wong FS, Anderson P, Davis GR, Dowker SE. 1998. Determination of mineral concentration in dental enamel from x-ray attenuation measurements. Connect Tissue Res 38:61-72.

Elliott JC. 1994. Hydroxyapatite and nonstoichiometric apatites, in Structure and Chemistry of the Apatites and Other Calcium Orthophosphates, pp 111-186, Elsevier Science B.V., Amsterdam.

Elliott JC. 1997. Structure, crystal chemistry and density of enamel apatites. In. Wiley Online Library, 54-72.

Escamilla-García E, Alcázar-Pizaña AG, Segoviano-Ramírez JC, Del Angel-Mosqueda C, et al. 2017. Antimicrobial Activity of a Cationic Guanidine Compound against Two Pathogenic Oral Bacteria. International Journal of Microbiology. 1-9.

Fang F, Szleifer I. 2003. Competitive adsorption in model charged protein mixtures: Equilibrium isotherms and kinetics behavior J Chem Phys.119:1053.

Fasman GD. 1996. Circular Dichroism and the Conformational Analysis of Biomolecules. vol. 738, Plenum Press, Berlin.

Featherstone JD. 2000. The science and practice of caries prevention. J Am Dent Assoc, vol 131, page 887-899.

Featherstone JD. 2008. Dental caries: a dynamic disease process. Australian Dental Journal. 53, 286-91.

Featherstone JDB, Goodman P, Mclean JD. 1979. Electron-Microscope Study of Defect Zones in Dental Enamel. Journal of Ultrastructure Research, 67, 117-123.

Fejerskov O, Kidd EA. 2004. Clinical cariology and operative dentistry in the twenty first century, in Dental Caries (eds. Fejerskov O, and Kidd EA), Blackwell Munksgaard.

Fejerskov O, Manji F, Bader JD. 1990. Risk assessment in dentistry. Chapel Hill: University of North Carolina Dental Ecology Pp 215-17.

Ferguson DB. 1999. The salivary glands and their secretions, in Oral Bioscience, pp118-150, Churchill-Livingstone, Edinburgh.

Fielding LA, Mykhaylyk OO, Armes SP, Fowler PW, Mittal V, Fitzpatrick S. 2012. Correcting for a density distribution: Particle size analysis of core-shell nanocomposite particles using disk centrifuge photosedimentometry. Langmuir. 28:2536–2544.

Fincham AG, Belcourt AB. 1981. Dental Enamel Matrix Sequences of Two Amelogenin. Biosci Rep, 1 (10): 771-778.

Fincham AG, Moradian O. 1999. The Structure Biology Of The Developing Dental Enamel Matrix. J Struct Bio 126 (3): 270-299.

Fink AL. 1995. Compact intermediate states in protein folding Annu. Rev. Biophys. Biomol. Struct, 24, pp. 495-522.

Fleming S, Ulijn RV. 2014. Design of nanostructures based on aromatic peptide amphiphiles. Chem. Soc. Rev. 43, 8150 – 8177.

Gao XJ, Elliott JC, Anderson P. 1991. Scanning and contact microradiographic study of the effect of degree of saturation on the rate of enamel demineralisation, Caries Res 70: 1332-1337.

Garrett JR. 1999. Effects of autonomic nerve stimulation on salivary parenchyma and protein Secretion, in Neural Mechanisms of salivary gland secretion, pp 131- 150. eds Garrett JR, Ekström J, and Anderson LC, Frontiers of Oral Biology, vol 11, Karger, Basel.

Gibbons RJ, Hay DI, Schlesinger DH. 1991. Delineation of a segment of adsorbed salivary acidic proline-rich proteins which promotes adhesion of Streptococcus gordonii to apatitic surfaces, Infect Immun, 59(9):2948-54.

Gibbons RJ, Hay DI, Cisar JO, Clark WB.1988. Adsorbed salivary proline-rich protein 1 and statherin: receptors for type 1 fimbriae of Actinomyces viscosus T14V-J1 on apatitic surfaces, Infect Immun, 56(11):2990-3

Gibbons RJ, Hay DI. 1988. Human salivary acidic proline-rich proteins and statherin promote the attachment of Actinomyces viscosus LY7 to apatitic surfaces, Infect Immun, 56(2):439-45

Gmür R, Thurnheer T, Guggenheim B. 1999. Dominant cross-reactive antibodies generated during the response to a variety of oral bacterial species detect phosphorylcholine, J. Dent. Res. 78:77-85.

Goobes G, Goobes R, Schueler-Furman O, Baker D, Stayton PS. 2006. Folding of the C-terminal bacterial binding domain in statherin upon adsorption onto hydroxyapatite crystals. Proc. Natl. Acad. Sci. USA.103:16083–16088.

Goobes G, Goobes R, Shaw WJ, Gibson JM, Long JR, et al. 2007a. The structure, dynamics, and energetics of protein adsorption-lessons learned from adsorption of statherin to hydroxyapatite Magn. Reson. Chem. 45: S32–S47.

Goobes R, Goobes G, Shaw WJ, Drobny GP, Campbell CT, et al. 2007b. Thermodynamic roles of basic amino acids in statherin recognition of hydroxyapatite. Biochemistry 46, 4725–4733.

Gorbunoff MJ .1985. Protein chromatography on hydroxyapatite columns. Methods Enzymol 117:370–380.

Guidry MW, Mackenzie FT. 2003. Experimental study of igneous and sedimentary apatite demineralisation: control of pH, distance from equilibrium, and temperature on demineralisation rates. Geochim Cosmochim Acta; 67: 2949-2963.

Gururaja TL, Levine MJ. 1996. Solid-phase synthesis and characterization of human salivary statherin: A tyrosine- rich phosphoprotein inhibitor of calcium phosphate precipita- tion. Peptide Res. 9, 283–289.

Hannig C, Hannig M, Attin T. 2005. Enzymes in the acquired enamel pellicle. Eur J Oral Sci 113:2–13.

Hannig M, Balz M. 2001. Protective properties of salivary pellicles from two different intraoral sites on enamel erosion. Caries Res. 35:142-8.

Hannig M. 1999. Ultrastructural investigation of pellicle morphogenesis at two different intraoral sites during a 24-h period. Clin Oral Investig 3:88-95.

Hannig M. 2002. The protective nature of the salivary pellicle, Int Dent J, 52 (5): 417-423.

Hara AT, Ando M, Gonzalez-Cabezas C, Cury JA, Serra MC, Zero DT. 2006. Protective effect of the dental pellicle against erosive challenges in situ. J Dent Res 85:612-616.

Hara TA, Zero TD. 2010 The caries environment: saliva, pellicle, diet and hard tissue ultrastructure. Dent Clin North Am.54(3):455–467.

Hardt M, Witkowska HE, Webb S, Thomas LR, Dixon SE, Hall SC, Fisher SJ. 2005. Assessing the effects of diurnal variation on the composition of human parotid saliva: quantitative analysis of native peptides using iTRAQ reagents. Anal. Chem. 77, 4947– 4954.

Harris DA, Bashford CL. 1987. Spectrophotometry and Spectrofluorimetry: A Practical Approach. Oxford: IRL Press.

Hay DI, Bowen WH. 1996. The functions of salivary proteins, in Saliva and Oral Health, pp 105-123 (eds. Edgar, W.M., O'Mullane, D.M.), British Dental Association, London.

Hay DI, Moreno EC. 1989. Statherin and the acidic proline-rich proteins, in Human saliva: clinical chemistry and microbiology, pp 132-150 ed. Tenovuo, J.O., CRC Press Inc., Boca Raton.

Hay DI, Schluckebier SK, Moreno EC. 1982. Equlibrium dialysis and ultrafiltration studies of calcium and phosphate binding by human salivary

proteins. Implications for salivary supersaturation with respect to calcium phosphate salts, Calcif Tissue Int, 34: 531-538.

Hay DI. 1995. Salivary factors in caries models, Adv Dent Res, 9(3): 239-243.

Hay DI. 2003. The adsorption of salivary proteins by hydroxyapatite and enamel. Archs oral Biol., 12, p. 937.

Hector MP, Linden RWA. 1999. Reflexes of salivary secretion, in Neural Mechanisms of salivary gland secretion, pp196-218, (eds Garrett, J.R., Ekström, J., and Anderson, L.C.), Frontiers of Oral Biology, vol 11, Karger, Basel.

Held P .2003. Peptide and Amino Acid Quantification Using UV Fluorescence in Synergy HT Multi-Mode Microplate Reader. https://www.biotek.com/resources/application-notes/peptide-and-amino-acid-quantification-using-uv-fluorescence-in-synergy-ht-multi-mode-microplate-reader/

Helmerhorst EJ, Oppenheim FG. 2007. Saliva: a dynamic proteome. J Dent Res.86:680– 693.

Helmerhorst EJ, Traboulsi G, Salih E, Oppenheim FG. 2010. Mass spectrometric identification of key proteolytic cleavage sites in statherin affecting mineral homeostasis and bacterial binding domains. J Proteome Res 9: 5413-5421.

Hicks J, Garcia-Godoy F, Flaitz C. 2003. Biological factors in dental caries: role of saliva and dental plaque in the dynamic process of demineralization and remineralization (part 1). J Clin Pediatr Dent, 28, 47-52.

Higuchi WI, Cesar EY, Cho PW, Fox JL. 1984. Powder suspension method for critically re-examining the two-site model for hydroxyapatite demineralisation kinetics. J Pharm Sci; 73.146-153.

Hjerten S, Levine O, Tiselius A. 1965. Protein chromatography on calcium phosphate columns, Arch Biochem Biophys, 65(1):132-55.

Humphrey SP, Williamson RT. 2001. A review of Saliva: normal composition, flow, and function, J Prosthet Dent, 85: 162-9.

Huq NL, Cross KJ, Reynolds EC. 2000. Molecular modelling of a multiphosphorylated sequence motif bound to hydroxyapatite surfaces. Journal of Molecular Modeling 6: 35–47.

Huq NL, Cross KJ, Ung M, Myroforidis H. et al. 2007. A review of the salivary proteome and peptidome and saliva-derived peptide therapeutics. Int. J. Pept. Res. Ther.13, 547–564.

Iijima M, Moradian-Oldak, J. 2004. Control of octacalcium phosphate and apatite crystal growth by amelogenin matrices, J Mater Chem, 14, 2189-99.

Imfeld T. 1996. Dental erosion. Definition, classification and links, Eur J Oral Sci;104 (2 (Pt 2)): 151-155.

Iontcheva I, Oppenheim FG, Troxler RF.1997. Human salivary mucin MG1 selectively forms heterotypic complexes with amylase, proline-rich proteins, statherin, and histatins, J Dent Res 76, 734-43.

Ito T, Sun L, Bevan MA, Crooks RM. 2004. Comparison of nanoparticle size and electrophoretic mobility measurements using a carbon-nanotube-based coulter counter, dynamic light scattering, transmission electron microscopy, and phase analysis light scattering, Langmuir. 20,6940–6945.

Jalevik B, Odelius H, Dietz W, Noren J.2001. Secondary ion mass spectrometry and X-ray microanalysis of hypomineralized enamel in human permanent first molars. Arch Oral Biol.46:239–47.

Jensen JL, Lamkin MS, Oppenheim FG. 1992. Adsorption of human salivary proteins to hydroxyapatite – a comparison between whole saliva and glandular salivary secretions. J Dent Res 71: 1569–1576.

Jensen JL, Lamkin MS, Troxler RF, Oppenheim FG. 1991. Multiple forms of statherin in human salivary secretions. Arch Oral Biol; 36(7):529–534.

Johnson NW, Poole DF, Tyler JE. 1971. Factors affecting the differential demineralisation of human enamel in acid and EDTA. A scanning electron microscope study. Archives of Oral Biology, 16, 385-96.

Johnsson M, Levine MJ, Nancollas GH. 1993. Hydroxyapatite binding domains in salivary proteins, Crit Rev Oral Biol Med, 4(3-4):371-8.

Jones DT. 1999. Protein secondary structure prediction based on position-specific scoring matrices. J. Mol. Biol. 292: 195-202.

Kautsky MB, Featherstone JDB. 1993. Effect of salivary components on demineralisation rates of carbonated apatites, Caries Res, 27 (5): 373-377.

Kawasaki K, Weiss KM. 2003. Mineralized tissue and vertebrate evolution: The secretory calcium-binding phosphoprotein gene cluster, Procl Natl Acad Sci 100 (7), 4060-5.

Khurshid Z, Najeeb S, Mali M, Moin SF, Raza SQ, et al. 2017 Histatin peptides: Pharmacological functions and their applications in dentistry. Saudi Pharm J. Jan;25(1):25-31.

Khurshid Z, Naseem M, Sheikh Z, Najeeb S, Shahab S, Zafar MS. 2016b. Oral antimicrobial peptides: types and role in the oral cavity. Saudi Pharm. J. 24 (5), 515–524.

Khurshid Z, Zohaib S, Najeeb S, Zafar MS, Rehman R, Rehman IU. 2016a. Advances of Proteomic Sciences in Dentistry. Int. J.Mol. Sci. Sci. 17:728.

Kidd EAM, Fejerskov O. 2004. What constitutes dental caries? Histology of carious enamel and dentin related to the action of cariogenic biofilm. J Dent Res. 83. Spec No C: C35-8.

Kidd EAM. 2005. Essentials of Dental Caries. The disease and its management 3rd Ed. Oxford: Oxford University Press.

Kielbassa AM, Shohadai SP, Schulte-Mönting J. 2001. Effect of saliva substitutes on mineral content of demineralized and sound dental enamel. Support Care Cancer 9:40–47.

Kim DE, Chivian D, and Baker D. 2004. Protein structure prediction and analysis using the Robetta server. Nucleic Acids Res. 32, W526–W531. http://robetta.bakerlab.org/. Accessed Jun. 6.2016.

Kim N, Remmele RL Jr, Liu D, Razinkov VI, Fernandez EJ, Roberts CJ. 2013. Aggregation of anti-streptavidin immunoglobulin gamma-1 involves fab unfolding and competing growth pathways mediated by ph and salt concentration Biophys Chem, 172 (26-36).

Kirkham J, Zhang J, Brookes SJ, Shore RC, Bonass WA, Dam, Wallwork ML, et al. 2000. Evidence for charge domains on developing enamel crystal surfaces, J Dent Res, 79 (12): 1943-1947.

Kochanska B, Kedzia A, Kamysz W, Mackiewicz Z, Kupryszewski G. 2000. The effect of statherin and its shortened analogues on anaerobic bacteria isolated from the oral cavity. Acta Microbiol. Pol. 49 (3–4), 243–251.

Kosoric J, Williams AD, Hector MP, Anderson P. 2007. A synthetic peptide based on a natural salivary protein reduces demineralisation in model systems for dental caries and erosion. Int J Pept Res Ther; 13: 497–503.

Koutsoukos PG, Valsami-Jones. 2004. Principles of phosphate demineralisation and precipitation, in Phosphorus in Environmental Technology: Principles and Applications, (ed. E. Valsami-Jones), IWA Publishing.

Kresak M, Moreno EC, Zahradnik RT, Hay DI. 1977. Adsorption of amino acids onto hydroxyapatite. J. Colloid Interface Sci. 59, 283–292.

Kumar S, Nussinov R. 2002. Close-Range Electrostatic Interactions in Proteins. ChemBioChem. 3 (7): 604–617.

Kurivan J, Konforti B, Wemmer D. 2012. The Molecules of Life: Physical and Chemical Principles. Published by Garland Science.pp 950-967.

Kurrat R, Ramsden JJ, Prenosil JE. 1994. Kinetic model for serum albumin adsorption: experimental verification. J Chem Soc Faraday Trans; 90:587.

Kyte J, Doolittle RF. 1982. A simple method for displaying the hydropathic character of a protein. Journal of Molecular Biology. 157 (1): 105–32.

Lagerlof F. 1983. The effect of flow rate on the ionized calcium concentration of human parotid saliva, Caries Res, 16; 123-128.

Lamkin MS, Arancillo AA, Oppenheim, FG. 1996. Temporal and compositional characteristics of salivary protein adsorption to hydroxyapatite, J Dent Res, 75(2):803-8.

Lamkin MS, Oppenheim FG. 1993. Structural features of salivary function. Crit Rev Oral Biol Med 4:251-9.

Lamprecht C, Hinterdorfer P, Ebner A. 2014. Applications of biosensing atomic forcemicroscopy inmonitoring drug and nanoparticle delivery, Expert Opin. Drug Deliv. 11, 1237–1253.

Larden MJ, Thorsen A. 1974. Fluoride and enamel solubility. Scandinavian Journal of Dental Research, 82, 455-61.

Larsen MJ, Pearce EI. 2003. Saturation of human saliva with respect to calcium salts, Arch Oral Biol, 48(4):317-322.

Lee VM, Linden RW.1991. The effect of odours on stimulated parotid salivary flow in humans, Physiology & Behavior, 52, 6, 1121

Lee VM, Linden RW.1992. An olfactory-submandibular salivary reflex in humans. Exp. Physiol. 77, 221–224

LeGeros RZ. 1994. Biological and synthetic apatites, in Hydroxyapatite and Related materials, CRC press.

Lendenmann U, Grogan J, Oppenheim FG. 2000. Saliva and dental pellicle–a review. Adv Dent Res 14, 22–28.

Li J, Helmerhorst EJ, Yao Y, Nunn ME, Troxler RF. Oppenheim F.G. 2004. Statherin is an in vivo pellicle constituent: identification and immuno-quantification, Arch. Oral Biol. 49 379–385.

Liljemark WF, Bloomquist CG. 1981. Isolation of a protein-containing cell surface component from Streptococcus sanguis which affects its adherence to saliva-coated hydroxyapatite. Infect Immun 34:428-434.

Lindh L. 2002. On the adsorption behaviour of saliva and purified salivary proteins at solid/liquid interfaces. Swed Dent J Suppl 26:1–57.

Linding R, Schymkowitz J, Rousseau F, Diella F, Serrano L. 2004. A comparative study of the relationship between protein structure and beta-aggregation in globular and intrinsically disordered proteins. J Mol Biol. 2004; 342:345–353.

Lingawi H. 2012. Effect of divalent metal cations on hydroxyapatite demineralisation kinetics relevant to dental caries and erosion. Institute of Dentistry, Queen Mary's School of Medicine and Dentistry University of London.

Listl S, Galloway J, Mossey PA, Marcenes W .2015. Global economic impact of dental diseases. J Dent Res 94(10):1355–61.

Littman H. 2005. Cariology Theories Past and Present. Compendium of Continuing Education in Dentistry, 14: 748-750.

Long JR, Shaw WJ, Stayton PS, Drobny GP. 2001. Structure and dynamics of hydrated statherin on hydroxyapatite as determined by solid-state NMR, Biochemistry, 25;40(51):15451-5.

Louis-Jeune C, Andrade-Navarro MA, Perez-Iratxeta C. 2012. Prediction of protein secondary structure from circular dichroism using theoretically derived spectra. Proteins vol. 80,374-381.

Lussi A, Hellwig E. 2001. Erosive potential of oral care products, Caries Research, 35 (1): 52-56.

Lussi A. 2006. Dental erosion in children, Monogr oral sci,20, page 140-151.

Mafe S, Manzanares JA, Reiss H, Thomann JM, Gramain P. 1992. Model for the demineralisation of calcium hydroxyapatite powder. J Phys Chem; 96: 861-866.

Manconi B, Fanali C, Cabras T, Inzitari R, Patamia M, Scarano E, et al. 2010. Structural characterization of a new statherin from pig parotid granules. Journal of Peptide Science;16(6):269–75.

Mann S. 2001. Biomineralization: Principles and Concepts in Bioinorganic Materials Chemistry. Oxford: Oxford University Press.

Margolis HC, Kwak SY, Yamazaki H. 2014. Role of mineralization inhibitors in the regulation of hard tissue biomineralization: relevance to initial enamel formation and maturation. Front Physiol. 5:339.

Margolis HC, Moreno EC. 1992. Kinetics of hydroxyapatite demineralisation in acetic, lactic, and phosphoric acid solutions. Calcif Tissue Int; 50: 137-143.

Margolis HC, Moreno EC. 1994. Composition and cariogenic potential of dental plaque fluid, Crit Rev Oral Biol Med, 5 (1): 1-25

Marsh PD, Nyvad B. 2008. The Oral Microflora and Biofilms on Teeth. In Dental Caries: The Disease and Its Clinical Management. 2nd ed. Oxford: Blackwell Munksgaard.

Marsh PD. 1999. Microbiologic Aspects of Dental Plaque and Dental Caries, Dental Clinics of North America, 43(4): 599-614.

Marsh PD. 2004. Dental plaque as a microbial biofilm. Caries Research, 38, 204-211.

Marshall AF, Lawless KR. 1981. TEM study of the central dark line in enamel crystallites. Journal of Dental Research, 60, 1773-82.

Marthaler TM. 2003. Successes and drawbacks in the caries-preventive use of fluorides lessons to be learnt from history", Oral Health Prev Dent, 1(2): 129-140.

Masica DL, Ash JT, Ndao M, Drobny GP, Gray JJ. 2010. Toward a Structure Determination Method for Biomineral-Associated ProteinUsing Combined Solid- State NMR and Computational Structure Prediction. Structure,18, 1678–1687.

Matsuo S, Lagerlof F. 1991. Relationship between total and ionized calcium concentrations in human whole saliva and dental plaque fluid, Arch Oral Biol, 36 (7), 525-527.

McDonald EE, Goldberg HA, Tabbara N, Mendes FM, and Siqueira WL. 2011. Histatin 1 resists proteolytic degradation when adsorbed to hydroxyapatite." Journal of dental research 90 2: 268-272.

McKinney RM, Spillane JT, Pearce GW. 1966. A simple method for determining the labeling efficiency of fluorescein isothiocyanate products. Anal Biochem.14(3):421–428.

Meureman JH, and ten Cate JM. 1996. Pathogenesis and modifying factors of dental erosion, Eur J Oral Sci 104; 199-206.

Meuzelaar H, Vreede J, Woutersen S. 2016 Influence of Glu/Arg, Asp/Arg, and Glu/Lys Salt Bridges on α-Helical Stability and Folding Kinetics. Biophys J. 7;110(11):2328-2341.

Micsonai A, Wien F, Kernya L, Lee Y-H, Goto Y, Réfrégiers M, Kardos J. 2015. Accurate secondary structure prediction and fold

recognition for circular dichroism spectroscopy Proc. Natl. Acad. Sci. USA 112 E3095–103.

Moradian-Oldak J. 2012. Protein- mediated enamel mineralization. Frontiers in Bioscience: A Journal and Virtual Library, 17, 1996–2023.

Moreno EC, Kresak M, Hay DI. 1982. Adsorption thermodynamics of acidic proline-rich human salivary proteins onto calcium apatites, J Biol Chem, 25;257(6):2981-9.

Moreno EC, Kresak M, Hay DI. 1984. Adsorption of molecules of biological interest onto hydroxyapatite, Calcif Tissue Int, 36(1):48-59.

Moreno EC, Kresak M, Hay DI. 1991. Adsorption of salivary proteins onto Ca apatites, Biofouling, 4: 3-24.

Moreno EC, Kresak M, Hay DI. 1978. Adsorption of two human parotid salivary macromolecules on hydroxy-, fluorhydroxy- and fluorapatites. Arch Oral Biol 23:523–533.

Moreno EC, Kresak M, Kane JJ, Hay DI. 1987. Adsorption of proteins, peptides, and organic acids from binary mixtures onto hydroxyapatite. Langmuir. 3:511—9.

Moreno EC, Varughese K, Hay DI. 1979. Effect of human salivary proteins on the precipitation kinetics of calcium phosphate. Calcif Tissue Int 28: 7–16.

Moynihan P, Petersen PE. 2004. Diet, nutrition and prevention of dental diseases, Public Health Nutrition: 7; 1A: 201-26.

Muirhead H, Perutz MF. 1963. Structure of haemoglobin. A three-dimensional Fourier synthesis of reduced human haemoglobin at 5.5 Å resolution. Nature. 199:633-8.

Mutahar M, Carpenter G, Bartlett D, German M & Moazzez R. 2017b. The presence of acquired enamel pellicle changes acid-induced erosion from demineralisation to a softening process. Scientific Reports volume 7, Article number: 10920.

Mutahar M, O'Toole S, Carpenter G, Bartlett D, Andiappan M, Moazzez R. 2017a. Reduced statherin in acquired enamel pellicle on eroded teeth compared to healthy teeth in the same subjects: An in-vivo study. In PLoS One. Aug 24;12(8).

Naganagowda GA, Gururaja TL, Levine MJ. 1998. Delineation of conformational preferences in human salivary statherin by 1H, 31P NMR and CD studies: sequential assignment and structure-function correlations, J Biomol Struct Dyn, 16(1):91-107.

Nanci A, 2017. Ten Cate's Oral Histology: Development, Structure, and Function. 9th edition. Toronto, Ontario, Canada: Mosby-Year Book. Pp.122-137.

Nancollas GH. 1974. Physicochemistry of demineralization and remineralization. J Dent Res. 53:297–302.

Ndao M, Ash JT, Stayton PS, Drobny GP. 2010. The Role of Basic Amino Acids in the Molecular Recognition of Hydroxyapatite by Statherin using Solid State NMR urf. Sci., 604, L39.

Niemi LD, Johansson I. 2004. Salivary statherin peptide-binding epitopes of commensal and potentially infectious Actinomyces spp. delineated by a hybrid peptide construct. Infect Immun; 72:782–787.

Noble JE, Knight AE, Reason AJ, Di Matola A, Bailey MJ. 2007. A comparison of protein quantitation assays for biopharmaceutical applications. Mol. Biotechnol. 37, 99–111.

Norde W, MacRitchie F, Nowicka G, Lyklema J. 1986. Protein adsorption at solid-liquid interfaces: reversibility and conformation aspects. J. Colloid Interface Sci. 112, 447–456.

Norde W. 1986. Adsorption of proteins from solution at the solid–liquid interface. Adv. Colloid Interface Sci. 25 pp. 267–340.

Oakley MT, Bulheller BM, Hirst JD. 2006. First-Principles Calculations of Protein Circular Dichroism in the Far-Ultraviolet and Beyond, Chirality, 8, 340–347.

Oberg K, Chrunyk BA, Wetzel R, Fink AL. 1994. Nativelike secondary structure in interleukin-1-beta inclusion bodies by attenuated total reflectance FTIR. Biochemistry, 33, pp. 2628-2634.

Oesterle LJ, Shellhart WC, Belanger GK. 1998. The use of bovine enamel in bonding studies. American Journal of Orthodontics and Dentofacial Orthopedics.114: 514–519.

Oudhoff MJ, Bolscher JG, Nazmi K, Kalay H, van't Hof W, Amerongen AV, et al. 2008. Histatins are the major wound-closure stimulating factors in human saliva as identified in a cell culture assay. FASEB J 22:3805-3812.

Pace CN, Scholtz JM. 1998. A helix propensity scale based on experimental studies of peptides and proteins. Biophysical Journal. 75 (1): 422–7.

Pace CN, Vajdos F, Fee L, Grimsley G, Gray T .1995. How to measure and predict the molar absorption coefficient of a protein? Protein Science 4: 2411–2423.

Patamia M, Messana I, Petruzzelli R, Vitali A, Inzitari R, Cabras T. et al. 2005. Two proline-rich peptides from pig (Sus scrofa) salivary glands generated by pre-secretory pathway underlying the action of a proteinase cleaving ProAla bonds. Peptides.;26:1550–1559.

Pecora P. 2000. Dynamic Light Scattering Measurement of Nanometer Particles in Liquids J. Nanoparticle Res. 2:123–131.

Pezzotti G, Zhu WL, Boffelli M, Adachi T, Ichioka H, Yamamoto T, Marunaka Y, and Kanamura N. 2015. Vibrational algorithms for quantitative crystallographic analyses of hydroxyapatite-based biomaterials: I, theoretical foundations. Analytical and Bioanalytical chemistry, Volume: 407 Issue: 12 Pages:3325-3342.

Pindborg, J.J. (1970) Pathology of the Dental Hard Tissue, Munksgaard, Copenhagen;321-21.

Poole DF, Johnson NW. 1967. The effects of different demineralizing agents on human enamel surfaces studied by scanning electron microscopy. Archives of Oral Biology, 12, 1621-34.

Poumier F, Schaad Ph, Haikel Y, Voegel JC, Gramain Ph. 1996. Demineralisation of lysozyme-coated hydroxyapatite, Colloids Surfaces B: Biointerfaces, 7, 1-8.

Proctor GB, Hamdan S, Carpenter GH, Wilde P. 2005. A statherin and calcium enriched layer at the air interface of human parotid saliva, Biochem J, 1;389 (Pt 1):111-6.

Proctor GB. 1999. Effects of automatic de-nervations on protein secretion and synthesis by salivary glands, in Neural Mechanisms of salivary gland secretion, pp150-165, (eds Garrett JR, Ekström J, and Anderson LC), Frontiers of Oral Biology, vol 11, Karger, Basel.

Public Health England .2016. Tackling poor oral health in children local government’s public health role.

Rahman M, Laurent S, Tawil N, Yahia L, Mahmoudi M. 2013. Protein-Nanoparticle Interactions: The Bio-Nano Interface. The Springer Series in Biophysics. volume 15. p69-71

Raj PA, Johnsson M, Levine MJ, Nancollas GH. 1992. Salivary statherin: Dependence on sequence, charge, hydrogen bonding potency, and helical conformation for adsorption to hydroxyapatite and inhibition of mineralization, J Biol Chem, 267 (9), 5968-76.

Raj PA, Marcus E, Sukumaran DK. 1998.Structure of human salivary histatin 5 in aqueous and nonaqueous solutions Biopolymers 45(1):51-67.

Reynolds EC, Black CL, Cross KJ, Eakins D, Huq NL,Morgan MV, et al. 1999. Advances in enamel remineralization: anticariogenic casein phosphopeptide-amorphous calcium phosphate. J Clin Dent. (2):86-88.

Reynolds EC. 1987. The prevention of sub-surface demineralization of bovine enamel and change in plaque composition by casein in an intra-oral model, J Dent Res, 66(6):1120-7.

Reynolds EC. 1998. Anticariogenic complexes of amorphous calcium phosphate stabilized by casein phosphopeptides:a review. Spec Care Dentist Jan-Feb 18:1 8-16.

Richardson CF, Johnsson M, Raj PA, Levine MJ, Nancollas GH. 1993. The influence of histatin-5 fragments on the mineralization of hydroxyapatite. Arch Oral Biol. 38:997-1002.

Rijnkels M, Elnitski L, Miller W, Rosen JM. 2003. Multispecies comparative analysis of a mammalian-specific genomic domain encoding secretory proteins. Genomics. 82:417–432.

Roberts CJ. 2014. Therapeutic protein aggregation: mechanisms, design, and control. Trends Biotechnol. 32, 372–380.

Robinson C, Briggs HD. 1981. Chemical Changes during Formation and Maturation of Human Enamel; Arch Oral Bio, 26(12): 1027-1033.

Robinson C, Shore RC. 2000. The Chemistry of Enamel Caries; Crit Rev Oral Bio Med, 11(4), 481–495.

Robinson C, Kirkham J, Shore R. 1995. Dental enamel: Formation to Destruction, Boca Raton, Fla.; London, CRC.

Roehrich A, Drobny G. 2013. Solid-State NMR Studies of Biomineralization Peptides and Proteins. Chem. Res. 46 (9), pp 2136–2144.

Romero MJ, Nakashima S, Nikaido T, Ichinose S, Sadr A, Tagami J. 2015. Inhibition of hydroxyapatite growth by casein, a potential salivary phosphoprotein homologue. Eur J Oral Sci 123: 288-296.

Rykke M, Rolla G,Smistad G, Karlsen J. 1995. Micelle-like structures in human saliva, Colloids Surfaces B: Biointerfaces, 4, 33-44.

Rykke M, Rolla G, Smistad G, Young A, Karlsen J. 1996. Zeta potentials of human salivary micelle-like particles, Colloids Surfaces B: Biointerfaces, 6, 51-56.

Salih E, Siqueira WL, Helmerhorst EJ, Oppenheim FG. 2010. Large-scale phosphoproteome of human whole saliva using disulfidethiol

interchange covalent chromatography and mass spectrometry. Anal Biochem, 407(1), 19-33.

Santos O, Kosoric J, Hector MP, Anderson P, Lindh L .2008. Adsorption behaviour of statherin and a statherin peptide onto hydroxyapatite and silica surfaces by in situ ellipsometry J Colloid Interface Sci. ;318:175–182.

Sapp JP, Eversole, LR, Wysocki GP. 2004. Contemporary Oral and Maxillofacial Pathology. ed 2, St. Louis, Mosby.

Schaad P, Poumier F, Voegel JC, Gramain P.1997. Analysis of calcium hydroxyapatite demineralisation in non-stoichiometric solutions. Colloids Surf A; 121: 217-228.

Schlesinger DH, Hay DI, Levine MJ. 1989. Complete primary structure of statherin, a potent inhibitor of calcium phosphate precipitation, from the saliva of the monkey, Macaca arctoides, Int J Pept Protein Res, 34(5):374-80.

Schlesinger DH, Hay DI. 1977. Complete covalent structure of statherin, a tyrosine-rich acidic peptide which inhibits calcium phosphate precipitation from human parotid saliva. J Biol Chem, 252 (5), 1689-95.

Schmid FX. 1997. Optical spectroscopy to characterize protein conformation and conformational changes. In: Creighton TE (ed.) Protein Structure: A Practical Approach, pp. 261–297.

Schmid, F.-X. 2001. Biological Macromolecules: UV-visible Spectrophotometry. www.eLS. John Wiley & Sons Ltd, Chichester.

Schuck P. 1997. Use of surface plasmon resonance to probe the equilibrium and dynamic aspects of interactions between biological macromolecules. Annu. Rev. Biophys. Struct. 26:541–566.

Seibert JA, Boone JM. 2005. X-ray imaging physics for nuclear medicine technologists. Part 2: X-ray interactions and image formation. J Nucl Med Technol, 33, 3-18.

Seibert JA. 2004. X-ray imaging physics for nuclear medicine technologists. Part 1: Basic principles of x-ray production. J Nucl Med Technol, 32, 139-47.

Shah S, Kosoric J, Hector M, Anderson P. 2011. An in vitro scanning microradiography study of the reduction in hydroxyapatite demineralization rate by statherin-like peptides as a function of increasing N-terminal length. Eur J Oral Sci. 119: 13–18.

Sharma S, Berne BJ, Kumar SK. 2010. Thermal and Structural Stability of Adsorbed Proteins. Biophysical Journal, 99(4), 1157–1165.

Shaw WJ .2015. Solid-state NMR studies of proteins immobilized on inorganic surfaces. Solid State Nucl Magn Reson 70:1–14.

Shaw WJ, Long JR, Dindot JL, Campbell AA, Stayton PS, Drobny GP. 2000. Determination of Statherin N-Terminal Peptide Conformation on Hydroxyapatite Crystals. J. Am. Chem. Soc., 122, 1709–1716.

Shellis RP, Barbour M, Jones S, Addy M. 2010. Effects of pH and acid concentration on erosive demineralisation of enamel, dentine, and compressed hydroxyapatite. European Journal of Oral Sciences, 118, 475-482.

Shellis RP, Dibdin GH. 2000. in Teaford MF, MereditH-M, and Ferguson MWJ (Eds.), Development, Function and Evolution of the Teeth. University Press, Cambridge, pp. 242–251.

Shellis RP, Wahab FK. 1993. The Hydroxyapatite Ion Activity Product in Acid-Solutions Equilibrated with human enamel at 37ºC. Caries Research, 27(5):365-72.

Shimotoyodome A, Kobayashi H, Tokimitsu I, Matsukobo T. 2006. Statherin and histatin 1 reduce parotid saliva promoted Streptococcus mutans strain MT8148 adhesion to hydroxyapatite surfaces. Caries. Res, 40, 403–411.

Silverstone L. 1981. Dental caries: aetiology, pathology and prevention, Macmillan.

Simoni R, Hill R, Vaughan M, Tabor H. 2003. A classic Instrument: The Beckman DU Spectrophotometer and is inventor. J. Biol. Chem., 278, 49, 1.

Siqueira WL, Custodio W, McDonald EE. 2012. New insights into the composition and functions of the acquired enamel pellicle. J Dent Res 91:1110-1118.

Siqueira WL, Margolis HC, Helmerhorst EJ, Mendes FM, Oppenheim FG. 2010. Evidence of intact histatins in the in vivo acquired enamel pellicle. J Dent Res 89:626-630.

Siqueira WL, Salih E, Wan DL, Helmerhorst EJ, Oppenheim FG. 2008.Proteome of human minor salivary gland secretion. J Dent Res. 87:445–450.

Smith CE. 1998. Cellular and chemical events during enamel maturation. Crit. Rev. Oral Biol. Med.; 9:128–161.

Smith CEL, Poulter JA, Antanaviciute A, Kirkham J, Brookes SJ, Inglehearn CF, et al. 2017. Amelogenesis Imperfecta; Genes, Proteins, and Pathways: Frontiers in Physiology, 8, 435.

Smith GS. 2007. The polarization of skylight: an example from nature Am. J. Phys.75, 25, 35.

Smith PM. 1992. Mechanisms of secretion by salivary glands, in in Saliva and Oral Health, pp 9-27, (eds. Edgar, W.M., O'Mullane, D.M.), British Dental Association, London.

Soares RV, Lin T, Siqueira CC, Bruno LS, Li X, Oppenheim FG. Et al. 2004. Salivary micelles: identification of complexes containing MG2, sIgA, lactoferrin, amylase, glycosylated proline- rich protein and lysozyme, Arch Oral Biol, 49 (5), 337-43.

Spanos N, and Koutsoukos PG. 2001. Model studies of the effect of orthophosphol-L-serine on biological mineralization, Langmuir 17, 866-72.

Sreerama N, Woody RW. 2000. Estimation of protein secondary structure from circular dichroism spectra: comparison of CONTIN, SELCON, and CDSSTR methods with an expanded reference set. Anal. Biochem. 287, 252–260.

Stayton PS, Drobny GP, Shaw WJ, Long JR, Gilbert M. 2003. Molecular recognition at the protein-hydroxyapatite interface, Crit Rev Oral Biol Med,14(5):370-6.

Striolo A, Jayaraman A, Genzer J, Hall CK. 2005. Adsorption of comb copolymers on weakly attractive solid surfaces J. Chem. Phys. 2005, 123.

Sugiyama K, Ogata K. 1993. High performance liquid chromatographic determination of histatins in human saliva. J Chromatogr 619:306–309.

Sung SS. 2015. Peptide folding driven by Van der Waals interactions. Protein Sci. 24, 1383.

Takuma S. 1980. Demineralization and Remineralization of Tooth Substance - an Ultrastructural Basis for Caries Prevention. Journal of Dental Research, 59, 2146-2156.

Tang R, Hass W, Wu W, Gulde S, and Nancollas GH. 2003. Constant composition demineralisation of mixed phases II. Selective demineralisation of calcium phosphates. J Colloid Interface Sci; 260:379–384.

Tavafoghi M, Cerruti M. 2016. The role of amino acids in hydroxyapatite mineralization. J. R. Soc. Interface 13:20160462.

Thomann JM, Voegel JC, Gramain P. 1990. Kinetics of demineralisation of calcium hydroxyapatite powder. III: pH and sample conditioning effects. Calcif Tissue Int; 46: 121-129.

Thomann JM, Voegel JC, Gramain P. 1993. Quantitative model for the demineralisation of calcium hydroxyapatite with a permselective ionic interface. J Coll Interf Sci; 157: 369-374.

Tsai H, Bobek LA. 1998. Human salivary histatins: promising anti-fungal therapeutic agents. Crit. Rev. Oral Biol. Med. 9, 480–497.

Tsuda H, Arends J. 1994.Orientational micro-Raman spectroscopy on hydroxyapatite single crystals and human enamel crystallites. J Dent Res. 73:1703–1710.

UniProt: the universal protein knowledgebase. 2017. Nucleic Acids Res. 45: D158-D169. (http://www.uniprot.org). Accessed; jun. 10 2016.

Vasina EN, Dejardin P, Rezaei H, Grosclaude J, Quiquampoix H. 2005. Fate of prions in soil: Adsorption kinetics of recombinant unglycosylated ovine prion protein onto mica in laminar flow conditions and subsequent desorption. Biomacromolecules.;6:3425–3432.

Vasina EN, Déjardin P. 2004. Adsorption of α-chymotrypsin onto mica in laminar flow conditions. Adsorption kinetic constant as a function of tris buffer concentration at pH 8.6. Langmuir; 20:8699–8706.

Vitkov L, Hannig M, Nekrashevych Y, Krautgartner WD. 2004. Supramolecular pellicle precursors, Eur J Oral Sci,112(4):320-5.

Vitorino R, Lobo MJ, Duarte JR, Ferrer-Correia AJ, et al. 2005. The role of salivary peptides in dental caries. Biomed Chromatogr.19(3):214–222.

Voegel JC, Frank RM. 1977. Stages in the demineralisation of human enamel crystals in dental caries. Calcif Tissue Res, 24, 19-27.

Waite JH, Qin XX. 2001. Polyphosphoprotein from the adhesive pads of Mytilus edulis. Biochemistry, vol.40, no.9, pp. 2887–2893.

Wallwork ML, Kirkham J, Chen H, Chang SX, Robinson C, Smith DA, Clarkson BH. 2002. Binding of dentin noncollagenous matrix proteins to biological mineral crystals: an atomic force microscopy study, Calcif Tissue Int. 71(3):249-55.

Wang W, Nema S, Teagarden D. 2010. Protein aggregation pathways and influencing factors. Int. J. Pharm. 390, 89–99.

Waterman HA, Blom C, Holterman HJ, Gravenmade EJ, Mellema J. 1988. Rheological properties of human saliva. Arch. Oral Biol. 8, 589–596.

Weiss WF, Young TM, Roberts CJ. 2009. Principles, approaches, and challenges for predicting protein aggregation rates and shelf life. J Pharm Sci.; 98:1246–77.

White SC, Pharoah MJ. 2008. The evolution and application of dental maxillofacial imaging modalities. Dental Clinics of North America, 52, 689-705.

White W, Nancollas GH. 1977. Quantitative Study of Enamel Demineralisation under Conditions of Controlled Hydrodynamics. Journal of Dental Research, 56, 524-530.

WHO, Media centre (2012), Fact sheet N°318.

Wikiel K, Burke EM, Perich JW, Reynolds EC, Nancollas GH.1994. Hydroxyapatite mineralization and demineralization in the presence of synthetic phosphorylated pentapeptides, Arch Oral Biol, 39 (8), 715-21.

Woody RW. 2010. A significant role for high-energy transitions in the ultraviolet circular dichroism spectra of polypeptides and proteins, Chirality, 22, 1E, E22.

Xie H, Gibbons RJ, Hay DI. 1991. Adhesive properties of strains of Fusobacterium nucleatum of the subspecies nucleatum, vincentii and polymorphum, Oral Microbiol Immunol, 6(5):257-63.

Xu C, Reed R, Gorski JP, Wang Y, Walker MP. 2012. The distribution of carbonate in enamel and its correlation with structure and mechanical properties. J Mater Sci.47:8035–43.

Xu T, Levitz S, Diamond R, Oppenheim F.1991. Anticandidal activity of major human salivary histatins. Infect. Immun. 59 (8), 2549–2554.

Yanagisawa T, Miake Y. 2003. High-resolution electron microscopy of enamel-crystal demineralization and remineralization in carious lesions. Journal of Electron Microscopy, 52, 605-613.

Yao Y, Berg EA, Costello CE, Troxler RF, Oppenheim FG. 2003. Identification of protein components in human acquired enamel pellicle and whole saliva using novel proteomics approaches, J Biol Chem, 14; 278 (7): 5300-8.

Yao Y, Lamkin MS, Oppenheim FG. 1999. Pellicle precursor proteins: acidic proline-rich proteins, statherin, and histatins, and their crosslinking reaction by oral transglutaminase. J Dent Res 78: 1696–1703.

Yao Y, Lamkin MS, Oppenheim FG. 2000. Pellicle precursor protein crosslinking: characterization of an adduct between acidic proline-rich protein (PRP-1) and statherin generated by transglutaminase. J Dent Res 79: 930–938.

Yin A, Margolis H, Grogan J, Yao Y, Troxler R, Oppenheim F. 2003 Physical parameters of hydroxyapatite adsorption and effect on candidacidal activity of histatins. Arch. Oral Biol. 48:361–368.

Yin A, Margolis H, Yao Y, Grogan J, Oppenheim FG. 2006. Multi-component adsorption model for pellicle formation: the influence of salivary proteins and non-salivary phospho proteins on the binding of histatin 5 onto hydroxyapatite Arch Oral Biol, 51, pp. 102-110.

Yuwei F, Zhi S, Janet MO. 2009. Controlled remineralization of enamel in the presence of amelogenin and fluoride. Biomaterials 30, 478–483.

Zahradnik R, Moreno E. 1977. Progressive stages of subsurface demineralization of human tooth enamel. Archives of Oral Biology, 22, 585-591.

Zahradnik RT, Moreno EC, Burke EJ.1976. Effect of salivary pellicle on enamel subsurface demineralization in vitro, J Dent Res, 55(4):664-70.

Zero DT. 1996. Etiology of dental erosion-extrinsic factors; European Journal of Oral Sciences, 104.

Zheng T, Boyle A, Marsden HR, Valdink D, Martelli G, Raap J, Kros A. 2015. Probing coiled-coil assembly by paramagnetic NMR spectroscopy. Org. Biomol. Chem 13, 1159–1168.

Zhu L, Liu H, Witkowska HE, Huang Y, Tanimoto K, Li W. 2014. Preferential and selective degradation and removal of amelogenin adsorbed on hydroxyapatites by MMP20 and KLK4 in vitro. Front Physiol. 5: 268.

Ziegler J, Wachtel H. 2005. Comparison of cascade impaction and laser diffraction for particle distribution measurements. Aerosol Med. 18:311–324.

Appendix 1 BSODR poster (Cardiff, 2015).

Queen Mary University of London

Institute of Dentistry
Dental Physical Science Unit

Barts and The London School of Medicine and Dentistry

Co-operativity of Statherin and Histatin-1 in Demineralisation of Carious and Erosive HAp Model

Huda Almandil, Maisoon AL-Jawad, Tony Williams, Paul Anderson

Aim

The aim of this *in vitro* study is to measure the effect of statherin-21 (STN21) and histain-1(HTN38) individually and in combination on the demineralisation rate of previously demineralised hydroxyapatite (HAp) using scanning microradiography (SMR)

Introduction

Salivary proteins such as statherin (STN43) are known to influence de- and re-mineralisation. STN21(D pS pSEE KFLRR IGRFG YGYGP Y) is an analogue peptide that contains the N-terminal 21 residues similar to STN43. The active N-terminal is involved in inhibition of precipitation and responsible for binding with Ca^{2+}.

HTN38 (D pSHEK RHHGY RRKFH EKHHS HREFP FYGDY GSNYL YDN) similar to salivary proline-rich proteins, is also understood to inhibit crystal growth of calcium phosphate salts, but does not inhibit spontaneous precipitation.

Method

- Six HAp discs were mounted within SMR cells (Fig.1,2) three scanning positions were located on each disc for the measurement of the rate of mineral loss (RD_{HAp}).
- The discs were exposed to caries simulating demineralising solutions (pH 4.0, 0.1M acetic acid) for 72 hours.
- After preliminary acidic exposure, the HAp discs were rinsed thoroughly with distilled water and then exposed to 2.0ml of the test solution containing the peptides dissolved in phosphate-buffered saline (PBS) at a concentration of 0.2mM.
- 24hrs later the HAp discs were then exposed to the acidic demineralisation solution for a further 72 hours.
- HAp disc exposed to PBS was used as a negative control.
- RD_{HAp} was measured continuously using real time SMR.

Fig.1. SMR cell with HAp disc mounted in it. With dimensions of 40.0 mm x 50.0 mm and centrally located chamber of 20.0 mm diameter and 6.0 mm in depth.

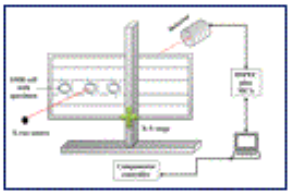

Fig.2.SMR machine with SMR cells and X-ray detector.

Results

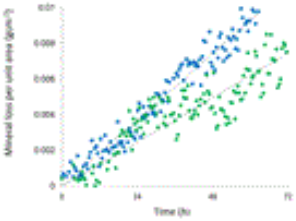

Fig.3. Comparing the gradient of the measured slope before and after exposure to STN21. The rate of mineral loss per area for HAp before peptide exposure was $1.58x10^{-6}$ gcm^{-2} h^{-1}, and after was $1.04x10^{-6}$ gcm^{-2} h^{-1}.

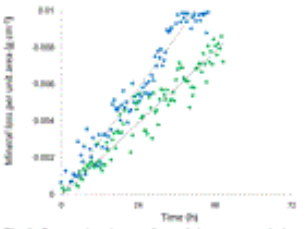

Fig.4. Comparing the gradient of the measured slope before and after exposure to HTN38. The rate of mineral loss per area for HAp before peptide exposure was $2.40x10^{-6}$ gcm^{-2} h^{-1}, and after was $1.50x10^{-6}$ gcm^{-2} h^{-1}.

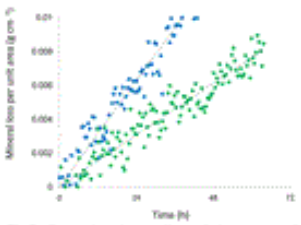

Fig.5. Comparing the gradient of the measured slope before and after exposure to STN21+HTN38. The rate of mineral loss per area for HAp before peptide exposure was $2.60x10^{-6}$ gcm^{-2} h^{-1}, and after was $1.10x10^{-6}$ gcm^{-2} h^{-1}.

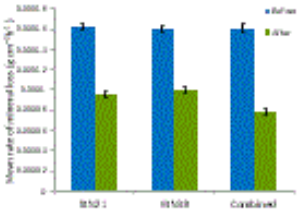

Fig.6. The data shows significant reduction ($p< 0.05$) in demineralisation rate using STN21 and HTN38 by 40.0±3.2% and 39.2±2.9% respectively. The peptides in combination showed a 52.80±2.2% reduction in demineralisation rate.

Conclusions

This study has shown that STN21 and HTN38 have considerable effect in reducing HAp demineralisation under caries/erosive simulation conditions. Their increase in efficacy in combination suggests a cooperative mode of action. This suggests that STN21, HTN38, and a combination of both can be used as a therapeutic agent for preventive treatment of enamel demineralisation.
Further understanding of the underlying molecular mechanism and kinetics of adsorption of these species is needed to explain the effects observed.

h.b.a.almandil@qmul.ac.uk

Appendix 2 The 11th European Symposium on Saliva poster (Netherlands, 2017).

Queen Mary University of London

Institute of Dentistry
Dental Physical Science Unit

Barts and The London School of Medicine and Dentistry

Salivary Peptide Adsorption onto Hydroxyapatite, and Effects on Demineralisation Inhibition

H. B. ALMANDIL* , M. AL-JAWAD, R. A.D. WILLIAMS , P. ANDERSON

Background

- Statherin (STN) is a salivary peptide involved in demineralisation inhibition (Fig.1A). The acidic N-terminal is responsible for binding Ca^{2+} and inhibition of precipitation of hydroxyapatite (HA). The acidic N-terminal has 3 acidic residues and 2 phosphoserines
- Synthetic STN21 contains only the N-terminal 21 residues (in box).

DpSpSEEKFLRRIGRFGYGYGPYQPVPEQPLYPQPYQPQYQQYTF

- Histatin-1 (HTN) is a salivary peptide which also binds Ca^{2+}, but does not inhibit spontaneous precipitation of HA (Fig.1B). The N-terminal has only 2 acidic residues and 1 phosphoserines.
- Synthetic HTN21 contains only the N-terminal 21 residues (in box).

DpSHEKRHHGYRRKFHEKHHSHRFFPFYGDYGSNYLYDN

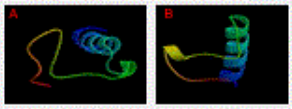

Fig. 1: Predicted 3D structure of STN (A), and HTN (B) using ROBETTA showing an α-helix conformation at the N-terminal of both peptides that fits geometrically with HA crystal lattice (Long *et al.* 2001).

Aim

To understand the mechanism by which full length statherin, histatin1, and their N-terminal 21-mer analogues, both individually, and in combination, inhibit hydroxyapatite demineralisation.

Objectives

- To measure the adsorption of the salivary peptides both individually and in combination, onto HA beads, using spectrophotometry
- To measure the efficacy of the salivary peptides both individually, and, in combination, on inhibition of demineralisation, using Scanning Microradiography (SMR).
- To investigate the relation between salivary peptide adsorption and demineralisation inhibition.

Methods

Spectophotometric measurement of salivary peptide adsorption onto HA beads

Each peptide solution (individual and combination) were mixed with HA beads (2 mg/ml). For the shorter length peptides additional labels were appended (Fig.2,3).The change in absorbance was measured until equilibrium was achieved (Fig.4, Table 1). The amount adsorbed (nmol/mg) was calculated from the equation

$$Amount\ adsorbed = \frac{(A_0 - A_i)}{A_0} \times N_A \times nmol$$

Where A_0 is the initial absorbance, A_i is the absorbance at saturation, N_A is Avogadro's number, and nmol is the amount of peptide.

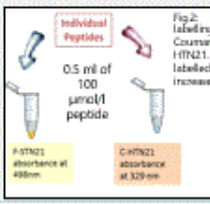

Fig.2: Fluorescein (498 nm) labelling of STN21 and Coumarin (329 nm) labelling of HTN21. The peptides were labelled with different tags to increase the absorbance signal.

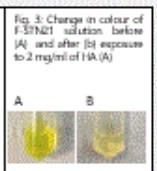

Fig. 3: Change in colour of F-STN21 solution before (A) and after (B) exposure to 2 mg/ml of HA (A)

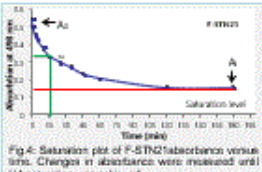

Fig.4: Saturation plot of F-STN21absorbance versus time. Changes in absorbance were measured until HA saturation was achieved.

Peptides	$(A_i - A_f)$ (±SE)	$T_{0.5}$ /min (±SE)
STN	0.089 (±0.08)	5(±0.1)
HTN	0.024 (±0.014)	3 (±0.1)
STN21	0.28 (±0.02)	15(±0.34)
HTN21	0.053 (±.004)	15(±0.13)
STN21+HTN21	0.111 (±.0.04)	1(±0.02)
STN21+HTN	0.462 (±0.01)	1(±0.34)
STN+HTN21	0.077 (±0.01)	3(±0.03)
STN+HTN	0.088 (±0.02)	3(±0.07)

Table 1: Absorbance values at saturation and $T_{0.5}$

Scanning Microradiography measurement of changes in mineral mass (SMR)

Acetic acid (100 mmol/l, pH 4.0) was circulated over HA discs located within SMR cells for 72 h. The discs were then exposed for 24 h to 2.0 ml of the test peptides (100 or 200 µmol/l). The demineralisation solution was then circulated for a further 72 h. (Fig.5)

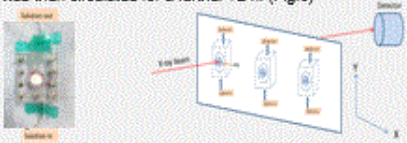

Fig. 5: SMR environmental cell, and a schematic representation of SMR X-Y scanning stage with multiple SMR cells containing HA discs.

Overall Results

- STN-21 combined with either HTN, or HTN-21, showed the highest and fastest HA adsorption, the highest demineralisation inhibition.
- HTN-21 showed the lowest HA adsorption and demineralisation inhibition of all. It was also one of the slowest to adsorb to HA.
- HTN showed superior properties to its 21-mer in all tests. HTN showed superior properties to its 21-mer in all tests.
- STN and its 21-mer were similar in HA adsorption and demineralisation inhibition, however STN21 adsorbed at a slower rate (Fig. 6).

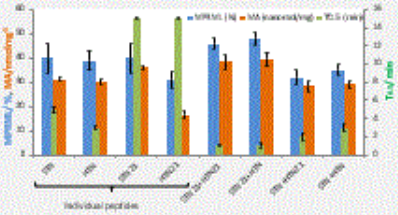

Fig.6: Demineralisation inhibition (blue bars), peptide adsorption (orange bars), and $T_{0.5}$ (green bars)

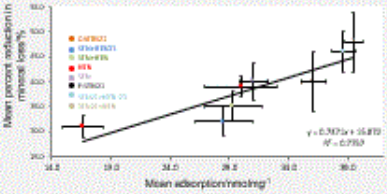

Fig. 7: Correlation of demineralisation inhibition and HA adsorption data. (0.77) showing positive relationship.

Conclusions

- Full length peptides bind faster to HA compared to their 21-mers.
- STN21 combinations have higher affinity to HA than combinations with full length STN.
- Absence of residues 22 onwards reduces the demineralisation inhibition efficacy of HTN, but not of STN.
- Increased demineralisation inhibition is associated with greater peptide binding.

h.b.a.almandil@qmul.ac.uk

Appendix 3 RML value for HA and enamel, and the standard error for all the scanned positions on samples before and after exposure to 100, and 200 µmol/l of STN, HTN STN21 and HTN21.

Sample HA	Scan point		Before exposure to peptide	After exposure to 200 µmol/l	Sample HA	Scan point		Before exposure to peptide	After exposure to 200 µmol/l
HTN	A1	RML (10^{-4} g cm^{-2} h^{-1})	1.60	1.01	**HTN21**	B1	RML (10^{-4} g cm^{-2} h^{-1})	1.96	1.49
		±SE (10^{-4} g cm^{-2} s^{-1})	0.00245	0.00259			±SE (10^{-4} g cm^{-2} s^{-1})	0.001222	0.001878
		PRML (%)	-	**36.8**			PRML (%)	-	**23.97**
HTN	A2	RML (10^{-4} g cm^{-2} h^{-1})	1.47	0.95	**HTN21**	B1	RML (10^{-4} g cm^{-2} h^{-1})	1.97	1.33
		±SE (10^{-4} g cm^{-2} s^{-1})	0.00144	0.00252			±SE (10^{-4} g cm^{-2} s^{-1})	0.001438	0.00122
		PRML (%)	-	**35**			PRML (%)	-	**32.48**
HTN	A3	RML (10^{-4} g cm^{-2} h^{-1})	1.28	0.7	**HTN21**	B3	RML (10^{-4} g cm^{-2} h^{-1})	1.94	1.21
		±SE (10^{-4} g cm^{-2} s^{-1})	0.00454	0.00454			±SE (10^{-4} g cm^{-2} s^{-1})	0.00125	0.000245
		PRML (%)	-	**45**			PRML (%)	-	**37.62**
HTN	A4	RML (10^{-4} g cm^{-2} h^{-1})	1.96	1.03	**HTN21**	B4	RML (10^{-4} g cm^{-2} h^{-1})	1.90	1.32
		±SE (10^{-4} g cm^{-2} s^{-1})	0.00122	0.00198			±SE (10^{-4} g cm^{-2} s^{-1})	0.001345	0.00259
		PRML (%)	-	**47**			PRML (%)	-	**30.52**
HTN	A5	RML (10^{-4} g cm^{-2} h^{-1})	2.37	1.54	**HTN21**	B5	RML (10^{-4} g cm^{-2} h^{-1})	1.90	1.29
		±SE (10^{-4} g cm^{-2} s^{-1})	0.00493	0.00413			±SE (10^{-4} g cm^{-2} s^{-1})	0.001874	0.0013249
		PRML (%)	-	**35.02**			PRML (%)	-	**32.10**
HTN	A6	RML (10^{-4} g cm^{-2} h^{-1})	2.32	1.50	**HTN21**	B6	RML (10^{-4} g cm^{-2} h^{-1})	1.82	1.27
		±SE (10^{-4} g cm^{-2} s^{-1})	0.003230	0.00231			±SE (10^{-4} g cm^{-2} s^{-1})	0.001222	0.0018738
		PRML (%)	-	**35.34**			PRML (%)		**30.2**

Sample HA	Scan point		Before exposure to peptide	After exposure to 100 µmol/l	Sample HA	Scan point		Before exposure to peptide	After exposure to 100 µmol/l
HTN	C1	RML (10^{-4} g cm^{-2} h^{-1})	1.88	1.39	**HTN21**	D1	RML (10^{-4} g cm^{-2} h^{-1})	1.33	1.02
		±SE (10^{-4} g cm^{-2} s^{-1})	0.00040710	0.00034856			±SE (10^{-4} g cm^{-2} s^{-1})	0.0012218	0.0018738
		PRML (%)	-	**26.06**			PRML (%)	-	**23.30**
HTN	C2	RML (10^{-4} g cm^{-2} h^{-1})	1.96	1.49	**HTN21**	D2	RML (10^{-4} g cm^{-2} h^{-1})	1.31	1.00
		±SE (10^{-4} g cm^{-2} s^{-1})	0.00012218	0.0018738			±SE (10^{-4} g cm^{-2} s^{-1})	0.0012218	0.0012218
		PRML (%)	-	**23.97**			PRML (%)	-	**23.7**
HTN	C3	RML (10^{-4} g cm^{-2} h^{-1})	1.83	1.30	**HTN21**	D3	RML (10^{-4} g cm^{-2} h^{-1})	1.88	1.42
		±SE (10^{-4} g cm^{-2} s^{-1})	0.00041376	0.00039618			±SE (10^{-4} g cm^{-2} s^{-1})	0.0004071	0.0003485
		PRML (%)	-	**28.96**			PRML (%)	-	**24**
HTN	C4	RML (10^{-4} g cm^{-2} h^{-1})	1.76	1.28	**HTN21**	D4	RML (10^{-4} g cm^{-2} h^{-1})	1.83	1.36
		±SE (10^{-4} g cm^{-2} s^{-1})	0.00040710	0.00043336			±SE (10^{-4} g cm^{-2} s^{-1})	0.0002548	0.0001
		PRML (%)	-	**27.3**			PRML (%)	-	**25.7**
HTN	C5	RML (10^{-4} g cm^{-2} h^{-1})	1.90	1.42	**HTN21**	D5	RML (10^{-4} g cm^{-2} h^{-1})	1.75	1.35
		±SE (10^{-4} g cm^{-2} s^{-1})	0.00013452	0.00025968			±SE (10^{-4} g cm^{-2} s^{-1})	0.003452	0.009
		PRML (%)	-	**25.2**			PRML (%)		**22.8**
HTN	C6	RML (10^{-4} g cm^{-2} h^{-1})	1.96	1.39	**HTN21**	D6	RML (10^{-4} g cm^{-2} h^{-1})	1.01	0.81
		±SE (10^{-4} g cm^{-2} s^{-1})	0.00013218	0.0014728			±SE (10^{-4} g cm^{-2} s^{-1})	0.005367	0.002
		PRML (%)		**29**			PRML (%)		**20**

Sample enamel	Scan point		Before exposure to peptide	After exposure to 200 µmol/l	Sample enamel	Scan point		Before exposure to peptide	After exposure to 200 µmol/l
HTN	A1	RML (10^{-4} g cm^{-2} h^{-1})	6.30	5.53	**HTN21**	B1	RML (10^{-4} g cm^{-2} h^{-1})	4.91	4.24
		±SE (10^{-4} g cm^{-2} s^{-1})	0.0014758	0.0016378			±SE (10^{-4} g cm^{-2} s^{-1})	0.0005367	0.0002
		PRML (%)		**12.22**			PRML (%)	-	**13.64**
HTN	A2	RML (10^{-4} g cm^{-2} h^{-1})	7.90	6.94	**HTN21**	B2	RML (10^{-4} g cm^{-2} h^{-1})	5.77	4.77
		±SE (10^{-4} g cm^{-2} s^{-1})	0.0017247	0.00799			±SE (10^{-4} g cm^{-2} s^{-1})	0.0004923	0.0003024
		PRML (%)		**12.15**			PRML (%)	-	**17.33**
HTN	A3	RML (10^{-4} g cm^{-2} h^{-1})	6.20	5.31	**HTN21**	B3	RML (10^{-4} g cm^{-2} h^{-1})	6.20	5.31
		±SE (10^{-4} g cm^{-2} s^{-1})	0.00026366	0.00022545			±SE (10^{-4} g cm^{-2} s^{-1})	0.00013645	0.00025367
		PRML (%)		**14.35**			PRML (%)	-	**14.5**
HTN	A4	RML (10^{-4} g cm^{-2} h^{-1})	5.77	4.7	**HTN21**	B4	RML (10^{-4} g cm^{-2} h^{-1})	4.48	3.38
		±SE (10^{-4} g cm^{-2} s^{-1})	0.00023546	0.00028961			±SE (10^{-4} g cm^{-2} s^{-1})	0.0013216	0.0013218
		PRML (%)		**18.54**			PRML (%)		**15.1**
HTN	A5	RML (10^{-4} g cm^{-2} h^{-1})	3.63	3.24	**HTN21**	B5	RML (10^{-4} g cm^{-2} h^{-1})	3.62	3.04
		±SE (10^{-4} g cm^{-2} s^{-1})	0.00015685	0.00035357			±SE (10^{-4} g cm^{-2} s^{-1})	0.0013576	0.00013645
		PRML (%)		**10.7**			PRML (%)	-	**16.02**
HTN	A6	RML (10^{-4} g cm^{-2} h^{-1})	3.06	2.5	**HTN21**	B6	RML (10^{-4} g cm^{-2} h^{-1})	2.86	2.37
		±SE (10^{-4} g cm^{-2} s^{-1})	0.00014848	0.00023567			±SE (10^{-4} g cm^{-2} s^{-1})	0.0015218	0.00012548
		PRML (%)		**18.3**			PRML (%)	-	**17.3**

Sample enamel	Scan point		Before exposure to peptide	After exposure to 100 µmol/l	Sample enamel	Scan point		Before exposure to peptide	After exposure to 100 µmol/l
HTN	C1	RML (10^{-4} g cm^{-2} h^{-1})	6.33	5.11	**HTN21**	D1	RML (10^{-4} g cm^{-2} h^{-1})	5.49	4.85
		±SE (10^{-4} g cm^{-2} s^{-1})	0.00033232	0.0006373			±SE (10^{-4} g cm^{-2} s^{-1})	0.00059629	0.00040315
		PRML (%)	-	**19**			PRML (%)	-	**12**
HTN	C2	RML (10^{-4} g cm^{-2} h^{-1})	6.1	5.23	**HTN21**	D2	RML (10^{-4} g cm^{-2} h^{-1})	5.74	4.8
		±SE (10^{-4} g cm^{-2} s^{-1})	0.00059377	0.00044378			±SE (10^{-4} g cm^{-2} s^{-1})	0.00052303	0.0004316
		PRML (%)	-	**14**			PRML (%)	-	**16**
HTN	C3	RML (10^{-4} g cm^{-2} h^{-1})	5.1	4.52	**HTN21**	D3	RML (10^{-4} g cm^{-2} h^{-1})	7.01	6.15
		±SE (10^{-4} g cm^{-2} s^{-1})	0.00024654	0.0001385			±SE (10^{-4} g cm^{-2} s^{-1})	0.00022983	0.0002349
		PRML (%)	-	**11**			PRML (%)	-	12
HTN	C4	RML (10^{-4} g cm^{-2} h^{-1})	5.54	4.69	**HTN21**	D4	RML (10^{-4} g cm^{-2} h^{-1})	6.83	5.8
		±SE (10^{-4} g cm^{-2} s^{-1})	0.0024733	0.00023456			±SE (10^{-4} g cm^{-2} s^{-1})	0.0012213	0.00029766
		PRML (%)	-	**15**			PRML (%)	-	**15**
HTN	C5	RML (10^{-4} g cm^{-2} h^{-1})	5.74	4.8	**HTN21**	D5	RML (10^{-4} g cm^{-2} h^{-1})	5.38	4.46
		±SE (10^{-4} g cm^{-2} s^{-1})	0.0016736	0.00015736			±SE (10^{-4} g cm^{-2} s^{-1})	0.00023086	0.00023388
		PRML (%)	-	**16**			PRML (%)	-	**17**
HTN	C6	RML (10^{-4} g cm^{-2} h^{-1})	5.49	4.7	**HTN21**	D6	RML (10^{-4} g cm^{-2} h^{-1})	6.15	5.4
		±SE (10^{-4} g cm^{-2} s^{-1})	0.0019734	0.00018829			±SE (10^{-4} g cm^{-2} s^{-1})	0.00025497	0.00025497
		PRML (%)		**14**			PRML (%)		**12**

Sample HA	Scan point		Before exposure to peptide	After exposure to 200 µmol/l	Sample HA	Scan point		Before exposure to peptide	After exposure to 200 µmol/l
STN	E1	RML (10^{-4} g cm^{-2} h^{-1})	1.586	1.02	**STN21**	F1	RML (10^{-4} g cm^{-2} h^{-1})	2.45	1.71
		±SE (10^{-4} g cm^{-2} s^{-1})	0.0013249	0.00799			±SE (10^{-4} g cm^{-2} s^{-1})	0.001222	0.001878
		PRML (%)	-	**35.6**			PRML (%)	-	**30**
STN	E2	RML (10^{-4} g cm^{-2} h^{-1})	1.60	1.04	**STN21**	F1	RML (10^{-4} g cm^{-2} h^{-1})	2.41	1.83
		±SE (10^{-4} g cm^{-2} s^{-1})	0.00024547	0.00025968			±SE (10^{-4} g cm^{-2} s^{-1})	0.001438	0.00122
		PRML (%)	-	**35**			PRML (%)	-	**24**
STN	E3	RML (10^{-4} g cm^{-2} h^{-1})	2.84	1.41	**STN21**	F3	RML (10^{-4} g cm^{-2} h^{-1})	2.92	1.41
		±SE (10^{-4} g cm^{-2} s^{-1})	0.00025367	0.00024547			±SE (10^{-4} g cm^{-2} s^{-1})	0.0014376	0.00014376
		PRML (%)	-	**50**			PRML (%)	-	**52**
STN	E4	RML (10^{-4} g cm^{-2} h^{-1})	2.59	1.01	**STN21**	F4	RML (10^{-4} g cm^{-2} h^{-1})	2.69	1.27
		±SE (10^{-4} g cm^{-2} s^{-1})	0.000232	0.000298			±SE (10^{-4} g cm^{-2} s^{-1})	0.0012218	0.00012218
		PRML (%)	-	**57**			PRML (%)	-	**53**
STN	E5	RML (10^{-4} g cm^{-2} h^{-1})	1.90	1.32	**STN21**	F5	RML (10^{-4} g cm^{-2} h^{-1})	1.59	1.02
		±SE (10^{-4} g cm^{-2} s^{-1})	0.00493	0.00413			±SE (10^{-4} g cm^{-2} s^{-1})	0.00049378	0.00040710
		PRML (%)	-	**30**			PRML (%)	-	**36**
STN	E6	RML (10^{-4} g cm^{-2} h^{-1})	2.32	1.45	**STN21**	F6	RML (10^{-4} g cm^{-2} h^{-1})	1.60	1.01
		±SE (10^{-4} g cm^{-2} s^{-1})	0.003230	0.00231			±SE (10^{-4} g cm^{-2} s^{-1})	0.00043336	0.00043089
		PRML (%)	-	**37**			PRML (%)		**37**

Sample HA	Scan point		Before exposure to peptide	After exposure to 100 µmol/l	Sample HA	Scan point		Before exposure to peptide	After exposure to 100 µmol/l
STN	G1	RML (10^{-4} g cm^{-2} h^{-1})	1.63	1.14	**STN21**	H1	RML (10^{-4} g cm^{-2} h^{-1})	1.8	135
		±SE (10^{-4} g cm^{-2} s^{-1})	0.00348	0.00354			±SE (10^{-4} g cm^{-2} s^{-1})	0.00245	0.002878
		PRML (%)	-	**30**			PRML (%)	-	**25**
STN	G2	RML (10^{-4} g cm^{-2} h^{-1})	1.47	1.09	**STN21**	H2	RML (10^{-4} g cm^{-2} h^{-1})	1.97	1.36
		±SE (10^{-4} g cm^{-2} s^{-1})	0.00346	0.00334			±SE (10^{-4} g cm^{-2} s^{-1})	0.00243	0.00222
		PRML (%)	-	**25**			PRML (%)	-	**29.9**
STN	G3	RML (10^{-4} g cm^{-2} h^{-1})	1.57	1.18	**STN21**	H3	RML (10^{-4} g cm^{-2} h^{-1})	2.08	1.35
		±SE (10^{-4} g cm^{-2} s^{-1})	0.00454	0.00454			±SE (10^{-4} g cm^{-2} s^{-1})	0.000125	0.000245
		PRML (%)	-	**24.8**			PRML (%)	-	**28**
STN	G4	RML (10^{-4} g cm^{-2} h^{-1})	1.96	1.4	**STN21**	H4	RML (10^{-4} g cm^{-2} h^{-1})	1.88	1.4
		±SE (10^{-4} g cm^{-2} s^{-1})	0.00275	0.00266			±SE (10^{-4} g cm^{-2} s^{-1})	0.0001246	0.000259
		PRML (%)	-	**28.5**			PRML (%)	-	**25.5**
STN	G5	RML (10^{-4} g cm^{-2} h^{-1})	1.60	1.19	**STN21**	H5	RML (10^{-4} g cm^{-2} h^{-1})	1.88	1.39
		±SE (10^{-4} g cm^{-2} s^{-1})	0.00356	0.00342			±SE (10^{-4} g cm^{-2} s^{-1})	0.003874	0.003249
		PRML (%)	-	**25.6**			PRML (%)	-	**26**
STN	G6	RML (10^{-4} g cm^{-2} h^{-1})	1.32	0.96	**STN21**	H6	RML (10^{-4} g cm^{-2} h^{-1})	2.26	1.6
		±SE (10^{-4} g cm^{-2} s^{-1})	0.00423	0.00431			±SE (10^{-4} g cm^{-2} s^{-1})	0.001245	0.001874
		PRML (%)	-	**27**			PRML (%)		**29**

Sample enamel	Scan point		Before exposure to peptide	After exposure to 200 µmol/l	Sample enamel	Scan point		Before exposure to peptide	After exposure to 200 µmol/l
STN	E1	RML (10^{-4} g cm^{-2} h^{-1})	6.07	6.31	**STN21**	F1	RML (10^{-4} g cm^{-2} h^{-1})	4.07	3.12
		±SE (10^{-4} g cm^{-2} s^{-1})	0.00145	0.00165			±SE (10^{-4} g cm^{-2} s^{-1})	0.00358	0.00328
		PRML (%)	-	**20.4**			PRML (%)	-	**23.3**
STN	E2	RML (10^{-4} g cm^{-2} h^{-1})	2.18	2.00	**STN21**	F1	RML (10^{-4} g cm^{-2} h^{-1})	4.45	3.24
		±SE (10^{-4} g cm^{-2} s^{-1})	0.00294	0.00264			±SE (10^{-4} g cm^{-2} s^{-1})	0.00355	0.00354
		PRML (%)	-	**8.25**			PRML (%)	-	**27.2**
STN	E3	RML (10^{-4} g cm^{-2} h^{-1})	3.56	2.59	**STN21**	F3	RML (10^{-4} g cm^{-2} h^{-1})	4.99	3.36
		±SE (10^{-4} g cm^{-2} s^{-1})	0.00264	0.00274			±SE (10^{-4} g cm^{-2} s^{-1})	0.00225	0.00295
		PRML (%)	-	**27.24**			PRML (%)	-	**32.6**
STN	E4	RML (10^{-4} g cm^{-2} h^{-1})	3.26	2.78	**STN21**	F4	RML (10^{-4} g cm^{-2} h^{-1})	3.88	2.81
		±SE (10^{-4} g cm^{-2} s^{-1})	0.0022624	0.00275			±SE (10^{-4} g cm^{-2} s^{-1})	0.00294	0.00269
		PRML (%)	-	**26**			PRML (%)	-	**26.3**
STN	E5	RML (10^{-4} g cm^{-2} h^{-1})	1.90	1.42	**STN21**	F5	RML (10^{-4} g cm^{-2} h^{-1})	2.88	2.1
		±SE (10^{-4} g cm^{-2} s^{-1})	0.00271	0.00253			±SE (10^{-4} g cm^{-2} s^{-1})	0.001874	0.0013249
		PRML (%)	-	**23**			PRML (%)	-	**26**
STN	E6	RML (10^{-4} g cm^{-2} h^{-1})	1.01	0.81	**STN21**	F6	RML (10^{-4} g cm^{-2} h^{-1})	2.86	2.56
		±SE (10^{-4} g cm^{-2} s^{-1})	0.002731	0.00231			±SE (10^{-4} g cm^{-2} s^{-1})	0.00126	0.001176
		PRML (%)	-	**20**			PRML (%)		**11**

Sample HA	Scan point		Before exposure to peptide	After exposure to 200 µmol/l	Sample HA	Scan point		Before exposure to peptide	After exposure to 200 µmol/l
STN	G1	RML (10^{-4} g cm^{-2} h^{-1})	3.47	2.8	**STN21**	H1	RML (10^{-4} g cm^{-2} h^{-1})	1.96	1.49
		±SE (10^{-4} g cm^{-2} s^{-1})	0.00135	0.00159			±SE (10^{-4} g cm^{-2} s^{-1})	0.001452	0.001838
		PRML (%)	-	**19**			PRML (%)	-	**24**
STN	G2	RML (10^{-4} g cm^{-2} h^{-1})	3.09	2.5	**STN21**	H2	RML (10^{-4} g cm^{-2} h^{-1})	1.97	1.54
		±SE (10^{-4} g cm^{-2} s^{-1})	0.00156	0.00184			±SE (10^{-4} g cm^{-2} s^{-1})	0.001343	0.001722
		PRML (%)	-	**20**			PRML (%)	-	**21**
STN	G3	RML (10^{-4} g cm^{-2} h^{-1})	5.82	4.50	**STN21**	H3	RML (10^{-4} g cm^{-2} h^{-1})	6.31	5.11
		±SE (10^{-4} g cm^{-2} s^{-1})	0.00167	0.00182			±SE (10^{-4} g cm^{-2} s^{-1})	0.001725	0.0001645
		PRML (%)	-	**23**			PRML (%)	-	**19**
STN	G4	RML (10^{-4} g cm^{-2} h^{-1})	4.9	3.91	**STN21**	H4	RML (10^{-4} g cm^{-2} h^{-1})	5.7	4.55
		±SE (10^{-4} g cm^{-2} s^{-1})	0.00272	0.00298			±SE (10^{-4} g cm^{-2} s^{-1})	0.002345	0.002859
		PRML (%)	-	**20**			PRML (%)	-	**21**
STN	G5	RML (10^{-4} g cm^{-2} h^{-1})	4.40	3.6	**STN21**	H5	RML (10^{-4} g cm^{-2} h^{-1})	5.48	4.45
		±SE (10^{-4} g cm^{-2} s^{-1})	0.00253	0.00213			±SE (10^{-4} g cm^{-2} s^{-1})	0.003874	0.003249
		PRML (%)	-	**18**			PRML (%)	-	**19**
STN	G6	RML (10^{-4} g cm^{-2} h^{-1})	5.12	4.1	**STN21**	H6	RML (10^{-4} g cm^{-2} h^{-1})	5.38	4.32
		±SE (10^{-4} g cm^{-2} s^{-1})	0.003230	0.00231			±SE (10^{-4} g cm^{-2} s^{-1})	0.002232	0.0028538
		PRML (%)	-	**19.9**			PRML (%)		**20**

Appendix 4 RML values for HA and enamel, and the standard error for all the scanned position on the samples before and after exposure to peptides when in combination.

Sample HA	Scan point		Before exposure to peptide	After exposure to 200 µmol/l	Sample HA	Scan point		Before exposure to peptide	After exposure to 200 µmol/l
STN+HTN	A1	RML (10^{-4} g cm^{-2} h^{-1})	1.83	1.26	**STN+HTN21**	B1	RML (10^{-4} g cm^{-2} h^{-1})	0.877	0.601
		±SE (10^{-4} g cm^{-2} s^{-1})	0.00730	0.00159			±SE (10^{-4} g cm^{-2} s^{-1})	0.00231	0.00208
		PRML (%)	-	**31**			PRML (%)	-	**31**
STN+HTN	A2	RML (10^{-4} g cm^{-2} h^{-1})	1.76	1.37	**STN+HTN21**	B1	RML (10^{-4} g cm^{-2} h^{-1})	0.782	0.619
		±SE (10^{-4} g cm^{-2} s^{-1})	0.00146	0.000154			±SE (10^{-4} g cm^{-2} s^{-1})	0.00217	0.00252
		PRML (%)	-	**22**			PRML (%)	-	**21**
STN+HTN	A3	RML (10^{-4} g cm^{-2} h^{-1})	1.81	1.14	**STN+HTN21**	B3	RML (10^{-4} g cm^{-2} h^{-1})	0.985	0.601
		±SE (10^{-4} g cm^{-2} s^{-1})	0.0017	0.00124			±SE (10^{-4} g cm^{-2} s^{-1})	0.00163	0.00145
		PRML (%)	-	**37**			PRML (%)	-	**39**
STN+HTN	A4	RML (10^{-4} g cm^{-2} h^{-1})	2.36	1.52	**STN+HTN21**	B4	RML (10^{-4} g cm^{-2} h^{-1})	0.947	0.642
		±SE (10^{-4} g cm^{-2} s^{-1})	0.00152	0.00258			±SE (10^{-4} g cm^{-2} s^{-1})	0.00124	0.000118
		PRML (%)	-	**36**			PRML (%)	-	**32**
STN+HTN	A5	RML (10^{-4} g cm^{-2} h^{-1})	2.51	1.41	**STN+HTN21**	B5	RML (10^{-4} g cm^{-2} h^{-1})	0.998	0.619
		±SE (10^{-4} g cm^{-2} s^{-1})	0.00263	0.00199			±SE (10^{-4} g cm^{-2} s^{-1})	0.00182	0.001710
		PRML (%)	-	**44**			PRML (%)	-	**38**
STN+HTN	A6	RML (10^{-4} g cm^{-2} h^{-1})	2.67	1.55	**STN+HTN21**	B6	RML (10^{-4} g cm^{-2} h^{-1})	0.721	0.5
		±SE (10^{-4} g cm^{-2} s^{-1})	0.00120	0.00181			±SE (10^{-4} g cm^{-2} s^{-1})	0.00073	0.00089
		PRML (%)	-	**42**			PRML (%)		**31**

Sample HA	Scan point		Before exposure to peptide	After exposure to 200 µmol/l	Sample HA	Scan point		Before exposure to peptide	After exposure to 200 µmol/l
STN21+HTN	C1	RML (10^{-4} g cm^{-2} h^{-1})	2.59	1.15	**STN21+HTN21**	D1	RML (10^{-4} g cm^{-2} h^{-1})	1.69	1.01
		±SE (10^{-4} g cm^{-2} s^{-1})	0.00230	0.00219			±SE (10^{-4} g cm^{-2} s^{-1})	0.00162	0.00120
		PRML (%)	-	**56**			PRML (%)	-	**40**
STN21+HTN	C2	RML (10^{-4} g cm^{-2} h^{-1})	2.67	1.19	**STN21+HTN21**	D2	RML (10^{-4} g cm^{-2} h^{-1})	1.66	0.779
		±SE (10^{-4} g cm^{-2} s^{-1})	0.00286	0.0002154			±SE (10^{-4} g cm^{-2} s^{-1})	0.00183	0.00172
		PRML (%)	-	**55**			PRML (%)	-	**53**
STN21+HTN	C3	RML (10^{-4} g cm^{-2} h^{-1})	2.56	1.48	**STN21+HTN21**	D3	RML (10^{-4} g cm^{-2} h^{-1})	1.68	0.684
		±SE (10^{-4} g cm^{-2} s^{-1})	0.002717	0.002524			±SE (10^{-4} g cm^{-2} s^{-1})	0.00285	0.00234
		PRML (%)	-	**42**			PRML (%)	-	**59**
STN21+HTN	C4	RML (10^{-4} g cm^{-2} h^{-1})	3.90	1.82	**STN21+HTN21**	D4	RML (10^{-4} g cm^{-2} h^{-1})	1.54	0.845
		±SE (10^{-4} g cm^{-2} s^{-1})	0.00275	0.00265			±SE (10^{-4} g cm^{-2} s^{-1})	0.00254	0.00278
		PRML (%)	-	**53**			PRML (%)	-	**45**
STN21+HTN	C5	RML (10^{-4} g cm^{-2} h^{-1})	4.26	3.29	**STN21+HTN21**	D5	RML (10^{-4} g cm^{-2} h^{-1})	1.51	0.897
		±SE (10^{-4} g cm^{-2} s^{-1})	0.00176	0.00139			±SE (10^{-4} g cm^{-2} s^{-1})	0.00192	0.00160
		PRML (%)	-	**23**			PRML (%)	-	**41**
STN21+HTN	C6	RML (10^{-4} g cm^{-2} h^{-1})	3.99	1.98	**STN21+HTN21**	D6	RML (10^{-4} g cm^{-2} h^{-1})	1.54	0.92
		±SE (10^{-4} g cm^{-2} s^{-1})	0.00170	0.00182			±SE (10^{-4} g cm^{-2} s^{-1})	0.00164	0.00138
		PRML (%)	-	**50**			PRML (%)		**40**

Sample enamel	Scan point		Before exposure to peptide	After exposure to 200 µmol/l	Sample enamel	Scan point		Before exposure to peptide	After exposure to 200 µmol/l
STN+HTN	A1	RML (10^{-4} g cm^{-2} h^{-1})	5.31	4.24	**STN+HTN21**	B1	RML (10^{-4} g cm^{-2} h^{-1})	3.08	2.68
		±SE (10^{-4} g cm^{-2} s^{-1})	0.00194	0.001329			±SE (10^{-4} g cm^{-2} s^{-1})	0.002431	0.002208
		PRML (%)	-	**20.15**			PRML (%)	-	**12.9**
STN+HTN	A2	RML (10^{-4} g cm^{-2} h^{-1})	5.46	3.59	**STN+HTN21**	B2	RML (10^{-4} g cm^{-2} h^{-1})	3.19	2.44
		±SE (10^{-4} g cm^{-2} s^{-1})	0.00173	0.00209			±SE (10^{-4} g cm^{-2} s^{-1})	0.00238	0.00289
		PRML (%)	-	**34**			PRML (%)	-	**23.5**
STN+HTN	A3	RML (10^{-4} g cm^{-2} h^{-1})	4.82	3.5	**STN+HTN21**	B3	RML (10^{-4} g cm^{-2} h^{-1})	3.62	2.83
		±SE (10^{-4} g cm^{-2} s^{-1})	0.00147	0.00182			±SE (10^{-4} g cm^{-2} s^{-1})	0.00113	0.00175
		PRML (%)	-	**27**			PRML (%)	-	**21.8**
STN+HTN	A4	RML (10^{-4} g cm^{-2} h^{-1})	4.16	3.93	**STN+HTN21**	B4	RML (10^{-4} g cm^{-2} h^{-1})	5.98	4.89
		±SE (10^{-4} g cm^{-2} s^{-1})	0.00195	0.00138			±SE (10^{-4} g cm^{-2} s^{-1})	0.02624	0.002318
		PRML (%)	-	**5.6**			PRML (%)	-	**18.22**
STN+HTN	A5	RML (10^{-4} g cm^{-2} h^{-1})	3.65	3.37	**STN+HTN21**	B5	RML (10^{-4} g cm^{-2} h^{-1})	6.35	5.35
		±SE (10^{-4} g cm^{-2} s^{-1})	0.001463	0.001589			±SE (10^{-4} g cm^{-2} s^{-1})	0.00172	0.00160
		PRML (%)	-	**7.7**			PRML (%)	-	**15.8**
STN+HTN	A6	RML (10^{-4} g cm^{-2} h^{-1})	3.92	3.1	**STN+HTN21**	B6	RML (10^{-4} g cm^{-2} h^{-1})	7.39	5.79
		±SE (10^{-4} g cm^{-2} s^{-1})	0.00120	0.00181			±SE (10^{-4} g cm^{-2} s^{-1})	0.00173	0.00169
		PRML (%)	-	**21**			PRML (%)		**21.6**

Sample enamel	Scan point		Before exposure to peptide	After exposure to 200 µmol/l	Sample enamel	Scan point		Before exposure to peptide	After exposure to 200 µmol/l
STN21+HTN	C1	RML (10^{-4} g cm^{-2} h^{-1})	3.82	2.95	**STN21+HTN21**	D1	RML (10^{-4} g cm^{-2} h^{-1})	3.14	2.45
		±SE (10^{-4} g cm^{-2} s^{-1})	0.00174	0.00159			±SE (10^{-4} g cm^{-2} s^{-1})	0.00287	0.00256
		PRML (%)	-	**22.5**			PRML (%)	**-**	**28**
STN21+HTN	C2	RML (10^{-4} g cm^{-2} h^{-1})	3.64	2.45	**STN21+HTN21**	D2	RML (10^{-4} g cm^{-2} h^{-1})	3.23	2.57
		±SE (10^{-4} g cm^{-2} s^{-1})	0.00196	0.001764			±SE (10^{-4} g cm^{-2} s^{-1})	0.00219	0.00276
		PRML (%)	-	**32.7**			PRML (%)	**-**	**20.4**
STN21+HTN	C3	RML (10^{-4} g cm^{-2} h^{-1})	2.83	2.25	**STN21+HTN21**	D3	RML (10^{-4} g cm^{-2} h^{-1})	2.87	2.1
		±SE (10^{-4} g cm^{-2} s^{-1})	0.0017	0.00112			±SE (10^{-4} g cm^{-2} s^{-1})	0.00133	0.00174
		PRML (%)	-	**20**			PRML (%)	**-**	**26.8**
STN21+HTN	C4	RML (10^{-4} g cm^{-2} h^{-1})	3.89	2.53	**STN21+HTN21**	D4	RML (10^{-4} g cm^{-2} h^{-1})	3.4	2.55
		±SE (10^{-4} g cm^{-2} s^{-1})	0.0027	0.0025			±SE (10^{-4} g cm^{-2} s^{-1})	0.00147	0.00183
		PRML (%)	-	**34.9**			PRML (%)	-	**25**
STN21+HTN	C5	RML (10^{-4} g cm^{-2} h^{-1})	4.26	3.13	**STN21+HTN21**	D5	RML (10^{-4} g cm^{-2} h^{-1})	4.33	3.3
		±SE (10^{-4} g cm^{-2} s^{-1})	0.002476	0.002139			±SE (10^{-4} g cm^{-2} s^{-1})	0.00174	0.00132
		PRML (%)	-	**26**			PRML (%)	**-**	**24**
STN21+HTN	C6	RML (10^{-4} g cm^{-2} h^{-1})	4.46	3.49	**STN21+HTN21**	D6	RML (10^{-4} g cm^{-2} h^{-1})	4.94	3.9
		±SE (10^{-4} g cm^{-2} s^{-1})	0.00230	0.002182			±SE (10^{-4} g cm^{-2} s^{-1})	0.00138	0.00155
		PRML (%)	-	**21.7**			PRML (%)		**21**

Sample enamel	Scan point		Before exposure to peptide	After exposure to 200 µmol/l	Sample enamel	Scan point		Before exposure to peptide	After exposure to 200 µmol/l
STN+HTN	A1	RML (10^{-4} g cm^{-2} h^{-1})	5.31	4.24	**STN+HTN21**	B1	RML (10^{-4} g cm^{-2} h^{-1})	3.08	2.68
		±SE (10^{-4} g cm^{-2} s^{-1})	0.00194	0.001329			±SE (10^{-4} g cm^{-2} s^{-1})	0.002431	0.002208
		PRML (%)	-	**20.15**			PRML (%)	-	**12.9**
STN+HTN	A2	RML (10^{-4} g cm^{-2} h^{-1})	5.46	3.59	**STN+HTN21**	B2	RML (10^{-4} g cm^{-2} h^{-1})	3.19	2.44
		±SE (10^{-4} g cm^{-2} s^{-1})	0.00173	0.00209			±SE (10^{-4} g cm^{-2} s^{-1})	0.00238	0.00289
		PRML (%)	-	**34**			PRML (%)	-	**23.5**
STN+HTN	A3	RML (10^{-4} g cm^{-2} h^{-1})	4.82	3.5	**STN+HTN21**	B3	RML (10^{-4} g cm^{-2} h^{-1})	3.62	2.83
		±SE (10^{-4} g cm^{-2} s^{-1})	0.00147	0.00182			±SE (10^{-4} g cm^{-2} s^{-1})	0.00113	0.00175
		PRML (%)	-	**27**			PRML (%)	-	**21.8**
STN+HTN	A4	RML (10^{-4} g cm^{-2} h^{-1})	4.16	3.93	**STN+HTN21**	B4	RML (10^{-4} g cm^{-2} h^{-1})	5.98	4.89
		±SE (10^{-4} g cm^{-2} s^{-1})	0.00195	0.00138			±SE (10^{-4} g cm^{-2} s^{-1})	0.02624	0.002318
		PRML (%)	-	**5.6**			PRML (%)	-	**18.22**
STN+HTN	A5	RML (10^{-4} g cm^{-2} h^{-1})	3.65	3.37	**STN+HTN21**	B5	RML (10^{-4} g cm^{-2} h^{-1})	6.35	5.35
		±SE (10^{-4} g cm^{-2} s^{-1})	0.001463	0.001589			±SE (10^{-4} g cm^{-2} s^{-1})	0.00172	0.00160
		PRML (%)	-	**7.7**			PRML (%)	-	**15.8**
STN+HTN	A6	RML (10^{-4} g cm^{-2} h^{-1})	3.92	3.1	**STN+HTN21**	B6	RML (10^{-4} g cm^{-2} h^{-1})	7.39	5.79
		±SE (10^{-4} g cm^{-2} s^{-1})	0.00120	0.00181			±SE (10^{-4} g cm^{-2} s^{-1})	0.00173	0.00169
		PRML (%)	-	**21**			PRML (%)		**21.6**

Sample enamel	Scan point		Before exposure to peptide	After exposure to 200 µmol/l	Sample enamel	Scan point		Before exposure to peptide	After exposure to 200 µmol/l
STN21+HTN	C1	RML (10^{-4} g cm^{-2} h^{-1})	3.82	2.95	**STN21+HTN21**	D1	RML (10^{-4} g cm^{-2} h^{-1})	3.14	2.45
		±SE (10^{-4} g cm^{-2} s^{-1})	0.00174	0.00159			±SE (10^{-4} g cm^{-2} s^{-1})	0.00287	0.00256
		PRML (%)	-	**22.5**			PRML (%)	**-**	**28**
STN21+HTN	C2	RML (10^{-4} g cm^{-2} h^{-1})	3.64	2.45	**STN21+HTN21**	D2	RML (10^{-4} g cm^{-2} h^{-1})	3.23	2.57
		±SE (10^{-4} g cm^{-2} s^{-1})	0.00196	0.001764			±SE (10^{-4} g cm^{-2} s^{-1})	0.00219	0.00276
		PRML (%)	-	**32.7**			PRML (%)	**-**	**20.4**
STN21+HTN	C3	RML (10^{-4} g cm^{-2} h^{-1})	2.83	2.25	**STN21+HTN21**	D3	RML (10^{-4} g cm^{-2} h^{-1})	2.87	2.1
		±SE (10^{-4} g cm^{-2} s^{-1})	0.0017	0.00112			±SE (10^{-4} g cm^{-2} s^{-1})	0.00133	0.00174
		PRML (%)	-	**20**			PRML (%)	**-**	**26.8**
STN21+HTN	C4	RML (10^{-4} g cm^{-2} h^{-1})	3.89	2.53	**STN21+HTN21**	D4	RML (10^{-4} g cm^{-2} h^{-1})	3.4	2.55
		±SE (10^{-4} g cm^{-2} s^{-1})	0.0027	0.0025			±SE (10^{-4} g cm^{-2} s^{-1})	0.00147	0.00183
		PRML (%)	-	**34.9**			PRML (%)	-	**25**
STN21+HTN	C5	RML (10^{-4} g cm^{-2} h^{-1})	4.26	3.13	**STN21+HTN21**	D5	RML (10^{-4} g cm^{-2} h^{-1})	4.33	3.3
		±SE (10^{-4} g cm^{-2} s^{-1})	0.002476	0.002139			±SE (10^{-4} g cm^{-2} s^{-1})	0.00174	0.00132
		PRML (%)	-	**26**			PRML (%)	**-**	**24**
STN21+HTN	C6	RML (10^{-4} g cm^{-2} h^{-1})	4.46	3.49	**STN21+HTN21**	D6	RML (10^{-4} g cm^{-2} h^{-1})	4.94	3.9
		±SE (10^{-4} g cm^{-2} s^{-1})	0.00230	0.002182			±SE (10^{-4} g cm^{-2} s^{-1})	0.00138	0.00155
		PRML (%)	-	**21.7**			PRML (%)		**21**